Deterministic Fast Scramblers

Tomohiro Hashizume

A thesis submitted for the degree of
Doctor of Philosophy

Department of Physics and SUPA
UNIVERSITY OF STRATHCLYDE

February 2023

This thesis is the result of the author's original research. It has been composed by the author and has not been previously submitted for examination which has led to the award of a degree.

Signed:

Date:

Abstract

Fast scramblers are quantum systems which spread many-body entanglement in a timescale which only grows logarithmically with the system size N. As originated in the theoretical investigations of the non-equilibrium properties of black holes, it is conjectured that they set $\mathcal{O}(\log N)$ bound on how fast a physical system can scramble information.

In this thesis, we propose and investigate two deterministic fast scramblers—a Hamiltonian quantum spin system and a Floquet (iterative) quantum circuit. The models we investigate are on a sparsely coupled graph, where two sites are connected if they are separated by an integer power of 2. We show that these models interpolate between nearest-neighbor spin systems in linear (Euclidean) and tree-like (2-adic) geometries. The fast scrambling dynamics, then, emerges as a result of the loss of locality in the models near the point where the underlying geometry transitions.

Furthermore, we investigate how deterministic and fast scrambling dynamics influence the systems' robustness to entanglement destroying operations by performing random projective measurements to the Floquet scrambler. We investigate the critical properties of the measurement-induced phase transitions and dynamically generated quantum error-correcting codes of the model. In both analyses, we found that the fast scrambling dynamics plays a role in protecting the entanglement.

The models we propose can be implemented in the near-term experiments. The Hamiltonian fast scrambler can be implemented with cold atoms in an optical cavity by utilizing the Zeeman shift induced by an external magnetic field. The Floquet fast scrambler can be implemented with cold atoms with optical tweezer array, where a complex geometry is created by systematically changing neighboring atoms through shuffling operations. These models provide rich playgrounds for investigating fast scrambling dynamics and corresponding phenomena in the contexts of both theory and experiment.

Ignoramus et ignorabimus

Emil du Bois-Reymond [1]

Acknowledgements

Throughout my childhood, I was always fascinated by the popular science books written by Susskind, and his open lectures *Theoretical Minimum* that was available through, now discontinued, iTunesU which I was viewing on a small screen of, this is also discontinued, a device called iPod. 10 years later, I cannot believe that I am working on a very topic which the foundational works were laid by the same person that I admire. This cannot have happened without my PhD adviser, Prof. Andrew J. Daley, and I would like to take this opportunity to express my utmost gratitude to him and everything that have he had offered me for the last 5 years. Without you, everything that have happened in this part of my life, wouldn't have happened. I cannot thank you enough.

Now, I would like to dedicate a few sentences to express gratitude to Dr. Gregory S. Bentsen. Without you, honestly, I wouldn't have made this much progress on any of the research that we did. Thank you so much for the time you spend on stimulating discussions, insightful comments, paper recommendations, and helping the paper writing. I know, I wasn't the sharpest tool in the shed, but you have sharpened me well enough to cut the grasses to cultivate a tiny, a very tiny portion of the unknown world. I am still saving a bit of the bourbon that you have given me as a present for the publication of the first, first author paper. I will save it and carry it around until the time we meet in person somewhere in the world!

I then, would like to thank my viva committee: Prof. Dieter Jaksch, Prof. Jonathan Pritchard, and Prof. Kali Wilson, for hosting and organizing the viva, and providing me with the constructive and insightful comments and interesting discussions. It was a very long viva, yet I had a lot of fun discussing and clarifying the details of my research.

I would like to also thank the members of the QOQMS group. I still remember the first day I have ever entered the office of postdocs, and meeting Anton Buyskikh. Without your help, I wouldn't have survived the first year of my PhD. I also remember the first day when the desk was assigned in the room 727 and meeting Araceli, Jorge, Rosaria, and Liviu. And then I was introduced to all the other PhD students, Jack, Jacopo, Matteo, and Stuart. You were all wonderful cohorts and, at the same time, the best partners in crime. I would also like to

thank Prof. Luca Tagliacozzo, Prof. Peter Kirton, and the postdocs: Dr. François Damanet, Dr. Callum Duncan, Dr. Gerard Pelegrí, Dr. Johannes Kombe, and Dr. Natalie Pearson, for various stimulating discussions and inputs. Outside our group, I first would like to thank Dr. Wojciech Roga. I will never forget about all the stimulating discussions on physics and other topics we have had over a pint or a cup of coffee. You have also provided me with so much, including a place to live for cheap in Glasgow, and I will forever be thankful for those. I would also like to thank Dr. Arthur la Rooij for various discussions on physics, and inputs on this thesis. Last but not least, I would like to thank Timothy Briggs for keeping our computational system alive and working all the time. Without you, I wouldn't have had so many results in such a short time!

Outside of Strathclyde I would like to thank Prof. Ian McCulloch, my former supervisor, who, despite me leaving the group, have given me opportunities to collaborate on interesting topics, which unfortunately, couldn't be covered in this thesis. Without you, I wouldn't have met Prof. Jad C. Halimeh, Prof. Debasish Banerjee, and Prof. Philipp Hauke, whom I had great collaborations on the research on lattice gauge theory. I would also like to thank the external collaborators: Sebastian Weber, Prof. Steve Gubser, and Prof. Monika Schleier-Smith for the interesting and stimulating collaborations and discussions.

Finally, I would like to thank all of my friends and I especially want to thank my family, who have supported me through this insane journey. Honestly, I couldn't have done this without you all!

In memory of Prof. Steve Gubser and my grandparents—Hitoshi Seito and Toshiko Hashizume.

Contents

Part I

Introduction

Chapter 1

Introduction

> Until the early 1950s, I was in the grip of the idea that Everything *Is Particles*…, I recall my second period Everything *Is Fields*…, now I am in the grip of a new vision, that everything *Is Information.*
>
> ---
>
> John Archibald Wheeler [2]

“Panta rhei”—everything flows—as it is famously put into words by Heraclitus [3, 4]: every state in a physical system is subjected to a dynamical change. The motivation for Newton in writing *Philosophiæ Naturalis Principia Mathematica* [5], is the formulation of the universal law behind the motion of celestial bodies, which is a symbol of order and at the same time a symbol of change. Beyond mechanics, “no heat flows from a colder to a warmer object” as famously stated by Clausius [6, 7], forms the foundation of thermodynamics, and hence statistical mechanics and condensed matter physics, lie on the observation of macroscopic dynamics, which tends to evolve towards equilibrium. Thus, the study of dynamics has always been at the heart of physics.

One of the key properties of Newton’s equation of motion is in its determinism. As famously put by Laplace [8], this determinism assures the uniqueness of the final state of a system given a complete knowledge of the initial state. This is assured by Liouville’s theorem for the conservation of the phase space volume. Contrary to the classical mechanics, a classical sense of the determinism is forbidden due to the Heisenberg’s uncertainty principle [9, 10]. However, the determinism in the evolution of a quantum state is assured by the unitarity of Schrödinger’s equation [11] in the absence of dissipation. Thus, similarly to classical mechanics, quantum mechanics, the microscopic laws of physics, assures the determinism up to the measurement. The classical determinism and the unitarity of quantum mechanics assures the information embedded in the initial state is conserved in the physical world.

The laws of thermodynamics [12–14], however, predict the existence of processes with loss of information. How the arrow of time [12] emerges from an underlying deterministic, irreversible, and unitary microscopic dynamics, has been one of the big underlying questions in statistical mechanics. As Anderson stated in the article *More Is Different* [15], there seems to be a whole region between microscopic single body physics and macroscopic many-body physics that we do not yet understand.

The reconciliation of the thermodynamic principles from quantum mechanics has been one of the major focuses in the field of condensed matter physics. The attempts started from the studies of classical chaotic systems [16–19] and ergodic hypotheses [20–23], and they are expanded to their quantum analogues—quantum chaos [24–28] and the eigenstate thermalization hypothesis [28–30]. Such theoretical developments revealed dynamical natures of mesoscopic systems as well as revealing the constituents of both classical and quantum chaotic systems.

1.1 Fast Scramblers

The laws of physics, at a microscopic level, are reversible. Reversibility implies that the laws of physics do not have a preferred direction in time. However, in a macroscopic level, the second law of thermodynamics tells us of the existence of irreversible processes. In the thermodynamics, the degree of irreversibility is quantified by the change in thermodynamic entropy of an isolated system, which does not decrease in a process. The emergence of irreversible thermodynamic processes from the reversible microscopic laws of physics has long been an active topic of research [28, 30–32].

One important theoretical discovery that connects the reversible microscopic dynamics and the irreversible macroscopic dynamics came from the study of the dynamics of black holes [33–41]. The concept of black hole complementarity [42–45] is a paradox which comes from the randomness of thermal Hawking radiation [42, 43] of a black hole and the unitarity of quantum mechanics.

A black hole is a celestial body, which forms as a result of a gravitational collapse of a massive star. Due to its large gravitational force, the escape velocity exceeds the speed of light and entraps anything that passes the Schwarzchild horizon within it. Since no particles whether massless or massive, cannot get out of a black hole, the information carried by those particles seems to be lost forever. However, a black hole is known to radiate [42, 43]. The radiation is thermal, and has a profile corresponding to a black body with a temperature that is inversely proportional to the surface area of the black hole.

The thermal nature of the Hawking radiation posed a contradiction to the unitarity of quantum mechanics, because it implied the destruction of information. This paradox was suggested by Page [46] and formulated in the late 1900s by Susskind, and it is called black hole complementarity [44–46]. This is because a truly thermal state does not contain information since its property depends only on one parameter, the temperature of a system. One may argue that extra information may be stored in other features of a black hole. However, due to the *no hair* theorem [40, 47], a black hole can only have four physical parameters: mass, angular momentum, charge, and temperature [42, 43]. Thus in the mid 1900s, the reconciliation of two apparently contradicting ideas—thermal and information destroying Hawking radiation, and information conserving quantum mechanics—was a topic of discussion.

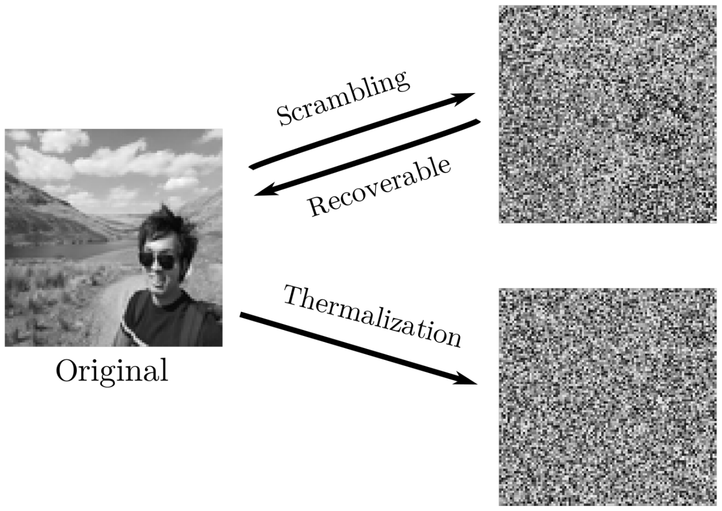

Figure 1.1: **Scrambling and Thermalization** An image is scrambled by permuting two pixels sequentially for 10^4 times (top). The image with the same intensity profile as the original image but generated randomly (bottom). In the case of scrambling, the original image (i.e. the information in the initial state) can be recovered by inverting the permutations. When the image is thermalized with an external reservoir, such an operation for recovering the original image is not possible.

Resolution has been proposed by Susskind in 1990s, through a holographic interpretation of the Bekenstein-Hawking entropy (BH entropy) of black holes [48–51]. The holographic principle states that the information is embedded at the surface. The problem, however, remained, because the principle implied a cloning of quantum information onto the Schwarzschild horizon of a black hole.

The cloning paradox goes as follows. Imagine Alice with her qubit, and she is just about to pass the horizon. If the black hole is massive (large) enough, then for her, she wouldn't detect that she has passed the horizon, because the spacetime is locally flat. Therefore, her qubit is not expected to be disturbed, and remains with her beyond the Schwarzchild horizon. However, for an external observer, Bob, who is at a point far away from the horizon, it will look as if the qubit is stuck on the surface of the horizon. Thus, there exists two identical qubits in the system—one on the surface and one with Alice. This directly contradicts the no-cloning theorem of quantum information [52].

An attempt to resolve the quantum information cloning paradox was made by Susskind, Thorlacius, and Sekino by considering the timescale necessary for the observer outside a black hole to recover the quantum state out of the Hawking radiation [53, 54]. In order to avoid the cloning, the shortest time allowed for the complete retrieval of information must be longer than the time for any observers who are present to fall behind the horizon. The retrieval time, t_{ret}, turns out to scale like $t_{\mathrm{ret}} \propto \log N$, where N is the number of degrees of freedom (i.e. number of particles); and the timescale t_{ret} is dual to the scrambling time, which is the time it takes for a perturbation to spread over all the degrees of freedom of a system. This implies that black holes are scramblers which can spread information, or a perturbation, exponentially fast with respect to the system size [53–55].

1.1.1 Scramblers

A scrambler [53, 54, 56] is a physical system which spreads the information over its degrees of freedom. To give an example of a scrambler, a system which exhibits diffusion or ballistic transport are scramblers so long as the system is isolated and no information from the initial state is lost.

In the information theory, the information typically comes in “bits” consists of 0s and 1s [57, 58]. In order to physically manipulate and transfer the information, these bits must be encoded into physical states of a system which represent the strings of 0s and 1s. Initially localized information is, therefore, the bits that are encoded in a locally accessible states, and scrambling dynamics further encode them into states in a larger state space spanned by the entire system.

In this context, the conservation of information in a closed system is assured by Liouville’s theorem in the classical mechanics and the unitarity in the quantum mechanics [51]. The description of a state of a system is self-consistent and does not require the help of an external system. This fails when a component of a system, such as particles and energy, escapes into the external reservoir; in this case, the information is lost.

A fundamental difference between the processes of thermodynamics and scrambling is the conservation of information inscribed in the initial state. As depicted in Fig. 1.1, scramblers conserve the information about their initial state throughout its dynamics [45, 51, 53, 59]. However, when a system thermalizes, the information is lost into a reservoir or when the microscopic features are ignored, and the recovery of the initial state becomes impossible [51].

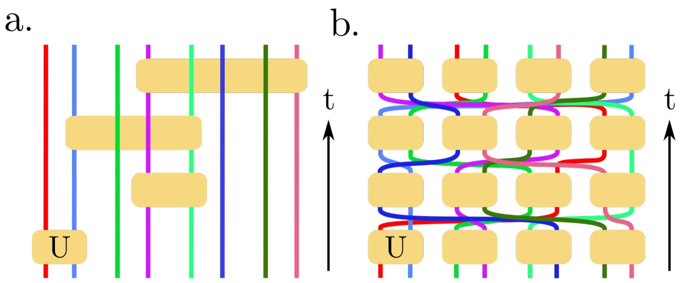

FIGURE 1.2: **The two formulation of random all-to-all circuits.**
a. A realization of a random all-to-all circuit. At each layer, a randomly chosen pair of qubits, where the world line of each qubit is represented by a colored line, is evolved by a randomly chosen unitary gate (orange squares). b. Parallelized random all-to-all circuit. At each layer, $N/2$ non-overlapping pairs of qubits are evolved under $N/2$ randomly chosen unitary gates in parallel. Here the time t is measured as the number of layers in the circuit.

The process of scrambling has the corresponding timescale, called the scrambling time t_*, for initially localized information to spread across the degrees of freedom N. In the slowest limit, we have localized systems [60–63] where the scrambling time increases exponentially with N, $t_* \propto \exp N$. The scrambling time of diffusive processes grow polynomially, $t_* \propto N^{\frac{2}{D}}$, where D is the physical dimension of the system. Ballistic transport has the scrambling time which still scales polynomially $t_* \propto N^{\frac{1}{D}}$. In the fastest limit, we have fast scramblers where the scrambling time grows logarithmically $t_* \propto \log N$. The fast scrambling conjecture states that fast scramblers are the fastest dynamical process which spread information over the system in the timescale $t_* \propto \log N$ [53, 54], and black holes are conjectured to saturate this bound.

1.1.2 Fast Scramblers

The fast scrambling conjecture motivated the search for other models that saturate the fast scrambling bound ($t_* \propto \log N$). A classical example of such a system was already know, and it is a special case of spreading of diseases ($\risingdotseq$ information) in a population [55, 64]. When the population is large and the recovery rate of the disease is 0, which is commonly known as the SI model in the field of epidemiology [65], the number of infected people increase exponentially at the beginning, followed by the saturation of the infected individuals (analogous to the information holding individuals) in the population.

A quantum mechanical analogue of the model and a prototypical example of a quantum fast scrambler is a circuit consists of random two-qubit gates. A randomly coupled all-to-all circuit [53, 55, 59], is illustrated in Fig. 1.2 a. and b., is an N-qubit system that is subjected to a random unitary evolution. Here a qubit is a two-level quantum systems which holds the information in terms of quantum-bits, "qubits", where 0 and 1 are represented by the two states of a qubit [66].

One way to realize such a circuit is, at each layer, to evolve a random pair of qubits evolves with a randomly chosen unitary operator as shown in Fig. 1.2 a. Here the time is proportional to the number of circuit layers, or also called the depth of the circuit. The depth of the circuit therefore measures the total time which the state is evolved in the unit of time. In this circuit realization, only one gate is applied at each layer of the circuit.

The information encoded in the qubits propagate through the circuit by the unitary gates in the form of a correlation, or equivalently known as an entanglement. When a random unitary gate is applied to a pair of qubits, the two qubits almost always get entangled when they are not previously in contact. The information propagates through the system whenever qubit that is already correlated to the information gets entangled with a non-correlated qubit. In this random circuit, in order for the information localized at a qubit is completely scrambled, $\mathcal{O}(N \ln N)$ layers are required [53, 59].

This process can be made more efficient by allowing the parallel applications of random unitary gates on $N/2$ non-overlapping pairs of qubits at each layer, as depicted in Fig. 1.2 b. This reduces the total circuit depth required for initially localized information to spread. In this case, the required time (=circuit depth) scales like $\mathcal{O}(\ln N)$ [53, 59], and hence this model is a fast scrambler. We call this model a random all-to-all circuit. This process is not restricted to the random two-qubit gates, and this is generally true for gates over any finite number of qubits [53, 59][1].

The proposal of the fast scrambling conjecture and the discoveries of the concrete examples from quantum circuit and potential continuous time model such as black holes which saturates the bound, lead to the search of other realizations of fast-scramblers in both the theoretical and the experimental realm. Especially, the

---

[1] The change in the number of qubits on which a gate acts, only change the base of the logarithm. The constant factor will be absorbed into the constant of proportionality which differed for an individual model or an implementation.

construction of Hamiltonian, hence deterministic, fast scramblers were in great interest due to its implications not only in the high-energy physics, but also for their implications in condensed matter physics. One of the early examples of Hamiltonian fast scramblers was discovered by Kitaev. It is a model now known as the Sachdev-Ye-Kitaev model (SYK model) [67–69], a model of interacting Majonara fermions with random nonlocal 4-body interactions.

The existence of the Hamiltonian fast-scrambler implied the existence of a bound to the speed of which a state can evolve. A system with rapid evolution of a state with extreme sensitivity to an initial state is called a chaotic system. One way to quantify how fast information scrambles in such a system is to look at how operator evolves in time, which can be quantified by the Out-of-Time-Order Correlator (OTOC). The OTOC is related to the magnitude of a commutator of local operators in two different points of space and time, where large OTOC implies strong mixing of local operators, and hence strong information scrambling. The SYK model has a property which the growth of OTOC saturates the fastest bound called Maldacena-Shenker-Stanford bound in the limit of the large number of fermions; the timescale of the saturation of OTOC in the SYK model scales like $t_* \propto \log N$ [70, 71].

Although the SYK model is Hamiltonian in nature, it still relies on random interactions and disorder averaging. The discovery of the SYK model assured the existence of the Hamiltonian fast scramblers and led to the intensive search for other realizations of them. As a result, completely deterministic fast scramblers have later found in various condensed matter systems such as atoms in an optical cavity with quasiperiodic interactions [72] and spins interacting with long-range interactions with terms which break a permutation symmetry [73, 74].

1.2 Fast-Scrambling Dynamics on a Sparsely Coupled Graph

In this thesis, in order to model the fast scrambling dynamics, we take an approach based on a model on a sparsely coupled graph proposed by Gubser *et al.* [75]. The model interpolates between the two incompatible geometries—linear and treelike. It is inspired by the p-adic version of the Anti-de Sitter/Conformal Field Theory (AdS/CFT) the correspondence. The AdS/CFT correspondence [53, 76–78] is

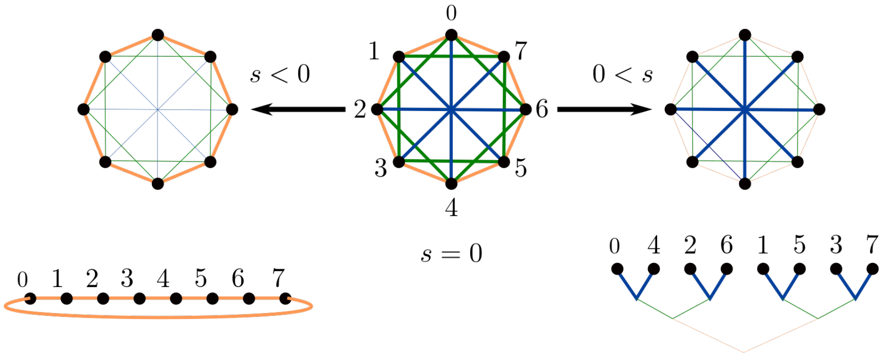

FIGURE 1.3: **Two limits of the sparsely coupled interaction graph.** A sparsely coupled interaction graph, $J_{\text{sp}}(i-j)$, with a tunable parameter s. A nearest neighbor in the familiar linear (Euclidean) geometry is recovered in the limit of $s = -\infty$ (left). In the limit of $s = \infty$, the interaction becomes nearest neighbor in a treelike geometry (right). At $s = 0$, the geometry is neither linear nor treelike.

a conjecture from a theory of quantum gravity, which conjectures that there is a duality between the geometry of Anti-de Sitter space [40] and a strongly correlated quantum system living at the edge of the space. The conjecture is studied in the various settings, and one of the studies are done in a geometry which is governed by p-adic distance as a measure of the closeness of matter (c.f. Ch. 2.6). A simpler treelike structure of spacetime, which emerges from the geometry governed by the p-adic distance, is hoped to provide a simple yet rich playground for understanding various aspects of the correspondence.

The key idea behind the sparsely coupled model lies in the incompatibility in the notion of “locality” in the two geometries—linear and treelike. The principle of locality in the field of physics states that a change in physical state at a give point only affects its immediate surroundings and does not immediately affect something in distance by skipping matters (fields) in between [36, 79–86][2]. In the case of the linear (Euclidean) geometry, a perturbation given at an origin propagates the space and affect the surroundings from the points which has small Euclidean distance from the origin to the points that have large Euclidean distance (Fig. 1.3 left). In the case of the treelike (p-adic) geometry, on the other hand, the notion of distance is related to the number of edges (branches of the tree) between the two

---

[2] Here we are not discussing violation of Bell’s inequality caused by the measurement of a quantum state in space-like separated points. The limitation on how information travels is strictly given by the Einstein’s theory of relativity, which does not allow transmission faster than the speed of light or the deterministic teleportation of information without a classical communication channel. For a review and discussion on this topic, c.f. [84].

qubits as shown in Fig. 1.3 right [75, 87, 88]; the definition of the p-adic distance is discussed in detail in Ch. 2.6.

In the case of the treelike geometry, the distance between qubit i and qubit j decreases as the number of times which $|i-j|$ can be divided by p increases. This property makes treelike geometry to be fundamentally incompatible with the linear geometry, because the qubits that are close in the treelike geometry is far away when they are ordered in the linear geometry [75]. Inspired by this incompatibility of locality in these geometries, Gubser *et al.* [75] have observed a similarity between a field theory governed by p-adic numbers and a model on a sparsely coupled graph in certain limits. The Hamiltonian of the Gubser's sparsely coupled model is

$$H = \sum_{ij} J_{\mathrm{sp}}(i-j)\phi_i\phi_j - \sum_j \phi_j, \tag{1.1}$$

where ϕ is a real scalar field. The interaction function $J_{\mathrm{sp}}(i-j)$ is defined on a sparsely coupled graph as depicted in Fig. 1.3 (middle), where two-body interactions only occur if and only if the site indices are differ by integer powers of p:

$$J_{\mathrm{sp}}(i-j) = \begin{cases} |i-j|^s & \text{when } |i-j| = p^n,\ n = 0,1,2,3,\cdots \\ 0 & \text{Otherwise} \end{cases}, \tag{1.2}$$

with $p = 2$.

The model interpolates between two geometries with incompatible notions of locality by tuning a parameter $s \in \mathbb{R}$. Gubser *et al.* [75] have shown that the spectrum of the model converges to the nearest-neighbor model in the linear (Euclidean) geometry in the $s = -\infty$ limit (Fig. 1.3 left), while it converges to the nearest-neighbor model in the treelike ($p = 2$-adic) geometry in the limit of $s = \infty$ (Fig. 1.3 right).

As s is tuned, the model must undergo a transition in its underlying geometry. The conjecture which is investigated in this thesis is, that such a transition in analogous fully quantum mechanical systems, occurs at $s = 0$. At the critical point (or in the critical region), we show that the model is fast scrambling because the notion of locality is no longer well defined at such a point—the underlying geometry is neither linear nor treelike. Furthermore, we show that in this limit, the fast scrambling dynamics can be observed without relying on random interactions.

1.3 Towards Simulating and Observing the Deterministic Fast Scramblers

The technological advancements of hardware and algorithms in both classical and quantum computing have made studies of strongly correlated quantum systems possible [89–107]. However, due to the incompatibility between the geometry of the sparsely coupled models and the Euclidean nature of the space where the physical world resides, constructing an experimental procedure for simulating and observing the quantum mechanical nature of considered models are challenging. Furthermore, the numerical simulation of the fast scramblers in the fully quantum regime is also a challenge due to the exponentially increasing degrees of freedom associated with the rapidly growing entanglement across the available degrees of freedom.

These constrain the state-of-art numerical methods such as Matrix Product States (MPS) [91, 92, 97, 108–116], due to the quickly spreading entanglement across the system. In this thesis, we propose various models of deterministic fast scramblers, and verify their dynamics numerically using extended MPS methods which efficiently compute the correlators for short timescale. In addition, we use the methods on a restricted subspace, namely the stabilizer state algorithms [90, 117–119], which can simulate thousands of spins for the restricted operations. Possible experimental implementations of the deterministic fast scramblers accessible in near-term experiments using cold atoms are also discussed.

1.4 Beyond the Unitary Dynamics

The efficiency of a quantum system in spreading entanglement is closely related to how sensitive the system is to the local erasure of information during dynamics. In recent years, the effect of competition between scrambling dynamics, which generates many-body entanglement, and processes such as local measurements, which destroy the entanglement, has attracted great interest. The Measurement-Induced

Phase Transition (MIPT) [119–124] is a phenomenon which occurs as a result of such a competition. In MIPT, the entanglement structure of the steady state transitions sharply from the volume-law entanglement to the area-law entanglement due to excessively applied local measurements. Since its discovery, the study of MIPT has been extended to purification dynamics [125], and the properties of the dynamically generated Quantum Error-Correcting Codes (QECCs) [125, 126]. Those studies revealed that the critical points and its associated universality class depend largely on the underlying geometry of a system, and with the right geometry, a system can protect the many-body entanglement being destroyed from the excessive local measurements.

In the context of deterministic fast scramblers, a natural question to ask is how the properties of MIPTs and dynamically generated QECC are affected by the underlying fast scrambling dynamics and determinism. In the literature, the effects of fast scrambling dynamics on random models have been investigated through the studies of MIPTs in the SYK model [127–129] and random circuits [123, 124, 130]. The effects of determinism are also investigated in the local nearest-neighbor circuits [121, 122] and integrable fermionic models [131, 132]. These studies revealed that long-range interactions enhance the system's ability to protect entanglement, and a possibility of detecting the transitions without relying on the random interactions and random local measurements.

Fast scrambling dynamics also have an effect on the properties of dynamically generated QECCs. A quantum system is susceptible to noise, and therefore removal of errors on a quantum state due to such noise is a crucial procedure in order to have a working quantum computer. Quantum error correction is a procedure for detecting and correcting such errors, and this is done by encoding a state in to much more qubits, in a way which an error can be detected through a measurement on one of the redundant qubits that span a code space [66, 117, 118, 133, 133]. The QECC defines how a state is mapped to a state in a code space. The code rate is the ratio between the number of logical qubits that are stored in a state and the actual number of qubits that are required to represent a state, and the code distance quantifies how many errors must be introduced until the errors are no longer correctable.

The effects of deterministic fast scramblers with nonlocal interactions on the MIPTs are still remained as a gap in the literature. Thus our interest is on how the properties of MIPTs change as a model transition from being a deterministic local scrambler to a deterministic nonlocal fast scrambler. The circuit which has high MIPT critical points and long code distances can provide a reliable way of generating the highly entangled states, while having little or no effect from the local decoherence in the process. The generated highly entangled states in the subcritical regime are known to be used as resources for quantum computing [134, 135]. In this thesis, we investigate the MIPTs and the QECC properties of the sparsely coupled model by tuning the parameter which controls the maximum distance of the long-range coupling. We show that the introduction of nonlocal couplings significantly increases the MIPT critical point, while keeping the universality class of the transition to remain in 1+1-dimension. We also show that, when the underlying circuit is fast scrambling, the code distance becomes extensive for a fixed code rate (i.e. the amount of information in the code).

1.4.1 Towards Numerically Simulating the Fast Scrambling Dynamics

As the technology for classical computing advances, it allows the numerical simulations of quantum systems beyond the regimes where properties of physical systems are analytically tractable [89–91, 94, 136]. These numerical techniques are used to predict and verify various experimental and observational outcomes [137–140]. In order to verify that the proposed models are fast scrambling, the prediction of the logarithmic scaling on various correlators which quantify the entanglement across the system, are necessary. However, due to the exponentially increasing dimensions of the Hilbert space with respect to the system size, simulation of large-scale quantum dynamics are difficult.

To go beyond the exact diagonalization while not destroying the quantum mechanical nature of the model, there exists various numerical techniques. Such methods include the Density-Matrix Renormalization Group (DMRG) algorithm [89, 141], which has been uncovering the ground state properties of strongly correlated systems. The algorithm is extended and reformulated using MPS [109–111, 113, 142], which is a representation of quantum states, that accurately captures the area-law entangled states in one dimension. This made the algorithm more accessible and even more expandable beyond the ground state search. One key expansion is the invention of algorithms for simulating the exact dynamics. Such algorithms include time evolving block decimation algorithm [143] and time-dependent DMRG [91].

Although the MPS are best at efficiently representing a state that is sufficiently localized, there are attempts on expanding the algorithms beyond such constraints [92, 94, 97, 144–147]. In recent years, a time evolution algorithm based on the Time Dependent Variational Principle (TDVP) [94, 97, 116, 144, 148] made the efficient time-dependent simulation of MPS beyond the locally interacting systems, possible.

In spite of the developed state-of-art MPS algorithms, simulating systems with strong long-range interactions beyond one hundred qubits or short times is still challenging. To go beyond this limit, and to see the emerging scaling, we adopt techniques from the field of quantum information. Clifford circuits [118, 149] are a class of circuits which acts on a restricted subspace spanned by the states called stabilizer states. The circuit maps tensor products of Pauli operators called a Pauli string, to some other Pauli string. When the circuit acts on stabilizer states—N-qubit states which are uniquely defined by the simultaneous eigenstate of N Pauli strings—the dynamics is known to be simulated efficiently using a classical computer in polynomial time because of the Gottesman-Knill theorem [90, 118, 149, 150].

Despite the reduced degrees of freedom in the Clifford circuits, they are known to exhibit rich features that are unique to the quantum mechanics, such as quantum entanglement [119, 121–124, 126, 151–157]. Furthermore, the dynamics on random Clifford circuits well approximates the dynamics of the general quantum random circuits because random gates in the Clifford algebra follow unitary 2-design [151, 158, 159]. Thus, they are used to efficiently simulate the entanglement spreading in various quantum systems [119, 160, 161], purification process [123], and dynamics that are subjected to the projective measurements [119–124].

1.4.2 Towards Experimentally Observing the Fast-Scrambling Dynamics

The technological advancement in atomic, molecular, and optical physics made the precision manipulations of atoms and photons possible [96, 162–172]. Experimental platforms such as trapped ions [96, 162, 164, 165], atoms in an optical cavity [166, 170–172], and Rydberg (neutral) atoms [163, 167–169], made probes of both static and dynamical properties of systems with tunable continuous long-range interactions in one and higher dimensions, possible.

However, due to the dimensional and locality constraints that are imposed by the nature, experimental realization of non-continuous long-range interactions, which appears on a sparsely coupled interaction graph, is a challenge. In order to overcome this problem, and to realize the sparsely coupled quantum systems, two different approaches are proposed in this thesis. One is an approach based on proposal [166] using atoms in an optical cavity. In this approach the atom-atom interactions are mediated by the photons in a cavity. By adding a linear magnetic field gradient, the detuning in the energy levels induced by the gradient forbids all the interatomic interactions mediated by the Raman process, except for the atoms that are at the right distance from one another, hence with the right detuning. This enables us to create tunable long-range interactions, where the interaction strength is tunable for every available interatomic distances.

Although the speed of light is still the limit on how fast the atoms can interact, this timescale is vanishingly small in comparison to the timescale set by the strength of the interaction, which is typically of $\mathcal{O}(100)$ μs [102]. Thus, the $\log N$ scaling of the scrambling time at the fast-scrambling limit is expected to persist for any system size for the constant interaction strength, making the realization a fast scrambler with the physical time. Furthermore, a protocol for measuring the OTOC is also proposed for such an experimental setup using echoes and time reversal dynamics [173], making it an ideal experimental platform for simulating and detecting the fast scrambling dynamics.

The other approach we take in this thesis utilizes the manipulations of neutral atoms using optical tweezers [105, 174, 175]. The non-trivial couplings are induced by shuffling of atoms and implementing local interactions. The rich geometries which emerge upon carefully engineered shuffling procedures, provide a playground for both experimental and theoretical condensed matter physics [104, 105, 175, 176]. With this scheme, we show that the interaction on a sparsely coupled graph is naturally recovered with Faro shuffling [177] and nearest-neighbor interactions via van der Waals interactions of Rydberg states [163, 168, 178–180].

Unlike the atoms-in-cavity approach, the Hamiltonian of this approach is iterative and time-dependent (Floquet), making the system to behave as an iterative quantum circuit. Due to the necessity for the shuffling of atoms for realizing the effective long-range interactions, the transport time makes the implementation of the scheme to scale linearly with the system size. However, the problem on scaling can be overcome by adjusting the physical time between the layers to the worst transport time which happens at the largest system size. Although this experimental realization is not "fast" in the physical time, the long coherence time of the atomic qubits and the fact that the realization only rely on the nearest-neighbor gates make the procedure reliable and scalable for implementing long-range and fast-scrambling quantum circuits in the near term experiments. Furthermore, The protocols for detecting the scrambling time in the quantum circuits are also known in this approach, which is the quantum teleportation protocol [59, 181, 182]; this is also explored in this thesis.

1.5 Overview

Inspired by Gubser's field theoretical model on a sparsely coupled graph, in this thesis, we propose deterministic fast scramblers and investigate their dynamical properties. We investigate two implementations: one is a Hamiltonian fast scrambler, which can be implemented in near-term experimental platforms with atoms in an optical cavity, and the other is a Floquet (quantum circuit) fast scrambler, which can be implemented in near-term experimental platforms with cold atoms in arrays of optical tweezers. The rest of the thesis is divided into four parts: the theoretical background is discussed in the first part (Part II), research results are discussed on the following two parts (Part III and Part IV), and finally we conclude and give an outlook in Part V.

In Part II, we introduce background theories on fast scramblers. In Ch. 2, we review first, the entanglement entropy in quantum systems, then we introduce fast scrambling conjecture and the constraints which prohibit fast scrambling in local systems. We also discuss how the locality can be broken by introducing a sparsely coupled model which naturally interpolates between two geometries with incompatible notions of geometry. In Ch. 3, we connect the fast scrambling dynamics to the chaotic quantum systems and review how the chaotic dynamics has been diagnosed in quantum systems with non-trivial correlators and properties of random matrices. Finally, in Ch. 4, we introduce the numerical methods that are used in this thesis for verifying and quantifying the fast scrambling dynamics.

In Part III we look at two implementations of the deterministic fast scramblers. First, we propose a fast scrambling quantum spin Hamiltonian on a sparsely coupled graph, which can be implemented with atoms in an optical cavity (Ch. 5). We show that, by tuning the interaction strengths, the underlying geometry of the model transitions from linear to treelike; and at the transition the model becomes a fast scrambler due to the loss of notion of locality. We show that in the fast scrambling limit, the underlying level statistics of the Hamiltonian becomes chaotic, and emergent logarithmic lightcone in few and many-body regimes. Then in Ch. 6, we introduce a Floquet scrambler on a sparsely coupled graph, which is dual to a quantum circuit. In this Floquet formulation, we first investigate a family of random circuits on a sparse coupling graph with a parameter which tunes the underlying geometry. By studying the entanglement structure and teleportation properties, we show that the fast scrambling dynamics also emerges at the point where the underlying geometry transitions. Then we discuss how the model can be implemented in the near-term experiment with atoms in optical lattice and optical tweezers. Finally, we show that fast scrambling dynamics persist even in the limit where all the gates are replaced with a deterministic set of gates, which makes the circuit a Floquet fast scrambler.

In Part IV, we investigate the non-unitary dynamics of the deterministic fast scramblers. In Ch. 7, we investigate the competition between the scrambling dynamics, which tends to spread many-body entanglement across different degrees of freedom in the system, and local measurements, which act to destroy the entanglement. This is done by studying the MIPTs and the properties of dynamically generated QECCs on a sparsely coupled model. We investigate three different MIPTs on a deterministic circuit which interpolates from a local slow scrambler to a nonlocal fast scrambler, and study how introductions of longer nonlocal couplings in the model affect the critical properties of the MIPTs. We then study the code properties of the dynamically generated QECCs of the deterministic fast scrambler with infrequent measurements, and show that the code distances become extensive in the fast scrambling limit. We show that the robustness towards the local projective measurements can be significantly increased just by adding $\mathcal{O}(1)$ nonlocal interactions to each qubit.

Finally in Part V, we conclude this thesis with summary and outlook.

1.6 Contributions During the PhD

The author of this thesis has contributed to the following publications and presentations for the completion of this PhD.

1.6.1 Publications on the Works Related to this Thesis

- G. Bentsen, T. Hashizume, A. S. Buyskikh, E. J. Davis, A. J. Daley, S. S. Gubser, and M. Schleier-Smith, "Treelike interactions and fast scrambling with cold atoms," *Physical Review Letters,* **123**, 130601 (2019). [183].

  The author of this thesis produced the data for the figures 2 and 3 of the article, has written part of the corresponding texts, and has produced the data and written the text on section II. B. (Fig. S2) of the supplementary material.

- G. Bentsen, T. Hashizume, E. J. Davis, A. S. Buyskikh, M. H. Schleier-Smith, and A. J. Daley, "Tunable geometries from a sparse quantum spin network," in *Optical,Opto-Atomic, and Entanglement-Enhanced Precision Metrology II*, edited by S. M. Shahriar and J. Scheuer (SPIE, San Francisco, United States, 2020) p. 138. [184].

  The author of this thesis has drawn the figure 2, has produced the data for the figures 3 and 4, and has written the texts for the corresponding captions and the sections.

- T. Hashizume, G. S. Bentsen, S. Weber, and A. J. Daley, "Deterministic Fast Scrambling with Neutral Atom Arrays," *Physical Review Letters,* **126**, 200603 (2021). [185].

  The author of this thesis has produced the data for the figures 1, 2, 3, and 3, has written the corresponding texts in the main text, and has written and produced the data for the sections III, IV, and VI a. of the supplementary material.

- T. Hashizume, G. Bentsen, and A. J. Daley, "Measurement-induced phase transitions in sparse nonlocal scramblers," *Physical Review Research,* **4** 013174 (2022). [186].

  The author of this thesis has produced all the data and text of the corresponding figure captions, and has written the sections II, III, IV, V, and VII.

The author of this thesis has also contributed to the part of the texts of the other sections, as well as all the appendix excluding the section E.

- T. Hashizume, S. Kuriyattil, A. J. Daley, and G. Bentsen, "Tunable Geometries in Sparse Clifford Circuits," *Symmetry,* **14**, 666 (2022). [187].
  The author of this thesis has produced the data for the figures 3 and 4, has written the sections 4 and 5, and has contributed to the various parts of the texts of the main text. The author of this thesis has also written the sections B, E, F, G, H, and I of the appendix.

1.6.2 Presentations on the Works Related to this Thesis

Poster DesOEQ Annual Meeting & DOQS Workshop, October 2018, University of Strathclyde, Glasgow, UK,

Poster DesOEQ mid term review, March 2019, University of Strathclyde, Glasgow, UK.

Poster SUPA annual gathering, May 2019, University of Strathclyde, Glasgow, UK.

Presentation University of Waterloo and Strathclyde Research Colloquium, November 2020, University of Waterloo, Waterloo, Canada, University of Strathclyde, Glasgow UK.

Presentation APS March Meeting, March 2021, virtual (Chicago, USA).

Poster PQI, April 2021, virtual (Pittsburgh Quantum Institute, Pittsburgh, USA).

Presentation APS DAMOP Meeting, May 2021, virtual (Orland USA).

Poster Boulder Summer School, July 2021, virtual (Boulder USA).

Presentation DesOEQ 2021, September 2021, University of Strathclyde, Glasgow, UK.

1.6.3 Other Publications

- T. Hashizume, I. P. McCulloch, and J. C. Halimeh, "Dynamical phase transitions in the two-dimensional transverse-field Ising model," *Physical*

Review Research, **4**, 013250 (2022). [188].
The author of the thesis produced all the data in the main text and the appendix, has written the captions of the corresponding figures, and has contributed to the parts of the main text.

- T. Hashizume, J. Halimeh, P. Hauke, and D. Banerjee, "Ground-state phase diagram of quantum link electrodynamics in (2+1)-d," *SciPost Physics*, **13**, 017 (2022). [189].
  The author of this thesis has produced all the figures and the data for the paper, and has written most of the main text and the appendix.

1.6.4 Other Presentations

Presentation Visiting Dr. François Damanet, virtual (University of Liège, Liège, Belgium).

Part II

Background

Chapter 2

Quantum Entanglement and Fast Scrambling Dynamics

> When you have eliminated the impossible, whatever remains, however improbable, must be the truth.
>
> Sherlock Holmes [190]

Entropy is first introduced in statistical mechanics, in order to quantify the number of microscopic states which contributes towards a macroscopic state. This quantity was generalized by Shannon [57] for quantifying the amount of information which certain systems (messages) hold. Whether these two quantities—one describes the physical state, and one describes abstract mathematical properties—represents the same quantities or not, has been the interest for both physicists and information theorists [191–193].

In quantum mechanics, an ensemble of states can be defined in which entropy can be well-defined due to its probabilistic feature. With such a property quantum information theory can be formulated with its own notion of entropy [79, 80]. Quantum entanglement [11, 79, 80, 194, 195] is one of the properties of the entropy of quantum states which distinguishes the classical notion of entropy to that in quantum systems. With Quantum entanglement, one can introduce long distance correlations which cannot be increased through local operation and classical communication. Since its discovery, how such a *strange correlation* plays fundamental role in physical systems has been a topic of research across various fields of physics.

One important aspect of entanglement which we focus in this thesis is the dynamical generation of entanglement. In quantum systems with local interactions, the speed of which entanglement can be generated across different parts of the system is restricted by the Lieb-Robinson bound [81, 196–198]. The bound restricts the distance which correlation can reach to increase linearly in time with velocity v_s. Since the "distance" between sites is a quantity which is defined by the underlying geometry of a system, dynamics of the system often provides insight into the underlying geometry and locality of the system [102].

The fast scrambling conjecture is another bound which limits on how fast different parts of a system can be entangled [53, 54]. The conjecture states that the time t_* for the information to be scrambled across the system cannot scale faster than $t_* \propto \log N$, and black holes are physical systems which saturate this bound. Due to the Lieb-Robinson bound, however, reaching this bound with systems consisting only of finite short-range interactions, is impossible. Therefore, the notion of locality in the model must be broken in order to reach the fast scrambling limit.

In this chapter, we introduce the theory of quantum entanglement entropy, and restrictions in its dynamical properties which comes from the locality of the underlying geometry. We also review an attempt on breaking such restrictions to reach the fast scrambling limit by introducing a model which interpolates between the geometries with incompatible notions of locality. The rest of this chapter is structured as follows: in §2.1, we introduce classical information theory. Then in §2.2 the measures of classical information are expanded to the quantum information. In §2.3, we introduce the notion of locality defined by the metric of the underlying geometry of a model, and the Lieb-Robinson bound, where we show how an area-law entangled state can dynamically reach volume-law entanglement. In §2.4, we introduce the fast scrambling conjecture. The notion of a lightcone is introduced in §2.5, and its version for systems with long-range interactions with an emergent polynomial lightcone is reviewed. Then, in §2.6, we introduce a geometry spanned by the p-adic numbers, which the incompatible notion of locality to the familiar Euclidean geometry; and we introduce a sparse model once again as a model, where its underlying geometry interpolates between Euclidean and 2-adic geometries as a parameter s is tuned. Finally, in §2.7, we conclude this chapter.

2.1 Entropy as a Measure of Information

Entropy is a quantity rooted in statistical mechanics [6, 7], often understood as a measure of randomness [199]. Given the available macroscopic states ω, the entropy of a thermal system is expressed as

$$S = -k_B \sum_{\omega} p(\omega) \ln p(\omega), \tag{2.1}$$

where $p(\omega)$ is the probability of a system taking a macroscopic state ω [200].

The entropy in statistical mechanics has a much deeper meaning beyond a measure of randomness and reversibility. In 1948, Shannon published *The mathematical theory of communication* [57]. In it, he laid down a series of qualities which a measure of information must satisfy. He especially considered a stochastic system and how much information can be gained from measurements. He concluded that the measure $\mathcal{S}$[1] must have the following form

$$\mathcal{S}_A = -\sum_{i=0}^{|A|-1} p_i \ln p_i, \tag{2.2}$$

---

[1] It is conventional to use H in the field of information theory, however here $\mathcal{S}$ is used to distinguish Shannon entropy from the physical entropy S and Hamiltonian H.

where system A, $A = \{a_0, \cdots, a_{|A|-1}\}$, has states a_i, which occurs with probability p_i and the subscript i is an index over all possible states in A. The measure of information $\mathcal{S}$ has the same form as the definition of thermodynamic entropy, and therefore, it was named entropy (Shannon entropy).

The entropy in information theory is a measure of how much information can be gained through a measurement of a probabilistic event given the knowledge of the probability distribution. The rarer the event, more information can be obtained when it occurs. Shannon entropy can also be used to quantify the correlation between two systems. The larger the correlation, less uncertain the state of the other becomes when one system is measured, thus making the amount of information of the correlated variables smaller.

This can be shown by considering the total entropy of a system composed of two random variables. Given random variables X and Y, the following inequality holds between the entropy of a whole system $\mathcal{S}(XY)$ and the entropy of its parts, $\mathcal{S}(X)$ and $\mathcal{S}(Y)$:

$$\mathcal{S}(XY) \leq \mathcal{S}(X) + \mathcal{S}(Y), \tag{2.3}$$

which follows from the Jensen inequality of a concave function [201]: Here XY denotes the union of sets X and Y.

$$\begin{aligned} I(X, Y) = \mathcal{S}(X) + \mathcal{S}(Y) - \mathcal{S}(XY) &= \sum_{(x,y)\in(X,Y)} p(x, y) \ln \frac{p(x, y)}{p(x)p(y)} \\ &\geq -\ln \sum_{(x,y)\in(X,Y)} p(x, y) \frac{p(x)p(y)}{p(x, y)} = 0. \end{aligned} \tag{2.4}$$

This quantity $I(X, Y) = \mathcal{S}(X) + \mathcal{S}(Y) - \mathcal{S}(XY)$ is called mutual information. This quantifies the information shared between two random variables, or equivalently the correlation between the two. The entropy of the whole, therefore is smaller than the sum because of the redundancy of the information shared between the parts X and Y.

2.1.1 Tripartite Mutual Information

The mutual information can be generalized to the cases of more than two random variables [202, 203]. In this thesis, we use a generalized mutual information called

X	Y	Z	p
0	0	0	1/4
0	1	1	1/4
1	0	1	1/4
1	1	0	1/4

Table 2.1: **List of all the possible states of a system of classical random variables X, Y, and Z.** The system XYZ can take 4 states and each state can occur with the probability 1/4. While variables X and Y take a value of either 0 or 1 randomly with equal probability, Z is constrained as a binary sum of X and Y.

Tripartite Mutual Information (TMI) [123, 204–211],

$$I(X:Y:Z) = I(X,Y) + I(X,Z) - I(X,YZ), \tag{2.5}$$

where YZ denotes the union of variables Y and Z. This quantity measures how much of information in X is embedded globally in random variables Y and Z.

Unlike the mutual information, TMI can take a negative value. To illustrate the meaning of this negativity, here we provide an example with two independent classical random variables X and Y which takes a value of either 0 or 1 with equal probability, and a variable $Z = X + Y \mod 2$. The mutual information of Z and X, and hence, Z and Y are (using Table 2.1):

$$\begin{aligned} I(Z,X) &= \mathcal{S}(Z) + \mathcal{S}(X) - \mathcal{S}(ZX) \\ &= -\sum_{z\in\{0,1\}} \frac{1}{2}\ln\frac{1}{2} - \sum_{x\in\{0,1\}} \frac{1}{2}\ln\frac{1}{2} + \sum_{(x,z)\in\{(0,0),(0,1),(1,0),(1,1)\}} \frac{1}{4}\ln\frac{1}{4} \\ &= I(Z,Y) = 0. \end{aligned} \tag{2.6}$$

where $I(Z,X) = I(Z,Y)$ comes from the symmetry between the variables X and Y. Similarly, $I(Z,XY)$ is evaluated as (Table 2.1):

$$\begin{aligned} I(Z,XY) = \sum_{z\in\{0,1\}} -\frac{1}{2}\ln\frac{1}{2} - \sum_{(x,y)\in\{(0,0),(0,1),(1,0),(1,1)\}} \frac{1}{4}\ln\frac{1}{4} \\ + \sum_{(x,y,z)\in\{(0,0,0),(0,1,1),(1,0,1),(1,1,0)\}} \frac{1}{4}\ln\frac{1}{4} = \ln 2. \end{aligned} \tag{2.7}$$

Here, the degrees of freedom given to Z are suppressed due to the relation $Z = X + Y \mod 2$. This gives rise to $\mathcal{S}(XY)$ canceling $\mathcal{S}(XYZ)$, leaving $I(Z,XY) =$

$\mathcal{S}(X) = \ln 2$. As a result, the TMI $I(X, Y, Z)$ of this toy example evaluates to:

$$I(X:Y:Z) = I(X,Y) + I(X,Z) - I(X,YZ) = 0 + 0 - \ln 2 = -\ln 2. \tag{2.8}$$

Here, it is clear that negativity of TMI comes from the fact that information of Z is globally embedded in the combined system XY, but the information is hidden in the individual components X and Y. Thus, the negativity of TMI, on a classical level, measures the degree of global embedding of information.

2.2 Quantum Entanglement Entropy

The notion of entropy is expanded for quantifying the correlations in quantum mechanical states by von Neumann [212]. He introduced a density operator ρ to describe a quantum state which represents a classical mixture, without well-defined phases between the available states [195]. Let p_i be the probability of measuring the state $|\omega_i\rangle$, then the density matrix is given by

$$\rho = \sum_i p_i \left|\omega_i\right\rangle \left\langle\omega_i\right| . \tag{2.9}$$

A pure state is a special case where $p_i = 1$, where for all other states, $p_i = 0$. With this, like the entropy in statistical mechanics, the entropy of a quantum mechanical state ρ, also known as von Neumann entropy, is defined as:

$$S = -\mathrm{Tr}\{\rho \ln \rho\} = -\sum_i p_i \ln p_i \geq 0, \tag{2.10}$$

where p_i are the real positive eigenvalues of ρ. This definition of the density matrix and entropy expands statistical mechanics to the quantum regime. In quantum mechanics, a thermal state with the temperature $T = 1/(k_B \beta)$ is $\rho = \mathrm{e}^{-\beta H}/\mathrm{Tr}\{\mathrm{e}^{-\beta H}\}$ where H is the Hamiltonian of the system.

Two systems X and Y are said to be entangled when the density matrix which describes the combined system ρ_{XY} *cannot* be expressed in the form

$$\rho_{XY} = \sum_i p_i \rho_X^i \otimes \rho_Y^i, \tag{2.11}$$

where ρ_X^i and ρ_Y^i are the density matrices of X and Y, and $\otimes$ is the Kronecker product. When the combined system is isolated and the state as a whole is a pure state $|\Psi\rangle$, the entanglement between X and Y can be quantified with the von Neumann entropy of the reduced density matrix ρ_X of subsystem X

$$S(X) = -\mathrm{Tr}\left\{\rho_X \ln \rho_X\right\} = S_Y = -\mathrm{Tr}\left\{\rho_Y \ln \rho_Y\right\} \geq 0, \tag{2.12}$$

where

$$\rho_X = \mathrm{Tr}_Y\{\rho_{XY}\}, \tag{2.13}$$

and $\mathrm{Tr}_Y\{\cdots\}$ is the partial trace over Y.

The equality in Eq. (2.12) is only satisfied when X and Y are not entangled. Inequality, on the other hand, implies that the global wavefunction $|\Psi\rangle$ cannot be decomposed into a tensor product of $|\Psi_X\rangle$ and $|\Psi_Y\rangle$ and

$$|\Psi\rangle \neq |\Psi_X\rangle \otimes |\Psi_Y\rangle\,, \tag{2.14}$$

where $|\Psi_X\rangle$ ($|\Psi_Y\rangle$) is a wavefunction which lives in the Hilbert space spanned by subsystem X (Y). This inseparability between two subsystems gives rise to shared information between two parts of the system that is beyond the reach of classical states.

The properties of quantum entanglement lie at the core of quantum simulation [66, 96, 98, 100, 213–218], quantum information [58, 66, 118, 133, 219–221], and quantum computation [66, 118, 133, 222–225]. Due to the existence of entanglement, in order to simulate a quantum system, one has to keep track of all the conditional probabilities between entangled parts of the system. This gives rise to the number of states, i.e. the dimension of the Hilbert space, in a system to increase exponentially with respect to the number of unit of component of a system (local Hilbert space dimension). Let D_{loc} be the number of degrees of freedom in a unit part, quantum system of interacting N such parts have the degrees of freedom $\mathcal{N}$, which increases exponentially, $\mathcal{N} = D_{\mathrm{loc}}^N$. As a result, quantum systems, in general, are hard to simulate with a classical computer.

2.2.1 Monogamy of Entanglement and Tripartite Mutual Information

Monogamy of entanglement is a bound which two entangled parts must obey when they are being entangled with a third party. It states that when two parts are maximally entangled, then they cannot be entangled at all with any other systems. In general, the monogamy implies the following bound in the mutual information between the parties X, Y, and Z [226–228]

$$S(X|Y) + S(X|Z) - S(X|YZ) \leq 0, \tag{2.15}$$

Here $S(X|Y)$ denotes the entropy of X conditioned that the value of Y is known.

TMI, can also be generalized to quantum mechanical states. Here the negativity of the quantity also imply the global embedding of information, in this case, the embedding of quantum information in terms of entanglement. The monogamy of entanglement discussed above implies that entanglement building up nonlocally across a system gives rise to negativity of the TMI [205, 206, 229, 230]. This is implied from the srong subadditivity

$$\begin{aligned} &I(X:Y:Z) = I(X,Z) - I(X,Z|Y) \leq 0 \\ \rightarrow\ &0 \leq I(X,Z) < I(X,Z|Y) = S(X|Y) + S(Z|Y) - S(XZ|Y), \end{aligned} \tag{2.16}$$

where the right-hand side is the left-hand side of Eq. (2.15) written in terms of the subsystem Y. Here, large negativity implies information in Y is strongly entangled across XZ (i.e. $S(X|Y) + S(Z|Y) \gg S(XZ|Y)$).

2.2.2 Area-Law and Volume-Law of Entanglement

In a classical system, at zero temperature the entropy goes to 0 both locally and globally due to the vanishing thermal fluctuations. In closed quantum systems with a non-degenerate ground state, even at zero-temperature, locally, the entropy can be non-vanishing. The origin of the fluctuation, in this case, is the local operators that do not commute with the Hamiltonian, where the expectation values are bounded by the Heisenberg uncertainty principle [9, 231–233].

For example, let us consider a quantum system with a Hamiltonian:

$$H = -H_{\text{order}} - gH_{\text{disordered}}, \tag{2.17}$$

where H_{order} represents terms which favors the order (e.g. the ferromagnetic order through nearest-neighbor Ising interaction) and $H_{\text{order breaking}}$ is the terms in the Hamiltonian which favors the loss of order (e.g. an external transverse field). When the two terms do not commute, the uncertainty principle

$$\left\langle \Delta H^2_{\text{order}} \Delta H^2_{\text{disordered}} \right\rangle \geq \frac{1}{4} \left| \langle [H_{\text{order}}, H_{\text{disordered}}] \rangle \right|^2, \tag{2.18}$$

where ΔO^2 of an operator O is $\Delta O^2 = O^2 - \langle O \rangle^2$ and $[A, B] = AB - BA$ is a commutator, tells us that even at zero temperature the fluctuations in both of the terms can never vanish. This causes, in the regime where the energy from the ordered part and the disordered part are comparable (typically $g \sim \mathcal{O}(1)$ in low-dimensional short-range systems), the restoration of order causes the energy penalty from the disorder-favoring part of the Hamiltonian. As a consequence, when g increases to the critical value, the large fluctuation in $H_{\text{disordered}}$ breaks the order of the ground state, and hence the phase transition occurs.

In a non-degenerate local and gapped quantum system, long-range correlations ought not to be expected in the low-energy regime. This is because a generation of long-range correlations in a local system tend to require excitations. For a gapped quantum system on a lattice, it is proven that the low-energy eigenstates of the Hamiltonian obey an area-law entanglement [232, 234, 235], where the entanglement entropy of a region X only increases proportionally to the area of the boundary of the region X, denoted as ∂X. In a one-dimensional system, we have $S(X) \sim \mathcal{O}(1)$.

When area-law entangled states are subjected to a quench, excitations spread the information about local states to sites that are far away. In ergodic systems, where local states are expected to explore most of the state space, given sufficiently long time, the entanglement per site is expected to saturate the monogamous bound. In such a case, unit parts of the subsystem X is almost maximally entangled to the complement region of X, which is denoted as $\bar{X}$. In this case, the entanglement entropy grows linearly with the size of (the number of the unit parts in) X, $|X|$:

$$S(X) \propto |X|. \tag{2.19}$$

This is called volume-law entanglement, because the entanglement entropy is proportional to the volume of region X.

In the case of a random state in a N D_{loc}-dimensional quantum system the state is shown to be volume-law entangled [236–238]:

$$S(X) \sim |X| \ln D_{\mathrm{loc}} - \frac{1}{2} D_{\mathrm{loc}}^{2|X|-|N|} \qquad \left(|X| < \frac{N}{2}\right), \tag{2.20}$$

for arbitrary subsystem of size $|X| < \frac{N}{2}$. The entanglement entropy of an arbitrary subsystem in such random states are no more than 1 bit off from its maximum value of $|X| \ln D_{\mathrm{loc}}$. This gives rise to negativity of the TMI of a tripartite system

$$I(X:Y:Z) \approx -(S_X + S_{YZ}) \approx -|N| \ln D_{\mathrm{loc}} \tag{2.21}$$

where X, Y, and Z are the regions of equal area in the system and $1 \ll N$ is the system size. The state which saturates this random state limit is called Page-scrambled state [53].

2.3 Entanglement Growth and Geometry

Since entanglement entropy is a quantity associated with the density matrix ρ, entanglement entropy also grows in time. Therefore, like ρ, its evolution is governed by the Hamiltonian of the system. In the case of a system which consists only of short-range interactions, the principle of locality tells us that information travels through a system by affecting its immediate surroundings. As a result, in such a system, information is expected to spread continuously over a space as a function of time t. Result of this type of entanglement generating dynamics is a transformation of initially an area-law state into a volume-law entangled state at large times. Thus, dynamics encodes information of the underlying geometric structure—namely, the notions of area and volume—of the Hamiltonian onto the entanglement structure of a state. In this section, we review the notion of locality by first introducing the metric, which defines the distance of a system, and then we review the Lieb-Robinson bound which puts locality constraint to quantum systems with finite short-range interactions.

2.3.1 Locality and Geometry

The notion of locality is closely tied to how distance is defined. The distance in a graph is defined by a metric function, $d(x, y)$, which defines closeness of two numbers (coordinates) x and y. The Euclidean space, which the universe believed to be approximated in the sufficiently small length scales, is defined through the Euclidean metric:

$$d_\infty(x, y) = |x - y|, \tag{2.22}$$

where $|\cdot|$ is the absolute value of a number.

The metric also define an order of physical quantities in the spacetime. The ordering defined by the Euclidean metric is consistent with our intuition on how natural numbers are ordered, $0 < 1 < 2 < 3 < \cdots$. This ordering based on the Euclidean distance is often referred as Archimedean ordering [239–242].

With a proper metric, the notion of "finite short-range interactions" can be defined without an ambiguity as finite-range interactions where their range is small compared to the system's length scale. Here, the length scale of the system is roughly proportional to the radius of the D-dimensional sphere which roughly embeds the system, hence the length scale is roughly proportional to $N^{1/D}$. The notion of locality, and the principle of locality which follows, can then be interpreted as the dynamics which influence the sites temporary in an ordered manner, where sites with smaller distances are affected strongly in early times, and later in time, the sites at longer distances are affected.

2.3.2 Lieb-Robinson Bound

In relativistic mechanics, the speed at which information can spread is limited by the speed of light. Likewise, in quantum mechanics, the speed is also limited even in the non-relativistic limit by a bound called Lieb-Robinson bound [81]. The bound states, that for a state evolving in a Hamiltonian with finite-range interactions, the degree of operator mixing, quantified by the commutator between an operator A at site i at time $t = 0$ and an operator B at site j at time $t = T$, follows the inequality

$$||[A_i(t=0), B(t=T)_j]|| \leq Ce^{-\mu(d(i,j)-vT)}, \tag{2.23}$$

where $[\cdot,\cdot]$ is the commutator, $||\cdot||$ and $d(i,j)$ is the distance between sites i and j, C and μ are positive constants. This bound implies, that for pairs of sites beyond the distance $d_{\mathrm{LR}} = v|T|$, the correlation between two operators are exponentially suppressed. Therefore, for sufficiently local models, information cannot spread faster than linearly in time.

With the Lieb-Robinson bound, the system is clearly divided into two: a region within the distance $d_{\mathrm{LR}} = v|t|$ and a region outside. A lightcone, in this context, is defined by the boundary between the region which the correlation has spread via the mixing of the local operators through the interaction ($d < d_{\mathrm{LR}}$) and the region which the correlation is exponentially suppressed ($d_{\mathrm{LR}} < d$). The lightcone is equivalently the cone formed by points at distance $d_{\mathrm{LR}} = v|T|$ at different times. As a result, a timescale for the information to reach all the components in the system is bounded from below by the number of sites in the system $t_* > CN^{1/D}$, where D is the Euclidean dimension of the system and C is a model-dependent constant.

2.4 The Fast Scrambling Conjecture

Despite the existence of the Lieb-Robinson bound, it is rare to find a quantum system where its scrambling dynamics saturates the bound. In classical kinetic theory, a perturbation introduced in a thermal system spreads in timescale t_* polynomially to the system size N as

$$t_* \propto N^{2/D}, \tag{2.24}$$

where D is the Euclidean dimension of the system. In a classical thermal system, t_* defines the timescale, which is required for a bit of information in a initially localized perturbation, to be delocalized into the whole system [53].

The Lieb-Robinson bound is saturated in the system with ballistic dynamics, where perturbation spread through a system with excitations with well-defined group velocity v_g. As established, in such a system, the timescale t_* of which a perturbation to spread across the system is expected to scale

$$t_* \propto N^{1/D}. \tag{2.25}$$

Due to the Lieb-Robinson bound, therefore, for quantum systems on a regular lattice, one cannot expect the t_* to scale any faster than this ballistic limit.

Now, let us consider the case of information retrieval from scrambling systems. Here, we consider a case where a (qu)bit of information is injected into a quantum system with state $|\psi\rangle$ at some point in space at time $t = 0$. In order for this information to be accessed by some observer at some spatial point, the information must first get to the observer. Let R be the distance between the point of injection to the observer, the time for information to travel the distance R scales like the scrambling time. Therefore, for a retrieval of information to succeed for an arbitrary R, one must wait for at least the scrambling time.

However, at the scrambling time, as argued, the state is scrambled. Therefore the state must be volume-law entangled at time $t = t_*$. At this time, the information is encoded globally in the system, therefore one must recover a (qu)bit of information by measuring most of the sites where the information has reached. Let B be a set of qubits which is collected, then it is known that the amount of information $i(B)$ that can be retrieved from B is [45]:

$$i(B) = S_{\text{thermal}}(B) - S(B), \tag{2.26}$$

where $S_{\text{thermal}}(B)$ is the thermal entropy of subregion B of a black-body radiation of a system with approximate local density matrix, and $S(B)$ is an actual entropy of B. If we assume that the scrambled steady state can be approximated with the Page-scrambled state, one requires collection of more than half of the system in order to recover the injected information. To give an example, in order to recover a bit of information thrown into a bathtub full of water, one must wait for half of the water to evaporate in order to recover the information from just measuring the evaporating molecules. Typically the time it takes to inspect half of the system is much longer than scrambling time, otherwise we will not be able to enjoy a warm cup of tea before they evaporate.

The story is different when the observer possesses a previous knowledge of the state of a system. Hayden and Preskill [59] showed that when the observer possesses the knowledge on half of the state, then the retrieval time can be as fast as the scrambling time,

$$t_{\text{scramble}} \sim t_{\text{retrieval}}. \tag{2.27}$$

In the context of the bathtub example, an observer recovers a (qu)bit of information as soon as the bath reaches the equilibrium with the injected information.

In an everyday context, this is not a troublesome case. However, in the context of black holes, such a fast timescale of information retrieval becomes troublesome because it may allow cloning of quantum information. Theoretically, with a knowledge of half of the radiation which comes from the Hawking radiation [42, 43], a qubit of information that have fallen across the horizon can be retrieved by the observer outside the black hole, while the same qubit of information is also present and trapped in the interior of the black hole.

In 2008, Sekino and Susskind [53, 54] showed that in order for to avoid the cloning of quantum information, the scrambling timescale t_* is necessary to be longer than the time which observer on the outside to fall within the Schwarzschild radius: $t_* \gtrsim \log R_{\text{BH}} \sim \log M_{\text{BH}}$, where R_{BH} is the Schwarzschild radius and M_{BH} is the mass of the black hole. The fast scrambling conjecture then states that black holes saturates the bound

$$t_{\text{retrieval}} \sim t_{\text{fast scrambler}} \propto \log N, \tag{2.28}$$

where N is the system size.

2.5 Logarithmic Lightcone in Models with Long-Range Interactions

Fast scramblers spread information exponentially fast in a system. The lightcone which it exhibits takes a form of $t_{\text{lightcone}} \propto \log d$, where d is the distance from the perturbation. Here $t_{\text{lightcone}}$ represents the time it takes for information to spread from the origin to a point at distance d. The timescale $t_{\text{lightcone}}$ becomes t_* when d spans the entire system $N^{1/D}$, where D is the dimension of the system. In order to achieve such a lightcone in a quantum system without random interactions, one needs to go beyond the regime where the Lieb-Robinson bound is applicable.

The first discussion reaching beyond such a regime is introduction of power-law decaying interactions. In this model, the strength of interactions between qubits decays with the distance d as $1/|d|^{\alpha}$. This gives rise to corrections beyond linear spreading of information predicted by the Lieb-Robinson bound [196–198]; for $\alpha > 0$, the bound scales as $t_{\text{lightcone}} \propto d^{q}$, where $q < 1$ is α dependent constant [198]. Fast scrambling is still not achievable with this crude treatment of providing continuous algebraically decaying interactions.

At $\alpha = 0$, the deterministic long-range models become mean-field like due to a strong permutation symmetry. The typical spin models such as long-range Ising and XY models reduce to a non-interacting model, namely the Lipkin-Meshkov-Glick (LMG) model. [243–245]. LMG-like models are known to show a recurrence time that scales linearly with the system size [246], which again forbids the emergence of the logarithmic lightcone. Therefore, in order to achieve the fast scrambling limit, the locality must be broken without introducing the strong permutation symmetry.

2.6 Beyond the Euclidean Geometry

In order to go beyond the constraints imposed by the Euclidean geometry, here we consider an alternative way to organize numbers called p-adic numbers and its associated geometry. p-adic numbers are another way to construct a continuum from a set of discrete numbers, like Euclidean metric can be used to define the gaps between rational numbers which irrational numbers fill to form the set of real numbers.

The filling of quotient number, to form a continuum is called Cauchy completion, and it is proven [247] that the quotient numbers can be Cauchy completed not only with Euclidean distance, but also with a metric called p-adic distance, $d_p(x, y)$. p-adic numbers [88] are a set of numbers formed by the Cauchy completion of the quotient number using p-adic norm as the metric, where p is a prime number. The p-adic distance $d_p(x, y)$ of two numbers are defined as follows:

$$d_p(x, y) = |x - y|_p, \tag{2.29}$$

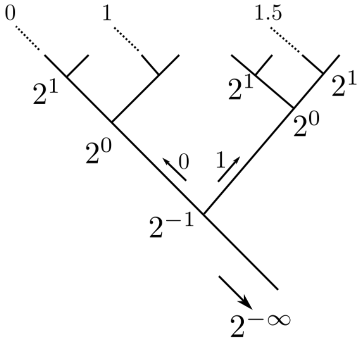

FIGURE 2.1: **A Bruhat-Tits tree.** A p-adic number x_p can be expanded uniquely with a set of integers a_n ($a_n = 0, 1, \cdots, p-1$) as $x_p = \sum_{k=-\infty}^{\infty} a_k p^k$. Starting from $n = -\infty$, a p-adic number can be uniquely identified as a path. Depicted is the Bruhat-Tits tree for $p = 2$. p-adic numbers lives at the end of the infinite path, where the left path is taken at the vertex 2^n if $a_n = 0$ and the right path is taken otherwise.

where $|\cdot|_p$ is a p-adic norm of a number. The p-adic norm of a number, x, is defined as:

$$|x|_p = p^{-v_p(x)}, \tag{2.30}$$

where $v_p(x)$ is p-adic valuation, it is the exponent of p in the prime factor of x. For example $v_2(2) = 1$, $v_2(1/2) = -1$, and $v_5(3) = 0$. As a Euclidean distance from 0 increases, the p-adic distance of a number from 0 decreases, where the p-adic distance between x and y is bounded by the largest of $|x|_p$ and $|y|_p$

$$|x + y|_p \leq \max\{|x|_p, |y|_p\}. \tag{2.31}$$

This property is called strong triangular inequality. Due to this property, the ordering defined using the Euclidean distance cannot be consistent with the ordering defined with p-adic distances. Hence, the notion of locality which arises from p-adic metric is incompatible to the locality defined by the Euclidean metric.

From the definition, it is evident that there are infinite amounts of numbers that are equally close to x in p-adic space. To graphically show the Hierarchical structure, here we present the tree representation of the p-adic numbers. Like a real number can be written as a sum of a power series, any p-adic number, x_p, can be written as a summation of a series

$$x_p = \sum_{k=-\infty}^{\infty} a_k p^k, \tag{2.32}$$

with $a_k \in \{0, 1, \cdots, p-1\}$. Starting from the infinitely small p-adic number as a boundary node, one can hop to any p-adic numbers by going down a fork of p branches like shown in Fig. 2.1, forming a discretized geometry which covers all the numbers in the set of p-adic numbers. The tree is known as Bruhat-Tits tree, or equivalently, the Bethe lattice with the coordination number of $p+1$. This must be contrasted to the real number line, where any number can be reached by moving continuously to the left (negative direction) or to the right (positive direction) of a number line.

2.6.1 Monna Map

For positive real numbers, there exists a way to map them, in a way they appear at the infinite boundary of the Bruhat-Tits tree. The map is called Monna map [248]. Here, we introduce a discrete version of this map following Gubser *et al.* [75]. For any integer X in a set $\{0, 1, \cdots, p^n - 1\}$, X can be written as

$$X = \sum_{k=0}^{n-1} x_k p^k \qquad\qquad x_k \in \{0, 1, \cdots, p-1\}\,. \tag{2.33}$$

In p-adic space, the integer X is mapped to the $X_p = \mathcal{M}(X)^{\text{th}}$ node at the boundary of the tree, where the Monna map $\mathcal{M}$ is defined as

$$X_p = \mathcal{M}(X) = \sum_{k=0}^{n-1} x_{n-k-1} p^k. \tag{2.34}$$

2.6.2 Implications of p-adic numbers in Physics

This treelike geometry, or equivalently, non-Archimedean geometry, of the p-adic numbers gives rise to the features that are interesting to be considered for a physical theory. One of the features is the naturally arising notion of a Planck-scale due to the discrete nature of the geometry. Also, the tree geometry naturally encompasses a hierarchical structure, which are abundant in nature. Motivated by such points, a study of p-adic version of quantum mechanical theories were conducted in the late 1980s by the various mathematicians and physicists [87, 249–256].

Furthermore, as shown in this section, the infinite set of p-adic numbers lives at the edge of the Bruhat-Tits tree. Due to this property, recently, physical theories on the p-adic field gained attention once again due to the similarity to AdS/CFT correspondence. The discretized geometry simplified some calculations, and it is known that a statistical mechanical model defined on the field show a de Sitter-like inflating universe [257]. The foundational works on the p-adic AdS/CFT correspondence are done by Steven Gubser [256, 258–260]. They have found striking similarities between the original version and the p-adic version of the correspondence. Although the implications of p-adic geometry on the physical theory in the Euclidean geometry have not been concretely established, p-adic AdS/CFT correspondence is an active field of research.

2.6.3 Sparsely Coupled Models

Inspired by the p-adic version of AdS/CFT correspondence and the simplified and discretized geometry of the p-adic field theory, a more simplified model on a discrete treelike geometry similar to the Bruhat-Tits tree [75, 261] was proposed by Gubser [75]. It is a sparsely coupled model with algebraically decaying (increasing) interactions

$$J(d) = \begin{cases} |d|^s & (d \text{ is an integer powers of 2}) \\ 0 & (\text{otherwise}) \end{cases}, \tag{2.35}$$

which was introduced in Ch. 1.2.

As discussed in Ch. 1.2, the model interpolates between two geometries, where locality is defined by the Euclidean norm (linear geometry, $s < 0$), and p-adic norm (treelike geometry, $0 < s$). This is evident as the interaction function decays monotonically with Euclidean distance between two sites for $s < 0$, up to the factor of powers of 2 in the distance; while the same goes for $0 < s$ with the 2-adic norm. However, near $s = 0$, the locality condition is no longer valid in either geometries while strong permutation symmetry is suppressed due to the sparseness of the coupling graph. Thus near $s = 0$, we expect the locality of the model to transition from one to the other incompatible geometry in the model, without going through the symmetry point. While the loss of locality in the absence of strong permutation symmetry appear in LMG-like models, we expect the strongly correlated quantum version of the sparsely coupled model to possess the strong scrambling behavior, which leads to the saturation of the fast scrambling bound.

2.7 Conclusion

In the fist part of this chapter (§2.1 and §2.2), we reviewed entropy as a measure of information in channels and measure of entanglement in quantum systems. Here we established that the global embedding of information can be quantified by the negativity of TMI, and the same quantity in quantum mechanical systems puts a bound on the degree of entanglement shared over many parties. We also discussed the area- and the volume-law entangled states, where the geometric structure of a non-degenerate Hamiltonian appears in the structure of its eigenstates.

In the second half of the chapter, we discussed the bounds of the entanglement generating dynamics in isolated quantum systems. Here we established that entanglement generation of quantum systems with finite short-ranged interactions can only spread correlations polynomially in time $t_* \sim N^{1/D}$, producing a linear lightcone (§2.3). Then in §2.4, we introduced the fast scrambling conjecture, where the timescale for entanglement to be generated across all parts of the system can scale as fast as logarithmically with system size $t_* \gtrsim \log N$. Finally in §2.5 and §2.6, we discussed the attempt to break the restriction of the Lieb-Robinson bound by introducing long-range interactions. This is done by considering a geometry spanned by the p-adic numbers, which has incompatible notion of locality to the Euclidean geometry. Here we reintroduced a sparsely coupled model as a model which interpolates between Euclidean and 2-adic geometry, where it is conjectured that fast scrambling dynamics occurs at a point where geometry transitions from one to the other.

Because entanglement entropy does not have an associated well-defined operator, the quantity is very hard to be observed or numerically computed. However, it can be a powerful tool to diagnose scrambling dynamics when it can be directly accessed because it provides the amount of information encoded in the quantity. The lightcone on the other hand, can be accessed in terms of correlators such as two point correlators. However, near the fast scrambling limit, one needs to access exponentially large distance scale in order to observe a logarithmic growth of scrambling time. Therefore, one needs more ways to diagnose scrambling and its associated timescale. In the next chapter, Ch. 3, we review the connection between chaotic systems and fast scramblers in order to provide more insight into and potential tools that can be adopted from the quantum chaos for diagnosing the fast scrambling dynamics.

Chapter 3

Fast Scramblers and Quantum Chaos

> Does the flap of a butterfly's wings in Brazil set off a tornado in Texas?
>
> Edward N. Lorenz [262]

In classical mechanics, a chaotic system is a system where evolution of a state is unpredictable due to its sensitivity on a small change in initial conditions. One of the first example of such a system is the motion of three (or more) celestial bodies, studied extensively by Poincare [263]. However, the precise research on such systems had to wait for the invention of computers, this is because any perturbations from the integrable systems remains non-chaotic due to the Kolmogorov–Arnold–Moser theorem [264–266]. The serious study of chaotic models was started by the work by Lorenz on the famous Lorenz system [17], where numerical simulation played a key role in showing and diagnosing the chaotic behaviors of the system.

The discussion of classical chaos has also been expanded to the quantum regime. One of the motivations for studying quantum chaos is to study the mechanism on how isolated quantum systems thermalize despite the underlying unitary dynamics [27, 30, 31, 31, 267–269]. With the advancement in theoretical, numerical, and experimental techniques, the mechanism of thermalization in isolated quantum system is beginning to be revealed. Especially the prethermalization dynamics [28, 188, 270], which occurs before the scrambling (thermalization) time, has been actively studied because they can be simulated with variational methods [147, 188, 270] and probed experimentally [271, 272].

In order to gain further intuition on fast scrambling dynamics, understanding the nature of chaotic dynamics in quantum systems is important. This small chapter is dedicated to methods of diagnosing chaos in quantum systems. We mainly look at two methods. First, in §3.1, we introduce Out-of-Time-Order Correlators (OTOCs), which quantify the degrees of operator mixing in quantum systems. In fast scramblers, it gives rise to the exponential growth, similarly to the exponential divergence in the phase space trajectories in classical chaos. Then in §3.2, we introduce random matrix theory, which has been used to describe complex many-body systems. Finally in §3.3 we conclude this chapter.

3.1 Out-of-Time-Order Correlators

In classical chaos theory, the chaotic behavior is often related to the exponentially diverging paths in phase space with respect to time t, after a small perturbation δX is given to the initial condition of a system at $t = 0$. This divergence in the paths gives raise to the Lyapunov exponent λ_L [16, 70, 273]

$$C(t) = \left\langle \frac{\delta x(t)}{\delta x(0)} \right\rangle = \langle \{x(t), p(0)\}_{\mathrm{PB}} \rangle \sim \mathrm{e}^{\lambda_{\mathrm{L}} t}, \tag{3.1}$$

where $\{\cdot\}_{\mathrm{PB}}$ denotes the classical Poisson bracket on the Hamiltonian equation of motion.

In quantum mechanics, unitarity hinders chaotic behaviors to occur in isolated quantum systems. This is because unitarity ensures the overlap of two wavefunctions, $|\psi_0(0)\rangle$ and $|\psi_1(0)\rangle$, to be preserved in time:

$$\langle \psi_0(0) | \psi_1(0) \rangle = \langle \psi_0(t) | \psi_1(t) \rangle \,. \tag{3.2}$$

However, in nature, there are many systems which possess a chaotic behavior. In quantum systems, the apparent chaotic behavior is hypothesized to occur as a result of the operator mixing. This quantum version of the Lyapunov exponent naturally arises as a result of the quantization of the above Poisson bracket [25, 70, 206, 273–275], and it is called Out-of-Time-Order Correlator (OTOC), $\hat{C}$:

$$\hat{C}(t) = \langle (i\hbar\,[\hat{x}(t), \hat{p}(0)])^2 \rangle = -\hbar^2 \,\langle [\hat{x}(t), \hat{p}(0)]^2 \rangle \sim \mathrm{e}^{\lambda_{QL} t}, \tag{3.3}$$

where $\langle \cdot \rangle$ denotes the expectation value, and $[\cdot]$ denotes a commutator of operators $\hat{A}$ and $\hat{B}$ ($[\hat{A}, \hat{B}] = \hat{A}\hat{B} - \hat{B}\hat{A}$), and λ_{QL} is the quantum Lyapunov exponent. Throughout this thesis, we fix $\hbar = 1$. Here a hat is given to the operators in order to explicitly show that they are quantum operators. For the rest of the chapter, hats are omitted from the quantum operators.

3.1.1 Fast Scrambling Bound

For general quantum systems, the value of quantum Lyapunov exponent is not a trivial quantity. Simple dimensional analysis suggests that, λ_{QL} for a thermal state is $\lambda_{QL} \sim k_B T/\hbar$ with Boltzmann constant k_B. At room temperature, this quantity is approximately $\mathcal{O}(10^{13})$ per second. This is much too large, given the observation that bifurcation systems, such as dripping taps, have the Lyapunov exponent of $\mathcal{O}(10^{-1})$ per second [276].

This discrepancy of many orders of magnitude was explained by Maldacena *et al.* in 2016 [70], where the estimate is actually the maximum value of the quantum

Lyapunov exponent,

$$\lambda_{QL} \leq k_B T/\hbar. \tag{3.4}$$

They have also shown that the bound is saturated by the black holes and by the holographic dual systems, where they are also hypothesized to saturate the fast scrambling bound.

3.2 Random Matrix Theory

OTOC is a viable measure for chaos in quantum systems. However, the computation of a quantum Lyapunov exponent is difficult. This is due to the exponentially large Hilbert space and the limited magnitude of the commutator of local operators, which typically takes a value of $\mathcal{O}(1)$. The former prohibits exact calculation of the Lyapunov exponent in large systems, and the latter suppress the time which exponential growth can be observed because they saturate the maximum value in exponentially fast time in fast scramblers.

Due to these difficulties, historically, the determination of chaotic quantum systems relied on calculating the statistics of the spectrum of the Hamiltonian [24, 26, 277]. Level statistics is a measure of the frequency of the energy level separation in the spectrum of a system. This provides an accurate measure of quantum chaos even for small systems because the number of energy levels, and hence the number of spaces between the energies, increases exponentially with the system size.

In integrable systems, the level spacing $\Delta E_i = E_i - E_{i-1}$, where E_i is the i^{th} largest eigenenergies in the system, is given by the Poissonian distribution

$$P(\Delta E_i) \sim \mathrm{e}^{-c\Delta E_i}, \tag{3.5}$$

where c is a constant. When the dynamical process of a system can be approximated by the random coupling of degrees of freedom available in the system, the Hamiltonian can be written as a random matrix in a physically suitable set of basis vectors. In such a case, the degeneracy of the energy levels, which is the key feature in the integrable systems, is suppressed, and leads to a level distribution to be different from Poissonian statistics. The exact distribution for Hermitian random matrices follows the Dyson-Wagner statistics [24, 26, 269] as follows:

$$P(\Delta E_i) \sim (\Delta E_i)^{\lambda} \mathrm{e}^{-c(\Delta E_i)^2}, \tag{3.6}$$

where c is a positive constant, and λ is an integer associated to a distribution:

$\boldsymbol{\lambda} = \mathbf{1}$ for random matrix from the Gaussian orthogonal ensemble (random real Hermitian matrices).

$\boldsymbol{\lambda} = \mathbf{2}$ for random matrix from the Gaussian unitary ensemble (random complex Hermitian matrices).

Thus, by looking at a system's level statistics and estimating how close they are to the statistics of integrable/random matrices, the degree of chaos of the system can be determined.

Finally, it is important to note that, although fast scrambling implies the chaotic dynamics, the converse is not true; one such example is a randomly coupled nearest-neighbor model where information in the model spreads locally and does not exhibit fast-scrambling behavior [119, 151], while it still possess chaotic level statistics. As a result, the spectrum itself cannot be the diagnosis of fast scrambling. However, the fast scramblers must have a chaotic spectrum. When there is a large degeneracy in the spectrum, there exist some form of symmetry in the Hamiltonian which makes the energies of those degenerate states, which implies the existence of an integral of motion. The large degeneracy and the large number of the integral of motions tends to prohibit the scrambling of the information across the large degrees of freedom, and hence the system exhibits slow scrambling. Therefore, although the spectral features of a system cannot be an unambiguous diagnosis for fast scrambling, it provides the first test on whether the system can possess the fast-scrambling dynamics.

3.3 Conclusion

In this chapter, we reviewed quantum chaos and its relation to fast scramblers. In §3.1, we introduced Out-of-Time-Order Correlator (OTOC) as a quantum analogue of Lyapunov exponent for diverging phase space trajectory in classical chaotic systems. Similarly to the classical case, in quantum chaotic systems the OTOCs also grow exponentially with the associated quantum Lyapunov exponent λ_{QL}. In the fast scrambling limit, the quantum Lyapunov exponent saturates the bound $\lambda_{QL} \leq k_B T/\hbar$.

Then in §3.2 we introduced as a second diagnostic of quantum chaos based on the spectral property of a quantum Hamiltonian. Here the Dyson-Wigner statistics of the level spacing of random matrices are reviewed. We showed that although many of models which exhibit quantum chaos show level statistics that are consistent with that of random matrices, level statistics are not unambiguous diagnostics for quantum chaos. Thus, this can be used as a first test to sieve out the systems that are not chaotic.

Unlike entanglement entropy discussed in the last chapter (Ch. 2), OTOCs discussed in this chapter take the form of a commutator of operators, and hence it can be directly measured. However, due to the four point correlators acting on different points in space and time, accessing the correlator is difficult both numerically and experimentally. Furthermore, the level statistics that are discussed in this chapter are also a difficult quantity to be accessed as they require the knowledge of the full spectrum of the Hamiltonian. However, for small systems, these quantities can be accessed numerically in early times to quantify the chaotic nature of a system. In the next chapter (Ch. 4), we discuss the numerical methods that can be used to access these quantities in Hamiltonian quantum systems that are investigated in Ch. 5. Then in Ch. 4, we discuss the numerical methods that can be used to access entanglement entropy in quantum circuits. Those methods are then applied in Ch. 6 and Ch. 7 to assess fast scrambling dynamics and probe effects of entanglement destroying operations in the scrambling circuits.

Chapter 4

Numerical Methods

> 算学は何の為ぞや．難題易題，尽く明かさざるということ無きの術を学ぶなり．理を説くこと高尚なりといえども，術を解くこと迂闊なる者は，なんじ算学の異端なり
>
> 関孝和 [278]

In this chapter, we introduce numerical methods that can be used to solve of the dynamics of quantum spins and lattice systems. Due to the exponentially growing Hilbert space dimension with respect to the system size N, the computational cost can be expensive for the resources that are currently available. Thus, reduction of the degrees of freedom is necessary reach the system sizes beyond which can be calculated by the direct diagonalization of the Hamiltonian. The reduction of the degrees of freedom is commonly done by utilizing the symmetries and various constraints imposed on a system.

In this chapter, we introduce numerical methods for diagonalizing and time evolving quantum states in isolated quantum systems. In §4.1, we introduce a method for representing the Hamiltonian with a restricted number of excitations in the system, then introduce the exact diagonalization method for computing the spectrum of the Hamiltonian with the Krylov subspace method, and we also explain how the method can be used to approximate the matrix exponentiation for time evolving a state in a system. Then in §4.2, we introduce the matrix product representation of states and operators for efficient representation of sufficiently locally entangled states and local few-body operators. In the same section, we show how a matrix product operator can be vectorized such that it can be time evolved using matrix product state and operator methods for the calculation of quantities such as out-of-time-order correlators that are discussed in the previous chapter. Then in §4.3 we introduce tensor network representation of quantum states and dynamics, and show how 0^{th} order entanglement entropy is related to the minimal number of cuts required for isolating nodes in a tensor network. In §4.4, we introduce an efficient time evolving algorithm for stabilizer states, which can be used to simulate quantum circuits with a restricted set of gates. Finally in §4.5, we summarize the methods discussed in this chapter.

4.1 Exact Diagonalization

In quantum mechanical systems, a conserved quantity is associated with a commutativity of the symmetry operator with the Hamiltonian [195, 279–281].

$$[\mathcal{O}_{\text{conserve}}, H] = 0. \tag{4.1}$$

For example, in the case of quantum spin systems, the commutation of an operator $M = \sum_i S_i^z/S$, which measures the net magnetization in the z-direction, implies the conservation of the total magnetic field in the z direction. Here S is the magnitude of spin, and S_i^z is a spin-z operator, which obeys the following commutation relations in the three spatial dimensions x, y, and z:

$$\left[S_i^\sigma, S_j^\lambda\right] = iS_k^\theta \delta_{i,j}\epsilon_{\sigma\lambda\theta}, \tag{4.2}$$

where $\delta_{i,j}$ is Kronecker delta:

$$\delta_{i,j} = \begin{cases} 1 & (i = j) \\ 0 & (i \neq j) \end{cases}, \tag{4.3}$$

and $\epsilon_{\sigma\lambda\theta}$ is the antisymmetric tensor:

$$\epsilon_{\sigma\lambda\theta} = \begin{cases} 1 & (\sigma\lambda\theta = x, y, z, \text{ and their even permutations}) \\ -1 & (\text{odd permutations}) \\ 0 & (\text{otherwise}) \end{cases}. \tag{4.4}$$

The associated symmetry with this conservation law is the global $U(1)$ symmetry, which is a symmetry under global rotation.

In this section, we introduce a numerical method for computing quantum spin-1/2 ($S = 1/2$) systems of the form:

$$H = \sum_{0<d} \sum_i J(d) S_i^+ S_{i+d}^- + \text{H.C.} + g \sum_i S_i^z, \tag{4.5}$$

where $S^+ = S^x + iS^y$ and $S^- = S^x - iS^y$ are raising and lowering operators, $J(d)$ defines the interaction between two spins, and g is the strength of a transverse magnetic field. Here $d = 0$ is omitted in the first term because the term $S_i^+ S^- + H.C. = S^z + \text{H.C.} = 2S^z + I$, where I is an identity operator, adds an extra local field with strength $J(0)$. This Hamiltonian obeys the $U(1)$ symmetry with a quantized conserved quantity, $\langle M \rangle = \langle \sum_i 2S_i^z \rangle = -N + 2m$, where m is the number of spin excitations, *magnons*, in the system.

In general the Hamiltonian can be exactly solved by diagonalizing the matrix of dimension 2^N written in a set of orthogonal basis vectors $\{\boldsymbol{e}_i\}$. When it is solved and the corresponding eigenvalues and eigenvectors are determined, the dynamical and static properties of the Hamiltonian can be determined from the Schrödinger equation for a general state $|\psi(t)\rangle$ in the system at some time t:

$$\frac{\partial}{\partial t}|\psi(t)\rangle = -\frac{iH}{\hbar}|\psi(t)\rangle . \tag{4.6}$$

This naive method is often limited by the memory of the computational resources available by the system, because representing the Hamiltonian requires $\mathcal{O}(2^{2N})$ double precision numbers. However, with $U(1)$ symmetry, the Hamiltonian can be block-diagonalized, and solved separately for the sectors with different number of magnons m. The most trivial choice of basis vectors of the subspace is a basis, $|\psi\rangle_{\boldsymbol{m}}$, where spins are up for the sites specified by a vector $\boldsymbol{m}$ and down otherwise. When this treatment is done, the dimension of each subspace reduces down to $\binom{n}{k} = n!/k!(n-k)!$; hence the total number of elements in the matrix reduces down to $\sum_k \binom{n}{k}^2 = \binom{2n}{n} < 2^{2N}$.

4.1.1 Efficient Representation of the One Magnon Sector

In the case for $m = 1$, the basis states are given by, $|i\rangle$ for $0 \leq i < N$, where the i^{th} spin is up (positive eigenstate of S^z), and other spins are down (negative eigenstate of S^z). The dimension of the Hilbert space is reduced to $D_{m=1} = N$ from $D_{\text{full}} = 2^N$. For real valued function $J(d)$, the Hamiltonian can be represented in the matrix form

$$H = \begin{pmatrix} g & J(1) & J(2) & \cdots & J(N-2) & J(N-1) \\ J(1) & g & J(1) & \cdots & J(N-3) & J(N-2) \\ \vdots & \vdots & \vdots & & \vdots & \vdots \end{pmatrix} . \tag{4.7}$$

This matrix is called a circuilant matrix. The spectrum of this matrix is given by the discrete Fourier transform of $J(d)$ with $J(0) = g$ [282]

$$E(k) = \sum_d J(d)e^{-ikd}, \tag{4.8}$$

with eigenvectors

$$|E(k)\rangle = \sum_j \frac{1}{\sqrt{N}} e^{-ijk}|j\rangle , \ H_{m=1}|E(k)\rangle = E(k)|E(k)\rangle . \tag{4.9}$$

Thus, the evolution of any state $|\psi\rangle$ is given by the solution to the Schrödinger equation

$$\frac{\partial}{\partial t}|\psi(t)\rangle = -\frac{iH}{\hbar}|\psi(t)\rangle \;\rightarrow\; |\psi(t)\rangle = \left(\sum_k e^{-\frac{iE(k)}{\hbar}t}|E(k)\rangle\langle E(k)|\right)|\psi\rangle\,. \tag{4.10}$$

4.1.2 Efficient Representation of the Two Magnons Sector

For $m = 2$, the basis can be taken as $|m_1, m_2\rangle = S^+_{m_1}S^+_{m-1}|\Omega\rangle$ for all combinations of the positions of the excitations, $m_1 \neq m_2$, where $|\Omega\rangle$ is a state with all the spins down. The general state $|\psi\rangle$, can then be written as

$$|\psi\rangle = \sum_{m_1\neq m_2}\psi_{m_1m_2}|m_1m_2\rangle\,. \tag{4.11}$$

From the symmetry of the Hamiltonian, the basis states are required to be invariant under two symmetry transformations: permutation symmetry between m_1 and m_2, denoted as $\pi(m_1, m_2)$, and lattice translation symmetry $m_1 \rightarrow m_1 + 1$, $m_2 \rightarrow m_2 + 1$ denoted as $\theta(m_1, m_2)$. In general, a basis state can be represented by the translation and permutation operation on a state $|0, |m_1 - m_2|\rangle$

$$|m_1, m_2\rangle = \pi^p\theta^{|m_1-m_2|}|0, |m_1 - m_2|\rangle\,. \tag{4.12}$$

Therefore, a basis state can also be written as the sum of orthonormalized momentum basis states of the form

$$|K^{(k)}(|m_1 - m_2|)\rangle = \sum_l\sqrt{\frac{1}{\mathcal{N}_{|m_1-m_2|}N/2}}\mathrm{e}^{-ilk}\theta^l|0, |m_1 - m_2|\rangle\,, \tag{4.13}$$

where the normalization factor $\mathcal{N}_{|m_1-m_2|}N$ is the number of unique elements that can be reached from $(0, |m_1 - m_2|)$ with permutation and translation operations, and factor of $1/2$ is to account for redundancy from the permutation symmetry. For $m = 2$, the normalization factor is given by

$$\mathcal{N}_{|m_1-m_2|} = \begin{cases} 2 & (|m_1 - m_2| < N/2) \\ 1 & (|m_1 - m_2| = N/2) \end{cases}. \tag{4.14}$$

Since the Hamiltonian has translational symmetry, the matrix representation of the 2-magnon sector can be further block diagonalized by their momentum, where elements of the matrix of $Nk/2\pi^{\text{th}}$ momentum sector is given by (§4.1)

$$\begin{aligned} H^{(k)}_{|m_1'-m_2'|,|m_1-m_2|} &= J(|m_1'-m_2'|-|m_1-m_2|) \\ &\quad + J^*(|m_1'-m_2'|-|m_1-m_2|)e^{i\left(|m_1'-m_2'|-|m_1-m_2|\right)k} \\ &\quad + J(|m_1'-m_2'|+|m_1-m_2|)e^{-i|m_1-m_2|k} \\ &\quad + J^*(|m_1'-m_2'|+|m_1-m_2|)e^{i|m_1-m_2|k} \qquad (Lk/2\pi \text{ odd})\,. \end{aligned} \tag{4.15}$$

For even $Nk/2\pi$, in addition to the above, there is transition which involves $|m_1-m_2| = N/2$. They are given by:

$$H^{(k)}_{|m_1'-m_2'|,N/2} = \sqrt{2}\left(J(|m_1'-m_2'|-N/2) + J^*(|m_1'-m_2'|-N/2)e^{ik|m_1'-m_2'|}\right), \tag{4.16}$$

$$H^{(k)}_{N/2,|m_1-m_2|} = \left(H^{(k)}_{|m_1-m_2|,N/2}\right)^*, \tag{4.17}$$

$$H^{(k)}_{N/2,N/2} = 2J(0). \tag{4.18}$$

4.1.3 Krylov Method for Spectrum Determination and Evolution

With a matrix representation of the Hamiltonian, the static and dynamical properties of a system can be determined from its spectrum (eigenenergies) and the corresponding eigenstates of the Hamiltonian. In order to determine those quantities, the matrix must be diagonalized by finding the unitary transformation U, which transforms arbitrary basis in terms of the eigenbasis of the Hamiltonian,

$$H = U^\dagger \Lambda U, \tag{4.19}$$

where H is the Hamiltonian and Λ is a diagonal matrix which consists of the eigenenergies of the system.

In general, there are many ways to solve this problem numerically for general class of matrices [283]. However, by constraining the matrices of interest to a set of (real) Hermitian matrices, which are commonly used for representing the Hamiltonian of various physical systems, computation can often be efficient. Here we introduce the Krylov method for spectrum determination and time evolution of a state.

The Krylov subspace $\mathcal{K}$ is a subspace spanned by Dim$\{H\}$ non-orthonormal basis of the form

$$|\mathcal{K}_n\rangle \in \mathcal{K}_{\text{Dim}\{H\}} \equiv \left\{ |\psi\rangle, H|\psi\rangle, H^2|\psi\rangle, \cdots, H^{\text{Dim}\{H\}-1}|\psi\rangle \right\}. \tag{4.20}$$

The Lanczos algorithm [147, 283–285] utilizes the Krylov basis and tridiagonalizes a symmetric matrix in the following form:

$$H = M \begin{pmatrix} \alpha_0 & \beta_0 & & & & & \\ \beta_0 & \alpha_1 & \beta_1 & & & & \\ & \beta_1 & \alpha_2 & \beta_2 & & 0 & \\ & & \ddots & \ddots & \ddots & & \\ & & & \ddots & \ddots & \ddots & \\ & & 0 & & \beta_{\mathcal{L}-3} & \alpha_{\mathcal{L}-2} & \beta_{\mathcal{L}-2} \\ & & & & & \beta_{\mathcal{L}-2} & \alpha_{\mathcal{L}-1} \end{pmatrix} M^{\dagger}, \tag{4.21}$$

where $\mathcal{L}$ is a number of Lanczos steps in the Lanczos algorithm that is described in the following, and M is a Dim$\{H\}$ by $\mathcal{L}$ square matrix of the form

$$M = \Big(|V_0\rangle, |V_1\rangle, \cdots, |V_{\mathcal{L}-1}\rangle \Big), \tag{4.22}$$

where $|V_i\rangle$ are the orthonormal basis vectors.

These orthonormal basis vectors can be computed iteratively by solving the following recursive relationships. Setting a random vector $|\psi\rangle = |V_0\rangle$ as the starting vector:

$$\begin{aligned} H|\psi\rangle &= \alpha_0|V_0\rangle + \beta_0|V_1\rangle, \\ H|V_1\rangle &= \beta_0|V_0\rangle + \alpha_1|V_1\rangle + \beta_1|V_2\rangle, \\ &\vdots \\ H|V_n\rangle &= \beta_{n-1}|V_{n-1}\rangle + \alpha_n|V_n\rangle + \beta_n|V_{n+1}\rangle, \\ &\vdots \\ H|V_{\mathcal{L}-1}\rangle &= \beta_{\mathcal{L}-2}|V_{\mathcal{L}-2}\rangle + \alpha_{\mathcal{L}-1}|V_{\mathcal{L}-1}\rangle, \end{aligned} \tag{4.23}$$

and imposing the condition of orthonormality of two basis vectors,

$$\langle V_i | V_j \rangle = \delta_{i,j}, \tag{4.24}$$

the coefficients α and β are then, written as follows:

$$\alpha_n = \langle V_n | H | V_n \rangle \tag{4.25}$$

$$\beta_n = | (H - \alpha_n) | V_n \rangle - \beta_{n-1} | V_{n-1} \rangle |, \tag{4.26}$$

with $\beta_{-1} = 0$. As it can be seen in Eq. (4.23), at the n^{th} step of the algorithm, the subspace spanned by the generated orthonormal basis $|V_0\rangle, |V_1\rangle, \cdots, |V_n\rangle$ which is a linear super position of the 0^{th} to the n^{th} Krylov basis. Thus, Lanczos algorithm efficiently computes the Krylov subspace when stopped before the complete orthonormal basis vectors are computed.

With the new basis, the full eigenvalues of the Hamiltonian λ can be efficiently computed by solving the characteristic equation

$$\det\{\lambda I - H_{\text{tridiagonal}}\} = 0, \tag{4.27}$$

which has a recursion relation

$$\eta_{\mathcal{L}-1}(\lambda) = (\lambda - \alpha_{\mathcal{L}-1})\, \eta_{\mathcal{L}-2}(\lambda) - \beta^2_{\mathcal{L}-2} \eta_{\mathcal{L}-3}(\lambda), \tag{4.28}$$

where

$$\eta_n(\lambda) = \det\left\{\begin{pmatrix} \lambda - \alpha_0 & -\beta_0 & & & & \\ -\beta_0 & \lambda - \alpha_1 & -\beta_1 & & & \\ & -\beta_1 & \lambda - \alpha_2 & -\beta_2 & & 0 \\ & & \ddots & \ddots & \ddots & \\ & & & \ddots & \ddots & \ddots \\ & 0 & & & \beta_{n-1} & \lambda - \alpha_n \end{pmatrix}\right\}, \tag{4.29}$$

with $\eta_{-1}(\lambda) = 1$. The roots of the characteristic polynomial are the spectrum of the Hamiltonian, and this can be found using ordinary solvers (e.g. algorithms can be found in [286]).

When calculating the dynamical properties of a system, often determination of the full spectrum of the Hamiltonian can be more than is necessary. Given an initial state $|\psi(0)\rangle$, we are often interested in finding the time evolution of the state to some time t, and compute expectation values of various quantities. For evolution for a small amount of time $t \rightarrow t+\Delta t$, $\hbar|H|\Delta t \ll 1$, the matrix exponentiation can be approximated using a power series with an error of order $\mathcal{O}\left((\Delta t)^{\xi+1}\right)$, where ξ is the number of terms kept in the Taylor expansion. However, this can be done more efficiently by performing the Lanczos algorithm, which utilizes the structure of the Krylov subspace.

The Lanczos algorithm tridiagonalizes the Hamiltonian with the basis vectors of the sum of Krylov vectors up to of order $\mathcal{L}$ in the iterative application of $-iH\Delta t$, on $|\psi(0)\rangle$. This usually causes the coefficients α and β to be vanishingly small in the later steps of the algorithm because the higher order Krylov vectors does not, in general, contribute to the evolution of $|\psi(0)\rangle$ in a small time step. Unlike the Taylor expansion, the algorithm takes information about the state vector which is under evolution, therefore the error bound on the effect of applying an exponentiated matrix, which is approximated with much smaller tridiagonal matrix using the Lanczos algorithm, is often much smaller compared to the naive Taylor expansion [283, 285] of the same order. Thus, exponentiation of large and often sparse matrix representations of a Hamiltonian represented by a Hermitian matrix can be approximated well by exponentiation of a small and dense matrix with dimension $\mathcal{L} \ll \mathrm{Dim}\{H\}$.

4.2 Matrix Product States and Matrix Product Operators

In this section, we introduce an efficient state representation by restricting our state space to a set of states with low energy and locally confined entanglement profile, called a Matrix Product State (MPS) [89, 91, 108–114, 142, 147, 235, 287–292]. Then we show that similar representation can be used for operators, which is known as Matrix Product Operators (MPO) [113, 115, 145, 147, 293]. Finally we summarize a method for factorization of local quantum operators which can then be time evolved and used to compute quantities such as Out-of-Time-Order Correlators (OTOCs) that are discussed in the previous chapter.

4.2.1 Matrix Product States

MPSs are representations of pure quantum states $|\psi\rangle$, which decomposes the coefficient of a basis states $C_{\boldsymbol{\sigma}}$ into matrices A_i^{σ} in the form:

$$|\psi\rangle = \psi_{\boldsymbol{\sigma}} |\boldsymbol{\sigma}\rangle = \sum_{\boldsymbol{\sigma}} \mathrm{Tr}\{A_0^{(\sigma_0)} A_1^{(\sigma_1)} \cdots A_{N-2}^{(\sigma_{N-2})} A_{N-1}^{(\sigma_{N-1})}\} |\boldsymbol{\sigma}\rangle \tag{4.30}$$

where $\boldsymbol{\sigma} = (\sigma_0, \sigma_1, \cdots, \sigma_{N-2}, \sigma_{N-1})$ are the configurations of the local basis states (for example, ↑ or ↓ for a chain of spin-1/2), and the implicit product between A implies matrix multiplications of a form

$$A_n^{(\sigma_n)} A_{n+1}^{(\sigma_{n+1})} \equiv \sum_j \left(A_n^{(\sigma_n)}\right)_{ij} \left(A_{n+1}^{(\sigma_{n+1})}\right)_{jk}, \tag{4.31}$$

where j goes from 1 to a bond (auxiliary) dimension $\mathcal{D}_{[n,n+1]}$. With this representation, the required number of parameters for numerically representing a state is $N\bar{\mathcal{D}}^2 D_{\mathrm{loc}}$, where N is the system size, $\bar{\mathcal{D}}$ is a typical bond dimension, and D_{loc} is the dimension of the local Hilbert space. This is linear in N, which is advantageous in comparison to the previously discussed exact diagonalization methods, which at worst, the number of parameters grows exponentially with the system size, and at best, combinatorically.

Due to the property of the matrix product, the representation has gauge freedom on how matrices A are decomposed and merged with the neighboring matrices. Here we chose a Singular Value Decomposition (SVD) [113, 114, 142, 235, 293] of the form

$$A = U \Lambda V^{\dagger}, \tag{4.32}$$

where Λ is a diagonal matrix, and U and V are semi-unitary matrices which satisfy $U^{\dagger}U = I$ and $V^{\dagger}V = I$ respectively. Reshaping and contracting the indices σ and i, $(A_n^{\sigma_n})_{ij} \to (A_n)_{(\sigma_n,i),j}$, and performing the SVD, yields

$$(A_n)_{(\sigma_n,i),j} = \sum_{p.q} (U_n)_{(\sigma_n,i),p} (\Lambda_n)_{pq} (V_n)_{qj}, \tag{4.33}$$

where U can be reshaped back to $U_{i,l}^{\sigma}$ and the local state dependence can be taken away from the matrices Λ and V. U and V can then be contracted with the matrix to the right, $\left(A_{n+1}^{\sigma}\right)_{j,k}$. By doing this from $n = 0$ to $n = N-2$, one obtains a left canonicalized form of an MPS

$$|\psi\rangle = \sum_{\sigma} \mathrm{Tr}\{U_1^{\sigma_1} U_2^{\sigma_2} \cdots U_{n-2}^{(\sigma_{n-2})} \Psi_{n-1}^{(\sigma_{n-1})}\} \, |\boldsymbol{\sigma}\rangle \, . \tag{4.34}$$

Doing the same while leaving $V^\dagger$ from the right, a right (sweeping from $n = N-1$ to $n = 1$) canonicalized MPS can be obtained:

$$|\psi\rangle = \sum_{\sigma} \mathrm{Tr}\{U_1^{\sigma_1} U_2^{\sigma_2} \cdots U_{n-2}^{(\sigma_{n-2})} \Psi_{n-1}^{(\sigma_{n-1})}\} \, |\boldsymbol{\sigma}\rangle \, . \tag{4.35}$$

When the canonicalization is done simultaneously, and stopped at site l, then we get a mixed canonical form

$$|\psi\rangle = \sum_{\boldsymbol{\sigma}} U_1^{\sigma_1} U_2^{(\sigma_2)} \cdots U_{l-1}^{(\sigma_{l-1})} \Lambda_l^{\sigma_l} V_{l+1}^{\sigma_{l+1}} V_{l+2}^{(\sigma_{l+2})} \cdots V_{n-1}^{(\sigma_{n-1})} \, |\boldsymbol{\sigma}\rangle \, . \tag{4.36}$$

This representation is useful for computing a local expectation value of an operator, $O_{\sigma_l}^{\sigma_l'}$, which maps state σ to σ', due to the properties $U^\dagger U = I$ and $V^\dagger V = I$, the expectation value can be calculated as follows:

$$\langle O \rangle = \sum_{\sigma' \sigma} \mathrm{Tr} \left\{ \Lambda^{\sigma'} \left(\mathcal{O}^{\sigma'} \right)_{\sigma}^{\dagger} \Lambda^{\sigma} \right\} . \tag{4.37}$$

Furthermore, this representation can be used to efficiently calculate the bipartite entropy between sites $0, 1, \cdots, l$ and $l{+}1, l{+}2, \cdots, N{-}1$. Since the reduced density matrix of the subregion $0 \cdots l$ is a density matrix of a full state where $l = 1 \cdots N{-}1$ is traced out, the entropy is just the square of the Schmidt coefficients (values of $\Lambda_l^{\sigma_l}$). Hence, the von Neumann entropy between the two partitions is

$$\begin{aligned} S(\{0, 1, \cdots, l\}) &= -\mathrm{Tr} \left\{ (\Lambda_l^{\sigma_l})^\dagger \, \Lambda_l^{\sigma_l} \ln (\Lambda_l^{\sigma_l})^\dagger \, \Lambda_l^{\sigma_l} \right\} \\ &= \sum_i^{\mathcal{D}} |\lambda_i|^2 \ln |\lambda_i|^2 . \end{aligned} \tag{4.38}$$

From these properties of the MPS in the mixed canonical form, it is evident that the entanglement between two parts of the system is mediated by the bond dimension of the neighboring matrices. Naturally, as a consequence, even with a small value of the typical bond dimension $\bar{\mathcal{D}}$, a state with weak or spatially confined entanglement can be accurately represented. Thus, MPS provides an efficient representation of a set of quantum states with short-range correlations. This is especially works efficiently on the state with area-law entanglement, where the entanglement entropy of a region is only proportional to the area at the boundary of the region [113, 234, 235, 294].

4.2.2 Matrix Product Operators

Similarly to the MPS formulation, the operators can be represented as a form of a product of high-dimensional matrices (tensors). The Matrix Product Operator (MPO) representation [113, 115, 145, 147, 293] decomposes an operator acting on a Hilbert space:

$$O = \sum_{\boldsymbol{\sigma};,\boldsymbol{\sigma}} W^{\sigma'_1}_{\sigma_1} W^{\sigma'_2}_{\sigma_2} \cdots W^{\sigma'_{N-1}}_{\sigma_{N-2}} W^{\sigma'_{N-1}}_{\sigma_{N-1}} \left|\boldsymbol{\sigma'}\right\rangle \left\langle\boldsymbol{\sigma}\right| . \tag{4.39}$$

Given a sum of local few-body operators, matrix product representation of the Hamiltonian or general operators can be done as the following [115, 145, 147, 295, 296]: given an operator in the form

$$O = O_{\text{left},l} \otimes I_{\text{right}} + I_{\text{left}} \otimes O_{\text{right},l} + \sum_{i<l} \sum_{l<j} \sum_{q} O^q_i \otimes O^q_l \otimes O^q_j , \tag{4.40}$$

where $O_{\text{left},l}$ denotes a set of operators acting only on the left of site l, $O_{\text{right},l}$ denotes a set of operators acting on the right of site l, $I_{\text{left},l}$ ($I_{\text{right},l}$) is an identity operators that acts on the sites on the left (right) sites of l. The last summation term consists of all the operators that can be written as a product of local operators on the left ($i < l$), right ($j = l$) and at the site l, $O^q_i \otimes O^q_l \otimes O^q_j$.

Iteratively from the 0^{th} site, at l^{th} step, the operator O can be written in the upper triangular form as a following:

$$\begin{aligned} O &= I_0 \otimes O_{\text{right},0} + O'_0 \otimes O'_{\text{right},0} + O''_0 \otimes O''_{\text{right},0} + \cdots + O_0 \otimes I_{\text{right},0} + I \\ &= \begin{pmatrix} I_0 & O'_0 & O''_0 & \cdots & O_0 & I_0 \end{pmatrix} \begin{pmatrix} O_{\text{right},0} \\ O'_{\text{right},0} \\ O''_{\text{right},0} \\ \vdots \\ I_{\text{right}} \\ I_{\text{right}} \end{pmatrix}. \end{aligned} \tag{4.41}$$

Where the elements of the column vector to the right do not depend on the 0^{th} site, therefore performing the decomposition similarly on each element yielding an upper triangular matrix of the form,

$$O = \cdots \begin{pmatrix} I_l & & \cdots & & O'_l & \cdots & O''_l \\ & & & & & & \\ 0 & \cdots & 0 & \cdots & O'''_l & \cdots & O''''_l \\ & & & & & & \\ 0 & \cdots & 0 & \cdots & 0 & \cdots & I_l \end{pmatrix}_l \begin{pmatrix} O_{\text{Right},l} \\ \vdots \\ O'''''_{\text{Right},l} \\ \vdots \\ I_{\text{Right},l} \end{pmatrix}_{\text{Right}} , \tag{4.42}$$

where O_l with primes are there to show that it is general for any local operator at site l[1]. Thus, the operator consists of summation over locally confined and few bodied terms, like the Hamiltonian of a system, can be efficiently represented with MPO.

4.2.2.1 Time Evolution of Matrix Product Operators

In order to calculate quantities such as Out-of-Time-Order Correlators (OTOCs, c.f. Ch. 3.1), which involves expectation values of product of operators at different times in the system, the time evolution of matrix product operators are necessary. Here we show the vectorization of a local operator into the form of MPS, which can then be evolved using a time evolution algorithm for MPSs.

---

[1] operators can be null

The tensor product representation of a local operator O_l at site l is

$$O_l = (I_0) \otimes (I_1) \otimes \cdots \otimes (O_l) \otimes (I_{l+1}) \otimes \cdots \otimes (I_{N-1})\,. \tag{4.43}$$

Therefore, an MPO can be represented in the form,

$$O_l = \sum_{\boldsymbol{\sigma}_{\neq l}} \sum_{\sigma'_l} \sum_{\sigma_l} O^{\sigma'_l}_{\sigma_l} \left|\boldsymbol{\sigma}_{\neq l}\right\rangle \left|\sigma'_l\right\rangle \left\langle\sigma_l\right| \left\langle\boldsymbol{\sigma}_{\neq l}\right|\,. \tag{4.44}$$

The vectorization can then be done by reshaping the indices σ' and σ as, $\mathcal{O}^{\sigma'_l}_{\sigma_l} \rightarrow \mathcal{O}_{(\sigma'_l,\sigma_l)}$:

$$O_l = \sum_{\boldsymbol{\sigma}_{\neq l}} \sum_{(\sigma'_l,\sigma_l)} O_{(\sigma'_l,\sigma_l)} \left|\boldsymbol{\sigma}_{\neq l}\right\rangle \left|\sigma'_l\right\rangle \left|\sigma_l\right\rangle \left|\boldsymbol{\sigma}_{\neq l}\right\rangle\,. \tag{4.45}$$

Since it is now represented in the form of an MPS, the time evolution algorithms for MPS, such as the time-dependent-variational-principle [94, 97, 116, 144, 148] or other methods such as direct time evolution with matrix exponentiation [92], direct-MPO methods [145], or hybrid methods [147], can be used to obtain the time evolved vectorized operator. The time evolved vectorized MPO can then be reshaped back into the original basis to recover the time evolved operator $O_l(t)$.

For diagonal operators, the computation can be more efficient. By utilizing the fact that basis $\left|\boldsymbol{\sigma}_{\neq l}\right\rangle \left|\sigma'_l\right\rangle$ and $\left|\sigma_l\right\rangle \left|\boldsymbol{\sigma}_{\neq l}\right\rangle$ are symmetric. In this case, one only needs to compute the time evolution of the one of the basis of the square root of the operator $\sqrt{O_l}$. The time evolved operator can then be obtained by contracting the partially time evolved square rooted operator with its Hermitian conjugate. Let O_D be a local operator that is diagonal in local basis $\{|\sigma\rangle\}$. $\sqrt{O_D}$ in the MPS form is:

$$\sqrt{(O_D)} = \sum_{\boldsymbol{\sigma}_{\neq l}} \sum_{\sigma_l} \sqrt{(O_D)_{(\sigma_l,\sigma_l)}} \left(\left|\boldsymbol{\sigma}_{\neq l}\right\rangle \left|\sigma_l\right\rangle\right)_{\text{Left}} \otimes \left(\left|\sigma_l\right\rangle \left|\boldsymbol{\sigma}_{\neq l}\right\rangle\right)_{\text{Right}} \tag{4.46}$$

Time evolving $\sqrt{D}$ for time t by acting time evolution operator of Hamiltonian H_{Left}, which only acts on the left (original) basis, yields (with $\hbar = 1$):

$$\begin{aligned} e^{iH_{\text{Left}}\otimes I_{\text{Right}}t}\left(\sqrt{O_D}\right)_{\text{MPS}} = \sum_{\boldsymbol{\sigma}_{\neq l}}\sum_{\sigma_l}\Bigg[\sqrt{(O_D)_{(\sigma_l,\sigma_l)}}\left(e^{iH_{\text{Left}}t}\left|\boldsymbol{\sigma}_{\neq l}\right\rangle\left|\sigma_l\right\rangle\right)_{\text{Left}} \\ \otimes\left(\left|\sigma_l\right\rangle\left|\boldsymbol{\sigma}_{\neq l}\right\rangle\right)_{\text{Right}}\Bigg]. \end{aligned} \tag{4.47}$$

Putting it back into an operator form yields:

$$e^{iH_{\text{Left}}\otimes I_{\text{Right}}t}\left(\sqrt{O_D}\right)_{\text{MPO}} = \sum_{\boldsymbol{\sigma}_{\neq l}}\sum_{\sigma_l}\sqrt{(O_D)_{(\sigma_l,\sigma_l)}}e^{iH_{\text{Left}}t}\left|\boldsymbol{\sigma}_{\neq l}\right\rangle\left|\sigma_l\right\rangle\left\langle\sigma_l\right|\left\langle\boldsymbol{\sigma}_{\neq l}\right|. \tag{4.48}$$

Thus, $O_D(t)$ in the MPO form is obtained by contracting $e^{iH_{\text{Left}}t}\left(\sqrt{O_D}\right)_{\text{MPO}}$ with its Hermitian conjugate:

$$\begin{aligned} & e^{iH_{\text{Left}}t}\left(\sqrt{D}\right)_{\text{MPO}}\left(e^{iH_{\text{Left}}t}\left(\sqrt{O_D}\right)_{\text{MPO}}\right)^{\dagger} \\ &= \sum_{\boldsymbol{\sigma}_{\neq l}}\sum_{\sigma_l}\sqrt{(O_D)_{(\sigma_l,\sigma_l)}}e^{iH_{\text{Left}}t}\left|\boldsymbol{\sigma}_{\neq l}\right\rangle\left|\sigma_l\right\rangle\left\langle\sigma_l\right|\left\langle\boldsymbol{\sigma}_{\neq l}\right| \\ &\times\sum_{\boldsymbol{\sigma}'_{\neq l}}\sum_{\sigma'_l}\sqrt{(O_D)_{(\sigma'_l,\sigma'_l)}}\left|\boldsymbol{\sigma}'_{\neq l}\right\rangle\left|\sigma'_l\right\rangle\left\langle\sigma'_l\right|\left\langle\boldsymbol{\sigma}'_{\neq l}\right|e^{-iH_{\text{Left}}t} \\ &= e^{iHt}\left(\sum_{\boldsymbol{\sigma}_{\neq l}}\sum_{\sigma_l}D_{(\sigma_l,\sigma_l)}\left|\boldsymbol{\sigma}_{\neq l}\right\rangle\left|\sigma_l\right\rangle\left\langle\sigma_l\right|\left\langle\boldsymbol{\sigma}_{\neq l}\right|\right)e^{-iHt} = D(t). \end{aligned} \tag{4.49}$$

4.3 Tensor Network Representation of Quantum Dynamics

The diagrammatic notation of tensors was invented by Penrose in the late 1900s [297, 298]. In Penrose's diagrammatic notation, a tensor is represented by a solid shape with legs, where the legs represent indices (Fig. 4.1 a. (top)). For example, a product of two matrices M and M':

$$\mathcal{M}_{ik} = \sum_j (M)_{ij}(M')_{jk}, \tag{4.50}$$

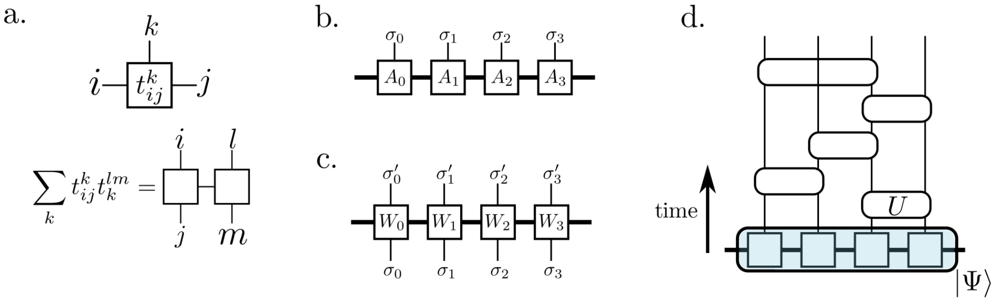

FIGURE 4.1: **Diagrammatic notation of a quantum state.** a. Penrose's diagrammatic representation of a tensor t_{ij}^{k} (above) and a dot product $\sum_k t_{ij}^k t_k^{lm}$ (below). b. A diagrammatic representation of an MPS. c. A diagrammatic representation of an MPO. d. Tensor network representation of a state $|\Psi\rangle$ (enclosed in a blue shade) evolving under two-qubit gates U (rectangles).

where $(M)_{ij}$ a number on i^{th} row and j^{th} column of a matrix, can be represented as a contraction of a leg between two tensors as shown in Fig. 4.1 a. (bottom).

A tensor network [91, 97, 101, 108, 113, 115, 142, 235, 287, 288, 290–294, 299–304] is a representation of a quantum mechanical state and its evolution as a contraction of tensors. As established in §4.2, coefficients of given basis states of a quantum state in an MPS form can be written as a product of matrices. As matrices are rank-2 tensors, a state can be represented in a diagrammatic form as a contraction of tensors as shown in Fig. 4.1 a. (below), where each box corresponds to A matrices in Eq. (4.30) and horizontal contraction for matrices with a fixed local basis $\sigma_i \in \boldsymbol{\sigma}$ yields the coefficient of a global basis state $\langle\psi|\boldsymbol{\sigma}\rangle$ of a state $|\psi\rangle$. Similarly, an operator can also be represented in the form shown in Fig. 4.1 c., where each box represents W matrices in Eq. (4.39). An operator acting on a state is then a contraction of leg corresponding to a local basis state σ, where an example of unitary two-qubit gates acting on $|\psi\rangle$ is shown in Fig. 4.1 d. Thus, an MPS, its time evolution with MPOs, and a quantum circuit, can be represented in a form of a tensor network.

4.3.1 Calculation of Renyi Entropy from a Tensor Network

With the large enough bond dimensions $\mathcal{D}$, any quantum state on a lattice with a finite local Hilbert space dimension can be represented with an MPS or analogous higher dimensional representation [294] (such as projected entangled pair states [292, 293, 300, 302, 305]). In general, representing an arbitrary state analytically

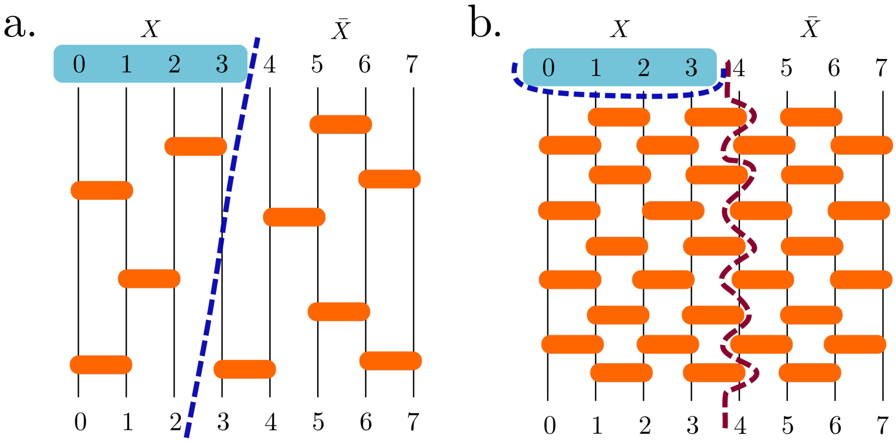

FIGURE 4.2: **Calculation of Renyi entropy of order 0 from the minimal cut.**
a. Haar random two-site gates typically generate nearly maximal entanglement. When there are not enough gates to maximally entangle $X = \{0, 1, 2, 3\}$ (blue shaded) to $\bar{X} = \{4, 5, 6, 7\}$, Renyi entropy of order 0 entropy, $S^{(0)}$, is given by the minimum number of legs of the tensors (orange squares) must be cut in order to isolate X. The minimum cut for this circuit is shown by a blue dotted line. b. When the cut along the boundary exceeds $\log_2 \mathrm{Dim}\{H_X\}$ (dark red, dotted) it is guaranteed that such a cut is not a minimum cut. In this case the minimal cut which isolates X is a trivial cut along the legs of the qubits in X (blue dotted line).

or using computer is not practical because for MPS, the required memory scales as $\propto N\mathcal{D}^2$ and associated computational complexity of MPS-MPO contraction scales as $\mathcal{D}^3$, while the maximum entropy scales only logarithmically: $\max\{S\} = \ln \mathcal{D}$ [142].

However, with tensor network representation, the entanglement structure of an output state of a strongly scrambling quantum circuit can be determined from the network diagram without the knowledge of an exact state. Here we provide a simple example of calculating the Renyi entropy of order 0 [306], $S^{(0)}$, of an output state of a random quantum circuit from a tensor network diagram.

Renyi entropy is a generalization of Shannon entropy, where the classical Renyi entropy of order α ($\mathcal{S}^{(\alpha)}$) is defined on some random variable X as

$$\mathcal{S}^{(\alpha)}(X) = \frac{1}{1-\alpha} \ln \left(\sum_i p_i^\alpha \right), \tag{4.51}$$

where p_i is a probability of obtaining a state $x_i \in X$. The definition expands to a quantum state (density matrix) ρ as [119, 307]

$$S^{(\alpha)} = \frac{1}{1-\alpha} \ln \mathrm{Tr}\{\rho^{\alpha}\}, \tag{4.52}$$

where the limit $\alpha \to 1$, we recover the von Neumann entropy [307] discussed in Ch. 2.2. The Renyi entropy of order 0, $S^{(0)}$, is given by the logarithm of the rank M of the state ρ

$$S^{(0)} = \ln M. \tag{4.53}$$

The computation of $S^{(0)}/\ln 2$, then, maps to a classical minimal cut problem [119, 122, 294, 308] in the following way: when a non correlated pair of two-level systems (qubits) in some region X and $\bar{X}$, where $\bar{X}$ is a complementary region of X, are entangled, the rank of the density matrix of region X, $\rho_X = \mathrm{Tr}_{\bar{X}}\rho$, increases by a factor of 2. For a circuit which consists of Haar random unitary two-qubit gates (c.f. Appendix A), when a gate is applied to two non-correlated pairs of qubits, they are almost guaranteed to be entangled [122, 151]. In this case, the circuit is drawn as a tensor network diagram as shown in Fig. 4.2, and the logarithm of the rank of the output state can be calculated by counting the minimal number of the legs of the tensors, which extends from region X to region $\bar{X}$. This is equivalent to the minimal number of cuts that must be made to isolate the qubits in X (Fig. 4.2 a. purple). At late times, the number becomes equivalent to the logarithm of the size of the Hilbert space dimension of X. In this case, the minimal cut becomes $|X|$, the number of cuts required to isolate the output qubits by its legs (Fig. 4.2 b. purple dotted line). Thus, the minimal cut shows the notion of locality in spacetime, and it captures the entanglement structure of the quantum state which lives at the boundary of a network.

4.4 State Evolution with Quantum Circuit Restricted to the Clifford Group

In sections §4.1 and §4.2, the reduction in the number of parameters for representing a quantum system is done based on the physical requirements. In this section, we introduce an approach based on algebraic requirements for reducing the degrees of freedom in order to numerically solve quantum systems with a large number of qubits.

4.4.1 Pauli Operators

In quantum information theory, a qubit is a two-level quantum system with levels $|0\rangle$ and $|1\rangle$. A single qubit state $|\psi\rangle$ then takes a form

$$|\psi\rangle = \theta_0 |0\rangle + \theta_1 |1\rangle, \tag{4.54}$$

with associated complex coefficients θ_0 and θ_1. By requiring $\sum_i |\theta_i|^2 = 1$, θ_0 and θ_1 can be specified with three real parameters (degrees of freedom), complex amplitude and phase of θ_0 and complex phase of θ_1.

Now, we look at a physical system, such as a spin-1/2 system with state $|0\rangle = |\downarrow\rangle$ and $|1\rangle = |\uparrow\rangle$. This is a valid quantum two-level system, and the three degrees of freedom correspond to the spatial orientation of the spin, described by the density matrix of an arbitrary pure state, can be parameterized as

$$\rho = \frac{I}{2} + s_1 S^x + s_2 S^y + s^3 S^z, \tag{4.55}$$

with

$$s_1 = \theta_1^* \theta_2 + \theta_1 \theta_2^* \tag{4.56}$$

$$s_2 = i(\theta_1 \theta_2^* - \theta_1^* \theta_2) \tag{4.57}$$

$$s_3 = |\theta_1|^2 - |\theta_2|^2 \tag{4.58}$$

$$1 = \sqrt{s_1^2 + s_2^2 + 3_3^2} = \sqrt{(|\theta_1|^2 + |\theta_2|^2)^2}, \tag{4.59}$$

where S^λ are spin operators which obeys the spin algebra introduced in (4.2). The parameter set (s_1, s_2, s_3) with constraint Eq. (4.59), maps to a set of position vectors of the points on a unit sphere in the three-dimensional Euclidean space known as the Bloch sphere [66, 309].

Generally, not all two-level systems have physical direction and corresponding observables like spin-1/2 systems. In such a case, we generalize the spin-1/2 operators as following:

$$
\begin{aligned}
\sigma_0 = \ I \ &= \begin{pmatrix} 1 & 0 \\ 0 & 1 \end{pmatrix}, \quad & \sigma_1 = 2S^x &= \begin{pmatrix} 0 & 1 \\ 1 & 0 \end{pmatrix}, \\
\sigma_2 = 2S^y &= i \begin{pmatrix} 0 & -1 \\ 1 & 0 \end{pmatrix}, \quad & \sigma_3 = 2S^z &= \begin{pmatrix} 1 & 0 \\ 0 & -1 \end{pmatrix},
\end{aligned} \tag{4.60}
$$

in the basis of eigenvectors of σ^3, which we define as $|0\rangle$ for a state with eigenvalue of -1 and $|1\rangle$ for $+1$. These σ_λ are called Pauli operators (matrices).

4.4.2 Stabilizer States

The idea of stabilizer formalism is to specify a multi-qubit state, *stabilizer state*, as a simultaneous eigenstate of chains of Pauli operators. The set of Pauli operators which specifies a state is called a stabilizer set.

Pauli strings P_i are tensor products of Pauli operators over N-qubit system and a phase $\omega = -1, 1, -i, i$,

$$
P_i \in \{\omega\sigma_0^{\lambda_0} \otimes \sigma_1^{\lambda_1} \otimes \cdots \otimes \sigma_{N-1}^{\lambda_{N-1}}\} \equiv \mathcal{P}^N, \tag{4.61}
$$

where $\sigma^{\lambda_0}, \cdots, \sigma^{\lambda_{N_1}}$ runs over all the possible Pauli operators $\sigma^0, \sigma^1, \sigma^2, \sigma^3$. A set of all Pauli strings form a group called N-qubit Pauli group, $\mathcal{P}^N$, that is closed in the multiplication.

A state $|\Sigma\rangle$ is said to be stabilized by a stabilizer $O_{|\Sigma\rangle}$ if $|\Sigma\rangle$ is a $+1$ eigenstate of $O_{|\Sigma\rangle}$. $O_{|\Sigma\rangle}$ stabilizes the state because the action of $O_{|\Sigma\rangle}$ on $|\Sigma\rangle$ does not change the state. Such a set of operator can be constructed by making use of the properties of $\mathcal{P}^N$. An operator, $O_{|\Sigma\rangle}$, which stabilizes and uniquely defines $|\Sigma\rangle$ is constructed from a set of N linearly independent Pauli strings, $\mathcal{P}_\Sigma^N \in \mathcal{P}^N$, that also stabilize the state $|\Sigma\rangle$, as following:

$$
\mathcal{O}_\Sigma = \frac{1}{2^N} \prod_{P \in \mathcal{P}_\Sigma^N}^{N} (P + I)\,. \tag{4.62}
$$

Here the linear independence of Pauli strings is equivalent to a Pauli string $P_i \in \mathcal{P}_\Sigma^N$ cannot be represented as some product of P_j $(j \neq i)$. With this constraint, $O_{|\Sigma\rangle}$ uniquely defines $|\Sigma\rangle$ as a simultaneous eigenstate of $P \in \mathcal{P}_\Sigma$ [66, 90, 118, 310].

4.4.3 Efficient Simulation of Stabilizer States with Clifford Gates

Consider a unitary operator $\mathcal{O}_C$ which transforms an element of $\mathcal{P}^N$ to some element in the same group. A group $\{O_C\} \equiv \mathcal{C}^N$ formed by such operators is called N-qubit Clifford group. The action of such a unitary operator on a stabilizer set O_Σ, produces some other stabilizer set $O_{|\Sigma'\rangle} = \mathcal{O}_C \mathcal{O}_\Sigma \mathcal{O}_C^\dagger$, which stabilizes a state $|\Sigma'\rangle = \mathcal{O}_C |\Sigma\rangle$. The evolution of a stabilizer state under actions of the elements of the Clifford group can, therefore, be simulated by keeping track of how N Pauli strings transform by the action of Clifford gates $O_C \in \mathcal{C}^N$.

A stabilizer state undergoing unitary evolution by the elements in the Clifford group is known to be classically computable in polynomial time [90, 118]. The simulation of the stabilizer states in Clifford circuit can be done efficiently with a logical operation on a N by $2N+1$ binary matrix M [90]. In this binary matrix, each row represents a Pauli string in a stabilizer. For each row, the l^{th} Pauli operator of the string is encoded by mapping the number of σ^0 to the l^{th} column and the number of σ^3 to the $N+l^{\text{th}}$ column. Consequently, having $\sigma^2 = i\sigma^1\sigma^3$ corresponds to $(1,1)$ on l^{th} and $N+l^{\text{th}}$ columns. The last column is reserved for tracking the overall phase ω of the string, where 0 corresponds to -1, and 1 corresponds to $+1$. As Clifford gates transform one Pauli string to another, evolution of a stabilizer state $|\Sigma\rangle$ can be kept track by altering the strings of initial P_Σ^N accordingly to the transformation rules [90].

It is proven that any N-qubit Clifford group can be generated from combinations of Hadamard (H), Phase (P) and Controlled-NOT (C-NOT) gates [66, 90, 118, 310] acting on different sets of qubits in a system. A Hadamard gate acting on a site maps operators σ^3 to σ^1 and σ^0 to σ^3 in a Pauli string. A Phase gate acting on a site, on the other hand, maps σ^1 to σ^2 and σ^2 to σ^1. A C-NOT gate, acting on two qubits, control qubit l and target qubit m, flips the target basis whenever the state of the l is $|1\rangle$, i.e.

$$\text{C-NOT}_{l,m} = \frac{1}{2}\left((I_l - Z_l) + (I_l + Z_l)X_m\right). \tag{4.63}$$

By computing the unitary transformation on all elements in the 2-qubit Pauli group, one finds that there are only 4 non-trivial transformation rules:

$$X_l I_m \text{ to } X_l X_m,\ \ I_l X_m \text{ to } I_l X_m,\ \ Z_l I_m \text{ to } Z_l I_m,\ \ I_l Z_m \text{ to } Z_l Z_m. \tag{4.64}$$

In this way, the transformation rules of the binary matrix are given as, for all rows i:

Hadamard gate on qubit l: $\omega_i = \omega_i \oplus x_{il} z_{il}$, exchange x_{il} and z_{ij} for all rows

Phase gate on qubit l: $\omega_i = \omega_i \oplus x_{il} z_{il}$, $z_{il} = z_{il} \oplus x_{il}$ for all rows

C-NOT gate on qubit m with qubit l as a control: $\omega_i = \omega_i \oplus x_{il} z_{im}(x_{im} \oplus z_{il} \oplus 1)$, $x_{im} = x_{il} \oplus x_{im}$, $z_{il} = z_{il} \oplus z_{im}$

Here $\oplus$ is an *exclusive or* operator and ω_i is the phase of i^{th} Pauli string. Thus, unitary evolution of stabilizer states under Clifford gates can be efficiently simulated with $N \times (2N+1)$ binary matrix with $\mathcal{O}(N)$ binary operations.

4.4.4 Projective Measurement on Stabilizer States

Now we consider performing a local projective measurement, which projects a local state to $|0\rangle$ or $|1\rangle$, on a stabilizer state. This measurement process only transforms a state when there exists a Pauli string with σ_l^1 at a measured site l in its stabilizer. In the case, the measurement outcome is discarded, which is the case for all simulations that are done in this thesis, the phase calculation can be completely omitted. Thus, the concern is only how a stabilizer O_Σ, and hence its Pauli strings transforms upon the measurement.

The measurement process proceeds as follows. Let p be the smallest row number where $x_{pl} = 1$, any non-zero x_{il} in other Pauli strings can be removed by multiplying p^{th} Pauli string to them, which is equivalent to a binary addition of p^{th} row. Now, set the p^{th} Pauli string $I_0 \otimes \cdots \otimes \sigma_l^3 \otimes \cdots I_{N-1}$. This is equivalent to nullifying the p^{th} row and set $z_{pl} = 1$. If there is no such p, then the local state of that qubit is, deterministically, $|0\rangle$ or $|1\rangle$. In this case the state, and hence the binary matrix remain the current state. Unlike the unitary operations, the projective measurements can, at worst, take $\mathcal{O}(N^2)$ operations [90]. However this is still manageable as it still only scales polynomially with the system size.

4.4.5 Entanglement Measure on Stabilizer States

The uniqueness of $|\Sigma\rangle$ given a stabilizer O_Σ tells us that O_Σ defined by Eq. (4.62) is a projector which projects a space onto a subspace $|\Sigma\rangle\langle\Sigma|$. This is nothing but the density matrix of the state $|\Sigma\rangle$. Therefore, the entanglement entropy of any subsystem A of $|\Sigma\rangle$ can be calculated readily by considering the partial trace over the Pauli strings [119, 123].

Expanding the products in Eq. (4.62) yields:

$$O_\Sigma = \frac{1}{2^N} \sum_{g \in \mathcal{G}} g, \tag{4.65}$$

where a set $\mathcal{G}$ is a set generated by all the possible products of $\{P_i\}$ and an identity $I^{\otimes N}$. The reduced density matrix on the subsystem X, ρ_X is obtained by tracing out the complement of X, $\overline{X}$. This is equivalent to removing the Pauli strings in which the parts corresponding to $\overline{X}$ is not an identity because Pauli matrices are traceless except for the identity $\sigma^0 = I$.

$$\rho_X = \mathrm{Tr}_{\overline{X}}\left[\rho\right] = \frac{2^{|\overline{X}|}}{2^N} \sum_{g_X \in \mathcal{G}_X} g_X = \frac{1}{2^{|X|}} \sum_{g_X \in \mathcal{G}_X} g_X, \tag{4.66}$$

where $\mathcal{G}_X \in \mathcal{G}$ is a set of all g with $\mathrm{Tr}_{\overline{X}}\{g\} \neq 0$ [119]. Let N_X be the number of linearly independent Pauli strings that generate g_X, then $\sum_{g_X \in \mathcal{G}_X} g_X$ is proportional to a projector of rank $2^{|X|-N_X}$ because this projector projects out the -1 eigenstates of its generators. Hence N_X is a binary rank of $M_{\overline{X}}$, where M is the binary matrix representing the state $|\Sigma\rangle$ and $M_{\overline{X}}$ is a matrix formed with columns from M which correspond to the Pauli operators in subsystem $\overline{X}$. This is evident from the row echelon form of the matrix.

With this representation, the von Neumann entropy $S(X)$ is given by

$$S(X) = (|X| - N_X) \ln 2. \tag{4.67}$$

From $2^{N_X + N_{\overline{X}}} = 2^N$,

$$S(X) = \left(\mathrm{rank}_{\mathrm{GF}(2)}(M_{\overline{X}}) - |\overline{X}|\right) \ln 2. \tag{4.68}$$

From $S(X) = S(\overline{X})$, we obtain

$$S(X) = \big(\mathrm{rank}_{\mathrm{GF}(2)}(M_X) - |X|\big)\ln 2. \tag{4.69}$$

Thus, the entanglement entropy of a stabilizer state can be computed from the rank of the binary matrix M that represents the state.

4.5 Conclusion

In attempt to simulate closed quantum systems with exponentially large Hilbert space dimension, in this section we introduced methods for reducing the size of the Hilbert space, such that a system can be solved analytically or numerically. The approaches that are taken in this chapter can be divided into two—reduction of effective Hilbert space based on its physical property and reduction of effective Hilbert space based on its algebraic properties.

For the approach based on the physical properties of a Hamiltonian, in §4.1, the reduction is made by focusing on a sector with a specified value of a conserved quantity. This method is useful for spectral analysis of non-interacting and systems with a small number of excitations, which connects to the spectral analysis of random matrices discussed in Ch. 3.2. Then in §4.2, we introduced Matrix Product State and Matrix Product Operator representations of quantum states and operators. Here we made reduction to the state space by considering a sector which is spanned by locally correlated states. This allows calculation of quantities such as OTOCs beyond the system sizes which can be reached by direct diagonalization. These methods are useful for simulating continuous time dynamics, which is discussed in Ch. 5. Finally in §4.3, the tensor network representation of MPS and MPO are introduced. Here we showed that for random quantum circuits, 0^{th} order computation of the entanglement entropy can be mapped to a classical minimal cut problem through the tensor network representation of a circuit. This method is used for 0^{th} order computation of entanglement entropy for large quantum circuits with measurements in Ch. 7.

For the approach based on the algebraic property of the Hamiltonian, in §4.4 we introduced Clifford circuits with stabilizer states. Here we showed that circuits can be constructed with three operations—Hadamard, Phase, and C-NOT gate—

and the dynamics can be simulated efficiently with an N by $2N$ binary matrix in polynomial time. This allows us to compute quantum circuits with thousands of qubits efficiently. This method is used in Ch. 6 and Ch. 7 to reach system sizes beyond which the former methods can reach.

Part III

Fast Scrambling Dynamics

Chapter 5

Time Independent Deterministic Hamiltonian Fast Scrambler

Black Holes are Fast Scramblers

Leonard Susskind [55]

Fast scramblers discussed in Ch. 1.1 are quantum systems which the scrambling (thermalization) time t_* only scales logarithmically with the system size N, $t_* \propto \log N$, Motivated by the experimental proposal of tunable long-range interactions with cold atoms in an optical cavity [166], and the physics of the fast scrambling conjecture discussed in Ch. 1.1 and in Ch. 2.4, in this chapter we study dynamical and spectral properties of quantum XY model on a sparsely coupled graph introduced in Ch. 1.2 and Ch. 2.6.3. The model has a parameter s, which tunes the geometry of the model between two incompatible notions of locality. For $s = -\infty$ the model has linear geometry where the locality is governed by the conventional Euclidean distance. For $s = \infty$ the model has treelike geometry where the locality is governed by the 2-adic metric discussed in §2.6. In this chapter, we investigate the level statistics and transport properties of the model to probe the scrambling property of the model, and transitions between linear and treelike geometries. We show that the model is fast scrambling, at the point of the transition.

Parts of this chapter are reproduced from sections that were written by the author of this thesis in the following publications: G. Bentsen, T. Hashizume, A. S. Buyskikh, E. J. Davis, A. J. Daley, S. S. Gubser, and M. Schleier-Smith, "Treelike interactions and fast scrambling with cold atoms," *Physical Review Letters,* **123**, 130601 (2019). [183]. and G. Bentsen, T. Hashizume, E. J. Davis, A. S. Buyskikh, M. H. Schleier-Smith, and A. J. Daley, "Tunable geometries from a sparse quantum spin network," in *Optical,Opto-Atomic, and Entanglement-Enhanced Precision Metrology II*, edited by S. M. Shahriar and J. Scheuer (SPIE, San Francisco, United States, 2020) p. 138. [184].

5.1 Introduction

As discussed in §2.4, fast scrambling conjecture defines the absolute speed limit on how fast information can spread across a quantum many-body system size N. The conjecture forbids the time t_*, for the information spread across the system from growing faster than logarithmically with N, $t_* \propto \log N$. A system which saturates this scaling bound is called a fast scrambler, and it is conjectured that black holes are fast scramblers [53, 70].

The conjecture also has practical importance because fast scramblers can encode quantum information across the system exponentially quickly. This begs the question on possibility of engineering the quantum systems that saturate the fast scrambling limit and observing the dynamics in the laboratory. The proposals

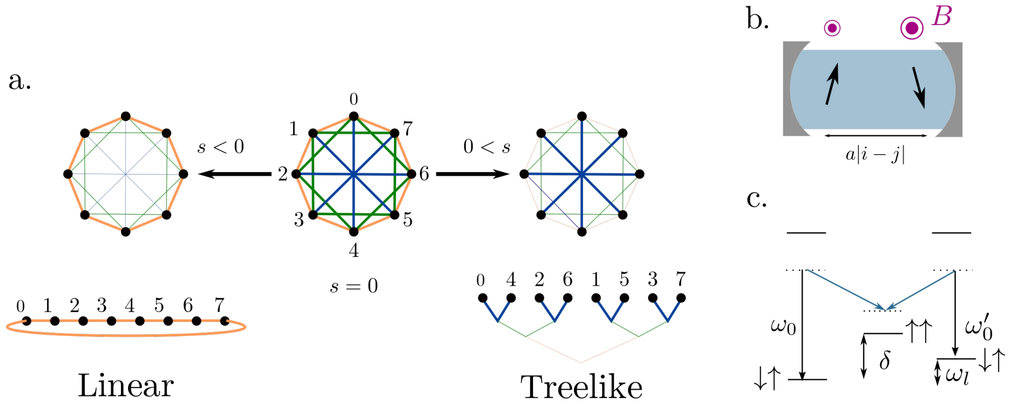

Figure 5.1: **Sparse coupling graph and an experimental scheme for implementing it.** a. A sparse coupling graph, in which the nodes are connected if and only if the distance (site numbers) between them are separated by integer powers of 2. A nearest neighbor in the familiar linear (Euclidean) geometry is recovered in the limit of $s = -\infty$ (left). In the limit of $s = \infty$, the interaction graph recovers a treelike structure (right). At $s = 0$, the graph is no longer local in either linear or treelike geometries. b. The spin system whose interactions are mediated by the photons in the cavity with a linear magnetic field gradient ΔB between two atoms at sites i and j that are separated by physical distance $d = a|i-j|$. c. Spin exchange interaction mediated by a cavity mode ω_c using a state split by δ which increases linearly with the distance between the two atoms $a\Delta B|i-j|$, due to the Zeeman effect, where a is the interatomic distance. The control field ω_0 drives the virtual Raman process. In this virtual process, a photon ω_0 is absorbed and emitted into the cavity with frequency ω_c only when it is rescattered by another atom by emission of ω_0'. In order for this emission to occur, the photon from laser with frequency ω_l must be tuned precisely $\omega_l = \omega_0 - \omega_0' = \omega a|i-j|$ to compensate the extra magnetic field applied on the second site due to the field gradient.

prior to this work are mainly based on randomly coupled models with nonlocal interactions [311, 312]. However, such a system is difficult to implement in near term experiments. The difficulty of creating arbitrary long-range couplings comes from the locality constraint that is imposed by nature. The locality of spacetime makes it difficult to engineer arbitrary long-range couplings, and the Lieb-Robinson bound [81, 313] forbids scrambling time t_* of a model with finite short-range interactions to increase faster than polynomially in N [198, 314–316].

In order to circumvent this problem we propose a quantum model with a tunable parameter s on a sparsely coupled graph (Fig. 5.1 a.), where interaction is only allowed when the two spins are separated by integer powers of 2. Especially, in this chapter, we study XY model on the graph because of the experimental feasibility using atoms in optical cavity. The model is inspired by the experimental proposal [166], which allows us to tune the interaction strength of the spin exchange interaction via Raman scattering (Fig. 5.1 b.) individually as a function of interatomic distance. By adding a magnetic field gradient ΔB, one can choose the specific distance that atoms must have in between them in order for them to interact. This is because the linear magnetic field gradient induces a Zeeman shift $\omega_Z = \omega a j$ on an atom at site j, where a is an interatomic distance. In order for the spin exchange to occur between a pair of atoms, the laser must also be tuned to compensate the gap between the Zeeman shift states of the two atoms at sites i and j, which is $\omega_Z = \omega a|i-j|$. Due to the linear magnetic field gradient, this gap is proportional to the interatomic distance, hence the atoms must be separated by the correct distance (Fig. 5.1 c.). As a consequence, the interaction strength can be precisely controlled in a level of individual interatomic distances. This can be done by adjusting the intensity of the laser frequency $\omega_l = \omega a|i-j|$, which corresponds to the difference in a Zeeman shift between the atoms separated by the physical distance $d = a|i-j|$.

In the following sections, we investigate the transition in the geometry, that is present in the sparsely coupled XY model with a tunable parameter s. In the limiting values of s, the model reduces down to a local model in two different geometries, linear ($s = -\infty$) and treelike ($s = \infty$), with incompatible notions of localities. At the transition point, which occurs at $s = 0$, the spectral and transport properties of the fast scramblers emerge as a result of the lack of the notion of locality. At this point, we show that the level statistics of the model become chaotic by an underlying fractal-like dispersion relation, and the transport properties of the model possess the features that are consistent with the fast scrambling conjecture. In §5.2, we introduce the model. Then in §5.3 we investigate the sector of the Hamiltonian where only a single excitation (single magnon) is present in the system. We show that in this regime, near the transition point at $s = 0$, the fractal like dispersion relation emerges, with a collapse of the polynomial lightcone into the logarithmic lightcone. In §5.4, we probe the many-body sectors of the Hamiltonian and show that the transition persists in this regime. Furthermore, we show that at the point of transition in geometry at $s = 0$, the level statistics recover that of the random matrices; and the lightcone formed by a rapidly mixing operators that is quantified by the Out-of-Time-Order Correlator (OTOC), which becomes logarithmic in the fast scrambling limit. Finally, in §5.5 we provide a summary and outlook.

5.2 The Model

The model we consider in this chapter is a quantum version of a sparsely coupled model proposed by Gubser *et al.* [75]. The Hamiltonian of the model is given by

$$H = \sum_{i,j} J_{\text{sparse}}(i-j) S_i^+ S_i^-, \tag{5.1}$$

where $J_{\text{sparse}}(i-j)$ has non-zero value only when two sites are separated by powers of 2,

$$J_{\text{sparse}}(i-j) = \begin{cases} J_s 2^{ls} & \text{when } |i-j| = 2^l,\ l = 0, 1, 2, \cdots \\ 0 & \text{otherwise} \end{cases}. \tag{5.2}$$

Here i and j are site numbers given to the individual spins ($i = 0, 1, 2, \cdots N-1$) in the order that is consistent with the linear geometry, s is a parameter which controls the strength of the algebraic dependency, and $S_i^{\pm}$ are spin raising $(+)$ lowering $(-)$ operator with the spin magnitude S. In this chapter, we consider a spin-1/2 model with $S = 1/2$. The interaction function Eq. (5.1) is normalized with a constant J_s,

$$J_s = \begin{cases} 1 & s < 0 \\ \left(\frac{N}{2}\right)^{-s} & 0 < s \end{cases}. \tag{5.3}$$

This is chosen such that in the limit $s = -\infty$ and $s = \infty$, the strength of the nearest-neighbor interactions becomes 1 in the linear and treelike geometries respectively.

The limiting behaviors of this model at $s = \pm\infty$, fall into two different geometries with incompatible notions of localities:

$s = -\infty$ Local interaction in Euclidean space with linear geometry. This is a Nearest Neighbor XY-model that we are familiar with.

$s = +\infty$ Local interaction in 2-adic space with treelike geometry. This limit corresponds to the coupling that are closest in the treelike geometry

When $s = 0$, the model loses the notion of locality because all the non-zero couplings available in the system becomes equal. In this limit, the geometry of the coupling graph is no longer linear or tree like. The scrambling time t_*, in this limit, in 0^{th} order, is governed by the number of pairwise interactions which is required for reaching the destination. The maximum length of the path required is given by the minimum number of additions/subtractions of powers of 2 required to hop from one site to the other. This is bounded by the minimum number of digits required to represent the largest site number available in the chain; and this scales like $\log_2 N$. From this 0^{th} order argument, it is already convincing that fast scrambling dynamics can appear near $s = 0$, if not exactly at $s = 0$.

The Hamiltonian has $U(1)$ symmetry that conserves the total number of spin-ups, in the axial direction of the z-axis. As discussed in Ch. 4.1, the number of spin-up excitation in z-direction, m, is also known as the number of magnons in the system. The Hamiltonian can be divided into the N non-interacting sectors classified by the number of magnons. The dimension of Hilbert space, $\binom{N}{m} = N!/(m!(N-m)!)$ is the number of ways to distribute m magnons to the N available sites in the system. Therefore, for small values of m, performing the numerical simulations is possible for large system size.

5.3 Single Magnon Sector

In this section, we consider the sector of the Hilbert space that only has one magnon excitation, $m = 1$. As discussed in Ch. 4.1, the dynamics in this regime can be solved analytically.

5.3.1 Spectral Properties and Dispersion Relation

First we study the spectrum at $s = 0$. Since the Hamiltonian is mapped to the model of non-interacting fermions, performing the Fourier transformation reveals the single magnon dispersion relation

$$E(k) = 2J_s \sum_{l=0}^{\log_2 N/2} 2^{ls} \cos\left(2^l k\right), \tag{5.4}$$

where $k = [0, 2\pi]$ is the wavenumber.

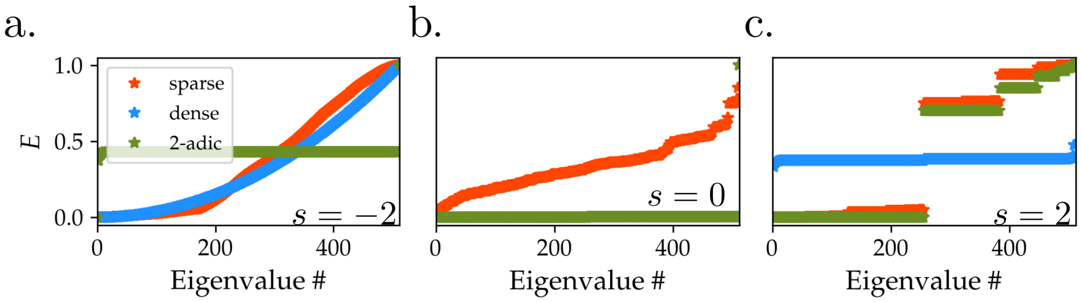

Figure 5.2: **Comparisons of the energy spectrum between the sparse (red), dense (blue), and 2-adic (green) coupling at $s = -2$, 0, and 2.** a. The single magnon energy spectrum of the models at $s = -2$. In this regime, the underlying geometry is linear, and hence the spectrum of the dense and sparse models agrees well. b. The single magnon energy spectrum of the models at $s = 2$. In this regime, the underlying geometry is treelike, and hence the spectrum of the 2-adic and sparse models agrees well. c. the single magnon energy spectrum of the models at $s = 0$. At this point, the interaction functions of the dense and 2-adic models become equivalent, and hence they overlap each other. At this point, the spectrum of the sparsely coupled model becomes completely different from the other two models due to the lack of the permutation symmetry. The dispersion relations are calculated for $N = 2^{10}$, and they are normalized such that the minimum value(s) are 0 and the maximum value(s) are 1. Eigenvalues are ordered in the ascending order.

Here, the inverse of a wavenumber is related to the periodicity in space. The continuity of the dispersion relation $E(k)$ in terms of k, therefore, is related to the spacial continuity; the analyticity of it is related to the well-defined group velocity of the quasiparticles, which also gives rise to the notion of locality in the system [317–319]. Therefore, in this subsection we study the smoothness and continuity of the dispersion relation in different values of s in order to grasp the change in geometric property, and hence the scrambling property of the model can be seen from the change in analyticity of the dispersion relation.

First we show that in the limits of $s = \pm\infty$, the model recovers the locality of the linear and treelike geometries by comparing the energy spectrum of the sparsely coupled model to dense and 2-adic coupling model with the same tunable parameter s. The dense and 2-adic coupling models are exactly same models as the Hamiltonian given by Eq. (5.1) except that the interaction functions are replaced with $J_{\mathrm{dense}}(i-j)$ and $J_{2-\mathrm{adic}}(i-j)$ respectively. The interaction functions of the dense and 2-adic model are defined as

$$J_{\text{dense}}(i-j) = J_s|i-j|^s \tag{5.5}$$
$$J_{2-\text{adic}}(i-j) = J_s|i-j|_2^{-s}, \tag{5.6}$$

where $|i-j|_2$ is the 2-adic norm of $i-j$ defined in Eq. (2.30). The two interaction functions—dense and 2-adic—unlike the sparse model, obey $J_{\text{dense}}(d_1) < J_{\text{dense}}(d_2)$ for $|d_1| < |d_2|$ and $J_{2-\text{adic}}(d_1) < J_{2-\text{adic}}(d_2)$ for $|d_1|_2 < |d_2|_2$, for $s < 0$ and $s > 0$ respectively. These conditions impose locality of linear geometry for dense interactions and treelike geometry for 2-adic interactions for $s < 0$ and $s > 0$ respectively. In Fig. 5.2, we compare the three dispersion relations for $s = -2$ and $s = 2$. The figure clearly shows that the behavior of the spectrum of the sparse model becomes closer to the dense model in the limit when the s is sufficiently negative. When s is sufficiently positive, on the other hand, the sparse model becomes closer to the 2-adic model. Near $s = 0$, the spectrum of both dense and 2-adic models become degenerate due to the emerging permutation symmetry on exchange of any pairs of spins within the system. However, such a strong symmetry is suppressed in the sparse model, resulting in the sparsely coupled model to have a very different spectrum to the other models.

Furthermore, near $s = 0$, in the thermodynamic limit ($\lim N \to \infty$), the dispersion relation has an interesting property. For $-1 < s < 0$, the infinite sum converges to a function known as a Weierstrass function [320]. It is a textbook example of a continuous but not smooth function, i.e. it is continuous but not differentiable everywhere [321, 322]. This can be clearly seen in the Fig. 5.3 (left). Despite the dispersion relation of the model in the regime of the linear geometry ($s < -1$) is smooth, This smoothness deforms to have fractal-like structure at $s = 0$. The rapid oscillation continues in the $s > 0$ regime, indicating that the group velocity picture is not applicable in the linear geometry for $-1 < s$.

Although the group velocity is not defined in the linear geometry, the smoothness can be recovered for large enough $0 < s$. This can be done by reordering the domain of $E(k)$ according to the 2-adic norm. For finite values of N, the wavenumbers k, are integer multiples of $2\pi/N$, $k = 2\pi k_n/N$ with an integer $k_n \in [0, N]$. On k_n, we perform the Monna map [75, 183, 248] introduced in Ch. 2.6.1. It reorders a set of integers $\{0, 1, \cdots 2^n - 1\}$ in a linear geometry to the treelike geometry, such that the 2-adic distance of the neighboring two are always minimal.

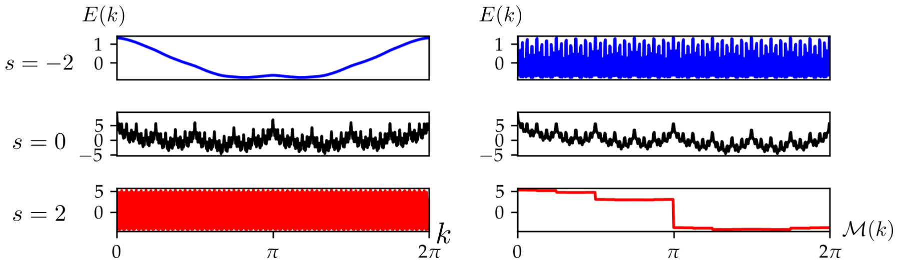

Figure 5.3: **The single magnon dispersion relation of the sparse model in linear and treelike geometry.** Left plots show the dispersion relation in the wavenumber ordered with the conventional metric of the linear geometry, where the closeness of two wavenumbers k_n and k'_n are defined by the Euclidean metric $d_\infty(k_n, k'_n) = |k_n - k'_n|$. Right plots show the dispersion relation in the wavenumber ordered with the metric of the treelike geometry. Here the closeness of the wavenumbers are defined with a small value in 2-adic metric $d_2(k_n, k'_n) = |k_n - k'_n|_2$. When the ordering is consistent with the geometry of the model, the dispersion relation of the model is almost everywhere continuous and differentiable (smooth). This can be seen, when the model is local in the linear geometry with $s = -2$ (top panels), the function is smooth in the wavenumbers of the linear geometry, yet the smoothness is not present in the wavenumber of the treelike geometry; and for $s = -2$ the relation is the opposite. Near $s = 0$ (middle panels), the dispersion relation is no longer smooth in either of the geometries, implying that the group velocity is no longer defined in either of the geometries.

The reordered spectrum is shown in Fig. 5.3 (right). After the reordering, the behavior of the function becomes smooth for sufficiently large $0 < s$, while the function loses smoothness in the treelike Fourier space for $0 < s < 1$, similarly to the loss of smoothness observed in the linear Fourier space for $-1 < s < 0$. We interpret the smoothness—continuity and differentiability—of $E(k)$ as a signature of the emergence of smooth geometry; while when the differentiability is lost, the dispersion relation is no longer smooth, and hence it indicates the lack of locality in the regime $|s| < 1$.

5.3.2 Single Magnon Transport

The effect of the loss of smoothness in the dispersion relation appears clearly in the single magnon dynamics of the model. We first look at how a localized spin-up state at site $N/2$ spreads across the system. For $m = 1$, the dynamics can be

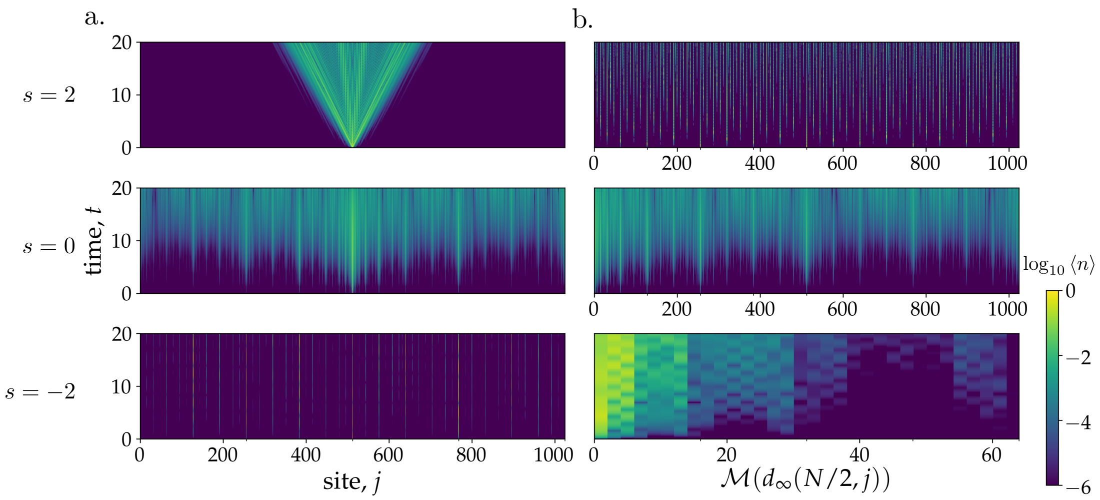

FIGURE 5.4: **Single particle dynamics of the sparse model.** a. Occupation of the magnon, $\langle n_j\rangle = S^z_j + 1/2$, for $N = 1024$ sites, evolved with a particle localized at a site $N/2$ plotted in Euclidean space for $s = -2$ (top), $s = 0$ (middle), and $s = 2$ (bottom), where d is a Euclidean distance from the site where initial excitation is placed. b. Occupation of the magnon, but the sites are rearranged by the Monna mapped distance from the site where initial excitation is placed, $\mathcal{M}(d)$. In the Euclidean space, for $s = -2$, a linear lightcone in the real space can be clearly observed (a. top). However for $0 \leq s$, the lightcone in the linear geometry deforms and no longer become properly defined (a. middle and bottom). On contrary, a polynomial lightcone is recovered in 2-adic space for $s = -2$ (b. bottom). At $s = 0$, the lightcone is not present in either of the geometries (middle panels).

analytically tractable as provided in §5.3. The occupation at time t is given by

$$\begin{aligned}\langle S^z_i(t)\rangle &= \langle n_i(t)\rangle - \frac{1}{2} = \langle S^+_i(t)S^-_i(t)\rangle - \frac{1}{2}\\ &= -\frac{1}{2} + \frac{1}{N^2}\sum_{k,k'}\sum_{r,s} e^{\mathrm{i}(k-k')i}e^{\mathrm{i}(E(k)-E(k'))t}e^{-i(kr+k's)t}\langle S^+_r S^-_s\rangle,\end{aligned} \tag{5.7}$$

where $\langle S^+_r S^-_s\rangle$ is the real space correlation at time $t = 0$.

Shown in the panels in Fig. 5.4 are the evolution of the particle occupation $\langle n_j(t)\rangle$ of the sparse model with a single particle placed at site $i = N/2$ at $t = 0$. The time evolution of the single magnon occupation number operator $\langle n_j(t)\rangle = \langle 0|\, S^-_i S^+_j(t)S^-_j(t)S^+_i\,|0\rangle$ in this sector of the Hamiltonian, also captures the Out-of-Time-Order Correlator (OTOC)

$$\begin{aligned}\mathcal{O}_{i,j}(t) &= \langle 0|\,[S^-_i, S^+_j(t)][S^-_i, S^+_j(t)]^\dagger\,|0\rangle = \langle 0|\, S^-_i S^+_j(t)S^-_j(t)S^+_i\,|0\rangle\\ &= \langle n_j(t)\rangle\,,\end{aligned} \tag{5.8}$$

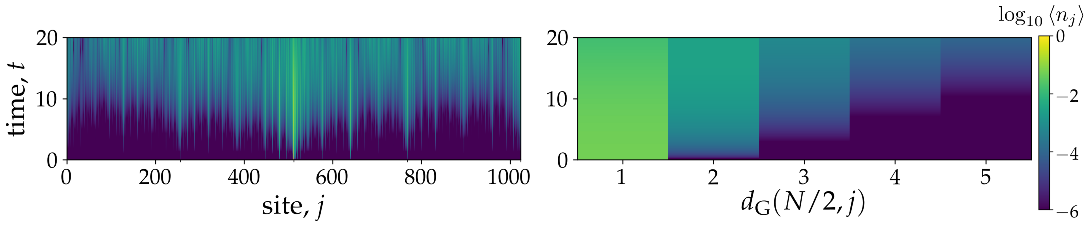

FIGURE 5.5: **Emergence of the lightcone at $s = 0$ in the graph geometry.** Occupation of the fermionic excitation, $\langle n_j\rangle = S^z_j + 1/2$, for $N = 1024$ sites, evolved with a particle localized at a site $N/2$ plotted in a real space for $s = 0$. Left is the dynamics with the sites rearranged in the real space and right is the sites rearranged by the graph distance from $N/2$. The emerging roughly linear lightcone in the right panel shows that the single excitation spreads locally in the graph geometry.

which quantifies the chaotic dynamics and the operator spreading in the system [25, 151, 206, 273, 277]. The transport of a single magnon reveals the geometry of the model with respect to the spectral parameter s. When s is sufficiently towards $-\infty$, the excitation spreads ballistically, forming a linear lightcone as expected from the nearest-neighbor models (Fig. 5.4 a. top).

On the contrary, when s is sufficiently large towards $+\infty$, the lightcone disappears, and we observe the excitation hopping discontinuously over the sites. This does not mean that the locality is lost completely; rather, the model becomes local in the treelike geometry, where the closeness between two sites is defined by the 2-adic norm $d_{p=2}(x, y)$. Following how the momentum is rearranged to recover the smoothness in the treelike geometry, shown in Fig. 5.4 b. is the same observable, but sites are arranged by the Monna mapped integer Euclidean distance from the initial excitation. The polynomial lightcone can be observed in this treelike geometry, recovering the locality, where the excitation hops sequentially in the treelike geometry.

At $s = 0$, however the dynamics is not local in either of the geometries as it is clearly shown in the middle panels of Fig. 5.4 a. and b. To understand the origin of this emerging nonlocality, we rearrange the sites according to the graph distance $d_G(x, y)$, which is the minimum number of hops required to move from site i to site j in the sparsely coupled graph. (for the precise definition c.f. Ch. 2.6). Shown in Fig. 5.5 are the same dynamics with the sites rearranged based on the graph distance from the site of the initial excitation. In the sparsely coupled graph, the graph distance of the graph is bounded above by the $\log_2(N/2)$. This is because the hopping on sparsely coupled graph can be mapped to a minimum number of addition/subtraction of integer powers of 2 required on the site number i to get site number j. The binary representation of $d_\infty(i,j) = |i-j| < N/2$ (periodic boundary condition) immediately tells us that the maximum number of hopping required is $\log_2(N/2)$ hops≡digits. The emergence of the roughly linear lightcone implies that like the graph distance, the time for the localized perturbation to spread across the system to grow similarly to the largest graph distance, $t_* \propto \log N$.

To quantify the emergence of the logarithmic lightcone, in Fig. 5.6, we plot the saturation time $\tilde{t}_\epsilon = t_\epsilon / \max\{t_\epsilon\}$, where t_ϵ is the time it takes for the occupation at a site to reach $1/N^{\text{th}}$ of the thermal value, $\epsilon = 1/N^2$. As shown in Fig. 5.6 a. i-ii., in the regimes where the interaction is local the signature of the lightcone appears as the polynomial dependence of the $\tilde{t}_\epsilon$ with respect to the distance function of the correct geometry. For $s=-3$, $\tilde{t}_\epsilon$ increases linearly with respect to the Euclidean distance, $d_\infty(N/2,j)$, as it is in the regime where interaction is short-ranged based on this definition of the distance. For $s=3$, on the other hand, the linear lightcone is not present in the linear geometry. However, the polynomial lightcone is present in the treelike geometry defined by the Monna mapped Euclidean distance $\tilde{t}_\epsilon \propto \mathcal{M}(d_\infty(N/2,i))^{3.33}$. The difference in the polynomial dependency indicates that the $s<0$ in linear and $0<s$ in treelike geometry are not exact dual.

In the regime where the dispersion relation becomes fractal, $-1 < s < 1$, the polynomial dependence of $\tilde{t}_\epsilon$ diminishes. As argued in §5.3.1 this is caused by the undefined group velocity due to the loss in the smoothness of the dispersion relation. In this regime, the saturation time is governed by the available paths in the coupling graph, instead of them being governed by the metric of the geometry. This is more apparent in the duality between the behavior of the saturation time in linear regime for $s<0$ and treelike regime for $0<s$ as shown in Fig. 5.6 b. (i-ii).

Finally, at $s=0$ we found that the distance dependence of the saturation time in the linear and treelike geometry becomes indistinguishable (Fig. 5.6 c. i and ii). At this point, the saturation time is bounded logarithmically with respect to the distance in both geometries. This logarithmic dependence can be explained as a result of the ballistic transport across the sparsely coupled graph. In this case, the t_ϵ at a site directly depends on the graph distance from the origin of the perturbation, which is bounded by the $\log_2 N/2$. The emergence of the linear lightcone with respect to the graph distance, d_G, is shown in Fig. 5.6 c. iii.

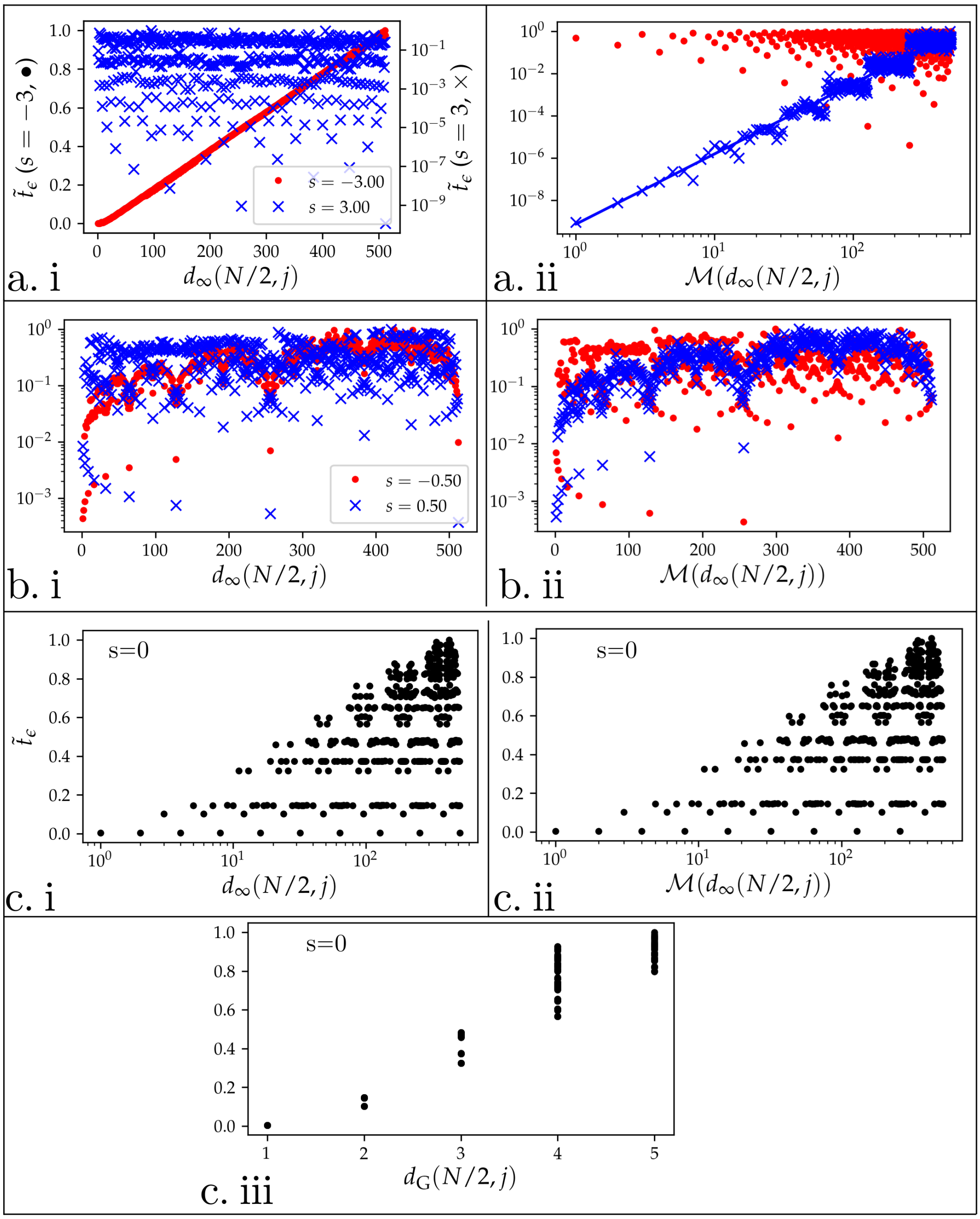

Figure 5.6: **Single particle saturation time on the sparsely coupled model.** The normalized saturation time, $\tilde{t}_\epsilon = t_\epsilon / \max\{t_\epsilon\}$ is plotted for the different values of s in different geometries, where t_ϵ is the time it takes for a single site occupation $\langle n_j \rangle$ to reach $\epsilon = 1/N^2$ for the single particle sector, where initial excitation is placed at $i = N/2$. a. i-ii. t_ϵ of the sites arranged by the Euclidean distance from the perturbation (i) and the Monna mapped distance from the perturbation (ii) for $s = -3$ (red circle) $s = +3$ (blue cross). The linear ($s = 3$) and polynomial ($s = -3$) lightcones emerges when the sites are arranged in the correct geometry (red and blue lines respectively). b. i-ii. The same plot for $s = -0.5$ (red circle) and $s = 0.5$ (blue cross). In these regimes, however, due to the loss of the smoothness in the dispersion relation, the lightcones eno longer exist in either of the geometries. c. i-iii. The saturation time at $s = 0$ plotted as a function of Euclidean (i), Monna mapped (ii), and the graph distance (iii). This figure was reproduced from [184].

To conclude, there are three distinct regimes in the single magnon sector ($m = 1$) of the sparse model as expected from its spectral property (Eq. (5.4)). Two regimes are the extreme limits near $s = \pm\infty$, where the localities in the linear ($s = -\infty$) and treelike geometry ($s = +\infty$) are recovered. The third regime $|s| < 1$, occurs when the smoothness of the dispersion relation is lost in the thermodynamic limit. Furthermore, we show that at $s = 0$, the exponentially fast spreading of the perturbation occurs and simultaneously, the linear and treelike geometries become indistinguishable. At this point, the timescale of the information spreading in the system increases linearly with the graph distance between the sites. The logarithmically scaling saturation time with respect to the system size $\sim \log N$, is an evidence for an emergence of the fast scrambling dynamics at $s = 0$.

5.4 Beyond Single Particle Physics

To show that the fully quantum regime is fast scrambling, we now move to the regime with multiple magnon excitations ($1 < m$). The previous section shows that at the single magnon $m = 1$ level, dynamics is fast scrambling dynamics at $s = 0$. In this section, we show that this feature persists in the many-body regime for $1 < m$.

5.4.1 Two Magnons Sector

In order to confirm the persistence of the logarithmic lightcone in the many-body regime, we first analyze the spectral and transport properties of the model with two magnon excitations $m = 2$. In this regime, as discussed in Ch. 4.1.2, the dimension of the Hilbert space only increases quadratically with the system size; and hence the exact calculation of the dynamical variables are still manageable for a large number of sites. The translation symmetry of the Hamiltonian makes the momentum a good quantum number. Hence, the Hamiltonian can be block-diagonalized into N hermitian matrices with a dimension which increase only linearly with N. This allows the numerical analysis of large system size.

Utilizing translation symmetry, the elements of block-diagonal Hamiltonian H_{μ_1,μ_2}, parameterized by a momentum k and the corresponding basis states ψ_{k,μ_j} is given

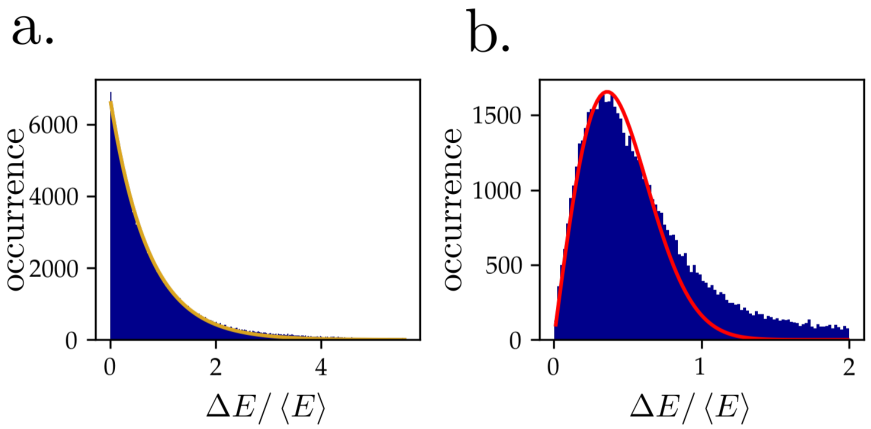

FIGURE 5.7: **Level statistics of the two magnon sector of the sparsely coupled model at $s = 0$.** a. The distribution of the level spacing $\Delta E/\langle \Delta E\rangle$ calculated after sorting the eigenenergies across all the momentum sectors. The yellow line is a fit to the distribution: occurrence $\approx 1.8 \times 10^4 e^{-1.3\Delta E}$. The agreement implies that the system is integrable. b. The distribution of the level spacing $\Delta E/\langle \Delta E\rangle$ calculated for each momentum, then combined across all the momenta. The red line is a fit to the distribution for $\Delta E/\langle \Delta E\rangle < 0.8$: occurrence $\approx 7.6(\Delta E/\langle \Delta E\rangle)e^{-3.8(\Delta E/\langle \Delta E\rangle)^2}$. When the level statistics are resolved by the momentum sectors, the level statistics recover that of the GOE.

by

$$\begin{aligned} H_{k,\mu_i,\mu_j} &= J_{\text{sparse}}(\mu_i - \mu_j) + J^*_{\text{sparse}}(\mu_i - \mu_j) e^{2\mathrm{i}\pi k(\mu_i - \mu_j)/N} \\ &+ J_{\text{sparse}}(\mu_i + \mu_j) e^{-2\mathrm{i}\pi k \mu_f/N} + J_{\text{sparse}}(\mu_i - \mu_j) e^{2\pi \mathrm{i} k \mu_i/N}, \end{aligned} \tag{5.9}$$

where μ_i and μ_j are the index given to the set of momentum eigenstates ψ_k. The physical state with a localized excitation at sites m_1, m_2 is given by

$$|m_1, m_2\rangle = S^+_{m_1} S^+_{m_2} |\downarrow\rangle = \sum_k \sqrt{\frac{1}{N}} \exp(\pi \mathrm{i} k(m_1 + m_2 - d_\infty(m_1, m_2))/L) \psi_{k,d_\infty(m_1,m_2)}. \tag{5.10}$$

We first, investigate the spectrum of the model at $s = 0$ by computing the level statistics of the eigenenergies of the two-magnon sector. Level statistics [269, 323], introduced in Ch. 3.2, is a study of the distribution of the level spacing, which is the gap between neighboring eigenenergies of the model. Immediately, we see that, like the single magnon sector, because the full two-magnon sector of the Hamiltonian is real symmetric and has translation symmetry, the sector is equivalent to a one magnon sector of the Hamiltonian of a complex network with the same symmetry of the sparsely coupled graph. Therefore, the full two-magnon sector is integrable. This implies that the level statistics of the two-magnon follow the integrable Poisson level statistics at $s = 0$:

$$P_{\text{Poisson}}(\Delta E) \propto e^{-c\Delta E}, \tag{5.11}$$

where c is a real constant, as shown in Fig. 5.7 a. However, when the level statistics are computed by the momentum sectors, it possesses a Gaussian Orthogonal Ensemble (GOE) [26]. The ensemble of symmetric matrices where elements are drawn from a Gaussian distribution:

$$P_{\text{GOE}}(\Delta E) \propto \Delta E e^{-c(\Delta E)^2}, \tag{5.12}$$

where c is a real constant. As shown in Fig. 5.7 b., the model follows GOE level statistics with a thickened tail. This further indicates that the model at $s = 0$ is chaotic.

In order to further confirm the emerging chaotic properties of the model at $s = 0$, we look at the OTOC of the form

$$\mathcal{O}_{i,j}(t) = \frac{1}{\mathcal{N}^2}\left(\sum_{l\neq i} \langle 0| S_i^- S_l^-\right)\left[S_j^z, S_i^z(t)\right]\left(\sum_{l\neq i} S_i^+ S_l^+ |0\rangle\right), \tag{5.13}$$

for $i = 0$ and for various values of j. Here, $\mathcal{N}$ is a normalization factor of the state $\sum_{l\neq i} S_i^+ S_l^+ |0\rangle$, $\mathcal{N} = \frac{1}{\sqrt{N-1}}$. The state $\sum_{l\neq i} S_i^+ S_k^+ |0\rangle$ is a superposition of a single magnon localized at site $i = 0$ and another particle completely delocalized in the real space. Although this is not equivalent to the OTOC of the finite temperature state, unlike the single-particle OTOC discussed in the previous section, it captures the spread of OTOC in a locally thermal bath with a finite particle occupation.

Shown in Fig. 5.8 a. is the saturation time of OTOC t_* at $s = 0$. It is the minimum time that takes for the OTOC $\mathcal{O}_{0,d}$ to reach $\epsilon = 1/N^2$. At $s = 0$, the sites with the fastest growth of OTOC are the ones that are connected to the site 0. For the general values of s near $s = 0$, to bound the lightcone from the above and below, we look at the slowest and the fastest growing sites within the intervals $2^m < d < 2^{m+1}$ for $m = 0, \ldots, N-2$. In the regime, where the linear lightcone vanishes ($|s| < 0$), the lightcone opens up, forming a gap between the upper and the lower bounds of the lightcone as observed in the dynamics of the single magnon sector. In this regime the lightcone cannot be defined uniformly. To analyze this

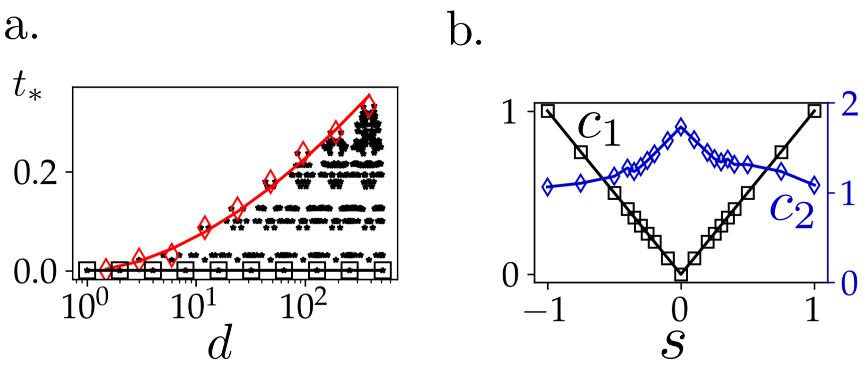

FIGURE 5.8: **Saturation time of OTOC of the two-magnons sector of the sparsely coupled model and the change in the dependency of the lightcone.** a. The saturation time t_* of OTOC $\mathcal{O}_{i,i+d}$, where t_* the minimal time for OTOC to grow to the value of $1/N^2$. Red diamonds are the slowest time of the sites between the intervals $2^m < d < 2^{m+1}$ and black squares are the sites which OTOCs grows fastest within the interval. The red and black lines of the best fit, $t_* = c_0 d^{c_1} (\ln d)^{c_2}$ and $t_* = c_0' d^{c_1}$ respectively (d is replaced with $\mathcal{M}(d)$ for $0 < s$). They bound the t_* from above and below; hence provides the upper and lower bounds of the lightcone. b. The parameters c_1 (black), and c_2 (red) that are used to fit the functional dependence of the red diamonds and black squares from Fig. a. As the polynomial dependence vanishes towards $s = 0$ accompanied by the logarithmic dependence emerging near $s = 0$.

regime instead, we can define the lower and the upper bound of the lightcone by considering the slowest and the fastest growing sites within the previously defined interval (red and black lines in Fig. 5.8 a.).

From the saturation times t_*, the bounds on the lightcone is computed by fitting a polynomial and logarithmic function of the form:

$$t_* = \begin{cases} c_0 d^{c_1} (\ln d)^{c_2} & \text{(Slowest)} \\ c_0' d^{c_1} & \text{(Fastest)} \end{cases} \tag{5.14}$$

to the fastest and the slowest growing sites, with free parameters c_0, c_0', c_1, c_2. As shown in Fig. 5.8 b., the polynomial dependency on the lightcone vanishes as s approaches $s = 0$ (c_1, black line). On the other hand, the logarithmic dependency parameterized with the exponent c_1 emerges as s approaches $s = 0$, and peaks at $s = 0$. This clearly shows that at $s = 0$, the nature of the lightcone is dominated by the logarithmic dependence with respect to the distance. Furthermore the behavior of the parameters c_1 and c_2 are symmetric about $s = 0$ for linear $s < 0$ and treelike $s > 0$.

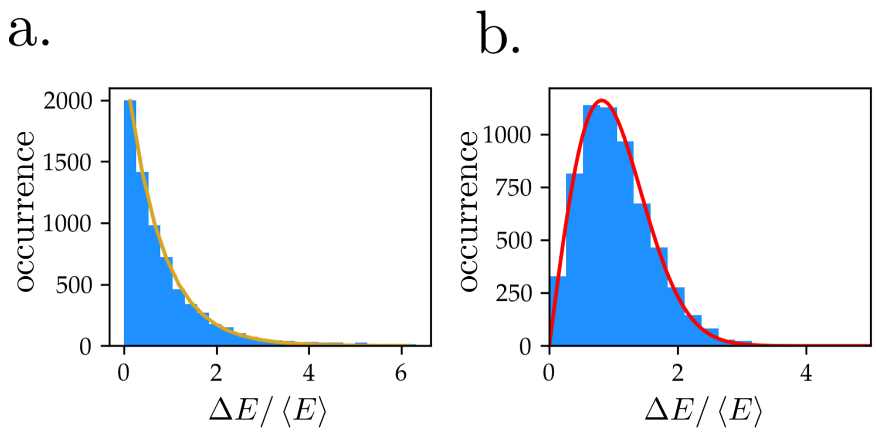

FIGURE 5.9: **The level statistics of the half-filling sector of the sparsely coupled model at $s = 0$.** a. The distribution of the level spacing $\Delta E/\langle\Delta E\rangle$ calculated after sorting the eigenenergies across all the momentum sectors. The yellow line is a fit to the distribution: occurence $\approx 5.4 \times 10^2 e^{-1.3\Delta E}$. The agreement implies that the system is integrable. b. The distribution of the level spacing $\Delta E/\langle\Delta E\rangle$ calculated for each momentum sector, then combined across them. The red line is a fit to the distribution for $\Delta E/\langle\Delta E\rangle < 0.8$: occurence $\approx 2.3 \times 10^3(\Delta E/\langle\Delta E\rangle)e^{-0.7(\Delta E/\langle\Delta E\rangle)^2}$. When the level statistics are resolved by the momentum, parity, and spin inversion symmetry, the level statistics recover that of the GOE. This implies that the presence of level repulsion in the individual symmetry sector.

For fixed m, taking the lattice size N to infinity causes the probability of taking two-body and higher order interactions to be infinitesimally small. Thus the transport property of $m = 1$ and $m = 2$ represents the dynamics of the many-body systems with sufficiently small $m/N \ll 1$. As observed, in this regime, the Hamiltonian has a fractal first-order dispersion relation. As the model approaches to $s = 0$, the level statistics approach to that of the GOE statistics.

5.4.2 Half-Filling Sector

To go beyond the limit $m/N \ll 1$, we investigate the model at half-filling, $m/N = 2$. In this regime, the dimensions of the Hilbert space increases combinatorially as $\binom{N}{N/2}$. This makes the spectral and dynamical analysis of the model difficult. Therefore, in this section we rely on the analysis with the Matrix Product State (MPS) algorithm [91, 94, 113, 116, 300, 324] (c.f. Ch. 4.2) in addition to the exact diagonalization, to reach the larger system size.

We first look at the level statistics in this regime. Shown in Fig. 5.9 is the level statistics of the half filled sector of $N = 16$. Despite the small system size, the

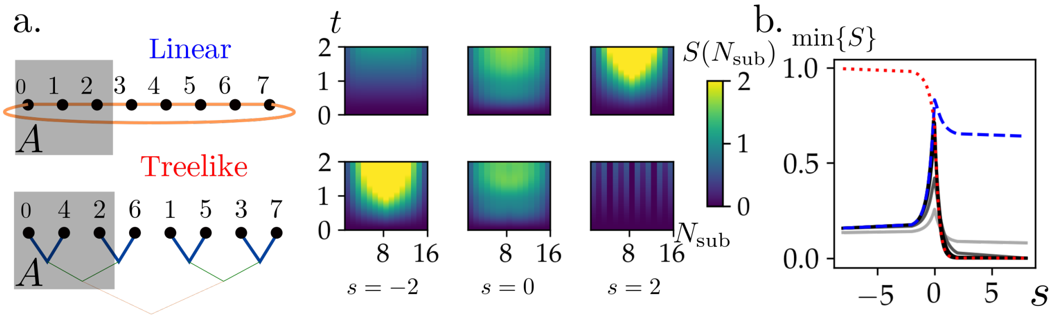

FIGURE 5.10: **Growth of entanglement entropy in the different geometries.** a. The entanglement entropy of the contiguous region of size N_{sub}. The initial state is an x-polarized state with the system size $N = 16$. The above panels show the subsystems of various size N_{sub} taken in the linear geometry, and panels below show the entropy of the subsystems taken from the treelike geometry for $s = -2$ (left), 0 (middle), and 2 (right). b. The minimum entanglement across all the possible partitions of size $N_{\text{sub}} = 1, 2, 4, 8$ (light to dark) at $t = 0.5$; and the minimum entanglement entropy of the contiguous region of size $N_{\text{sub}} = 8$ for the linear (blue dashed) and the treelike (red dotted) geometries.

size of the Hilbert space is in the order ten thousand, which is large enough for capturing the emerging non-trivial chaotic many-body phenomena [206]. When the level statistics are computed without resolving the eigenenergies by the symmetry sectors, the level statistics at $s = 0$ follows the Poisson distribution (Fig. 5.9 a.). This is expected because the matrix elements of the Hamiltonian can be given analytically as a sum of the elements of the single magnon dispersion relation with the phase which depends linearly on the distance from the center of masses, as expected from two magnons sector (Eq. (5.9)). When the level statistics are computed for individual symmetry sectors: namely the translation (momentum), parity, and spin inversion, they divert from the Poisson distribution as expected (Eq. (5.9) b.). Here the statistics approach to the GOE more closely compare to two magnons sector. This further indicates the emergence of chaotic behavior at $s = 0$ in the strongly interacting regime.

To analyze the transition between linear and treelike geometries at $s = 0$ and the emerging fast scrambling dynamics further, we now analyze how entanglement entropy evolves. The structure of the entanglement provides an even sharper signature of the locality. When the dynamics is local in the given geometry, the entanglement growth is suppressed to obey an area-law. Therefore, the deviations from the area-law growth of entanglement entropy can be used as a test for whether the interactions are local or not in the given geometry.

Here, we prepare a product state of each spin polarized in the x-direction as the initial state. Fig. 5.10 a. shows the von Neumann entropy of $S(A) = -\mathrm{Tr}\{\rho_A \ln \rho_A\}$ of a contiguous subsystem A of size $N_{\mathrm{sub}} = |A|$ in two geometries. Here ρ_A is a reduced density matrix in A, where $\rho_A = \mathrm{Tr}_{\bar{A}}\rho$, and $\mathrm{Tr}_{\bar{A}}$ denotes a partial trace over subsystem $\bar{A}$, which is the complementary region of A. A contiguous region is a region where every qubit in the region has at least one qubit that is adjacent to it in the same region. Here, we explicitly avoid the use of a phrase “continuous subsystem” and instead, we use “contiguous subsystem” because “continuous” serves as an antonym of a term “discrete”. Top panels show the entanglement entropy of the spins arranged in the linear geometry, and the bottom panels show the spins arranged in the treelike geometry via Monna map. As expected, when $|s|$ is sufficiently large, the locality, or equivalently the natural way to organize the spins, comes out in the suppressed growth across all the subsystem sizes. When the notion of the locality in the underlying dynamics is not compatible with the geometry, the entanglement grows quickly to the saturation. As shown in Fig. 5.10 b. partitioning the system with the contiguous regions in the linear geometry is always the optimal way to partition the system for $s < 0$ (blue dashed). On the other hand, partitioning the system in the treelike geometry is optimal for $s > 0$ (red dotted). These results are consistent with the lightcones and the notion of locality deduced from the dynamics of small magnon sectors.

When $s = 0$, however, the entanglement is always large for any partitioning with a fixed size, despite none of the partitions being fully saturated. Shown in Fig. 5.10 b. with the black lines are the minimal entanglement entropies from all the possible subsystems of sizes $N_{\mathrm{sub}} = 1$, 2, 4, and 8 (light to dark). For all the subsystem sizes, they show a peak at $s = 0$. This implies that all spins are coupled strongly to one another. Especially the contiguous cut in the two geometries and the minimal cut coincides at $s = 0$. This further confirms that at this point, the notion of locality is lost.

Finally, we end this chapter with the discussion of dynamical properties of the model beyond those which can be computed with the exact diagonalization. For this calculation, we use the MPS methods discussed in Ch. 4.2, to compute the Out-of-Time-Order Correlator (OTOC), $\mathcal{O}^{(\infty)}_{i,i+d}$, of the infinite temperature state. This takes the form:

$$\mathcal{O}^{(\infty)}_{i,i+d} = \frac{1}{\binom{N}{N/2}} \mathrm{Tr}\{\left[S^z_i, S^z_j(t)\right]^2\}, \tag{5.15}$$

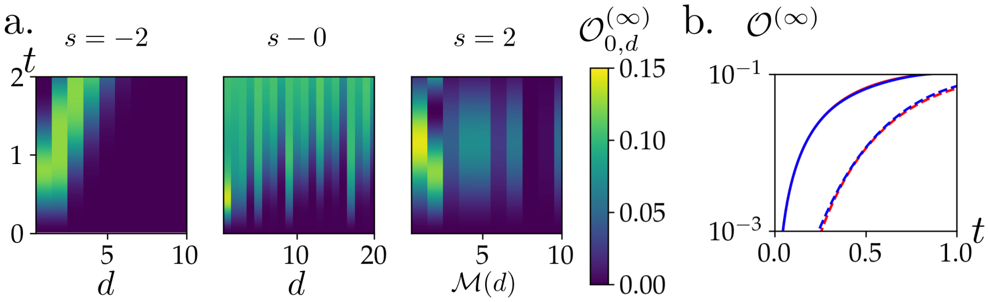

FIGURE 5.11: **Time evolution of OTOC computed using MPS.** a. OTOC $\mathcal{O}_{0,d}$ for $s = -2$ (left) $s = 0$ (middle), and $s = 2$ (right) plotted in the linear geometry (left and right) and the treelike geometry (right). For $s = \pm 2$, the lightcone is recovered in the geometry which the interactions are local. At $s = 0$, however, the polynomial lightcone deforms as it was observed in the fewer magnons sectors. b. The saturation of OTOC at sites that can be reached with one hop ($d = 2$ solid) and two hops ($d = 5$, dashed) in the interaction graph for the system sizes $N = 16$ (red) and $N = 32$ (blue). The quantities are simulated on a sparsely coupled model with open boundary condition with the maximum bond dimension of $\mathcal{D} = 100$.

where $\binom{n}{k}$ denotes a binomial coefficient $n!/k!(n-k)!$.

Shown in Fig. 5.11 a. are lightcones formed by the OTOC for the system size $N = 32$. These plots clearly show the three regimes—linear ($s = -2$), fast scrambling ($s = 0$), and treelike ($s = 2$)—as expected from the previous discussions on single magnon transport, OTOC in two magnons sector, and entanglement entropy in $m = N/2$ regime with $N = 16$. Furthermore, Fig. 5.11 b. (solid) shows the saturation of OTOC before it reaches the regime where it is expected to grow exponentially in the semi-classical limit. This is expected because of the discrete and finite local degrees of freedom which limits the maximum value of the OTOC at $\mathcal{O}(1)$. Nevertheless, the initial exponential suppression of the growth of the OTOC only depends on the graph distance. This further confirms that even in the strongly interacting regime, the model at $s = 0$ possesses a spectral and dynamical characteristics which are necessary for fast scrambler as a result of the crossover between the two incompatible geometries.

5.5 Conclusion and Outlook

In this chapter, we investigated an XY-model on a sparsely coupled graph with a coupling strength controlled by a tunable parameter s, which can be implemented in the experiment with cold atoms in an optical cavity. To show the model becomes fast scrambling at $s = 0$, we study the transition in the underlying geometry of the model as a function of s in the non-interacting, weakly interacting, and strongly interacting regime based on the number of magnon spin excitations $m = 1$, $m = 2$, and $m = N/2$. This was done by studying the spectral properties and transport properties of the model in the three regimes of s: $s < 0$, $s = 0$, and $0 < s$. In the non-interacting regime $m = 1$, We show that near $s = 0$, the transport property on the single magnon sector $m = 1$ is governed dominantly by the fractal-like dispersion relation. In the many-body regime $m > 1$, we show that the distribution of symmetry resolved spectral gaps recover the GOE level statistics at $s = 0$, which is a strong signature of the emergence of chaos at $s = 0$.

Furthermore, we have shown the transition in transport properties and locality of the model as the underlying geometry transitions from linear to treelike geometry as a function of s. We show that for large $|s|$, the lightcones are observed in the geometries that are consistent with the notion of locality that the model possesses. Namely, the lightcone appears in the linear geometry for s is negative, and it appears in the treelike geometry when s is positive. This is confirmed further by the emergence of logarithmic upper bound in the maximum saturation time of the OTOC at $s = 0$, accompanied by the rapid growth of correlations in the strongly interacting regime. the loss of geometry, and hence the notion of locality, at $s = 0$ is also confirmed in the structure of the entanglement entropy. At $s = 0$, the configuration which minimizes the entanglement entropy is no longer linear or treelike, indicating that any cut has maximal entropy despite the state have not reached the equilibrium. From the underlying chaotic spectrum and the logarithmic lightcones which emerge at $s = 0$, we provided numerical and analytical evidences that indicate the emergence of fast scrambling dynamics at $s = 0$.

The future prospects lie on implementing and probing the model in cavity-QED experiment, and confirming the emerging fast scrambling dynamics at $s = 0$. In recent years, there has been an active research on simulating high-temperature physics using cold atoms [325–327]. On the theoretical side, the connection of the sparsely coupled model to holographic theories [49, 51, 328] and underlying tensor network structures [294] may be studied. The nature of the transition from slow-scrambling to fast scrambling is also not well understood. It is hoped that further theoretical and experimental studies of the fast scramblers reveals more of their exotic natures.

Chapter 6

Floquet Fast Scrambler

> The mathematician's patterns, like the painter's or the poet's must be beautiful; the ideas like the colours or the words, must fit together in a harmonious way. Beauty is the first test: there is no permanent place in the world for ugly mathematics.
>
> ---
>
> Godfrey Harold Hardy [329]

In the previous chapter, we investigated a time independent Hamiltonian fast scrambler. In this chapter, we investigate a class of quantum circuits on a sparsely coupled graph. Similarly to the time independent model discussed in the previous chapter, the circuits have a tunable parameter s, which controls the probabilities of long-range two-qubit gates. We show that by tuning s, the underlying geometry of the model transitions from linear ($s < 0$) to treelike ($0 < s$) geometry. Near $s = 0$, we show that the locality of the circuit diminishes, and it becomes a fast scrambler with a system size invariant teleportation time t_c. Then we show that exactly at $s = 0$, the circuit remains to be a fast scrambler despite all the random gates being replaced with a set of deterministic gates. With this treatment, the circuit is equivalent to a spin model with a time-dependent periodic (Floquet) Hamiltonian, with a period $2 \log_2 N$. This deterministic fast scrambling circuit can provide highly entangled state in a timescale that only increases logarithmically with the system size, and access to the fast scrambling dynamics in a highly programmable manner.

Parts of this chapter are reproduced from sections that were written by the author of this thesis in the following publications: T. Hashizume, G. S. Bentsen, S. Weber, and A. J. Daley, "Deterministic Fast Scrambling with Neutral Atom Arrays," *Physical Review Letters*, **126**, 200603 (2021). [185]. and T. Hashizume, S. Kuriyattil, A. J. Daley, and G. Bentsen, "Tunable Geometries in Sparse Clifford Circuits," *Symmetry*, **14**, 666 (2022). [187].

6.1 Introduction

On the contrary to relying on imposing long-range interactions on a static array of atoms, the approach that we take in this chapter is a creation of effective long-range interactions through shuffling of the atoms, with the interaction of the neighboring atoms which follows. This shuffling-and-interacting scheme is motivated by the experiments on optically trapped cold neutral atoms [168, 169, 175, 176, 179, 180, 330–333] and manipulation of those with an array of optical tweezers [104, 174].

If the fast-scrambling can be achieved in the process of shuffling-and-interacting scheme, following the Susskind's random all-to-all model [53] (c.f. Ch. 1.1.2), the initial product state is expected to become a volume-law state after the $\mathcal{O}(\log N)$ shuffle-and-interaction steps. Here, we take the circuit interpretation, where one

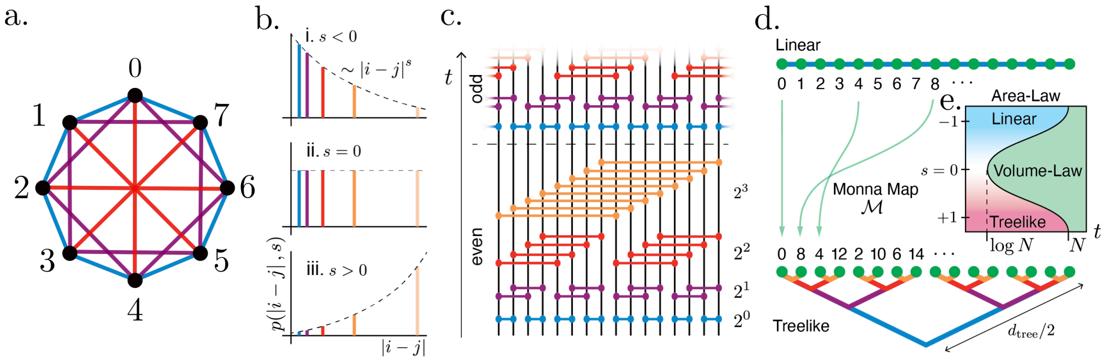

FIGURE 6.1: **Sparsely coupled graph, sparsely coupled circuit, its limiting geometries, and its dynamical phases.** a. A sparsely coupled graph. Two edges i and j are connected if and only if the distance $d_\infty(i,j) = |i-j|$ is integer powers of 2. Here, the periodic boundary condition is imposed such that $|i-j| = \min\{\text{abs}(i-j), N - \text{abs}(i-j)\}$. b. A sparsely coupled circuit which emerges from the Faro shuffling scheme. The sparsely coupled circuit, where two qubits interact if and only if they are separated by integer powers of 2, is recovered by removing even and odd bonds interchangeably for every other period. c. The probability of two-qubit gate being applied between sites i and j as a function of a tunable parameter s and inter-qubit distance $d_\infty(i,j)$. The probability distribution decays with the distance for $s < 0$, while it grows with distance for $s > 0$. At $s = 0$, the two-qubit gates are applied for all allowed pairs of neighboring qubits with the same probability. d. The two geometries, linear and treelike, with two incompatible notions of locality. Site indices given by following the Euclidean norm $d_\infty(i,j)$ naturally defines an order of sites consistent with the linear geometry (top). In treelike geometry, the closeness of the sites are defined by the 2-adic distance with emerging treelike hierarchical structure (bottom). The sites that are ordered in the linear geometry can be rearranged to a treelike geometry by performing Monna map (middle). e. (inset of d.) A sketch of a dynamical transition from linear area-law (blue) to treelike area-law (pink) regime as a function of s and transition to volume-law (green) entanglement entropy in time. This figure was reproduced from [187].

interaction step is regarded as a layer of circuit with gate applications between the neighboring atoms.

In an experimental setup, the physical time in a laboratory which is required for shuffling atoms may scales at worst $\mathcal{O}(N)$. However, this extra scaling can be ignored by adjusting the speed of transport such that the shuffling time is the worst possible time which occurs at the largest system size that can be achieved in the laboratory. Together with the long coherence time of the ground state atomic qubits, the scheme is expected to provide the scalability as well as the accessibility in the near-term experiments of fast-scrambling and highly nonlocal circuit models.

By choosing a correct shuffling scheme—the Faro shuffle—which moves every second atoms to the back of the array [177]—effective interactions can be restricted to the qubits that are 2^F away in the initial linear ordering, where F is the minimum number of shuffling operations required to be applied on the initial ordering. With this scheme, the sparse coupling pattern emerges naturally in this model (Fig. 6.1 a.). In this chapter, we probe the model by varying probability of the nearest-neighbor interactions as a function of F and a tunable parameter s (Fig. 6.1 b.). By setting a function to be monotonically decreasing ($s < 0$) or increasing ($s > 0$), as shown in Fig. 6.1 b., the model interpolates between two regimes with different underlying geometries. The linear geometry is recovered for large negative $0 < s$, where the correlation propagates continuously over the neighboring sites in the linear geometry as shown in Fig. 6.1 d. (top). We find in this regime, an area-law entanglement is recovered in the linear geometry in the early times (Fig. 6.1 e. blue). For large positive $0 < s$, on the other hand, treelike geometry, where closeness is defined with 2-adic norm (c.f. Ch. 2.6), emerges (Fig. 6.1 d. bottom).

We find that in this regime, an area-law entanglement is present in the treelike geometry in early times (Fig. 6.1 e. pink). In both regimes, the linear lightcone emerges as a result of the locally propagating correlation. After a time which scales polynomially with N, the lightcone hits the boundary multiple times, leading to the saturation in the amount of quantum information that can be held locally. When it occurs, an area-law entangled state transitions to a volume-law entangled state. Upon further evolution, the state reaches the Page-scrambling limit [236], where any given subsystem is maximally entangled with the rest of the system. Similarly to the model discussed in the previous chapter, near $s = 0$ the fast scrambling dynamics emerges as the linear and treelike lightcones collapse to transition from one geometry to the other. We show that this collapse of lightcone leads to the scrambling time t_*, the time it takes for initial product state to be Page-scrambled, to scale $t_* \propto \log N$.

In this chapter, we also probe the polynomial lightcones, which emerges from the different underlying geometries—linear, fast scrambling, and treelike—in the quantum circuit on a sparsely coupled graph. This is done through the numerical simulation of the dynamically changing entanglement structures. To simulate the circuit in great depth and large system size, we restrict the circuit to a restricted class of circuit called Clifford circuit [90, 118]. In §6.2, we introduce a sparse Clifford circuit, which we study in this chapter. In §6.3 we characterize the scrambling t_* of the different regime as a negativity of tripartite mutual information

$I(A:B:C)$ between three locally confined regions. We show that scrambling time $t_* \propto \mathcal{O}(N^a)$ increases polynomially when the geometry is compatible and $t_* \propto \mathcal{O}(1)$ otherwise. In §6.4, we further show the emergence of lightcone in a geometry that is compatible with the interaction. This is done by calculating the Bao-Altman teleportation probability $I_{|\mathrm{m}}(i,j)$ between the sites i and j [334]. We show that at and near $s=0$, the teleportation time becomes finite. In §6.5, we propose the experimental implementation of sparse Clifford circuit and Floquet deterministic fast scramblers using neutral atoms, with tweezers assisted shuffling protocol. Then in §6.6, we introduce a deterministic Floquet fast scrambler which emerges at $s=0$ by replacing the random two-qubit gates to a deterministic set of gates. By probing the entanglement structure we show that initial product state reaches the Page-scrambling limit in time $t_* \propto \log N$. We also show that Hayden and Preskill type of teleportation protocol performed on the circuit can immediately teleport a quantum state on arbitrary number of qubits in time $t_* \propto \log N$. Finally, in §6.7, we summarize our findings.

6.2 Sparse Clifford Circuits

We study Clifford circuits on a sparsely coupled graph. Sparse circuits are a class of circuits where the qubits numbered $i = 0, 1, \cdots N-1$ are coupled via two-qubit gates Q_{ij} when two qubits i and j are connected by an edge in a sparsely coupled graph. The sparsely coupled graph, which we consider in this chapter, is a graph where two vertices are connected if and only if the difference, $d_\infty(i,j)$, in the qubit numbers i and j is an integer power of 2: $d_\infty(i,j) = |i-j| = 2^l$ for $l = 1, 2, \cdots$ (Fig. 6.1 a.). In this chapter, if not stated explicitly, periodic boundary conditions are assumed, where the distance is defined as $|i-j| = \min\{\mathrm{abs}(i-j), N-\mathrm{abs}(i-j)\}$.

Following the analytical [177, 335], numerical [183], and experimental [102] studies, we introduce a tunable parameter s which controls the probability $p(|i-j|, s)$ of applying two qubit gates as a function of $d_\infty(i,j)$ as follows (Fig. 6.1 b.):

$$p(|i-j|, s) = \begin{cases} J_s |i-j|^s & \left(\text{when } |i-j| = 2^l,\ l = 0, 1, 2, \cdots\right) \\ 0 & (\text{otherwise}) \end{cases}, \tag{6.1}$$

where J_s is a normalization factor,

$$J_s = 2\left(\left(\frac{N}{2}\right)^s + 2\sum_{k=0}^{\log_2 N-2} 2^{ks}\right)^{-1}. \tag{6.2}$$

In order to recover the continuous time dynamics in the limit where a set of applied qubit gates only rotate a local state by small amount, we further impose nonlocal brickwork pattern to the circuit, as shown in Fig. 6.1 c. In the sparse nonlocal brickwork circuit, the circuit is represented as interchangeably stacked even and odd blocks. Each block is composed of $\log_2 N - 1$ circuit layers, and for each layer, two-qubit gates are applied to the qubits that are separated by distance 2^l with the probability $p(2^l, s)$, where l is the number of layers measured from the 0^{th} layer of the block. In order to avoid two-qubit gates to be applied on the same qubit in a given layer more than once for any s, for the layers in even (odd) block, we apply two-qubit gates $Q_{i,i+2^l}$ if and only if $i/2^l = 0 \mod 2$, ($= 1 \mod 2$ for odd). Finally, we insert a layer of circuit with two-qubit gates $Q_{i,i+N/2}$ for $i = 0, 1, \cdots, N/2 - 1$ with probability $p(N/2, s)$ right after applying the even block.

In this circuit construction, following Sekino and Susskind [53, 55], Bao *et al.* [334], and the random all-to-all model discussed in Ch. 1.1.2, we define a unit of time as a number of layers required such that on average, one gate is applied per qubit. This is treatment is necessary to recover an anisotropic transverse field Heisenberg Hamiltonian on a sparsely coupled graph, which is extensive and similar to the spin model discussed in Ch. 5, through the transformation discussed in [334]. With the normalization factor J_s defined in Eq. (6.2), a unit of time becomes exactly $2\log_2 N - 1$ circuit layers, i.e. $\Delta t = 1 \equiv 2\log_2 N - 1$ layers.

The two-qubit gates Q_{ij} are drawn randomly from a set of gates called two-qubit Clifford group [117, 118]. The two-qubit Clifford group $\mathbf{C}_2$ is a set of unitary operators which transforms a Kronecker product of two Pauli operators, also known as a Pauli string, to a different Pauli string. As discussed in Ch. 4.4, with this constraint, the state explores the state space spanned by the stabilizer states. Therefore, the dynamics can be exactly simulated in polynomial time using a classical computer, while capturing many-body entanglement [90, 117, 118]. Furthermore, the random Clifford gates are unitary 2-designs [336], hence the random Clifford unitary dynamics closely mirror the dynamics of random gates drawn from more general set of random unitaries [53, 59, 119, 151, 206]. With this treatment, the circuit with order of a thousand qubits can be simulated.

6.3 Scrambling and Negativity of Tripartite Information

First we quantify scrambling dynamics of the circuit by looking at how tripartite mutual information (TMI)

$$I(A:B:C) = I(A,B) + I(A,C) - I(A,BC) \tag{6.3}$$

of regions A, B, and C, defined in the different geometries evolves for the different values of s. Here, $I(A,B) = S(A) + S(B) - S(AB)$ is mutual information between regions A and B, and $S(A)$ is the von Neumann entropy of subregion A:

$$S(A) = -\mathrm{Tr}\{\rho_A \ln \rho_A\}, \tag{6.4}$$

where $\rho_A = \mathrm{Tr}_{\bar{A}}\rho$ is the reduced density matrix of A, ρ is the density matrix of the full state, $\mathrm{Tr}_{\bar{A}}$ is a partial trace over subregion $\bar{A}$, and $\bar{A}$ denotes the complementary subregion of A.

The negativity of TMI for three extensive regions serves as a degree of global embedding of initially localized information, the degree of scrambling, as reviewed in Ch. 2.1.1. Shown in Fig. 6.2 a. is a TMI calculated for three geometrically contiguous regions A, B, and C of size $N/4$, which divides the qubits into four equal partition of size $N/4$ in linear (left, Euclidean ordered) and treelike (right, Monna mapped, c.f. Ch. 2.6) geometries as depicted in Fig. 6.2 a. (top left). As defined in Ch. 5.4.2, a contiguous region is a region where every qubit in the region has at least one qubit that is adjacent to it in the same region.

The behavior of TMI varies drastically between the signs of s and the geometries. The locality of the interaction in a given geometry, gives rise to a long-lasting plateau where $I(A:B:C) = 0$. This is especially true in the case of large $|s|$: $1 \ll |s|$. In this regime, TMI becomes negative after the lightcone spreads across the system, which gives rise to the plateau duration that is extensive in N.

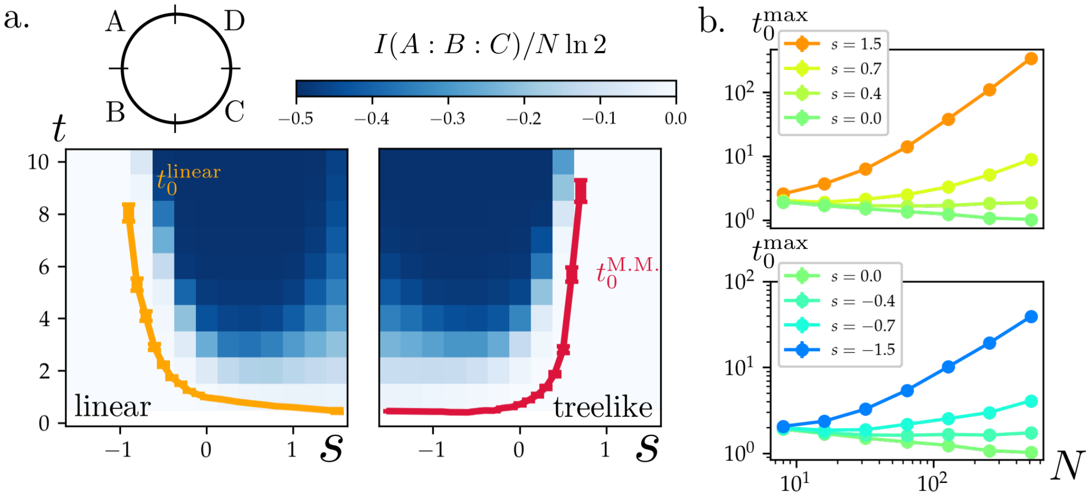

FIGURE 6.2: **Quantifying Scrambling Tripartite Mutual Information.** a. Tripartite mutual information $I(A:B:C)$ between the three contiguous region of $N/4$ (top left) of the output qubits for $s=-1.5,\cdots,1.5$ with step size $\Delta s=0.25$, in linear (left) and treelike (right) geometries for $N=512$. An initial plateau $I(A:B:C)=0$ (white) persists for extended amount of time when the interaction is local in a given geometry. At long times, information scrambles and gives rise to the substantial negativity in TMI (dark blue). When the interaction is nonlocal in a given geometry, however, the negativity is reached in the timescale of order $\mathcal{O}(1)$. ($0<s$ for the linear and $s<0$ for the treelike geometry) The length of the plateau is estimated by finding the time t_0 which takes for TMI to reach one bit of negativity, $I(A:B:C)=-\ln 2$, in linear (orange) and treelike (red) geometries. The error analysis on the points on the color plot is provided in Appendix B. b. The time t_0 for $s=0,\pm0.4,\pm0.7$ for system sizes $N=2^3,2^4,\cdots,2^9$. For $s<0$, t_0 is computed in the linear geometry, and for $0<s$, t_0 is computed in the treelike space. Error bars are shown or are smaller than the data points. Results are averaged over 10^3 circuit realizations. The initial state is a product state $|0\rangle^{\otimes N}$. This figure was reproduced from [187].

With this observation, we extract the timescale of a circuit's ability to scramble a bit of information as a duration t_0 of the $I(A:B:C)=0$ plateau. Precisely, t_0 is defined as the time when TMI reaches one bit of negativity: $I(A:B:C)=-\ln 2$. For $N=512$, t_0 is marked in Fig. 6.2 a. with orange for linear geometry and red for treelike geometry. As shown, t_0 approaches to $\mathcal{O}(1)$ constant as $|s|$ approaches 0, and the time is fixed at constant for the values of s with the geometry where the interactions are nonlocal.

To confirm the fast scrambling dynamics emerges at $s=0$, plotted on Fig. 6.2 b. is a timescale t_0 for different system sizes. For $1<|s|$, the timescale becomes extensive with the system size in the geometry that is compatible with the locality of the interactions. Namely, if the contiguous regions are taken in the linear geometry, the timescale grows as $t_0^{\text{linear}}\sim N$ for $s<-1$ (bottom), and polynomial

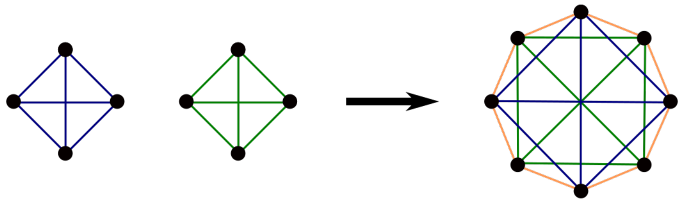

Figure 6.3: **Hierarchical Construction of the underlying coupling graph of the sparse Clifford circuit.** The sparse coupling graph of size N (right, $N = 8$) can be constructed by coupling two sparsely coupled graphs of size $N/2$ (left, $N/2 = 8$) by interleaving the sites and coupling them with the nearest neighbor couplings (right, orange). This figure was reproduced from [187].

dependence for treelike geometry is recovered $t_0^{\text{treelike}} \sim N^{s+0.1}$ for $1 < s$ (top). Near $s = 0$, we find that $t_0^{\max} = \max\{t_0^{\text{linear}}, t_0^{\text{treelike}}\}$ approaches $t = 1$. This implies that the single qubit is guaranteed to be scrambled in the time of order unity at $s = 0$.

6.3.1 The Limiting Behavior of t_0 at $s = 0$ in the Thermodynamic Limit

At $s = 0$, we have numerically given evidence of the convergence of the duration of plateau to $t_0 = 1$ in the thermodynamic limit $N \to \infty$. In this subsection, we explicitly show that this is the case by utilizing the hierarchical structure of the sparse Clifford circuit.

The sparse Clifford circuit of size N can be constructed hierarchically from the two circuits of size $N/2$. As shown in Fig. 6.3, this can be done by interleaving the qubits and inserting the nearest neighbor gates. Using this hierarchical construction, after doubling the system size from $N/2$ to N, without the presence of the nearest neighbor gates, TMI in the linear geometry after 1 periodic iteration of the circuit scales like $I_N(A:B:C) = 2I_{N/2}(A:B:C)$, where $I_N(A:B:C)$ represents the tripartite mutual information of a system size N. However, the addition of the nearest neighbor gates biases the circuit slightly towards the information to spread locally in the linear geometry. Therefore, the actual scaling in the linear geometry is smaller than 2.

Let $E(N) = N/2(2\log_2 N - 1)$ be the number of possible positions which the gates are allowed to be applied and $p_0(N) = \frac{2}{2\log_2 N-1}$ be the probability of interactions

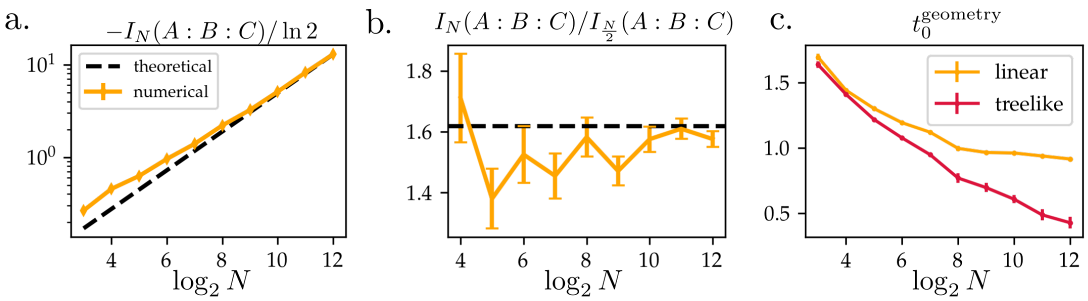

FIGURE 6.4: **Theoretical behavior of tripartite mutual information at $t = 1$ for $s = 0$.** a. Numerically computed $-I(A : B : C)$ (blue) and theoretically expected values $-I_N(A : B : C)/\ln 2 = I_{2048}\phi^{\log_2 N-11}/\ln 2$ (red) are plotted for the system sizes $N = 2^3, \cdots, 2^{12}$. The numerically obtained scaling law shows convergence towards the theoretical scaling law as the system size increases. b. The ratio of $I(A : B : C)$ for two different system sizes of N and $N/2$ for different system sizes at $t = 1$ and $s = 0$ for the system sizes $N = 2^3, \cdots, 2^{12}$. The numerically computed values (blue) are converging towards the golden ratio (black dotted) as the system sizes increase. c. t_0^{geometry} for two different geometries at $s = 0$ for $N = 2^3, \cdots, 2^{12}$. For sufficiently large N, saturation time in the linear geometry is always greater than that of the treelike geometry, and hence $t_0^{\max} = t_0^{\text{linear}}$. Quantities and their standard error are obtained by averaging from 5×10^1 (for $N = 2^{12}$) up to 5×10^3 (for $N = 2^4$) circuit realizations. This figure was reproduced from [187].

(if allowed) at $s = 0$. On average, the number of non-nearest-neighbor gates applied to the circuit is $(E(N) - N)p(N)$, which is not enough for having two scrambling circuits of size $N/2$. However, it is enough for creating one circuit configuration of the circuit of size $N/2$ at $t = 1$, and using the gates that are left upon creating a scrambling circuit of size $N/4$ with the leftover qubits, and so on. This process can be continued as the number of gates permits down to the circuit of size 2.

In the large system size limit, the dominant contributor to the tripartite mutual information will be the circuit of size $N/2$ and $N/4$. This is because the contributions become combinatorically smaller as the system size becomes smaller. This gives us a following approximate recursion relation:

$$I_N(A : B : C) \sim I_{N/2}(A : B : C) + I_{N/4}(A : B : C). \tag{6.5}$$

This relation implies that $I(A : B : C)$ to be monotonically decreasing with respect to the system size, provided that initial values are negative.

In the limit of large N, the recursion relation tells us that TMI scales likes a power of the golden ratio ϕ, because the relation Eq. (6.5) is that of the Fibonacci numbers with a different pair of the starting numbers [337]

$$I_N(A:B:C) \propto -\phi^{\log_2 N}. \tag{6.6}$$

Fig. 6.4 a. shows the theoretical line with $-I(A:B:C)/\ln 2 = I_{2^{12}}(A:B:C)\phi^{\log_2 N-12}/\ln 2$ with a black dotted line and the numerically obtained value of $-I(A:B:C)$ for the different system sizes at $t=1$ for $s=0$ (blue line). For the large system sizes, the theoretical behavior and the obtained numerical result agrees well.

Furthermore, in Fig. 6.4 b. the ratio of tripartite mutual information $I_N(A:B:C)/I_{N/2}(A:B:C)$ at $t=1$ for $s=0$ are plotted. As expected, the ratio converges towards the golden ratio as the system size increases. Thus, at $t=1$ and $s=0$, exponentially many more trajectories are expected to have negative tripartite information compare to the trajectories with non-negative values; and hence the timescale of t_0^{linear} approaches to 1 in the limit of $N \to \infty$.

The same argument applies for the treelike geometry. In this case, instead of the nearest-neighbor gates (in the linear geometry), the longest range gates (in the linear geometry) have to be taken out. Due to the circuit structure, which goes from the longest to the shortest range interactions in the treelike geometry, the time t_0^{treelike} is smaller than t_0^{linear} for large N (Fig. 6.4 c.). Therefore, t_0^{linear} converging to $t_0^{\text{linear}}=1$ in the limit of large N implies that $t_0^{\max}$ also converges towards $t_0^{\max}=\max\{t_0^{\text{linear}}, t_0^{\text{treelike}}\}=1$.

6.4 Emerging Many-Body Lightcone and Teleportation

In the previous section, we showed that the timescale for the TMI to reach negativity is no longer extensive near $s=0$. We have shown that at $s=0$, the negativity timescale converges towards $t=1$ in the thermodynamic limit. The result implies that the circuit can scramble at least one bit of information in a time of order unity near $s=0$. In this section, we further investigate the change in geometry of the circuit and the change in scrambling property as a function of s by examining the lightcone emerging from the teleportation property of the circuit.

The teleportation of quantum information is related to the information scrambling, as a teleportation from qubit i to qubit j can only occur when the information qubit i is present at j. The probability of the successful teleportation, therefore, is governed by the mutual information shared between the input and output qubits.

As discussed in the introduction, in 1+1 dimensional short-ranged systems, the information propagates along the lightcone, obeying the Lieb-Robinson bound. In the case of linear geometry, therefore, the radius of the region where teleportation succeeds increases linearly with time $|i-j| \sim v_s t$ and similarly in treelike geometry $|i-j|_2 \sim v_s t$, with the Lieb-Robinson velocity v_s; and the teleportation fails outside.

To test this in the sparse Clifford circuit, we follow the teleportation protocol proposed by Bao, Block, and Altman [334], that is based on the Hayden-Preskill-Yoshida-Kitaev teleportation protocol [59, 153, 181, 221, 334]. The protocol starts with maximally entangling an auxiliary qubit R_i with an input qubit $i = 0$ as illustrated in Fig. 6.5 a., and we let the system evolve with the sparse Clifford circuit. At the end of the evolution, we measure the conditional mutual information $I_{|m}(i, j)$

$$I_{|m}(i,j) = \left(S(R_i) + S(j) - S(R_i j)\right)_{|m}, \tag{6.7}$$

where the subscript $|m$ indicates that entropy is calculated after projective measurements with Pauli-z basis are performed on all the qubits except for R_i and j.

For sufficiently large and negative $s < 0$, the linear lightcone emerges in the linear geometry as shown in Fig. 6.5 a. top (black dashed). Here a qubit of information introduced at site $i = 0$ at time $t = 0$ propagates through the lattice with the Lieb-Robinson velocity $v_s \approx 3.0$. For the sufficiently large and positive $0 < s$, the apparent lightcone breaks down in the linear geometry (Fig. 6.5 a. bottom). However, in this regime, the lightcone can be recovered by performing the Monna map on the sites. In the Monna mapped, treelike geometry, the treelike lightcone is recovered, where the wave front of the teleporting region (dark orange) spreads linearly with the 2-adic distance like $|i-j|_2 = v_s t$ (Fig. 6.5 a. inset). These results clearly indicate that the model becomes a locally interacting model in the limit of large $|s|$; but the nature of locality depends on the sign of s.where positive $0 < s$

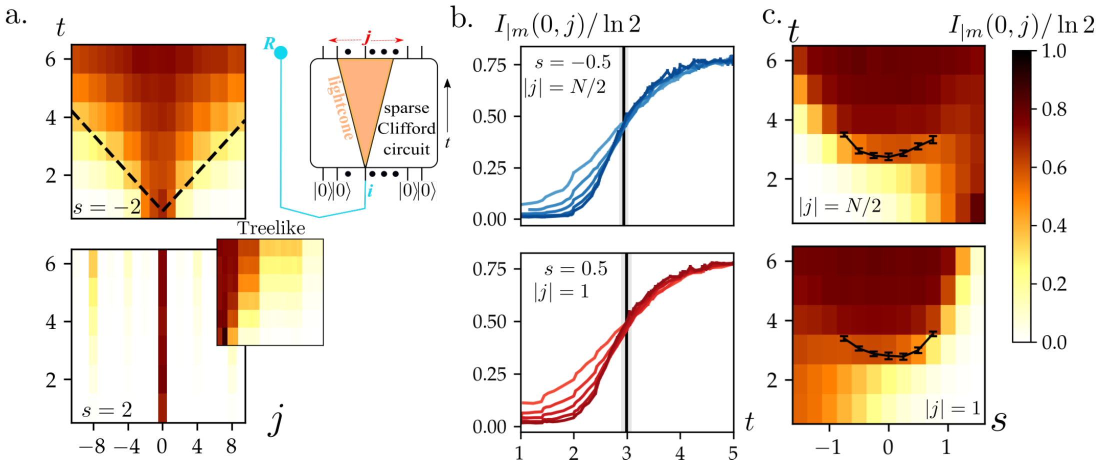

FIGURE 6.5: **Characterization of the geometries via quantum teleportation protocol**. The lightcone formed by the teleportation probability of the input qubit at site 0 and other sites j in the sparse Clifford circuit. The success of quantum teleportation is measured by the conditional mutual information $I_{|m}(i, j)$ between the ancillary qubit R, which is maximally entangled with the input i, and an output qubit j given that all the other sites in the system are locally measured. a. Lightcone formed by the conditional mutual information $I_{|m}(0, j)$, which characterizes the fidelity of the teleportation, in linear geometry for $s = -2$ (top) and $s = 2$ (bottom). A linear lightcone is clearly emerging for $s = -2$ in the linear geometry with the Lieb-Robinson velocity, $v_s \approx 3.0$, while the lightcone is broken for $s = 2$. However, the lightcone is recovered in the treelike geometries for $s = 2$, after rearranging the qubits via Monna map $\mathcal{M}$ (inset). Detailed error analysis of the color plot is provided in Appendix C.1. b. For $-1 < s < 1$, we found a system size independent crossing point at $t = t_c$ (black line with error indicated by gray shade), which indicates a finite-time phase transition in the teleportation fidelity from not teleporting ($t < t_c$) to teleporting ($t > t_c$) phase in the linear (top) and maximally separated in the treelike geometry (bottom). The critical times t_c between maximally separated pairs of qubits $i = 0, j$ in linear (Euclidean) distance $|i-j| = N/2$ (top, $s = 0.5$), and 2-adic treelike distance $|i-j|_2 = 1$ (bottom, $s = 0.5$) are extracted with the finite size scaling. c. The conditional mutual information for $N = 2^7$ between $i = 0$ and maximally separated qubit in Euclidean distance (top) and 2-adic distance (bottom). Similarly to b,, we have done finite size analysis for all the values of $s = -0.75, 0.75$ in the interval $\Delta s = 0.25$. The crossing of the conditional mutual information is not observed in the regime outside $-1 < s < 1$ in either of the geometries (black). The teleportation fidelity is calculated from up to 1.5×10^4 circuit realizations for the system size $N = 2^5, 2^6, \cdots, 2^{10}$. Detailed error analysis of the color plot is provided in Appendix C.2. The detailed finite scaling analysis of the critical teleportation times are provided in Appendix C.3. If not visible, error bars are smaller than the line width for lines in b. and c. This figure was reproduced from [187].

gives rise to locality in the linear geometry, and negative $s < 0$ gives rise to the locality in the treelike geometry.

Near $s = 0$, there exists a crossover regime where the model loses its locality in both of the geometries. In this regime, the lightcone breaks down in both geometries, and the fast scrambling dynamics emerges. In this regime, as established in the previous section, a qubit of information instantaneously delocalizes across the system in the timescale of $\mathcal{O}(1)$. As a result, we expect that a qubit of information that was initially in the qubit i, which is kept track in the form of the correlation in R, to be recovered in qubit j. This implies that the initial state at qubit i is recovered at a site j, and hence the teleportation succeeds with non-vanishing probability in the time that is independent to the system size.

In the randomly coupled all-to-all model, the $\mathcal{O}(1)$ time of teleportation appears as a critical time t_c in the thermodynamic limit [334]. In order to show that this is also the case for our model, we perform finite size analysis on $I_{|m}(i,j)$ for qubits at site $i = 0$ and site j, which is maximally separated in linear geometry $|i-j| = N/2$ (Fig. 6.5 b. top) and treelike geometry $|i = j|_2 = 1$ (bottom). Near $s = 0$, we observe a system size independent teleportation time t_c. Beyond this time, the teleportation succeeds with a finite probability with any pairs of qubits even in the thermodynamic limit. The similar critical time is observed in both geometries in the interval $-1 < s < 1$. The landscape of the conditional mutual information is plotted in Fig. 6.5 c. for $N = 128$ with calculated critical times marked in black.

The finite teleportation time is not observed beyond $|s| = 1$. This indicates that there is no such transition exists in the regimes where the information spreads locally across the system. Thus, it is established that the dynamics on the sparsely coupled model has two geometric regimes: the region where dynamics is local in linear geometry ($s < 0$), and the region where dynamics is local in treelike geometry ($s > 0$), which are separated by a region where dynamics is nonlocal and fast scrambling ($-1 < s < 1$).

6.5 Experimental Implementation

The circuits discussed in this chapter can be implemented straightforwardly using neutral atoms. In this section, we discuss the implementation of the sparse Clifford circuit using locally interacting neutral atoms in optical lattices. The sparse coupling pattern is achieved by exchanging the neighboring atoms via shuffling of atoms using a 2-dimensional optical tweezer array.

We use long-lived ground states $|0\rangle$ and $|1\rangle$ as the two states of a qubit. The single qubit gates can be implemented with the qubit rotations via Rabi oscillation

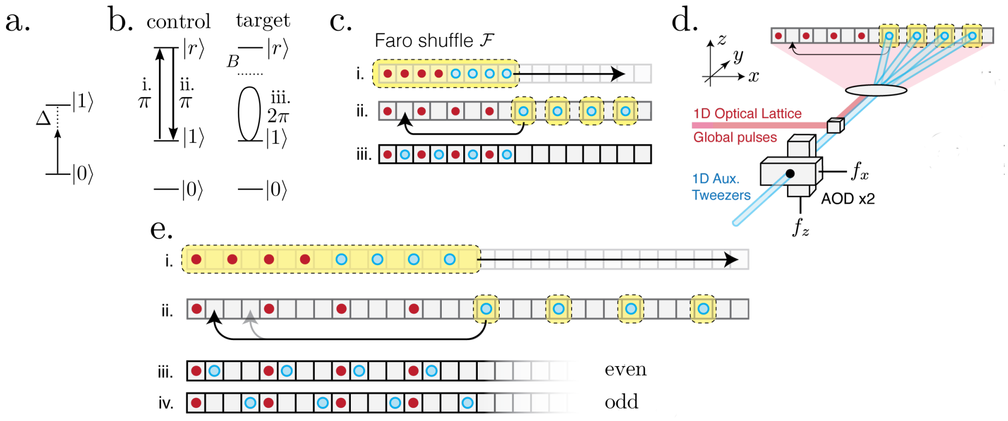

FIGURE 6.6: **Experimental realization of the sparse Clifford circuit.** a. Single qubit rotation via Rabi oscillation. The phase and Hadamard gates are equivalent to rotating about z-axis and $(x+z)/\sqrt{2}$-axis respectively, by angle π. This can be achieved by applying coherent AC-field. b. Implementation of Controlled-Z gate using Rydberg blockade. (i) The state $|1\rangle_c$ in the control qubit (atom) is moved up in the circular Rydberg state with π pulse. (ii) Then 2π pulse with the Rabi frequency which couples $|r\rangle_t$ and $|1\rangle_t$ of the target qubit is applied. When the state $|r\rangle_c$ is present, then due to the blockade B, the state $|1\rangle_t$ fails to gain the phase π, otherwise the target state transforms like $|1\rangle_t \to -|1\rangle_t$. Thus, the conditional phase accumulation on the state $|1\rangle_t$ target qubit is achieved. (iii) By applying the π pulse, de-excite $|r\rangle_c$ to $|1\rangle_c$ to recover the logical control qubit. c. Schematic diagram of Faro shuffle of atoms for the system size $N=8$. The Faro shuffling of atoms proceeds as follows: (i) double the interatomic distance. (ii) Move the last $N/2$ atoms, (iii) and interleave them in the first $N/2$ atoms. When N is an integer power of 2, the configuration is periodic with period of $\log_2 N$ shuffle operations i.e. $I \equiv \mathcal{F}^{\log_2 N}$, where I is an identity. d. Schematic diagram of the experimental realization of atomic Faro shuffle. Steps in c. can be realized with an optical tweezer array. Two AODs placed perpendicularly allow the tweezers to move freely in the x-z plane with entrapped atoms. e. The brickwork circuit can be recovered by expanding the lattice in step (i) to $3N$ lattice sites instead of $2N$. Even and odd layers can be achieved by placing the last $N/2$ atoms in either the left most (even, iii) or the right most (odd, iv) available sites in the contraction step (ii). This figure was reproduced from [185].

(Fig. 6.6 a.). The short-ranged (in the physical space) nearest-neighbor Controlled-Z interactions by utilizing the van der Waals interaction between the circular Rydberg states, which decays sharply as $1/|R|^6$, as shown in Fig. 6.6 b., where R is the physical distance between the atoms [104, 178–180, 338, 339]. The non-trivial long-range interactions that are present in the circuit are recovered by varying the neighboring atoms through shuffling.

The sparse Clifford circuit is recovered by adopting a shuffling scheme called a Faro shuffle. As shown in Fig. 6.6 c., the Faro shuffle $\mathcal{F}$ is a permutation operation which takes the last $N/2$ elements in an array of N elements, and interleaves them in the first $N/2$ elements [177, 340]. For example, the Faro shuffle for $N=8$ in two-line form is given as

$$\mathcal{F}_8 = \begin{pmatrix} 0 & 1 & 2 & 3 & 4 & 5 & 6 & 7 \\ 0 & 4 & 1 & 5 & 2 & 6 & 3 & 7 \end{pmatrix} \tag{6.8}$$

$$(\mathcal{F}_8)^2 = \begin{pmatrix} 0 & 1 & 2 & 3 & 4 & 5 & 6 & 7 \\ 0 & 2 & 4 & 6 & 1 & 3 & 5 & 7 \end{pmatrix}. \tag{6.9}$$

With this shuffling procedure, the difference in the qubit labels i, j of neighboring atoms after l Faro shuffling from the initial linear ordering of the qubits is dominated by $\mathrm{abs}(i - j) = 2^{n-l}$ for $0 < l < n$, for the system size, which is integer powers of 2.

In order to recover the sparse coupling pattern, we propose to operate the Faro shuffling in reverse $\mathcal{F}^{-1}$. By shuffling the atoms in the reversed order, the difference in the qubit labels increases with the number of shuffling operation l as $|i-j| = 2^l$ with period $\log_2 N$. In order to recover the sparse coupling pattern, the extra couplings, such as 1-5 in Eq. (6.8), must be removed. Because the Faro shuffling procedure itself requires control over the positions of the individual atoms, this can be done for free by tuning the interatomic distance when contracting the interatomic positions when going from step (ii) to step (i) in Fig. 6.6 c. Especially, the brickwork circuit can be achieved simply by expanding the array of atoms by $3N$ lattice sites instead of $2N$ in Fig. 6.6 c. (ii), as shown in Fig. 6.6 e. Even and odd interactions can be recovered by placing the last $N/2$ atoms in the left (even) or the right (odd) most available site in the contraction step as shown in Fig. 6.6 e. (ii). The probabilistic application of the gates can be achieved with the same technique.

The physical implementation of the Faro shuffling scheme can be done with 2-dimensional optical tweezer arrays controlled by two perpendicularly placed Acousto-Optic Deflectors (AODs) (Fig. 6.6 d.). The recent state-of-the-art experiment achieves the coherent transport of atoms with the speed of up to 0.55 μs/ms over the distance of 110 μm [104, 105]. This implies that sparse Clifford circuit of $N = 64$ can be implemented readily with the lattice spacing of 3 μm. It is hoped that in the future, these limits are increased.

6.6 Deterministic Floquet Fast Scrambler

In the previous section, we established that the sparse Clifford circuit has a transition from linear to treelike geometry near $s = 0$. In this section, we further establish that at $s = 0$ the fast scrambling limit can be reached with the deterministic sets of gates. The use of deterministic set of gates yields a straight forward experimental implementation in the near term cold atom experiments in the platform such as the one discussed in the previous section §6.5.

The Clifford circuit we use in this section is based on the sparse Clifford circuit. We use a slightly different circuit in order to make the circuit experimentally accessible with even fewer steps than the sparse Clifford circuit at $s = 0$. We propose a deterministic fast scrambling Clifford circuit, which consists of global single qubit rotation (phase and Hadamard gates), uniform nearest-neighbor Rydberg interaction via Controlled-Z (CZ) gates, and Faro shuffles.

In this section, we first define the deterministic circuit in §6.6.1. Then we show that this deterministic circuit produces maximally entangled state, called Page-scrambled state, after $2\log_2 N$ iterations of the circuit (§6.6.2). In §6.6.3, we further confirm the fast scrambling nature of the circuit by performing the Hayden-Preskill experiment. Similarly to the information dropped into a black hole [59, 181], we show that $|A|$ qubits of information that is localized in the initial state can be recovered from a random subregion R with $|R| = |A|$ qubits in the output state immediately after $2\log_2 N$ circuit iterations.

6.6.1 Deterministic Fast-Scrambling Clifford Circuit

As shown in Fig. 6.7, the building blocks of the deterministic fast scrambling Clifford circuit that consists of three components:

i. Global qubit rotation R by angle θ, ϕ.

ii. Global nearest-neighbor CZ interaction.

iii. Inverse Faro shuffle $\mathcal{F}^{-1}$

The deterministic fast scrambling Clifford circuit we propose is an iterative circuit that consists of global qubit rotations with phase P and Hadamard H gates of the

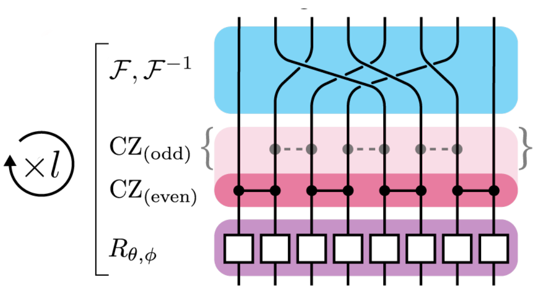

FIGURE 6.7: **Building block of the deterministic fast scrambling Clifford Circuit.** The deterministic fast scrambling Clifford circuit discussed in this section consists of a repetitive application of a block, which consists of the following three components: i. Global qubit rotation R by angle θ, ϕ. ii. Global nearest-neighbor Controlled-Z (CZ) gate. iii. (Inverse) Faro shuffle ($\mathcal{F}^{-1}$) $\mathcal{F}$. A scrambled state can be reached in $2\log_2 N$ applications of the block. This figure was reproduced from [185].

form:

$$P = \begin{pmatrix} 1 & 0 \\ 0 & i \end{pmatrix}, \quad H = \frac{1}{\sqrt{2}} \begin{pmatrix} 1 & 1 \\ 1 & 1 \end{pmatrix}. \tag{6.10}$$

The two-body interaction is mediated with Controlled-Z gates that are applied to even or odd bonds in the qubit array, where we take the first $\log_2 N$ iterations to be applied on the even bonds and next $\log_2 N$ iterations to be applied on the odd bonds. The couplings similar to sparse Clifford circuit are then recovered through the Faro shuffling operator $\mathcal{F}$. The deterministic fast scrambling Clifford circuit $\mathcal{E}_{\mathrm{s}}$ is

$$\mathcal{E}_{\mathrm{s}} = \left[\mathcal{F}^{-1}\mathrm{CZ}_{\mathrm{odd}} HP\right]^{\log_2 N} \left[\mathcal{F}^{-1}\mathrm{CZ}_{\mathrm{even}} HP\right]^{\log_2 N}. \tag{6.11}$$

Similarly to the last section in this chapter, from here and on wards, we define time t as the number of iterations of layers of circuit $\mathcal{F}^{-1}\mathrm{CZ}_{\mathrm{even(odd)}}HP$ applied to the system. Hence, an application of the circuit $\mathcal{E}_{\mathrm{s}}$ evolves a state from time $t = t_0$ to $t = t_0 + 2\log_2 N$. Here the normalization factor from the previous section is removed ($J_s = 1$) in order to compare the circuit properties with the random all-to-all circuit, the prototypical fast scrambling circuit, discussed in Ch. 1.1.2. In the next sections we show that fast scrambling dynamics can be observed in the circuit even in the deterministic and the sparse coupling limit.

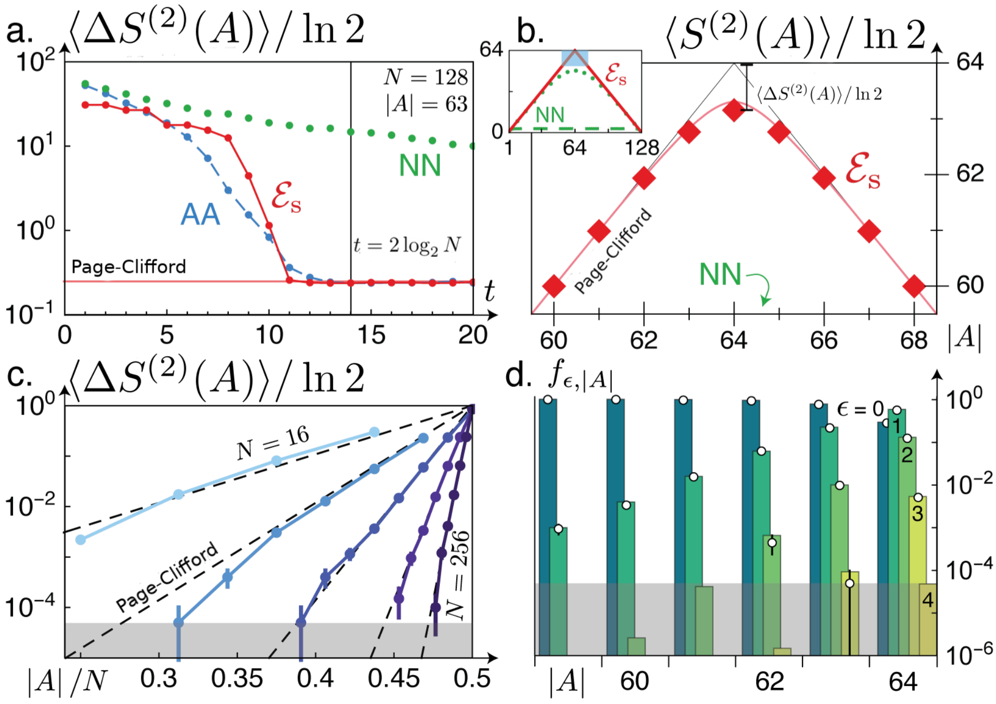

FIGURE 6.8: **Page-Scrambling in time $t = 2\log_2 N$.** a. The mean entropy deficit $\langle S^{(2)}(A)\rangle$ from the maximum value, for 2×10^4 random subsystems A, at each time t, for $|A| = N/2 - 1 = 63$ for $N = 128$ for nearest-neighbor (NN), randomly coupled all-to-all (AA), and deterministic fast scrambling circuit ($\mathcal{E}_\mathrm{s}$). The deficit of the circuit $\mathcal{E}_\mathrm{s}$ rapidly decreases and saturated the Page-Clifford limit of $\ln 2/4 \approx 0.17$ (red line) by the scrambling time $t = 2\log_2 N$ is reached. Similar behavior is observed for the randomly coupled all-to-all model, which is a known prototypical fast scrambler. The nearest-neighbor circuit, on the other hand, the deficit decreases linearly with time, and saturation is not observed in this timescale as expected. b. The Renyi entropy $\langle S^{(2)}(A)\rangle$ of the output states of $\mathcal{E}_\mathrm{s}$ at $t = 2\log_2 N$ for random subsystems A of sizes near $|A| = N/2$ (red diamonds). They saturate the Page-Clifford limit (red line) of a random-stabilizer state, as expected. In comparison, the same quantity for the nearest-neighbor circuit is far from the saturation of the limit (green, inset). c. The mean entropy deficit $\langle S^{(2)}(A)\rangle$ for different subsystem sizes and different system sizes ($N = 16$, 32, 64, 128, and 256, light to dark) at $t = \log_2 N$. Despite the finite size effect on $N = 16$, for all the system larger than $N = 16$ shows the saturation of the Page-Clifford limit (black dotted) from the below. d. The fraction $f_{\epsilon,|A|}$ of random subsystems A with $\langle S^{(2)}(A)\rangle / \ln 2 = \epsilon$, for $\epsilon = 0, 1, 2, 3$. $\epsilon = 0$ means that subsystem is maximally entangled with Renyi entropy $S^{(2)}(A) = |A| \ln 2$ (white circles). As shown, the configurations with large ϵ is exponentially suppressed, and the distribution agrees with the Page-Clifford limit (c.f. Appendix D and Appendix E, vertical bars, dark to light). The error bars are shown, or if not, then they are smaller than the markers. The gray shadowed region is the region where the noise from the sampling is not negligible. This figure was reproduced from [185].

6.6.2 Page-Scrambled State

We first show that $\mathcal{E}_\mathrm{s}$ is a fast scrambling by showing that an initial product state is Page-scrambled in time $t = 2\log_2 N$ that scales logarithmically with the system size N. The state is said to be Page-scrambled when the entanglement entropy of any given subsystem A is, on average, no more than 1 bit off from its maximal possible value [53, 236] as formulated in Ch. 2.2.2.

Despite the restricted Hilbert space spanned by the Clifford circuits, this is also the case for random stabilizer states. In the case of Clifford circuits, the Page-Clifford limit is given by $\Delta 2^{2|A|-N}\ln 2 < 1$ for any given subsystem A of size less than $|A| < N/2$ (Appendix D and Appendix E). To show this explicitly, we show the time evolution of the average entropy deficit $\langle \Delta S^{(2)}(A)\rangle$. The difference between the theoretically maximal value of the Renyi entropy of a subsystem A:

$$\Delta S^{(2)}(A) = \max\{S^{(2)}(A)\} - S^{(2)}(A) = |A|\ln 2 - S^{(2)}(A), \tag{6.12}$$

where $S^{(2)}(A)$ is the Renyi entropy of order 2, $S^{(2)}(A) = -\ln \mathrm{Tr}[\rho_A^2]$ with $\rho_A = \mathrm{Tr}_{\bar{A}}\rho$ For the stabilizer states, they coincide with the von Neumann entropy, and it has the maximum value $|A|\ln 2$.

Fig. 6.8 a. shows the entropy deficit plotted over time for $|A| = N/2-1 = 63$ for the system size $N = 128$. The deficit of the circuit $\mathcal{E}_\mathrm{s}$ quickly approaches the random state limit, the Page-Clifford limit of $\frac{1}{4}\ln 2$ before the time hits $t = 2\log_2 N$, similarly to the randomly coupled all-to-all model—the prototypical fast scrambler [53]. This is the case for $|A| < N/2$, at $t = 2\ln_2 N$, as evident in Fig. 6.8 b., the limit (red line) is saturated at all scales for $\mathcal{E}_\mathrm{s}$ circuit (red diamond). Furthermore, this saturation is consistent in all the subsystem sizes and all the system sizes that we investigated (Fig. 6.8 c.).

This result must be compared to the nearest-neighbor model (green dotted in inset), where the average entropy of a subsystem approaches linearly in time to the limit (Fig. 6.8 a., green); and at $t = 2\ln_2 N$ it is far from the limit in all sizes (Fig. 6.8 b., inset, green). This is due to the area-law entanglement as a result of the linear geometry. The geometrical constraint is forbidding the saturation of the limit at early times.

The ability of $\mathcal{E}_\mathrm{s}$ to delocalize the quantum information is more apparent in how the entropy of the random subsystems are distributed. Due to the property of the Clifford algebra, the entropies and hence the deficits are discrete quantities which come in bits $\langle \Delta S^{(2)}(A)\rangle / \ln 2 = \epsilon = 0, 1, 2, \cdots$. Shown in Fig. 6.8 d. is the distribution of the entropy deficit $\Delta S^{(2)}(A)$ of subsystems with the fixed size (white circles). It is clear that the fraction $f_{\epsilon,|A|}$ of the subsystem of size $|A|$ with the deficit ϵ is maximum at $\epsilon = 0$ and those with large deficit are exponentially suppressed for the subsystem size $|A| < N/2$. Furthermore, for all the system sizes, they are in the excellent agreement with the Page-Clifford limit.

6.6.3 Hayden-Preskill Experiment

In the previous section we have shown that circuit $\mathcal{E}_{\mathrm{s}}$ can scramble a z-polarized product state in order $\mathcal{O}(\log N)$ operations. In this section, we show that this is also the case for any initial state by investigating the teleportation property of the circuit $\mathcal{E}_{\mathrm{s}}$. The Page-scrambling, which was investigated in the previous section, implies that in order to recover a bit of information introduced to the initial pure state, one must collect $N/2$ qubits. In the context of black holes, the observer must wait for half of the black hole to evaporate in order to recover a bit of information fallen into the black hole [53]. The time takes for retrieving the quantum information, therefore increases polynomially with the system size N.

However, the information retrieval time can be faster when an observer has knowledge about the state of a black hole. The important revelation by Hayden and Preskill [59, 181, 182, 328] is that when the observer knows the state of the black hole, the information retrieval time becomes equivalent to the time it takes for information to be scrambled across the system. As a result, the fast scramblers, or black holes, immediately reflect quanta of information back into the environment in time $t = \mathcal{O}(\log N)$.

Following the original Hayden-Preskill experiment [59] (Fig. 6.9 a.), we perform a simple protocol which mimics a scrambling and evaporation dynamics of the black hole. We first create Einstein-Podolsky-Rosen (EPR) pairs between Bob's qubits B and the qubits into the black hole (scrambler(). Here, a black hole-like fast scrambler is simulated with the strongly scrambling quantum channel $\mathcal{E}_{\mathrm{s}}$. Then Alice also dumps her entangled pair into the black hole, making the total number of qubits which the circuit evolves to be $N = |A| + |B|$. The initial state $|\Psi(0)\rangle$

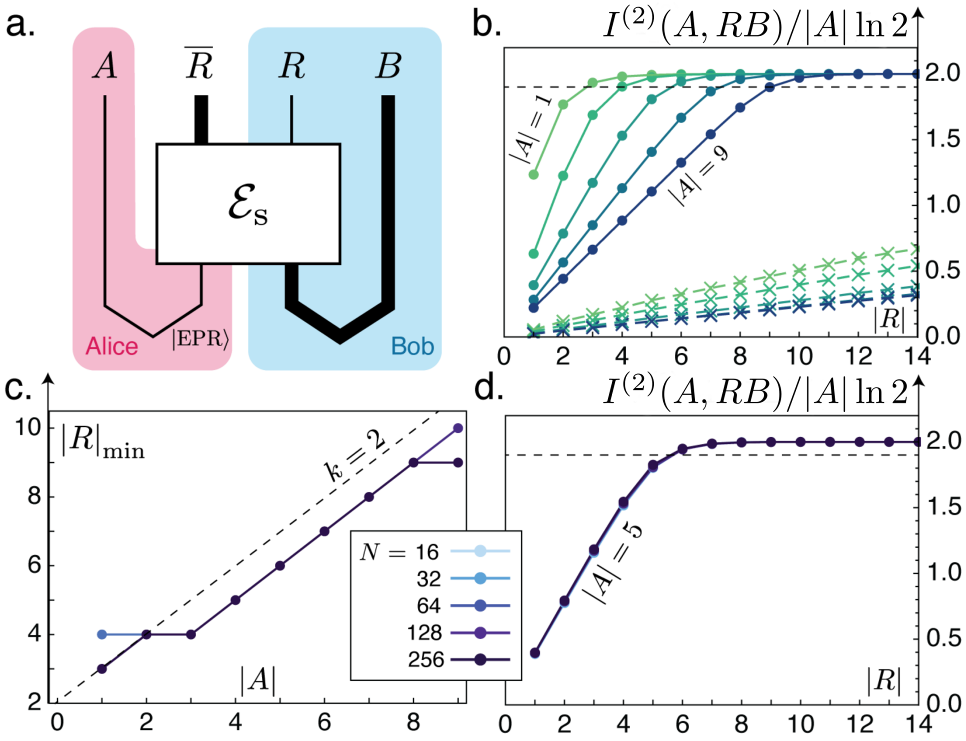

FIGURE 6.9: **Hayden and Preskill experiment performed with $\mathcal{E}_s$.** a. Hayden and Preskill experiment performed on $\mathcal{E}_s$. Alice and Bob throws half of the entangled qubit into the circuit. The scrambling in the circuit is characterized by the mutual information between Alice's qubit A (red) and Bob's qubits B and R (Blue), $I^{(2)}(A,RB)$, where R is chosen randomly from the output qubits. b. The mutual information $I^{(2)}(A,RB)$ and its dependence on the size of $|R|$ for $|A|=1,3,5,7,9$ (light to dark) for $N=128$. In the scrambling circuit $\mathcal{E}_s$, the mutual information rapidly increases and saturates to the maximum value $\max\{I^{(2)}(A,RB)\}/\ln 2 = 2|A|$ as soon as the size of $|R|$ becomes of order of the size of Alice's qubits $|A|$ (solid). Meanwhile $I^{(2)}(A,RB)$ for the nearest neighbor circuit, such a saturation is not observed in the regimes where $|R| \sim |A|$ in such an early time (dashed). c. The minimum $|R|_{\min}$ required for $I^{(2)}(A,RB)$ to reach 95% of its maximum value (black, dotted in b.) is plotted for different $|A|$ and different $N=16,32,64,128,256$ (light to dark). For sufficiently large system size $|A|/N \ll 1$, we observe Bob only requires $|R|_{\min} \geq |A|+k$ from the output to recover Alice's information. $I^{(2)}(A,RB)$ shows strong collapse over the multiple magnitudes of system sizes $N=16,32,64,128$ (light to dark) at fixed $|A|=5$ (light to dark). The quantities are calculated by averaging over up to 2×10^4 random subsystems R. Error bars are smaller than the markers, lines are guide to the eye. This figure was reproduced from [185].

is, therefore, given by

$$|\mathbf{\Psi}_0\rangle = \prod_{i=0}^{N-1} |\phi_i\rangle \tag{6.13}$$

$$|\mathbf{\Psi}_{\text{out}}\rangle = I_A \otimes \mathcal{E}_s \otimes I_B \, |\mathbf{\Psi}_0\rangle \,, \tag{6.14}$$

where

$$|\phi_i\rangle = \begin{cases} \frac{1}{\sqrt{2}} |\uparrow_{\text{bh}} \uparrow_{\text{A}}\rangle + |\downarrow_{\text{bh},i} \downarrow_{\text{A}}\rangle & (i < |A|) \\ \frac{1}{\sqrt{2}} |\uparrow_{\text{bh}} \uparrow_{\text{B}}\rangle + |\downarrow_{\text{bh},i} \downarrow_{\text{B}}\rangle & (|A| \leq i) \end{cases}. \tag{6.15}$$

Here A is a set of qubits held by Alice that are entangled to the black hole. The black hole, in this context, is simulated with the deterministic fast scrambling circuit $\mathcal{E}_{\text{s}}$, while Alice and Bob hold their part of the qubits in the vacuum.

Our interest is whether Bob can retrieve the Alice's quantum information from the randomly chosen sets of qubits R from the output state after evolving the Black Hole's qubits with $\mathcal{E}_{\text{s}}$ for time $t = 2\log_2 N$. We quantify this by computing the mutual information $I^{(2)}(A, RB)$ between the qubits which Alice holds (A) and the qubits which Bob holds (the radiation from the hole R and Bob's pair of qubits B):

$$I^{(2)}(A, RB) = S^{(2)}(A) + S^{(2)}(RB) - S^{(2)}(ARB), \tag{6.16}$$

where $S^{(2)}(X) = -\ln \text{Tr}\rho_X^2$ are the Renyi entropy of order 2 as defined in the previous section. If the qubits RB has some information about the state which Alice has thrown in at the $t = 0$, then the mutual information gains a non-zero value up to its maximum value,

$$\max\{I^{(2)}(I, RB)\} = 2|A| \ln 2 \qquad\qquad (\text{for } |A| < |B|). \tag{6.17}$$

As shown in Fig. 6.9 b., the mutual information $I^{(2)}(A, RB)$ between Alice's qubit A, and the Bob's qubits R and B reaches its maximum value as soon as Bob possesses the fraction of output qubits which is comparable to the amount of qubits which Alice has dumped $|R| \sim |A|$ (solid), while the nearest-neighbor circuit does not show such a rapid saturation (dotted). Furthermore, for sufficiently small $|A|/|N| \ll 1$, the number of output qubits $|R|$ required to recover the information that Alice has held, is system size independent (Fig. 6.9 c.). In this regime, the number of excess qubits k required to recover 95% of Alice's qubits, $|R| = |A| + k$, becomes constant $k = 2$. The scaling collapse is also observed over the multiple magnitudes of system sizes for $|A| = 5$ (Fig. 6.9 d.), which further confirms that this behavior is robust to finite-size effects.

6.7 Conclusion and Outlook

In this chapter, we investigated the circuit dynamics of the sparsely coupled model. Similarly to the previous proposals on the continuous time model discussed in Ch. 5, we introduced a tunable parameter s, which controls the probability of applications of the two-qubit gates as a function of distance. Consistent with the continuous model, we found that entanglement structure of the output states of the random sparsely coupled model possess the two incompatible geometries in the large $1 \ll |s|$ limit. Those limits are linear geometry for $s < 0$, and treelike geometry for $s > 0$. In those regimes, the single qubit scrambling time is polynomial in the geometry that is consistent with the locality of the entanglement structure.

For $|s| < 1$, we observed the transition in geometry, where, in this regime, the locality is no longer well-defined in both geometries. In this regime the single qubit scrambling time asymptotically approaches to $t_0 = \mathcal{O}(1)$ constant, and the lightcone is no longer defined clearly. This is also confirmed by $t_c = \mathcal{O}(1)$ single qubit teleportation time, These strongly suggests that at $s = 0$, the sparsely coupled circuit is also fast scrambling.

While it is clear that there exists three regimes of s with different underlying geometry, the nature of the transition between local regime $|s| > 1$, with a linear lightcone, and the fast scrambling regime $|s| < 1$ is not clear. Using the quantities such as tripartite mutual information or teleportation time t_c, one may find a phase transition between the local regime to the fast scrambling regime. The field theoretical, analytical investigation, such as quantum Brownian motions models and fermionic models, on the sparsely coupled models may also provide further insight into the nature of this transition [341, 342].

To further confirm the fast scrambling property of the sparsely coupled model at $s = 0$, we also studied the deterministic iterative (Floquet) fast scrambling circuit $\mathcal{E}_\mathrm{s}$ on a sparsely coupled graph. The circuit consists of $2\log_2 N$ parallel layers of two-qubit gates. We have shown that this deterministic circuit can create Page-scrambled state, after one iteration of $\mathcal{E}_\mathrm{s}$, similarly to a prototypical fast scrambler of randomly coupled all-to-all circuit. Furthermore, the Hayden and Preskill type teleportation experiment performed with $\mathcal{E}_\mathrm{s}$ has shown large mutual information between the qubits thrown in to the circuit by Alice and decoder qubits held by Bob after one circuit iteration. These logarithmic scaling in both scrambling time and teleportation time confirms that sparsely coupled circuit at $s = 0$ is a fast scrambler even with the deterministic sets of two-qubit gates.

The circuits that are studied in this chapter can be realized in the near term experiments with Rydberg atoms and shuffling using optical tweezers, for small system sizes $N \sim \mathcal{O}(10)$ [102]. Although scaling this to hundreds and thousands of qubits is a challenge, a magnitude increase in the system size $N \sim \mathcal{O}(100)$ is hoped to be achieved at $s = 0$ by using fully deterministic iterative (Floquet) circuit $\mathcal{E}_\mathrm{s}$. The first step of this scheme is already demonstrated [343].

The experimental realization of the fast scrambling circuit provides further insight into the connections between various fields of physics. They include: the fundamental speed limit on how fast information can spread [53, 81, 182, 206, 313, 314, 316], toy model for out-of-equilibrium physics of black holes [45, 48, 49, 53, 59, 257, 311, 312, 344–346], encoding and decoding of quantum information [181, 182, 236, 347], and quantum error-correcting codes [59, 347–350]. Although the circuits investigated in this chapter are all Clifford circuit, introducing the arbitrary amount of qubit rotations may be the interesting expansion to the proposal. It is hoped that this might be possible to realize in experiments in the near term future.

Part IV

Beyond the Unitary Dynamics

Chapter 7

Measurement-Induced Phase Transitions in Fast Scrambling Sparse Scramblers

God does not play dice.

Albert Einstein [351]

In the previous part of this thesis, we investigated the dynamics on a sparsely coupled model with tunable geometries. We showed that the fast scrambling dynamics emerges as the result of transition between the two geometries with incompatible notions of locality. In this chapter, we investigate further on the dynamics of the fast scramblers by probing the effect of random measurements. We especially focus on the nature of a phase transition called Measurement-Induced Phase Transition (MIPT), which occurs as a result of the competition between many-body scrambling, which creates entanglement between different parts of the system, and measurements, which destroys the entanglement. Here, we set a parameter p which tunes the probability of the projective measurements at each site per given time. In this phase transition, when p is smaller than a threshold probability $p < p_c$, the steady state will be composed of volume-law entangled states, while when p is larger $p_c < p$ then steady state is composed of area-law states.

The phase transition is also related to the system's ability of retaining the quantum information. The scrambling dynamics encodes quanta of information in the system as a nonlocal structure of entanglements (i.e. correlations), such that a locally introduced error can be detected and corrected by detecting the change in the structure. Quantum states with entanglement structure which uniquely identifies the introduced errors and reverse the errors are called Quantum Error-Correcting Codes (QECCs) [59, 123, 126, 154, 352]. In the context of the measurement induced phase transition, the dynamical generation of QECCs are known to take place in the regime with infrequent local measurements, deep in the volume-law phase $p \ll p_c$ [123, 126].

The transition was discovered in and studied extensively for 1-D nearest neighbor models [119, 121–123], and later extended to long-range models such as the randomly coupled all-to-all model [123, 124]. In this chapter, we are interested in the effect of determinism and long-range coupling on the MIPTs and the corresponding dynamically generated QECCs. The models that are investigated in this chapter are circuits on a family of deterministic circuits on a sparsely coupled graph. Similarly to the last part, in this model qubits are coupled if and only if they are separated by the distances $d_\infty(i,j) = |i-j|$ which are integer powers of 2. In addition, we introduce a tunable parameter q, which controls the locality of the interaction by truncating any interaction with distance longer than $2^q \leq d_\infty(i,j)$. For $q = \log_2 N$, as established in the last part, the circuit is fast scrambling; and hence by tuning the value of q, we investigate how the nature of MIPTs changes from the regime where circuit is slow scrambling ($q = 1$), to the regime where it is fast scrambling ($q = \log_2 N$).

We find that introduction of the extra long-range couplings significantly increases the critical point, while the critical properties retain the universality of the usual one-dimensional models. Furthermore, critical point of the transition can be close to that of the randomly all-to-all models, while only having fewer than $\mathcal{O}(10)$ interactions per site. The similar result also yields for the code distance, where the code distance becomes extensive for the full $q = \log_2 N$ depth circuit. The results show that the circuit that are robust to noise can be generated efficiently, deterministically, and iteratively with $\mathcal{O}(\log N)$ couplings per site; and the generated error-correcting code is robust to the local decoherence. The sparse, deterministic circuits with projective measurements discussed in this chapter can be implemented with the scheme discussed in Ch. 6.5.

Parts of this chapter are reproduced from sections that were written by the author of this thesis in the following publication: T. Hashizume, G. Bentsen, and A. J. Daley, "Measurement-induced phase transitions in sparse nonlocal scramblers," *Physical Review Research*, **4** 013174 (2022). [186].

7.1 Introduction

Measurement-Induced Phase Transitions (MIPTs) [119, 121–124] are transitions driven by a competition between scrambling dynamics, which generate entanglement across the system, and local measurement which tend to destroy the entanglement. Those transitions have generated theoretical interest in recent years [119–124, 151, 152, 156, 157] for their connection to the role of underlying geometry, as the measure of the system's robustness to the noise, and dynamical generation of error-correcting codes [123, 126]. The transition has been extensively studied on nearest neighbor models, and extended to the systems with long-range interactions [124, 353]. The transitions also have implications for the purification dynamics, where beyond the critical point, an initial mixed state gets purified after sufficiently long time. Such a transition is observed experimentally with trapped ions [123, 354].

Generation of many-body entangled states through evolution of simple quantum states, especially generating useful quantum states that can be used as a resource for quantum computing [66, 134, 135, 355, 356], or interesting many-body entangled states, has always been one of the goals of the experiments. However, generation of such complicated states is a challenge due to the noise which inevitably destroys the entanglement. Therefore, it is important to find ways to generate entanglement efficiently in a minimal implementation.

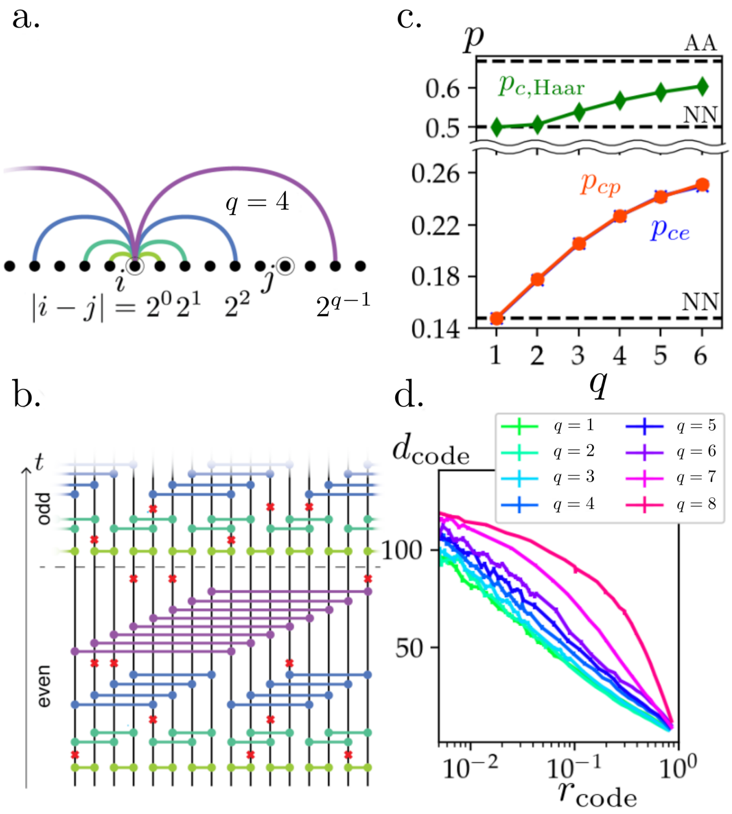

FIGURE 7.1: **Sparse fast scrambling PWR2$_q$ circuits with tunable nonlocality q subjected to random projective measurements.** a. and b. Two-qubit entangling gates Q_{ij} (green, turquoise, blue, purple) are applied between qubits i, j if and only if they are separated by an integer power of 2, $|i - j| = 2^{m-1}$ for $m = 1, \cdots, q$. These gates are applied in consecutive interaction layers at times $t = 1, \cdots, T$ in a nonlocal brickwork pattern arranged into alternating even and odd blocks. Projective single-qubit measurements (red crosses) occur with probability p between each interaction layer. The degree q of the resulting interaction graph (b) controls the nonlocality of interactions where the longest-range interactions occur between qubits initially separated by $d_{\max} = |i - j| = 2^{q-1}$. c. The critical measurement rates for the purification transition p_{cp} (red) and entanglement transition p_{ce} (blue) increase significantly with q, interpolating between the critical points found for random nearest neighbor (NN) models for $q = 1$ and random all-to-all (AA) models for larger q. Haar random circuits with identical coupling patterns show a similar improvement in robustness to measurement as q increases (green). d. In the mixed phase for $N = 256$ qubits, the maximum code distance d_{code} improves with q at fixed code rate r_{code}. Error bars are shown or are smaller than data points; lines are guides to the eye. This figure was reproduced from [186].

In connection to the previous parts of this thesis, we are especially interested in the role which deterministic quantum circuit plays, and the effect of introduction of longer-range couplings, which tunes the underlying dynamical property of the circuit from slow scrambling to fast scrambling. Due to its feasibility for experimental realization (Ch. 6.5) and emerging fast scrambling dynamics in a fully nonlocal regime as discussed in the previous part of this thesis, we are interested not only in the effect of fast scrambling dynamics on MIPT, but also how locality in the model affects the transition points of MIPTs and the code properties of the dynamically-generated QECCs.

For the model in this chapter, we introduce a parameter, q, which truncates the interaction that are longer than the distance $2^q \leq d = |i - j|$, where i and j are integers $0, 1, \cdots, N-1$ assigned to each qubit in the system (Fig. 7.1 a.). In this setup, $q = 1$ corresponds to the nearest-neighbor circuit, which is a slow scrambler, and $q = \log_2 N$ is a circuit with gates applied to all the available couplings, which is shown to possess fast scrambling dynamics. We demonstrate that the addition of only a few sparse nonlocal interactions can significantly improve the system's robustness to entanglement destroying operations, which leads to the significant increase in the critical measurement probability p_c. Furthermore, we show that the code distance of the dynamically-generated code in full deterministic sparsely coupled circuit with $q = \log_2 N$ becomes extensive in the system size N, similarly to the random all-to-all circuit (AA).

In this chapter, we probe three different types of MIPTs and the dynamically-generated error corrected codes in a family of circuits on a sparsely coupled graph. Firstly, in §7.2 we begin by defining the deterministic PWR2_q circuit that is studied in this work. Then in §7.3 we study MIPT with Haar random gates, by mapping the system to the classical percolation problem. In §7.4 we study the entanglement transition numerically in PWR2_q circuits with Clifford gates by looking at a tripartite mutual information $I(A : B : C)$ between three contiguous regions of the output qubits. In §7.5 we study the purification transition numerically for the same Clifford circuits as characterized by the purification time τ of a single qubit. In §7.6 we numerically study the properties of the dynamically-generated QECC in the mixed phase, where we demonstrate that introduction of nonlocal couplings significantly improves the code distance d_{code}. In §7.7 we consider the full PWR2_q circuit with $q = \log_2 N$ and compare its behavior to AA circuit. Finally, in §7.8 we summarize our findings and discuss potential future works.

7.2 Models

In this chapter, we again study a family of circuits on a sparsely coupled graph, where qubits $i, j = 0, \cdots N-1$ are only coupled if and only if the distance $d_\infty(i,j) = |i-j|$ between them is an integer power of 2, as shown in Fig. 7.1 a. As shown in the last part, this sparse nonlocal interactions generate fast scrambling dynamics, and can be implemented in the near term experimental platforms such as atoms in single-mode cavities [102] or neutral atoms with optical tweezers [185].

The circuit we study is inspired by the deterministic Floquet fast scrambler discussed in Ch. 6.6, where we study sparse nonlocal Floquet circuits consisting of parallel application of pairwise nonlocal two-qubit gates $Q_{ij} = Q_{ji}$ in a brickwork pattern as illustrated in Fig. 7.1 b. The timestep $t = 1, \cdots, T$ is defined by a single layer of exactly $N/2$ gates, where they are stacked in the order of small distance $d = 2^0$ to large distance $d = 2^{q-1}$ for each "block" of circuit. These blocks of circuit have two types—even and odd—where on even blocks, the gates are only placed between qubits i and j where $\lfloor i/d \rfloor$ is even, and where $\lfloor i/d \rfloor$ is odd for odd blocks. Those even and odd blocks are stacked alternately.

After each interaction layer at time t, projective measurements in the Pauli-z basis are randomly applied to individual qubits with probability p (Fig. 7.1 b. red cross). These projective measurements destroy the entanglement in the state by projecting the state into either of the eigenstates of the Pauli-z operator. We counter this by introducing nonlocal interactions in order to protect the entanglement by inscribing them across wider part of the system. In the PWR2_q circuits, the degree of nonlocality is parameterized with $q \leq \log_2 N$, where the two qubits gates over the distances which excess $2^q \geq d = |i-j|$ are truncated. As a consequence, PWR2_q circuits with $2^q/N \ll 1$ consist only of short-range couplings where the speed of entanglement spread is limited by some velocity v by the Lieb-Robinson bound [81, 314]. When $2^q/N \sim 1$, on the other hand, the interactions become non-local and the dynamics becomes fast scrambling. Therefore, in this model, the nonlocality parameter q provides a means to interpolate the PWR2_q circuits from slow to fast scrambling regime.

Two limiting regimes of the circuit are compared, in this chapter, to the two models: the Nearest Neighbor (NN) model, which is identical to this model with $q = 1$, is a prototypical scrambling circuit which exhibits MIPT, and it is studied extensively [121–123]. In contrast, the random all-to-all circuit (AA) is a prototypical fast scrambler proposed by Susskind [53], where at each time step, two qubit gates are applied to random $N/2$ pairs of qubits in the system in parallel.

For the two-qubit gates Q_{ij}, in this chapter, we investigate the MIPTs using two different sets of gates. In §7.3, Q_{ij} is taken to be drawn from a set of Haar random unitary gates. This allows us to map the critical phenomena to the percolation problem, where above the percolation threshold $p_{c,\text{Haar}}$ implies that there is no causal connection between initial and final state. In §7.4 to §7.6, we take $Q_{ij} = \text{CZ}_{ij}H_iH_j$, where $\text{CZ}_{ij} = \text{CZ}_{ji}$ is the controlled-Z gate on qubits i, j, and H_i, P_i are the Hadamard and Phase gates on qubit i respectively. The gate Q_{ij} entangles the two qubits in the state $|00\rangle$. Since the gates Q_{ij} used in those sections belong to Clifford group, they can be classically simulated efficiently up to thousands of qubits [90, 117, 118, 149]. In next sections (§7.3 to §7.6), we show that for each of these cases, the rapid creation of entanglement across the system mediated by the nonlocal interactions significantly increases the critical points of MIPT and code distances of the dynamically generated codes.

7.3 Percolation Transition in Haar Random PWR2_q Circuits

To demonstrate that nonlocal sparse interactions can improve a system's robustness to local measurements, we first study PWR2_q circuits consisting of Haar random nonlocal gates Q_{ij} acting between pairs of qubits (c.f. Appendix A). The zeroth-order Renyi entropy $S^{(0)}(A) = \ln M(A)$ of this circuit, where $M(A)$ is the rank of the reduced density matrix ρ_A of region A is known to be equivalent to the minimum number of cuts that is required to isolate the output qubits in the tensor network [122, 123]. As illustrated Fig. 7.2 a., percolation mapping maps each of the two-qubit Haar random gates to a tensor (green) with four legs connecting input and output qubits (black), and the projective measurement that cuts the legs of the tensors (red cross).

As discussed in Ch. 4.3.1, the mapping can be done because whenever a qubit in A is entangled with the environment, the effect is to increase the rank of ρ_A by a factor of 2, since applying a Haar random gate between two uncorrelated qubits almost always entangles them. In contrast, the projective measurements in the subsystem A destroy the entanglement, thus they reduce the rank by a factor of

2. Therefore, the number of factor 2 increase in $M(A)$ can be calculated simply by counting the legs which come out from the region A in the output qubits.

In the two limiting cases of the measurement probability p, we expect at $p = 0$ the tensor network has no cuts, and the minimal cut required is proportional to the volume of the region A; and at $p = 1$, there exists no bonds in the network, therefore, one does not need to cut any bonds to isolate A, and hence the rank $M(A)$ is $2^0 = 1$. Therefore, there must exist some threshold $p_{c,\mathrm{Haar}}$ which separates a regime where there exists connection between the initial qubit and output qubits, making the entropy to be proportional to the volume of (i.e. the number of qubits in) A, and a regime where there is no causal connection between initial and final states of the qubit due to excessive measurements.

The problem which asks the existence of the large clusters of sites connected by bonds in one end to the other end of a system is known to be a bond-percolation problem [122, 154, 357, 358]. In the thermodynamic limit, $\lim N \to \infty$, and for extensive time $T = \mathcal{O}(N)$, the transition point $p_{c,\mathrm{Haar}}$ corresponds to a threshold probability where below it, the network has at least one connected component of infinite extent.

Classical bond-percolation transitions of this type are well-studied in the literature [357], including on a wide variety of local and nonlocal networks [359, 360]. In the extreme local case of nearest-neighbor interactions (i.e. $q = 1$ in the PWR2_q family), the percolation mapping yields a bond-percolation problem on a two-dimensional square lattice, whose critical properties are known analytically [357, 361]. Near the critical point $p_{c,\mathrm{Haar}}^{\mathrm{NN}} = 1/2$, one can naturally define a correlation length ξ which captures the typical radius of connected components in the network. In this regime, the correlation length diverges algebraically like $\xi \sim |p - p_{c,\mathrm{Haar}}|^{-\nu}$, where $\nu = 4/3$ is the critical exponent [122, 357, 361].

The classical bond-percolation transition has also been studied in the opposite nonlocal limit where interactions become arbitrarily long-range. The percolation critical point of the random AA circuit was studied previously by Gullans and Huse [123] and more extensively by Nahum *et al.* [124]. The critical point of the AA network is known to be at $p_{c,\mathrm{Haar}}^{\mathrm{AA}} = 2/3$. Such a high critical point comes from the system's locally treelike structure in the limit of large system size, where the probability of the network having a local loop vanishes as $1/N$ [124].

7.3.1 Numerical Method for Simulating Bond Percolation

In order to find the critical point $p_{c,\text{Haar}}$ for each value of q, we numerically simulate bond-percolation on the corresponding network using the Newman-Ziff algorithm [358]. This algorithm calculates the various observables at different values of the bond occupation probability $\bar{p} = 1 - p$ in a computational time which scales only linearly with the number of bonds M in the network.

The algorithm proceeds by generating random configurations of a given network with $m = 1, 2, \cdots, M$ bonds being occupied; where this is done by adding one random bond at each step starting from an empty network. At each step of this process, one can keep track of the sizes of the connected components (clusters) in the network with the Union-Find algorithm [362, 363]. Observables such as cluster sizes and their moments can then be stored at the end of each step of the algorithm. The observable Q as a function of the bond occupation probability $\bar{p}$ can then be calculated by taking the microcanonical ensemble of the different configurations:

$$Q(\bar{p} = 1 - p) = \sum_m B(m, M, \bar{p}) Q_m = \sum_m \binom{M}{m} \bar{p}^m p^{M-m} Q_m, \tag{7.1}$$

where Q_m is the value of observable Q with m occupied bonds and $\binom{M}{m} = \frac{M!}{m!(M-m)!}$ is the binomial coefficient.

The calculation of the binomial distribution $B(m, N, \bar{p})$ is numerically unstable because one requires evaluations of the factorials of large numbers and addition of numbers which differ largely in their order of the magnitudes. Here we adopt a more stable method for evaluating the microcanonical ensemble introduced by Newman and Ziff [358]. If we normalize the binomial distribution by its peak value $m_{\max} = \bar{p}M$, this normalized binomial distribution $\tilde{B}(m, M, \bar{p})$ is defined recursively as

$$\tilde{B}(m, M, \bar{p}) = \begin{cases} \tilde{B}(m-1, M, \bar{p}) \frac{M-m+1}{m} \frac{\bar{p}}{1-\bar{p}} & (m > m_{\max}) \\ \tilde{B}(m+1, M, \bar{p}) \frac{m+1}{M-m} \frac{1-\bar{p}}{\bar{p}} & (m < m_{\max}) \end{cases}. \tag{7.2}$$

Therefore, the observable of interest can be calculating the following

$$Q(\bar{p} = 1 - p) = \frac{\sum_{m'} \tilde{B}\left(m', M, \bar{p}\right) Q_m}{\sum_{m'} \tilde{B}\left(m', M, \bar{p}\right)}. \tag{7.3}$$

7.3.2 Results

Here we interpolate between these two extreme limits using the nonlocality parameter q in the Haar random PWR2$_q$ circuit family, where $q = 1$ corresponds to the NN case and $q \sim \log_2 N$ approaches the AA case. The critical point $p_{c,\text{Haar}}$ and the critical exponent ν of the correlation length can be identified by calculating the Binder cumulant [364, 365],

$$b(p) = \frac{1}{2}\left(3 - \frac{\langle C_{\max}^4(p)\rangle}{\langle C_{\max}^2(p)\rangle^2}\right), \tag{7.4}$$

where $C_{\max}$ is the maximum cluster size in the nonlocal percolation network and $\langle\cdots\rangle$ denotes the averaging over different configurations of randomly-cut bonds. Near the critical point, we expect the Binder cumulant to obey the scaling law [364–366]

$$b(p) = f\left((p - p_{c,\text{Haar}})N^{1/\nu_{\text{Haar}}}\right), \tag{7.5}$$

which is governed by the same critical exponent ν that controls the divergence of the correlation length ξ near the critical point.

We plot the results of these numerical simulations in Fig. 7.2 b., for $q = 1, 3, 5$ across system sizes $N = 64, \cdots, 1024$ (light to dark blue). To extract the critical point $p_{c,\text{Haar}}$ we plot the Binder cumulant $b(p)$ (insets of Fig. 7.2 b.) and locate the crossing point as a function of system size N. At each fixed q in this analysis, we only consider the crossing point for sufficiently large system sizes $N > 2^q$, such that the longest-range interactions $d_{\max} = 2^{q-1}$ are never extensive. We then fit the scaling form Eq. (7.5) to the data near the critical point and use this to extract an estimate of the critical exponent ν_{Haar} for each value of q. Our resulting estimates for the critical point and critical exponent can be used to collapse the Binder cumulant $b(p)$ near the critical point to a single universal curve Eq. (7.5) as shown in the main panels of Fig. 7.2 b.

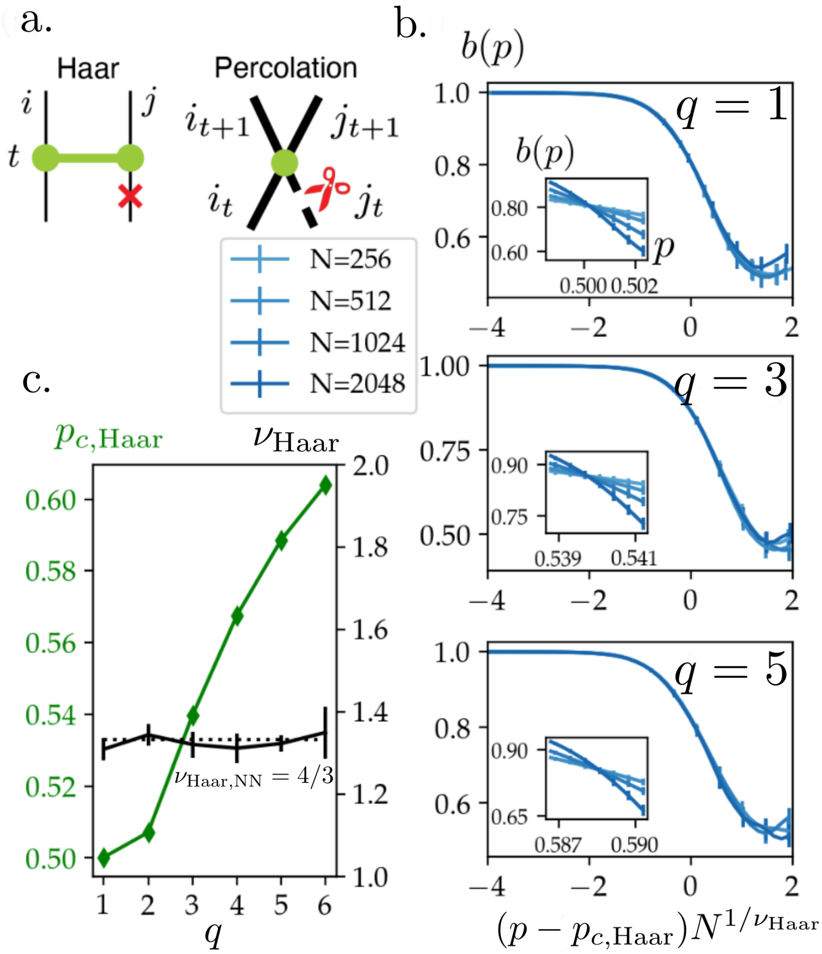

FIGURE 7.2: **Measurement-induced transitions in the PWR2$_q$ circuit family with Haar random gates.** a. Nonlocal circuits featuring Haar random gates can be mapped to a classical percolation network, where gates in the original circuit (green) correspond to sites in the percolation network, and projective measurements in the Haar random circuit (red crosses) correspond to cut bonds in the percolation network. b. The Binder cumulant $b(p)$ of the maximum cluster size in the classical percolation network for $q = 1, 3, 5$ (top to bottom) and system sizes $N = 256, 512, \cdots, 2048$ (light to dark blue). The critical point $p_{c,\mathrm{Haar}}$ is extracted from the crossing point of $b(p)$ across finite-size systems (insets). We observe good scaling collapse with critical exponent $\nu_{\mathrm{Haar,NN}} = 4/3$ (black dotted in c.) expected for a 1+1D NN circuit even for large nonlocality q. c. The percolation critical point $p_{c,\mathrm{Haar}}$ (green) increases with q; the critical exponent ν_{Haar} (black) is nearly constant as q varies, indicating that these nonlocal circuits near criticality likely belong to the same universality class for all $q < \log_2 N$. Error bars are shown or are smaller than markers; lines are guides to the eye. Detailed finite-size scaling analysis for all the values of q are provided in Appendix F.1. This figure was reproduced from [186].

We plot the resulting critical points $p_{c,\mathrm{Haar}}$ and critical exponents ν as a function of q in Fig. 7.2 c. The critical points clearly increase with nonlocality q; for $q \geq 5$, the critical point is closer to the AA limit than the NN limit. The critical exponent ν, on the other hand, appears to be largely independent of q and is consistent with the critical exponent $\nu_{\mathrm{Haar,NN}} = 4/3$ expected for a 1+1 NN model (Fig. 7.2 c., dotted black line). These results suggest that all Haar random PWR2_q models with $q < \log_2 N$ fall into the same universality class as the local 1+1D model in the thermodynamic limit. Nevertheless, these results also demonstrate that the critical point $p_{c,\mathrm{Haar}}$, a non-universal parameter, significantly increase with nonlocality q.

7.4 Entanglement Transition in Clifford PWR2_q circuits

The nonlocal classical percolation network we studied in the previous section demonstrated that just a few additional layers of nonlocal interactions can significantly increase the critical point of the Haar random PWR2_q circuit. In the following sections we turn our attention to deterministic nonlocal circuits composed entirely of Clifford gates. We choose interaction gates $Q_{ij} = Q_{ij} = \mathrm{CZ}_{ij} H_i H_j$ and show that the circuit's ability to withstand the destructive effects of local measurement is improved as a function of the nonlocality parameter q.

We begin our study of these nonlocal Clifford circuits by characterizing the entanglement at the output of the circuit as a function of the measurement rate p. We initialize the monitored PWR2_q circuit with a pure, separable z-polarized state, and find a phase transition in the tripartite mutual information $I(A:B:C)$ between three equal-size consecutive regions A, B, C of the output state as shown in Fig 7.3 a. The tripartite mutual information,

$$I^{(2)}(A:B:C) = I^{(2)}(A,B) + I^{(2)}(A,C) - I^{(2)}(A,BC), \tag{7.6}$$

is defined in terms of the mutual information $I^{(2)}(A,B) = S^{(2)}(A) + S^{(2)}(B) - S^{(2)}(AB)$, where $S^{(2)}(A) = -\ln \mathrm{Tr}\rho_A^2$ is the Renyi entropy of the subsystem A. Because the circuit consists entirely of Clifford gates, the Renyi entropy $S^{(2)}(A)$ is always equal to the conventional von Neumann entropy $S(A) = -\mathrm{Tr}\rho_A \ln \rho_A$, and we may therefore characterize the entanglement of the system entirely in terms of the Renyi entropies $S^{(2)}(A)$.

To extract the entanglement critical point p_{ce}, we perform a finite-size scaling analysis similar to the previous section. In Fig. 7.3 b., we plot the tripartite mutual information as a function of measurement rate p for various system sizes

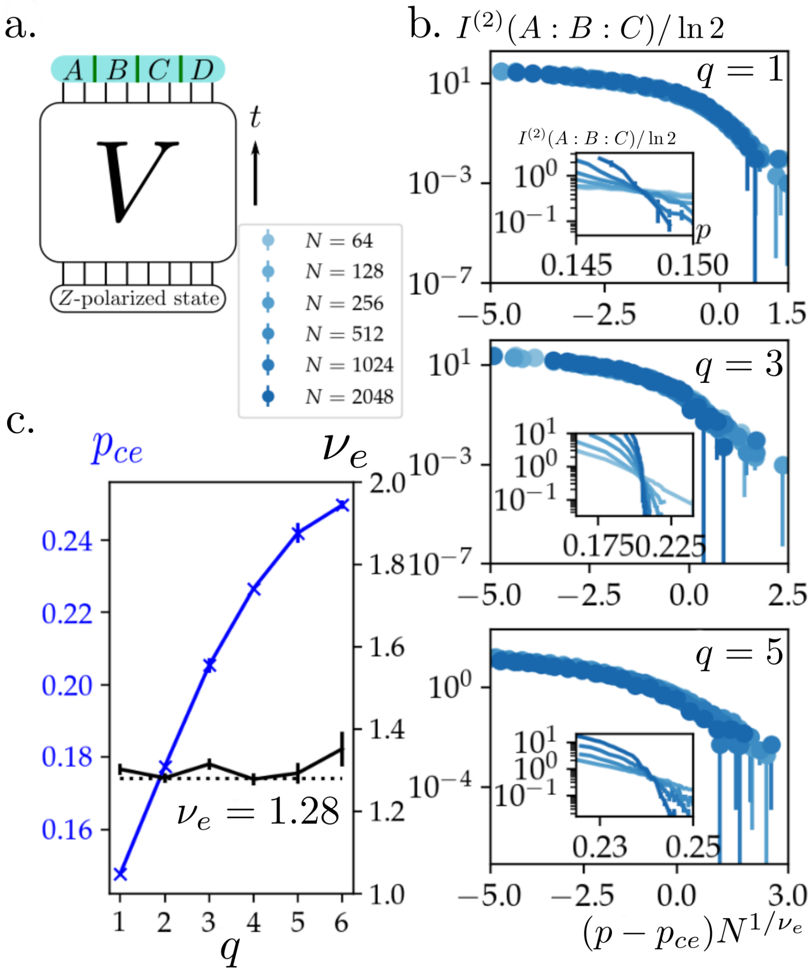

Figure 7.3: **Measurement-induced entanglement transition in the PWR2$_q$ circuit family with Clifford gates.** a. The circuit is initialized with a separable pure input state, while the output is divided into four equal regions A, B, C, D. b. Tripartite mutual information $I^{(2)}(A:B:C)$ for consecutive regions A, B, C in the PWR2$_q$ circuit for $q = 1, 3, 5$ (top to bottom) and system sizes $N = 64, 128, \cdots, 2048$ (light to dark blue). The critical point p_{ce} is extracted from the crossing point of Tripartite mutual information for $N = 64, 128, \cdots, 2048$ (insets); only sufficiently large system sizes $N > 2^q$ are used to estimate the critical point. Near p_{ce} we observe a scaling collapse with the critical exponent $\nu \approx 1.28$. c. The critical measurement rate p_{ce} (blue) increases significantly with q while the critical exponent ν_e (black) is consistent with the 1+1D critical exponent (dotted black) to within statistical fluctuations for all values of q. Detailed scaling analysis for all the values of q are provided in Appendix F.2. Error bars are shown or are smaller than data points; lines are guides to the eye. This figure was reproduced from [186].

$N = 64, 128, \cdots, 1024$ (light to dark blue). The critical point p_{ce} is determined by the crossing point of the tripartite mutual information across system sizes as shown in the insets of Fig. 7.3 b. Only sufficiently large system sizes $N > 2^q$ are used to extract the critical point. Near the critical point p_{ce} we expect the tripartite mutual information to obey the universal scaling law:

$$I^{(2)}(A:B:C) = f\left((p - p_{ce})N^{1/\nu_e}\right), \tag{7.7}$$

where f is a universal function and ν_e is the critical exponent of the correlation length ξ. After determining the critical point p_{ce} we fit this scaling form to each curve in Fig. 7.3 b. and use this to extract an estimate for the critical exponent ν_e. The resulting estimates for p_{ce} and ν_e allow us to collapse the original data down to a universal curve as shown in the main panels of Fig. 7.3 b. [123].

We plot the resulting estimates for the critical point p_{ce} and critical exponent ν in Fig. 7.3 c. for $q = 1, \cdots, 6$. Similar to our findings in the previous section, the non-universal critical point p_{ce} increases significantly with q. The critical exponent, however, is nearly constant across q, and is consistent with the critical exponent $\nu_e \approx 1.28(2)$ found numerically for $1 + 1D$ NN models [123] to within statistical fluctuations (Fig. 7.3 c.). This indicates that the measurement-induced transitions in these models likely fall into the same universality class as the completely local NN models. Nevertheless, the fact that the critical point p_{ce} increases with the nonlocality parameter q demonstrates that just a few additional layers of nonlocal interactions can substantially improve a circuit's ability to retain complex many-body entanglement even in the presence of local measurements, similar to our observations in the previous sections.

7.5 Single-Qubit Purification in Clifford $\mathrm{PWR2}_q$ Circuits

Another measure of a circuit's robustness to measurements is the timescale τ required to purify a single qubit that has been entangled with the system [125, 130]. In the absence of any measurements such a qubit will remain entangled with the system forever, but carefully-placed projective measurements can destroy the entanglement between the system and qubit, causing the qubit to collapse into a pure state. The typical timescale τ required for this purification process to occur can be used to characterize our circuit's ability to retain quantum information encoded in the initial state when subjected to noise. In particular, below a critical measurement rate $p < p_{cp}$ we expect the purification time to become extensive

$\tau \sim N^z$, indicating that quantum information can be robustly stored in the circuit despite the presence of repeated projective measurements at a rate p.

Although for nearest-neighbor circuits the purification critical point p_{cp} coincides with the entanglement critical point p_{ce}, we emphasize that these transitions can generically be different, as has been pointed out in the literature [123]. We are especially interested whether highly nonlocal circuits support an intermediate phase in between the two critical points, p_{cp} and p_{ce}, where the reference qubit has been purified, but where there is nevertheless still volume-law entanglement in the final state.

Here we study the possibility of such an intermediate phase in our nonlocal PWR2_q circuits by determining the single-qubit purification time τ. To determine the purification critical point p_{cp}, we maximally entangle a single reference qubit R with the system Q and apply $t = 4N$ layers of a unitary NN circuit to the system such that the qubit of information is scrambled deeply within the system [130] (Fig. 7.4 a., $U_{\text{thermalizer}}$). Then the monitored PWR2_q circuit is applied as illustrated in Fig. 7.4 a. At the end of each timestep t we compute the Renyi entropy $S^{(2)}(Q)$ of the system. The single qubit purification time τ is the number of timesteps required for the Renyi entropy to vanish from its initial value of $S^{(2)}(Q) = \ln 2$.

To extract the critical point p_{cp} for each $q < \log_2 N$ we perform a scaling analysis as shown in Fig. 7.4 b. for $q = 1, 3, 5$. Similar to the analysis of previous sections, the critical point is determined by the location of the crossing point of $\tau(p)$ as the system size N is varied, as shown in the insets of Fig. 7.4 b. The critical points p_{cp} obtained from this analysis are plotted in Fig. 7.4 c. and grow significantly with $q = 1, \cdots, 6$ in agreement with earlier analysis. In each of these cases the critical point p_{cp} of the purification transition agrees with the entanglement critical point p_{ce} within error bars. This strongly suggests that for $q < \log_2 N$ the critical points p_{cp}, p_{ce} are in fact identical and that there is no intermediate phase between the purification and entanglement phases [123].

Near the critical point, we expect the purification time to obey the universal scaling law

$$\tau(p) = N^z f\left((p - p_{cp})N^{1/\nu_p}\right), \tag{7.8}$$

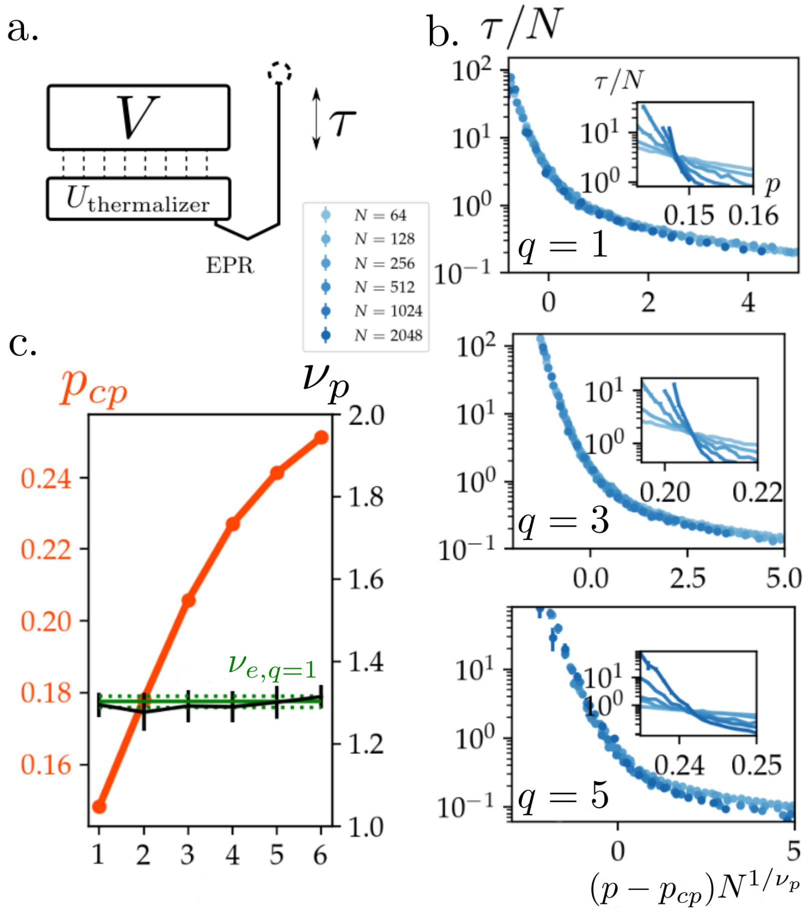

FIGURE 7.4: **Single-qubit purification transition in the PWR2$_q$ circuit family with Clifford gates.** a. Schematic diagram for single-qubit purification. b. Finite-size scaling for single-qubit purification time τ in the PWR2$_q$ circuit for $q = 1, 3, 5$ (top to bottom) and system sizes $N = 64, 128, \cdots, 2048$ (light to dark blue). Main figures show scaling collapse with critical exponent $\nu_p \sim 1.30$ and dynamical critical exponent $z = 1$ for $q = 1, 3, 5$. The critical point p_{cp} is determined by the crossing point of $\tau/L^{z=1}$ across system sizes $N > 2^q$ (insets). c. The purification critical point p_{cp} increases as a function of q, closely mirroring the increase in the entanglement critical point p_{ce} found in the previous section. The critical exponent, on the other hand, agrees with the ν_e for $q = 1$ ($v_{e,q=1}$, green) found in the entanglement criticality in the previous section within the error (green solid line, with 1-sigma fluctuations indicated by the green dashed line). Error bars are shown or are smaller than the data points; lines are guides to the eye. Detailed finite-size scaling analysis for all the values of q are provided in Appendix F.3. This figure was reproduced from [186].

where z is the dynamical exponent and ν is the critical exponent of the correlation length ξ. Based on our findings in previous sections, we expect the purification transition studied here for $q < \log_2 N$ to be in the same universality class as the purification transition in 1+1D NN models, which are believed to be governed by a conformal field theory with dynamical exponent $z = 1$ [122, 123, 130]. We therefore assume $z = 1$ and use the scaling form (7.8) to fit the data plotted in

Fig. 7.4 b. These fits yield estimates for the critical exponent ν_p, which we plot in Fig. 7.4 c. The resulting critical exponents $\nu_p = 1.30 \pm 0.02$ are largely independent of q and agree with the critical exponent of the entanglement transition v_e of the 1+1D NN model. This consistent with previous results showing that the critical behavior of the PWR2_q with fixed $q < \log_2 N$ is in the same universality class as the conventional 1+1D MIPT.

7.6 Quantum Error-Correcting Code Properties

Below the critical measurement rate $p < p_c$, the mixed phase is underpinned by a dynamically-generated Quantum Error-Correcting Code (QECC) [126, 156, 157, 352]. The improvement in the critical measurement rates $p_{c,\mathrm{Haar}}, p_{cp}, p_{ce}$ as a function of q observed in the previous sections suggests that circuits with highly nonlocal interactions generate improved quantum error-correcting codes in the mixed phase. An important characteristic of any QECC is its *code distance*, which is the smallest number of single-qubit errors required to transform any code state into any other—equivalently, the code distance is the minimal weight of all nontrivial logical operators. Here we estimate the contiguous code distance d_{code} for our nonlocal Clifford circuits, and show that the improved robustness to local measurements observed in the previous sections also generates QECCs with improved code distance.

To characterize a QECC in the mixed phase, we maximally entangle the system Q with a reference system R and study the Renyi entropy $S_R^{(2)}$ of the reference as well as the mutual information $I^{(2)}(A, R)$ between the reference and a subset $A \subset Q$ of the output qubits as shown in Fig. 7.5 a. In the language of quantum error-correction, the Renyi entropy determines the *code rate* $r_{\mathrm{code}} = S^{(2)}(R)/N \ln 2$ of the PWR2_q Clifford circuit, or the number of logical qubits that are encoded within the N-qubit system Q. We plot r_{code} as a function of p in Fig. 7.5 b.. for $N = 256$ and find that the code rate substantially improves with nonlocality $q = 1, \cdots, 8$ at any fixed measurement rate p, consistent with previous results. From Fig. 7.5 b., it is clear that for any fixed q, our choice of measurement rate $p < p_c$ below the critical point determines the code rate r_{code} of the underlying QECC.

We can also study the contiguous code distance d_{code} of the QECC in the mixed phase by analyzing the mutual information $I^{(2)}(A, R)$ between the reference R and subregions $A \subset Q$ of the system as shown in Fig. 7.5 a. [352]. For sufficiently small subregions A in the mixed phase $p < p_c$, one generically finds vanishing mutual information $I^{(2)}(A, R) = 0$, indicating that the region A contains no information about the reference R. In this circumstance we may safely discard any of the qubits in A and still reliably recover the quantum information shared between the reference and the system. In the language of error correction, we can view the subregion A as a set of qubits that has possibly been corrupted by errors. So long as $I^{(2)}(A, R) = 0$ we may simply discard these corrupted qubits and still recover the information contained in R. On the other hand, sufficiently large subregions A will ultimately yield $I^{(2)}(A, R) > 0$, implying that sufficiently large errors can degrade the correlations between the system and reference. The crossover point $|A|^*$ at which the mutual information becomes nonzero provides an estimate of the system's code distance d_{code} [352].

To extract an estimate of the contiguous code distance d_{code}, we plot the mutual information $I^{(2)}(A, R)$ as a function of the subregion size $|A|/N$ and look for the crossover point $|A|^*$ where the mutual information increase by one bit $\Delta I^{(2)}(A^*, R) = \ln 2$ (Fig. 7.5 c.). The effective code distance is given by $d_{\text{code}} = \langle |A|^* \rangle$ where $\langle \cdots \rangle$ is an average over different realizations of projective measurements in the circuit. We plot the resulting effective contiguous code distance as a function of q in Fig. 7.5 d., which shows a striking improvement of d_{code} with increasingly nonlocal interactions q. Moreover, by tuning the measurement rate $p < p_c$ and the nonlocality parameter q we can obtain quantum error-correcting codes with a variety of code rates and code distances. For fixed q we find the expected tradeoff between code rate and code distance that is typical in quantum error-correcting codes. By increasing the nonlocality parameter q we generate codes with significantly improved code distance d_{code} for any fixed code rate r_{code}. In this sense, the nonlocal interactions for $q \sim \log_2 N$ substantially improve the quantum error-correcting code properties in the mixed phase.

7.7 Fully Nonlocal and All-to-All Models

So far, we have considered PWR2_q circuits at fixed $q < \log_2 N$ where the longest-range interactions $d_{\max} = 2^{q-1}$ have been strictly smaller than the system size N.

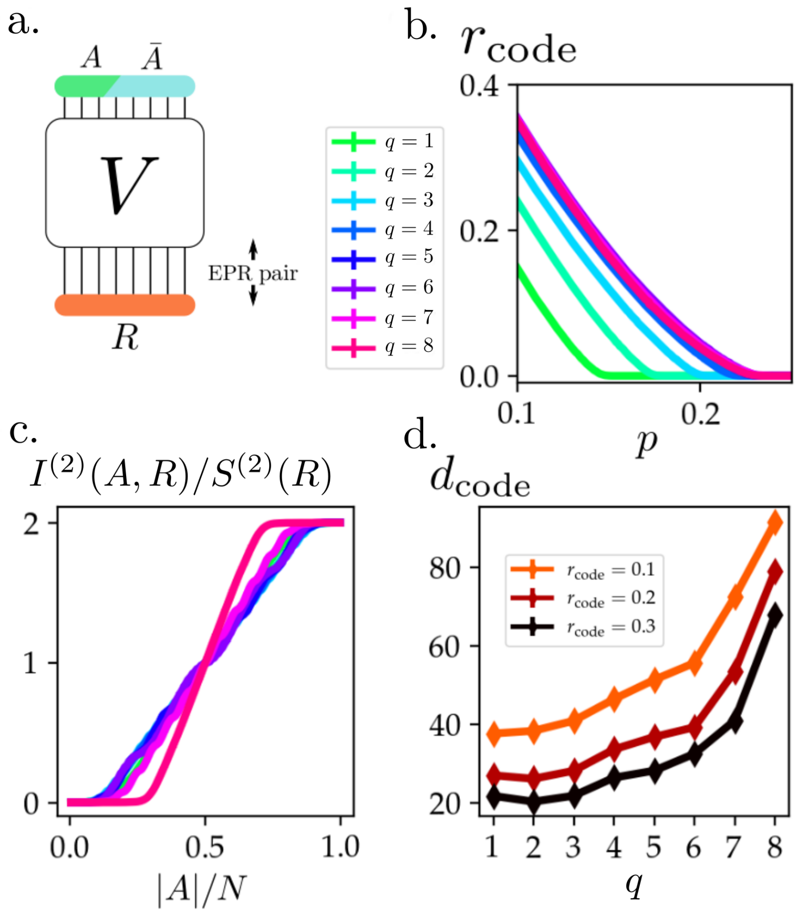

FIGURE 7.5: **Code rate and code distance for the PWR2$_q$ Clifford circuit family at time $t = 8N$.** a. To determine $r_{\text{code}}, d_{\text{code}}$, we examine the entropy $S^{(2)}(R)$ of a maximally-entangled reference R and the mutual information $I^{(2)}(A, R)$ between the reference and a subregion $A \subset Q$ of the output qubits. b. The code rate in the PWR2$_q$ circuit for $N = 256$ as a function of measurement rate p, improves significantly with q (green through red). c. Normalized mutual information as a function of subregion size for $p = 0.12$, deep in the mixed phase. The effective contiguous code distance d_{code} is determined by finding the minimum size of the linear bipartition $|A|$ to have the mutual information $I^{(2)}(A, \text{Ref.})$ of $\ln 2$. d. Code distance versus q at fixed code rates $r_{\text{code}} = 0.1, 0.2, 0.3$ (black, red, orange) for the system size $N = 256$. Error bars are shown or are smaller than data points; lines are guides to the eye. This figure was reproduced from [186].

In these cases we found that nonlocal interactions could substantially improve both the critical measurement rate p_c and the code distance d_{code} in the mixed phase. We now consider what happens in the 'complete' PWR2$_q$ circuit with $q = \log_2 N$, where the longest-range interactions $d_{\max} = N/2$ are extensive, and show that the behavior radically changes relative to the cases previously studied. In particular, the complete PWR2$_q$ circuit without measurements is known to be a fast scrambler capable of generating system-wide volume-law entanglement after only $t_* \propto \log N$ interaction layers [185]. In this section we demonstrate that the fast scrambling dynamics in this circuit leads to markedly improved code properties, including a nearly extensive contiguous code distance d_{code}. We also observe many similarities in this section between the complete PWR2_q circuit and a maximally nonlocal random AA model, another known fast scrambler which has no spatial geometry whatsoever. These similarities highlight the central role played by fast scrambling in determining the physics of the mixed phase in these circuits, and suggest that fast scrambling circuits may be governed by the same universal physics near the measurement-induced critical point.

We first study the complete PWR2_q circuit with Haar random gates, and numerically simulate the corresponding classical percolation network similar to §7.3. In that prior analysis we computed the Binder cumulant $b(p)$ of the network and estimated the critical point by fixing the parameter q and performing a finite-size scaling analysis in the system size N. In the present case, finite-size scaling is difficult to define consistently because the connectivity $q = \log_2 N$ of the graph is coupled to the system size N. Instead, we estimate a finite-size crossover point by computing the susceptibility,

$$\chi(p) = \langle C_{\max}^2(p) \rangle - \langle C_{\max}(p) \rangle^2, \tag{7.9}$$

of the resulting classical percolation network. In the thermodynamic limit, $N \to \infty$, the susceptibility diverges at the critical point; here we estimate the finite-size transition point by locating the peak $p_{\text{peak,Haar}}$ of the susceptibility $\chi(p)$ for each N.

The resulting finite-size crossover points are plotted in Fig. 7.6 a., where we compare to the crossover points for a random AA model analyzed using the same methods. The crossover points noticeably increase with N in both cases, and should therefore be considered as finite-size crossover points and not bona fide critical points. We also plot the value of the maximum cluster size at the peak $C_{\max}(p_{\text{peak,Haar}})$ in Fig. 7.6 b., and find that it increases as a power law with system size $C_{\max}(p_{\text{peak,Haar}}) \propto N^{\mu}$ with fractal dimension $d_f = 1.809 \pm 0.005$ for the complete PWR2_q circuit and 1.786 ± 0.005 for the random AA circuit. The similarity in the fractal dimension d_f between these two circuits suggests that they may be governed by the same universal physics near the critical point. Moreover, the fractal dimension in both cases differs from the analytical prediction $d_f = 91/48 \approx 1.896$ obtained from the two-dimensional percolation universality class. This suggests

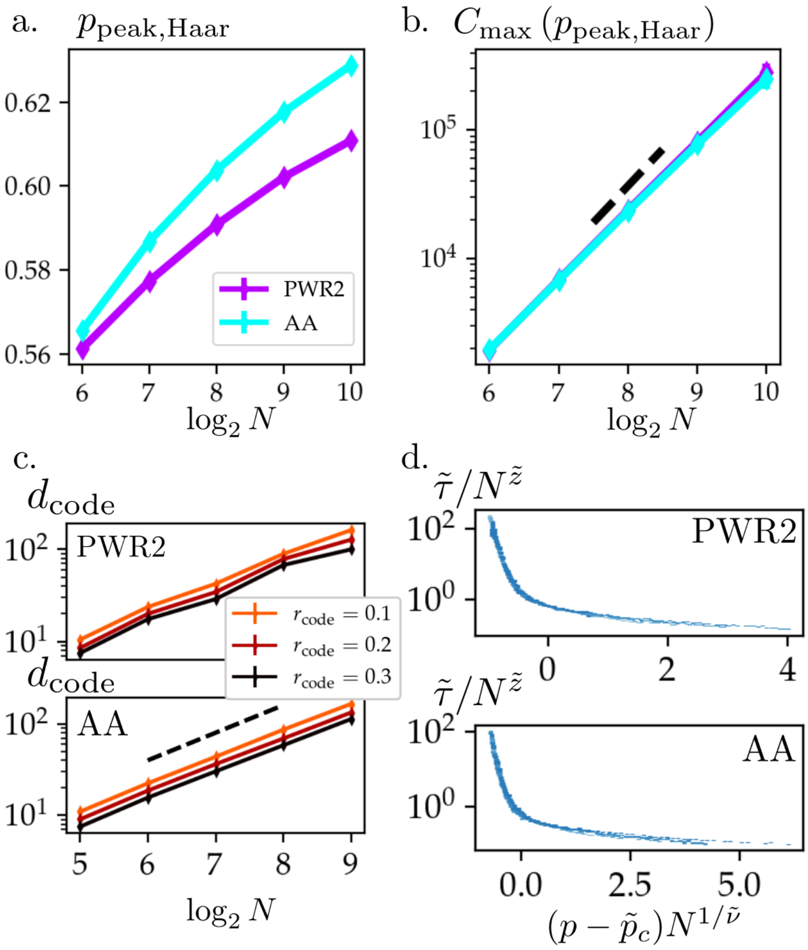

FIGURE 7.6: **Maximally nonlocal 'complete' PWR2$_q$ circuits with $q = \log_2 N$ and random AA circuits.** a. Crossover points $p_{\mathrm{peak,Haar}}$ as a function of system size N for the complete Haar random PWR2$_q$ circuit (purple) and for the random AA model (light blue). b. The maximum cluster size $C_{\max}$ at the peak $p_{\mathrm{peak,Haar}}$ grows as a power law N^{μ} with system size for the complete PWR2$_q$ circuit (purple) and the AA circuit (light blue), with exponents $d_f = 1.809 \pm 0.005$ and $d_f = 1.786 \pm 0.005$ respectively. Black dashed line shows the fractal dimension, $d_f = 91/48$, of the cluster at the critical point of two-dimensional system. c. The code distance for the complete PWR2$_q$ Clifford circuit (top) and the random AA Clifford circuit (bottom) for code rates $r_{\mathrm{code}} = 0.1, 0.2, 0.3$ (black, red, orange). In both cases, the code distance is nearly extensive, scaling like $d_{\mathrm{code}} \propto N^{\beta}$ with $\beta = 0.96 \pm 0.04$ (PWR2) and $\beta = 0.97 \pm 0.02$ (AA). d. Scaling collapse of the normalized single-qubit purification time $\tilde{\tau}(p)$ in the complete PWR2$_q$ Clifford circuit (top) and the random AA Clifford circuit (bottom). In both cases the data exhibits strong collapse according to the nonstandard scaling form in Eq. (7.10). Detailed finite-size scaling analysis are provided in Appendix F.4, and renormalization group calculation of $p_{\mathrm{peak,Haar}}$ of full PWR2$_q$ is provided in Appendix E.1. This figure was reproduced from [186].

that there is an abrupt change in the universality class from the $q < \log_2 N$ circuits to the complete PWR2$_q$ circuit.

Next, we turn our attention to circuits composed of Clifford circuits with two-qubit gates $Q_{ij} = \mathrm{CZ}_{ij}H_iH_j$ and study the quantum error-correcting codes that support the mixed phase. Again, we find striking similarities with the random AA circuit, suggesting that these models may be governed by the same universal physics. Using the methods discussed in §7.6, we extract the code distance d_{code} of the QECC in the mixed phase at fixed code rate r_{code}. We plot the results in Fig. 7.6 c. for code rates $r_{\text{code}} = 0.1, 0.2, 0.3$. Linear fits indicate a nearly extensive code distance, where $d_{\text{code}} \propto N^{\beta}$ with $\beta = 0.98 \pm 0.05$ for the PWR2 circuit and 0.96 ± 0.01 for the random AA circuit. The fast scrambling dynamics common to both of these models apparently generates similar quantum error-correcting codes with excellent properties deep in the mixed phase.

Finally, we study the single-qubit purification time τ in the complete PWR2$_q$ circuit with $q = \log_2 N$. Instead of the conventional scaling law Eq. (7.8) near the critical point, here we empirically find strong scaling collapse of τ only after normalizing by the number of interaction layers $q = \log_2 N$ within each even (or odd) block. This leads to a nonstandard scaling law

$$\tau / \log_2 N = \tilde{\tau}(p) = N^{\tilde{z}} \tilde{f}\left((p - \tilde{p}_c) N^{1/\tilde{\nu}}\right), \tag{7.10}$$

which yields strong data collapse for both the complete PWR2 model and the random AA model as shown in Fig. 7.6 d. This suggests that the critical point in the fast scrambling limit may be governed by a logarithmic scaling law Eq. (7.10) as opposed to the conventional scaling Eq. (7.8) that governs the phase transition in general short- and long-range models [130, 132]. The origin of this scaling behavior is an interesting topic for further investigation.

7.8 Conclusions

In this chapter, we investigated the MIPTs and the role which nonlocal interactions play in the system's robustness against entanglement destroying local measurements. By tuning the locality in the PWR2$_q$ circuit on a sparsely coupled graph with the parameter q, we interpolated between the nearest-neighbor regime (slow scrambler) and nonlocal regime (fast scrambling), and showed that MIPT critical points $p_{c,\text{Haar}}$, p_{ce}, and p_{cp} can be improved significantly. Quantities like critical exponents ν, for fixed $q < \log_2 N$, were shown to be not affected largely by the presence of nonlocal couplings retaining their values consistent with the 1-D universality class. We have also investigated how the properties of the dynamically generated quantum error-correcting code changes by adding nonlocal interactions. We have shown that while the system possesses 1-D universality class, the code distance d_{code} can be improved significantly by the addition of nonlocal couplings.

In the limit of a full PWR2_q circuit for $q = \log_2 N$, the underlying model at $p = 0$ becomes fast scrambling. In this limit, we found that the critical points and critical behavior of the MIPTs becomes comparable to a prototypical fast scrambling model (AA). Like AA, full PWR2_q also exhibited the code distance that is extensive $d_{\text{code}} \propto N^{\beta}$ with $\beta \approx 1$. Finally, we have observed a non-standard log-scaled scaling collapse in the single qubit purification time τ for both PWR2_q and AA circuits. This suggests that the MIPTs of both models may be described by the same universality class, which is related to transition from slow to fast scrambling regime. This may be an interesting phenomenon to be studied as a future work.

One of the motivations for studying the MIPT and the code properties of the deterministic circuit is for the feasibility in the near term experiments. In this chapter, we have shown that deterministic PWR2_q circuit can generate quantum error-correcting codes with long code distance that are robust to local measurements, with a simple iterative scheme. Furthermore, we have shown that the properties of those codes can be tuned. However, there is an experimental challenge for generating these codes due to the post selection problem, which comes from the probabilistic nature of the measurements of quantum states. The consequence is the need of exponentially many repetitions of the experiment in order to statistically analyze the nature of the output states. Therefore, in this context, the future work lies in investigating on methods which overcome the post-selection problem, and detecting the transition in experiment platforms such as atoms in an optical cavity, neutral atoms with tweezers, or trapped ions, where efficient implementation of the sparse fast scrambler is possible.

Part V

Conclusion

Chapter 8

Conclusions and Outlook

Wir müssen wissen,
Wir werden wissen.

David Hilbert [367]

In this thesis, we investigated a family of sparsely coupled models, which possess fast scrambling dynamics with logarithmic lightcones. We showed that such dynamics emerges from the vanishing notion of locality, due to the transition between two underlying geometries with incompatible notions of locality. Furthermore, we showed the possibility of engineering such systems in a near term experimental platforms using cold atoms in an optical cavity and cold atoms in optical tweezers, and proposed the ways to detect the fast scrambling dynamics and the corresponding transition in the underlying geometry.

Then we investigated how the fast scrambling dynamics can influence the systems' robustness on information destroying operations by studying various properties of measurement-induced phase transitions. We not only showed that sparsely coupled models in the fast scrambling regime can significantly increase the critical point of the transitions, we also showed that we can achieve introducing few long-range sparse couplings. These results not only have implications for potential experimental realizations, but also, provide hints pointing to efficient implementations of quantum circuits and algorithms which use significantly fewer gates and complexity than the naive implementations of locally interacting models, globally coupled models, or randomly coupled models. Below we provide the summary of the results and detailed outlook for each of the models.

In Ch. 5, we investigated the dynamics of the quantum XY model on a sparsely coupled graph, where spins that are integer power of two apart in distance can interact. We established that when the coupling strengths are equal, the model possess fast scrambling dynamics a with logarithmic lightcone. We show that as the model approaches the fast scrambling regime, the dispersion relation in the low excitation sectors of the Hamiltonian gain fractal-like features, while the level statistics of the many-body interacting sectors give rise to chaotic level statics.

The nature of sparsely coupled models of this type has not been extensively studied in the past, therefore, there are many future prospects regarding this model. In this thesis, we have only investigated the dynamics of the powers-of-2 XY model with local spin-$S = 1/2$ degrees of freedom. The obvious ways to expand the model are: to increase the basis of the power from powers-of-2 to powers-of-$b \gg 2$, increase the local degrees of freedom to larger values, and consider different inter-qubit couplings such as Ising and Heisenberg couplings. The ground state properties of such models may also be interesting.

For the powers-of-b models with $b > 2$, we would expect the model to be approximately b-dimensional hypercubic lattice of dimension $\log_b N$, where mean-field approaches becomes exact. This is because the b-nary representation of a number given to a site, can be interpreted as elements of $\log_b N$ dimensional vector, and in the case of the power-of-b model, the coupling is only allowed on the direction of the unit basis vectors of the $\log_b N$ dimensional Euclidean space. For powers-of-2 models with large local Hilbert space size, as the magnitude of the spins S becomes large, the model will become closer to the classical spin interactions, where the Mermin-Wagner theorem [368, 369] forbids phase transitions with spontaneous symmetry breaking. This may give rise to an interesting topological quantum phase and a phase transition near the geometric transition point.

Although investigations of such limiting cases might come with difficulties due to the model being highly delocalized and the exponentially large Hilbert space, investigation of ground state phases and mean-field dynamics may be possible with the currently available numerical and analytical techniques. For example, simulations using numerical techniques such as tree tensor networks [93, 101, 301, 349, 370–372], are expected to be fruitful, given that the model already having underlying treelike interaction structure in the limit of treelike geometry. In the limit of intermediate values of b and S, extended mean-field approaches, such as discrete truncated Wigner methods [373–375] may provide fruitful insight on the dynamics, as well as they may provide insight into the statics the model.

In Ch. 6, we investigated a Floquet fast scrambler that is implemented as a quantum circuit. The implementation also relies on the transition in geometry with two incompatible notions of locality, similarly to the time-independent case, where we show that on top of fast scrambling dynamics, near the fast scrambling regime the global embedding of information occurs with the finite teleportation time. Unlike the time-independent case, we introduced a spatial variation in the positions of the qubits in order to realize an exotic geometric feature which is not compatible with a realization in the flat Euclidean spacetime. For this, we proposed experimental implementations with cold atoms with optical tweezers, which is scalable to hundreds of qubits.

In the proposed scheme, we showed that exotic coupling patterns, like the sparsely coupled patterns, can be created in the number of operations of order $\mathcal{O}(\log N)$. Generation of complex coupling patterns may be useful when it comes to implement complex quantum algorithms. Unlike classical computers, in quantum systems copying a state is prohibited. Therefore, physically moving the array of qubits can be a viable way to transfer the quantum state for some architecture; especially, the slow growth of scrambling time in Floquet fast scrambling protocol with respect to the system size ($t_* \propto \log N$) may be used to compactify deep static circuits.

In the early years of classical computing, there were proposals to implement architecture based on a hypercubic array for parallel computing [376, 377]. However, its wide commercial use was rejected due to the cost on intnernodal communications. We have provided the possibility of implementing such an architecture via the shuffling of atoms, in a form which potentially reduces the cost of quantum computation due to fast entanglement generation over the qubits in the system. Although there is a cost to maintain the coherence of the qubits, this may be solved by the longer coherence times from the technological advancement on the manipulation methods of physical qubits, or with the advancement in quantum error-correcting techniques. The proposed architecture could also create various non-trivial graph states that may be used for resources for quantum computing [378–380].

Finally, in Ch. 7, we investigated the measurement-induced phase transitions in the sparsely coupled circuit models with tunable long-range interactions. Here we showed that addition of $\mathcal{O}(1)$ long-range interactions are sufficient for the critical points to be sufficiently close to the critical points of the long-range fast scrambling limit. We also showed that dynamically generated quantum error-correcting codes become extensive in the fast scrambling regime. These results indicate that quantum information held in those circuits are robust against decoherence up to a number of qubits that is proportional to the system size.

A future fruitful direction of research may be to investigate continuous time analogues of the models. Two potential discussions are: (1) the role of local dissipation when the underlying model is fast scrambling. (2) the study of Anderson and many-body localizations in the models with underlying fast scrambling dynamics.

Another future prospect may lie in the QECC nature of the sparsely coupled circuit models. In the regime where the treelike geometry governs the model, hyperbolic structure naturally arises. Such hyperbolic structures in the form of Bethe lattice-like graph with hierarchical structure may provide a further playground for toy models that investigate the error correcting nature of the AdS/CFT correspondence, such as the ones discussed by Haydeman *et al.* [349, 350]. Using the experimental procedure introduced in Ch. 6.5 of cold atoms trapped in optical tweezers, which can be scaled straightforwardly, one may find experimental procedures to probe such an exotic geometry with numbers of qubits of order of tens, hundreds, and thousands in the near future.

Finally, apart from the quantum spin-1/2 (qubit) models that are investigated in this thesis, there may be other models which possess fast scrambling dynamics when they are coupled sparsely. Such models include large-N models, such as random Brownian circuits [32, 341, 342] and sparse variants of SYK models with Majonara fermions [68, 127]. Although they will not be deterministic, they might provide analytical results which may reveal how fast scrambling dynamics emerges as the model recovers the permutation symmetry over branch swapping in the tree-like geometry. For the models with deterministic coupling, it may be interesting to investigate Kitaev chain-like fermionic models [319, 381] with four-body scattering terms, which mix the fermions in the same level of the hierarchical structure. This may give rise to exotic dynamical features which may provide further insight into how the different degrees of freedom can be coupled efficiently, and how the flow of information (direction of entanglement generation) in the system can be controlled.

The future prospects that are covered above only scrape the surface of the rich set of questions which deterministic fast scramblers and their associated underlying geometries give rise to. In the near future, we believe that quantum simulation will be simulating quantum systems that are beyond the reach of numerical simulation by classical computers; at the completion of this PhD, we are seeing the verge of such an era [98, 106, 382]. With the development of large-scale quantum simulators and universal quantum computers, we are expected to observe more and more exotic physics in the coming years. These results will, without any doubt, stimulate even greater theoretical discussion which moves us one step closer to the answers to the big questions in physics and even in other natural sciences. We hope that the future collaboration between theorists and experimental will further push the frontiers of physics and other natural sciences.

Bibliography

[1] du Bois-Reymond, Emil, "über die Grenzen des Naturerkennens," (1876).

[2] J. A. Wheeler, *Geons, Black Holes, and Quantum Foam* (WW Norton, New York, NY, 2000).

[3] Platon, *Cratylus* (Unknown Publisher, Greece, 4 Century B.C.).

[4] J. Burnet, *Early Greek Philosophy* (A. Black, 1892).

[5] I. Newton, *Philosophiae naturalis principia mathematica.* (Jussu Societatis Regiae ac Typis Josephi Streater. Prostat apud plures bibliopolas, Londini, 1687).

[6] R. Clausius, "Ueber die bewegende Kraft der Wärme und die Gesetze, welche sich daraus für die Wärmelehre selbst ableiten lassen," Annalen der Physik und Chemie **155**, 500–524 (1850).

[7] R. Clausius, "Ueber eine veränderte Form des zweiten Hauptsatzes der mechanischen Wärmetheorie," Annalen der Physik und Chemie **169**, 481–506 (1854).

[8] P. S. Laplace, "Analytical theory of probability," Courier, Paris (1812).

[9] W. Heisenberg, "über den anschaulichen Inhalt der quantentheoretischen Kinematik und Mechanik," Zeitschrift für Physik **43**, 172–198 (1927).

[10] W. Heisenberg, "Zur theorie des ferromagnetismus," Zeitschrift für Physik **49**, 619–636 (1928).

[11] E. Schrödinger, "An undulatory theory of the mechanics of atoms and molecules," Physical Review **28**, 1049–1070 (1926).

[12] A. S. Eddington, *The Nature of the Physical World* (Cambridge University Press, Cambridge, England, 1932).

[13] T. L. Duncan and J. S. Semura, “The deep physics behind the second law: Information and energy as independent forms of bookkeeping,” Entropy. An International and Interdisciplinary Journal of Entropy and Information Studies **6**, 21–29 (2004).

[14] T. L. Duncan and J. S. Semura, “Information Loss as a Foundational Principle for the Second Law of Thermodynamics,” Foundations of Physics **37**, 1767–1773 (2007).

[15] P. W. Anderson, “More is different,” Science **177**, 393–396 (1972).

[16] A. M. LYAPUNOV, “The general problem of the stability of motion,” International Journal of Control **55**, 531–534 (1992).

[17] E. N. Lorenz, “Deterministic Nonperiodic Flow,” Journal of the Atmospheric Sciences **20**, 130–141 (1963).

[18] R. M. May, “Simple mathematical models with very complicated dynamics,” Nature **261**, 459–467 (1976).

[19] S. Wolfram, *A New Kind of Science* (Wolfram Media, Champaign, IL, 2002).

[20] L. Boltzmann, “über die Mechanische Bedeutung des Zweiten Hauptsatzes der Wärmetheorie,” Wiener Berichte **53**, 195–220 (1866).

[21] G. D. Birkhoff, “Proof of the Ergodic Theorem,” Proceedings of the National Academy of Sciences of the United States of America **17**, 656–660 (1931).

[22] J. v. Neumann, “Proof of the Quasi-Ergodic Hypothesis,” Proceedings of the National Academy of Sciences **18**, 70–82 (1932).

[23] P. Walters, *Ergodic Theory: Introductory Lectures*, Lecture Notes in Mathematics ; 458 (Springer-Verlag, Berlin, Germany, 1975).

[24] E. P. Wigner, “Characteristic Vectors of Bordered Matrices With Infinite Dimensions,” Annals of Mathematics **62**, 548–564 (1955).

[25] A. I. Larkin and Y. N. Ovchinnikov, “Quasiclassical method in the theory of superconductivity,” Soviet Journal of Experimental and Theoretical Physics **28**, 1200 (1969).

[26] T. Guhr, A. Mueller-Groeling, and H. A. Weidenmueller, “Random Matrix Theories in Quantum Physics: Common Concepts,” Physics Reports **299**, 189–425 (1998).

[27] M. A. Porter, “An Introduction to Quantum Chaos,” (2001), arXiv:nlin/0107039 .

[28] L. D’Alessio, Y. Kafri, A. Polkovnikov, and M. Rigol, “From quantum chaos and eigenstate thermalization to statistical mechanics and thermodynamics,” Advances in Physics **65**, 239–362 (2016).

[29] J. M. Deutsch, “Quantum statistical mechanics in a closed system,” Physical Review A **43**, 2046–2049 (1991).

[30] M. Srednicki, “Chaos and Quantum Thermalization,” Physical Review E **50**, 888–901 (1994).

[31] M. Rigol, V. Dunjko, and M. Olshanii, “Thermalization and its mechanism for generic isolated quantum systems,” Nature **452**, 854–858 (2008).

[32] S. Sahu, S. Xu, and B. Swingle, “Scrambling dynamics across a thermalization-localization quantum phase transition,” Physical Review Letters **123**, 165902 (2019).

[33] A. Einstein, “über einen die Erzeugung und Verwandlung des Lichtes betreffenden heuristischen Gesichtspunkt,” Annalen der Physik **322**, 132–148 (1905).

[34] A. Einstein, “Zur elektrodynamik bewegter körper,” Annalen der Physik **322**, 891–921 (1905).

[35] A. Einstein, “Lichtgeschwindigkeit und statik des gravitationsfeldes,” Annalen der Physik **343**, 355–369 (1912).

[36] A. Einstein, “Zur theorie des statischen gravitationsfeldes,” Annalen der Physik **343**, 443–458 (1912).

[37] K. Schwarzschild, “über das gravitationsfeld eines massenpunktes nach der einsteinschen theorie,” Sitzungsberichte der Königlich Preußischen Akademie der Wissenschaften (Berlin) , 189–196 (1916).

[38] K. Schwarzschild, “On the gravitational field of a mass point according to Einstein’s theory,” (1999), arXiv:physics/9905030 .

[39] R. P. Kerr, “Gravitational Field of a Spinning Mass as an Example of Algebraically Special Metrics,” Physical Review Letters **11**, 237–238 (1963).

[40] K. S. Thorne, C. W. Misner, and J. A. Wheeler, *Gravitation* (Freeman, San Francisco, CA, 1973).

[41] T. E. H. T. Collaboration, “First M87 Event Horizon Telescope Results. I. The Shadow of the Supermassive Black Hole,” The Astrophysical Journal Letters **875**, 17 (2019).

[42] S. W. Hawking, “Particle creation by black holes,” Communications in Mathematical Physics **43**, 199–220 (1975).

[43] S. W. Hawking, “Breakdown of predictability in gravitational collapse,” Physical Review D **14**, 2460–2473 (1976).

[44] L. Susskind, L. Thorlacius, and J. Uglum, “The Stretched Horizon and Black Hole Complementarity,” Physical Review D **48**, 3743–3761 (1993).

[45] L. Susskind and L. Thorlacius, “Gedanken Experiments involving Black Holes,” Physical Review D **49**, 966–974 (1994).

[46] D. N. Page, “Is Black-Hole Evaporation Predictable?” Physical Review Letters **44**, 301–304 (1980).

[47] M. Heusler, “Stationary Black Holes: Uniqueness and Beyond,” Living Reviews in Relativity **1**, 6 (1998).

[48] J. D. Bekenstein, “Generalized second law of thermodynamics in black-hole physics,” Physical Review D **9**, 3292–3300 (1974).

[49] L. Susskind, “The World as a Hologram,” Journal of Mathematical Physics **36**, 6377–6396 (1995).

[50] R. Bousso, “The holographic principle,” Reviews of Modern Physics **74**, 825–874 (2002).

[51] L. Susskind and J. Lindesay, *Introduction to Black Holes, Information and The String Theory Revolution, an: The Holographic Universe* (World Scientific Publishing, Singapore, 2004).

[52] J. L. Park, “The concept of transition in quantum mechanics,” Foundations of Physics **1**, 23–33 (1970).

[53] Y. Sekino and L. Susskind, "Fast Scramblers," Journal of High Energy Physics **2008**, 065–065 (2008).

[54] L. Susskind, "Addendum to Fast Scramblers," (2011), arXiv:1101.6048 .

[55] L. Susskind, "Fast Scrambling," https://doi.org/10.48660/08030070 (2008).

[56] N. Lashkari, D. Stanford, M. Hastings, T. Osborne, and P. Hayden, "Towards the fast scrambling conjecture," Journal of High Energy Physics **2013**, 22 (2013).

[57] C. E. Shannon, "A mathematical theory of communication," The Bell System Technical Journal **27**, 379–423 (1948).

[58] F. A. Bais and J. D. Farmer, "The Physics of Information," (2007), arXiv:0708.2837 .

[59] P. Hayden and J. Preskill, "Black holes as mirrors: Quantum information in random subsystems," Journal of High Energy Physics **2007**, 120–120 (2007).

[60] P. W. Anderson, "Absence of diffusion in certain random lattices," Physical Review **109**, 1492–1505 (1958).

[61] S. Sarker and E. Domany, "Scaling theory of Anderson localization: A renormalization-group approach," Physical Review B **23**, 6018–6036 (1981).

[62] G. Carleo, F. Becca, M. Schiró, and M. Fabrizio, "Localization and glassy dynamics of many-body quantum systems," Scientific Reports **2**, 243 (2012).

[63] D. A. Abanin, E. Altman, I. Bloch, and M. Serbyn, "*Colloquium* : Many-body localization, thermalization, and entanglement," Reviews of Modern Physics **91**, 021001 (2019).

[64] X.-L. Qi and A. Streicher, "Quantum epidemiology: Operator growth, thermal effects, and SYK," Journal of High Energy Physics **2019**, 12 (2019).

[65] H. W. Hethcote, "Three Basic Epidemiological Models," in *Applied Mathematical Ecology*, Vol. 18, edited by S. A. Levin, S. A. Levin, T. G. Hallam, and L. J. Gross (Springer Berlin Heidelberg, Berlin, Heidelberg, 1989) pp. 119–144.

[66] M. A. Nielsen and I. L. Chuang, *Quantum Computation and Quantum Information: 10th Anniversary Edition* (Cambridge University Press, Cambridge, England, 2010).

[67] S. Sachdev and J. Ye, "Gapless spin-fluid ground state in a random quantum Heisenberg magnet," Physical Review Letters **70**, 3339–3342 (1993).

[68] A. Kitaev, "A simple model of quantum holography," https://online.kitp.ucsb.edu/online/entangled15/ (2015).

[69] J. Kim, E. Altman, and X. Cao, "Dirac fast scramblers," Physical Review B **103**, L081113 (2021).

[70] J. Maldacena, S. H. Shenker, and D. Stanford, "A bound on chaos," Journal of High Energy Physics **2016**, 106 (2016).

[71] B. Kobrin, Z. Yang, G. D. Kahanamoku-Meyer, C. T. Olund, J. E. Moore, D. Stanford, and N. Y. Yao, "Many-Body Chaos in the Sachdev-Ye-Kitaev Model," Physical Review Letters **126**, 030602 (2021).

[72] J. Marino and A. M. Rey, "Cavity-QED simulator of slow and fast scrambling," Physical Review A **99**, 051803 (2019).

[73] Z. Li, S. Choudhury, and W. V. Liu, "Fast scrambling without appealing to holographic duality," Physical Review Research **2**, 043399 (2020).

[74] R. Belyansky, P. Bienias, Y. A. Kharkov, A. V. Gorshkov, and B. Swingle, "Minimal Model for Fast Scrambling," Physical Review Letters **125**, 130601 (2020).

[75] S. S. Gubser, C. Jepsen, Z. Ji, and B. Trundy, "Continuum limits of sparse coupling patterns," Physical Review D **98**, 045009 (2018).

[76] J. M. Maldacena, "The Large N Limit of Superconformal Field Theories and Supergravity," International Journal of Theoretical Physics **38**, 1113–1133 (1999).

[77] O. Aharony, S. S. Gubser, J. Maldacena, H. Ooguri, and Y. Oz, "Large N Field Theories, String Theory and Gravity," Physics Reports , 204 (2000).

[78] S. Ryu and T. Takayanagi, "Holographic Derivation of Entanglement Entropy from AdS/CFT," Physical Review Letters **96**, 181602 (2006).

[79] J. S. Bell, "On the einstein podolsky rosen paradox," Physics Physique Fizika **1**, 195 (1964).

[80] J. F. Clauser, M. A. Horne, A. Shimony, and R. A. Holt, "Proposed Experiment to Test Local Hidden-Variable Theories," Physical Review Letters **23**, 880–884 (1969).

[81] E. H. Lieb and D. W. Robinson, "The finite group velocity of quantum spin systems," Communications in Mathematical Physics **28**, 251–257 (1972).

[82] J. F. Clauser and A. Shimony, "Bell's theorem. Experimental tests and implications," Reports on Progress in Physics **41**, 1881–1927 (1978).

[83] A. Aspect, P. Grangier, and G. Roger, "Experimental Tests of Realistic Local Theories via Bell's Theorem," Physical Review Letters **47**, 460–463 (1981).

[84] A. Peres and D. R. Terno, "Quantum Information and Relativity Theory," Reviews of Modern Physics **76**, 93–123 (2004).

[85] F. Nogueira, M. H. Caldeira, and J. M. Domingos, "Locality, relativity and Bell's inequalities," Physica Scripta **53**, 18–22 (1996).

[86] A. Einstein, *Relativity : The Special and General Theory: Original Version* (2017).

[87] R. Rammal, G. Toulouse, and M. A. Virasoro, "Ultrametricity for physicists," Reviews of Modern Physics **58**, 765–788 (1986).

[88] F. Q. Gouvêa, *P-Adic Numbers: An Introduction* (Springer, Berlin, Heidelberg, 1997).

[89] S. R. White, "Density matrix formulation for quantum renormalization groups," Physical Review Letters **69**, 2863–2866 (1992).

[90] S. Aaronson and D. Gottesman, "Improved simulation of stabilizer circuits," Physical Review A - Atomic, Molecular, and Optical Physics **70** (2004), 10.1103/PhysRevA.70.052328.

[91] A. J. Daley, C. Kollath, U. Schollwöck, and G. Vidal, "Time-dependent density-matrix renormalization-group using adaptive effective Hilbert spaces," Journal of Statistical Mechanics: Theory and Experiment **2004**, P04005 (2004).

[92] J. J. García-Ripoll, "Time evolution of Matrix Product States," New Journal of Physics **8**, 305–305 (2006).

[93] L. Tagliacozzo, G. Evenbly, and G. Vidal, "Simulation of two-dimensional quantum systems using a tree tensor network that exploits the entropic area law," Physical Review B **80**, 235127 (2009).

[94] J. Haegeman, J. I. Cirac, T. J. Osborne, I. Pižorn, H. Verschelde, and F. Verstraete, "Time-Dependent Variational Principle for Quantum Lattices," Physical Review Letters **107**, 070601 (2011).

[95] I. Bloch, J. Dalibard, and S. Nascimbène, "Quantum simulations with ultracold quantum gases," Nature Physics **8**, 267–276 (2012).

[96] J. W. Britton, B. C. Sawyer, A. C. Keith, C.-C. J. Wang, J. K. Freericks, H. Uys, M. J. Biercuk, and J. J. Bollinger, "Engineered two-dimensional Ising interactions in a trapped-ion quantum simulator with hundreds of spins," Nature **484**, 489–492 (2012).

[97] S. Paeckel, T. Köhler, A. Swoboda, S. R. Manmana, U. Schollwöck, and C. Hubig, "Time-evolution methods for matrix-product states," Annals of Physics **411**, 167998 (2019).

[98] F. Arute *et al.*, "Quantum supremacy using a programmable superconducting processor," Nature **574**, 505–510 (2019).

[99] B. Yang, H. Sun, R. Ott, H.-Y. Wang, T. V. Zache, J. C. Halimeh, Z.-S. Yuan, P. Hauke, and J.-W. Pan, "Observation of gauge invariance in a 71-site Bose-Hubbard quantum simulator," Nature **587**, 392–396 (2020).

[100] E. Altman *et al.*, "Quantum Simulators: Architectures and Opportunities," PRX Quantum **2**, 017003 (2021).

[101] G. Magnifico, T. Felser, P. Silvi, and S. Montangero, "Lattice quantum electrodynamics in (3+1)-dimensions at finite density with tensor networks," Nature Communications **12**, 3600 (2021).

[102] A. Periwal, E. S. Cooper, P. Kunkel, J. F. Wienand, E. J. Davis, and M. Schleier-Smith, "Programmable interactions and emergent geometry in an array of atom clouds," Nature **600**, 630–635 (2021).

[103] Y. Song, M. Kim, H. Hwang, W. Lee, and J. Ahn, "Quantum simulation of Cayley-tree Ising Hamiltonians with three-dimensional Rydberg atoms," Physical Review Research **3**, 013286 (2021).

[104] D. Bluvstein, H. Levine, G. Semeghini, T. T. Wang, S. Ebadi, M. Kalinowski, A. Keesling, N. Maskara, H. Pichler, M. Greiner, V. Vuletić, and M. D. Lukin, "A quantum processor based on coherent transport of entangled atom arrays," Nature **604**, 451–456 (2022).

[105] S. Ebadi, T. T. Wang, H. Levine, A. Keesling, G. Semeghini, A. Omran, D. Bluvstein, R. Samajdar, H. Pichler, W. W. Ho, S. Choi, S. Sachdev, M. Greiner, V. Vuletic, and M. D. Lukin, "Quantum Phases of Matter on a 256-Atom Programmable Quantum Simulator," Nature **595**, 227–232 (2021).

[106] A. J. Daley, I. Bloch, C. Kokail, S. Flannigan, N. Pearson, M. Troyer, and P. Zoller, "Practical quantum advantage in quantum simulation," Nature **607**, 667–676 (2022).

[107] K. Okunishi, T. Nishino, and H. Ueda, "Developments in the Tensor Network — from Statistical Mechanics to Quantum Entanglement," Journal of the Physical Society of Japan **91**, 062001 (2022).

[108] A. Klümper, A. Schadschneider, and J. Zittartz, "Matrix-product-groundstates for one-dimensional spin-1 quantum antiferromagnets," Europhysics Letters **24**, 293–297 (1993).

[109] S. Östlund and S. Rommer, "Thermodynamic limit of density matrix renormalization," Physical Review Letters **75**, 3537–3540 (1995).

[110] S. Rommer and S. Östlund, "Class of ansatz wave functions for one-dimensional spin systems and their relation to the density matrix renormalization group," Physical Review B **55**, 2164–2181 (1997).

[111] J. Dukelsky, M. A. Martín-Delgado, T. Nishino, and G. Sierra, "Equivalence of the variational matrix product method and the density matrix renormalization group applied to spin chains," Europhysics Letters **43**, 457–462 (1998).

[112] F. Verstraete, J. J. García-Ripoll, and J. I. Cirac, "Matrix product density operators: Simulation of finite-temperature and dissipative systems," Physical Review Letters **93**, 207204 (2004).

[113] I. P. McCulloch, "From density-matrix renormalization group to matrix product states," Journal of Statistical Mechanics: Theory and Experiment **2007**, P10014–P10014 (2007).

[114] I. P. McCulloch, "Infinite size density matrix renormalization group, revisited," (2008), arXiv:0804.2509 .

[115] B. Pirvu, V. Murg, J. I. Cirac, and F. Verstraete, "Matrix product operator representations," New Journal of Physics **12**, 025012 (2010).

[116] M. Yang and S. R. White, "Time Dependent Variational Principle with Ancillary Krylov Subspace," Physical Review B **102**, 094315 (2020).

[117] D. Gottesman, "Theory of fault-tolerant quantum computation," Physical Review A **57**, 127–137 (1998).

[118] D. Gottesman and G. L. Alamos, "The Heisenberg Representation of Quantum Computers," Proceedings of the XXII International Colloquium on Group Theoretical Methods in Physics , 32–43 (1998).

[119] A. Nahum, J. Ruhman, S. Vijay, and J. Haah, "Quantum Entanglement Growth under Random Unitary Dynamics," Physical Review X **7**, 031016 (2017).

[120] D. Aharonov, "Quantum to classical phase transition in noisy quantum computers," Physical Review A **62**, 062311 (2000).

[121] Y. Li, X. Chen, and M. P. A. Fisher, "Measurement-driven entanglement transition in hybrid quantum circuits," Physical Review B **100**, 134306 (2019).

[122] B. Skinner, J. Ruhman, and A. Nahum, "Measurement-Induced Phase Transitions in the Dynamics of Entanglement," Physical Review X **9**, 31009 (2019).

[123] M. J. Gullans and D. A. Huse, "Dynamical Purification Phase Transition Induced by Quantum Measurements," Physical Review X **10**, 041020 (2020).

[124] A. Nahum, S. Roy, B. Skinner, and J. Ruhman, "Measurement and Entanglement Phase Transitions in All-To-All Quantum Circuits, on Quantum Trees, and in Landau-Ginsburg Theory," PRX Quantum **2**, 010352 (2021).

[125] M. J. Gullans and D. A. Huse, "Scalable Probes of Measurement-Induced Criticality," Physical Review Letters **125**, 070606 (2020).

[126] S. Choi, Y. Bao, X.-L. Qi, and E. Altman, "Quantum Error Correction in Scrambling Dynamics and Measurement-Induced Phase Transition," Physical Review Letters **125**, 030505 (2020).

[127] S.-K. Jian, C. Liu, X. Chen, B. Swingle, and P. Zhang, "SYK meets non-Hermiticity II: Measurement-induced phase transition," Physical Review Letters **127**, 140601 (2021).

[128] C. Liu, P. Zhang, and X. Chen, "Non-unitary dynamics of Sachdev-Ye-Kitaev chain," SciPost Physics **10**, 048 (2021).

[129] P. Zhang, S.-K. Jian, C. Liu, and X. Chen, "Emergent Replica Conformal Symmetry in Non-Hermitian SYK$_2$ Chains," Quantum **5**, 579 (2021).

[130] M. Block, Y. Bao, S. Choi, E. Altman, and N. Y. Yao, "Measurement-Induced Transition in Long-Range Interacting Quantum Circuits," Physical Review Letters **128**, 010604 (2022).

[131] T. Müller, S. Diehl, and M. Buchhold, "Measurement-induced dark state phase transitions in long-ranged fermion systems," Physical Review Letters **128**, 010605 (2022).

[132] T. Minato, K. Sugimoto, T. Kuwahara, and K. Saito, "Fate of Measurement-Induced Phase Transition in Long-Range Interactions," Physical Review Letters **128**, 010603 (2022).

[133] P. Shor, "Algorithms for quantum computation: Discrete logarithms and factoring," in *Proceedings 35th Annual Symposium on Foundations of Computer Science* (1994) pp. 124–134.

[134] H. J. Briegel, D. E. Browne, W. Dür, R. Raussendorf, and M. Van den Nest, "Measurement-based quantum computation," Nature Physics **5**, 19–26 (2009).

[135] T.-C. Wei, "Measurement-Based Quantum Computation," Oxford Research Encyclopedia of Physics (2021), 10.1093/acrefore/9780190871994.013.31.

[136] N. Metropolis and S. Ulam, "The Monte Carlo Method," Journal of the American Statistical Association **44**, 335–341 (1949).

[137] H. E. Stanley and T. A. Kaplan, "Possibility of a Phase Transition for the Two-Dimensional Heisenberg Model," Physical Review Letters **17**, 913–915 (1966).

[138] K. G. Wilson, "The renormalization group: Critical phenomena and the Kondo problem," Reviews of Modern Physics **47**, 773–840 (1975).

[139] S. Trotzky, Y.-A. Chen, A. Flesch, I. P. McCulloch, U. Schollwöck, J. Eisert, and I. Bloch, "Probing the relaxation towards equilibrium in an isolated strongly correlated 1D Bose gas," Nature Physics **8**, 325–330 (2012).

[140] B. P. Abbott *et al.*, "Observation of Gravitational Waves from a Binary Black Hole Merger," Physical Review Letters **116**, 061102 (2016).

[141] S. R. White and R. M. Noack, "Real-space quantum renormalization groups," Physical Review Letters **68**, 3487–3490 (1992).

[142] U. Schollwöck, "The density-matrix renormalization group in the age of matrix product states," Annals of Physics **326**, 96–192 (2011).

[143] G. Vidal, J. I. Latorre, E. Rico, and A. Kitaev, "Entanglement in Quantum Critical Phenomena," Physical Review Letters **90**, 227902 (2003).

[144] J. Haegeman, T. J. Osborne, and F. Verstraete, "Post-matrix product state methods: To tangent space and beyond," Physical Review B **88**, 075133 (2013).

[145] M. P. Zaletel, R. S. K. Mong, C. Karrasch, J. E. Moore, and F. Pollmann, "Time-evolving a matrix product state with long-ranged interactions," Physical Review B **91**, 165112 (2015).

[146] J. Haegeman, C. Lubich, I. Oseledets, B. Vandereycken, and F. Verstraete, "Unifying time evolution and optimization with matrix product states," Physical Review B **94**, 165116 (2016).

[147] T. Hashizume, J. C. Halimeh, and I. P. McCulloch, "Hybrid infinite time-evolving block decimation algorithm for long-range multidimensional quantum many-body systems," Physical Review B **102**, 035115 (2020).

[148] P. Secular, N. Gourianov, M. Lubasch, S. Dolgov, S. R. Clark, and D. Jaksch, "Parallel time-dependent variational principle algorithm for matrix product states," Physical Review B **101**, 235123 (2020).

[149] D. Gottesman, "Class of quantum error-correcting codes saturating the quantum Hamming bound," Physical Review A **54**, 1862–1868 (1996).

[150] M. V. den Nest, "Classical simulation of quantum computation, the Gottesman-Knill theorem, and slightly beyond," Quantum Information and Computation **10**, 0258–0271 (2009).

[151] A. Nahum, S. Vijay, and J. Haah, "Operator Spreading in Random Unitary Circuits," Physical Review X **8**, 021014 (2018).

[152] F. G. S. L. Brandao, E. Crosson, M. B. Şahinoğlu, and J. Bowen, "Quantum Error Correcting Codes in Eigenstates of Translation-Invariant Spin Chains," Physical Review Letters **123**, 110502 (2019).

[153] B. Yoshida and N. Y. Yao, "Disentangling Scrambling and Decoherence via Quantum Teleportation," Physical Review X **9** (2019), 10.1103/PhysRevX.9.011006.

[154] Y. Bao, S. Choi, and E. Altman, "Theory of the phase transition in random unitary circuits with measurements," Physical Review B **101**, 1–29 (2020).

[155] M. Blake and N. Linden, "Quantum Circuits with Classically Simulable Operator Scrambling," Physical Review Letters **125**, 030502 (2020).

[156] R. Fan, S. Vijay, A. Vishwanath, and Y.-Z. You, "Self-organized error correction in random unitary circuits with measurement," Physical Review B **103**, 174309 (2021).

[157] C. M. Jian, Y. Z. You, R. Vasseur, and A. W. Ludwig, "Measurement-induced criticality in random quantum circuits," Physical Review B **101**, 1–12 (2020).

[158] C. Dankert, R. Cleve, J. Emerson, and E. Livine, "Exact and Approximate Unitary 2-Designs: Constructions and Applications," Physical Review A **80**, 012304 (2009).

[159] D. DiVincenzo, D. Leung, and B. Terhal, "Quantum data hiding," IEEE Transactions on Information Theory **48**, 580–598 (2002).

[160] A. Hamma, R. Ionicioiu, and P. Zanardi, "Bipartite entanglement and entropic boundary law in lattice spin systems," Physical Review A **71**, 022315 (2005).

[161] A. Hamma, R. Ionicioiu, and P. Zanardi, "Ground state entanglement and geometric entropy in the Kitaev model," Physics Letters A **337**, 22–28 (2005).

[162] D. Porras and J. I. Cirac, "Effective Quantum Spin Systems with Trapped Ions," Physical Review Letters **92**, 207901 (2004).

[163] D. S. Weiss, J. Vala, A. V. Thapliyal, S. Myrgren, U. Vazirani, and K. B. Whaley, "Another way to approach zero entropy for a finite system of atoms," Physical Review A **70**, 040302 (2004).

[164] S. Korenblit, D. Kafri, W. C. Campbell, R. Islam, E. E. Edwards, Z.-X. Gong, G.-D. Lin, L.-M. Duan, J. Kim, K. Kim, and C. Monroe, "Quantum simulation of spin models on an arbitrary lattice with trapped ions," New Journal of Physics **14**, 095024 (2012).

[165] R. Blatt and C. F. Roos, "Quantum simulations with trapped ions," Nature Physics **8**, 277–284 (2012).

[166] C.-L. Hung, A. González-Tudela, J. I. Cirac, and H. J. Kimble, "Quantum spin dynamics with pairwise-tunable, long-range interactions," Proceedings of the National Academy of Sciences **113** (2016), 10.1073/pnas.1603777113.

[167] H. Bernien, S. Schwartz, A. Keesling, H. Levine, A. Omran, H. Pichler, S. Choi, A. S. Zibrov, M. Endres, M. Greiner, V. Vuletić, and M. D. Lukin, "Probing many-body dynamics on a 51-atom quantum simulator," Nature **551**, 579–584 (2017).

[168] C. Gross and Immanuel Bloch, "Quantum simulations with ultracold atoms in optical lattices," Science **357**, 995–1001 (2017).

[169] D. Barredo, V. Lienhard, S. de Léséleuc, T. Lahaye, and A. Browaeys, "Synthetic three-dimensional atomic structures assembled atom by atom," Nature **561**, 79–82 (2018).

[170] M. A. Norcia, R. J. Lewis-Swan, J. R. K. Cline, B. Zhu, A. M. Rey, and James K. Thompson, "Cavity-mediated collective spin-exchange interactions in a strontium superradiant laser," Science **361**, 259–262 (2018).

[171] V. D. Vaidya, Y. Guo, R. M. Kroeze, K. E. Ballantine, A. J. Kollár, J. Keeling, and B. L. Lev, "Tunable-Range, Photon-Mediated Atomic Interactions in Multimode Cavity QED," Physical Review X **8**, 011002 (2018).

[172] E. J. Davis, G. Bentsen, L. Homeier, T. Li, and M. H. Schleier-Smith, "Photon-Mediated Spin-Exchange Dynamics of Spin-1 Atoms," Physical Review Letters **122**, 010405 (2019).

[173] B. Swingle, G. Bentsen, M. Schleier-Smith, and P. Hayden, "Measuring the scrambling of quantum information," Physical Review A **94**, 040302 (2016).

[174] A. W. Young, W. J. Eckner, W. R. Milner, D. Kedar, M. A. Norcia, E. Oelker, N. Schine, J. Ye, and A. M. Kaufman, "Half-minute-scale atomic coherence and high relative stability in a tweezer clock," Nature **588**, 408–413 (2020).

[175] P. Scholl, M. Schuler, H. J. Williams, A. A. Eberharter, D. Barredo, K.-N. Schymik, V. Lienhard, L.-P. Henry, T. C. Lang, T. Lahaye, A. M. Läuchli, and A. Browaeys, "Programmable quantum simulation of 2D antiferromagnets with hundreds of Rydberg atoms," Nature **595**, 233–238 (2021).

[176] D. S. Weiss and M. Saffman, "Quantum computing with neutral atoms," Physics Today **70**, 44–50 (2017).

[177] P. Diaconis, R. Graham, and W. M. Kantor, "The mathematics of perfect shuffles," Advances in Applied Mathematics **4**, 175–196 (1983).

[178] E. Urban, T. A. Johnson, T. Henage, L. Isenhower, D. D. Yavuz, T. G. Walker, and M. Saffman, "Observation of Rydberg blockade between two atoms," Nature Physics **5**, 110–114 (2009).

[179] M. Saffman, T. G. Walker, and K. Mølmer, "Quantum information with Rydberg atoms," Reviews of Modern Physics **82**, 2313–2363 (2010).

[180] M. Saffman, "Quantum computing with atomic qubits and Rydberg interactions: Progress and challenges," Journal of Physics B: Atomic, Molecular and Optical Physics **49**, 202001 (2016).

[181] B. Yoshida and A. Kitaev, "Efficient decoding for the Hayden-Preskill protocol," (2017), arXiv:1710.03363 .

[182] N. Bao and Y. Kikuchi, "Hayden-Preskill decoding from noisy Hawking radiation," Journal of High Energy Physics **2021**, 17 (2021).

[183] G. Bentsen, T. Hashizume, A. S. Buyskikh, E. J. Davis, A. J. Daley, S. S. Gubser, and M. Schleier-Smith, "Treelike interactions and fast scrambling with cold atoms," Physical Review Letters **123**, 130601 (2019).

[184] G. Bentsen, T. Hashizume, E. J. Davis, A. S. Buyskikh, M. H. Schleier-Smith, and A. J. Daley, "Tunable geometries from a sparse quantum spin network," in *Optical, Opto-Atomic, and Entanglement-Enhanced Precision Metrology II*, edited by S. M. Shahriar and J. Scheuer (SPIE, San Francisco, United States, 2020) p. 138.

[185] T. Hashizume, G. S. Bentsen, S. Weber, and A. J. Daley, "Deterministic Fast Scrambling with Neutral Atom Arrays," Physical Review Letters **126**, 200603 (2021).

[186] T. Hashizume, G. Bentsen, and A. J. Daley, "Measurement-induced phase transitions in sparse nonlocal scramblers," Physical Review Research **4**, 013174 (2022).

[187] T. Hashizume, S. Kuriyattil, A. J. Daley, and G. Bentsen, "Tunable Geometries in Sparse Clifford Circuits," Symmetry **14**, 666 (2022).

[188] T. Hashizume, I. P. McCulloch, and J. C. Halimeh, "Dynamical phase transitions in the two-dimensional transverse-field Ising model," Physical Review Research **4**, 013250 (2022).

[189] T. Hashizume, J. Halimeh, P. Hauke, and D. Banerjee, "Ground-state phase diagram of quantum link electrodynamics in $(2+1)$-d," SciPost Physics **13**, 017 (2022).

[190] A. C. Doyle, *The Case-Book of Sherlock Holmes*, 1st ed. (J. Murray : Cape, London, 1974).

[191] R. Landauer, “Irreversibility and heat generation in the computing process,” IBM Journal of Research and Development **5**, 183–191 (1961).

[192] R. Landauer, “Information is physical,” Physics Today **44**, 23–29 (1991).

[193] A. Bérut, A. Arakelyan, A. Petrosyan, S. Ciliberto, R. Dillenschneider, and E. Lutz, “Experimental verification of Landauer’s principle linking information and thermodynamics,” Nature **483**, 187–189 (2012).

[194] A. Einstein, B. Podolsky, and N. Rosen, “Can Quantum-Mechanical Description of Physical Reality Be Considered Complete?” Physical Review **47**, 777–780 (1935).

[195] J. J. Sakurai and S. F. Tuan, *Modern Quantum Mechanics*, rev. ed. (Addison-Wesley Pub. Co, Reading, Mass, 1994).

[196] M. B. Hastings and T. Koma, “Spectral Gap and Exponential Decay of Correlations,” Communications in Mathematical Physics **265**, 781–804 (2006).

[197] T. Kuwahara and K. Saito, “Strictly Linear Light Cones in Long-Range Interacting Systems of Arbitrary Dimensions,” Physical Review X **10**, 031010 (2020).

[198] M. C. Tran, A. Y. Guo, C. L. Baldwin, A. Ehrenberg, A. V. Gorshkov, and A. Lucas, “Lieb-Robinson Light Cone for Power-Law Interactions,” Physical Review Letters **127**, 160401 (2021).

[199] D. V. Schroeder, *An Introduction to Thermal Physics* (Addison Wesley, San Francisco, CA, 2000).

[200] J. W. Gibbs, *Elementary Principles in Statistical Mechanics: Developed with Especial Reference to the Rational Foundations of Thermodynamics* (C. Scribner’s sons, 1902).

[201] J. L. W. V. Jensen, “Sur les fonctions convexes et les inégalités entre les valeurs moyennes,” Acta Mathematica **30**, 175–193 (1906).

[202] D. R. Wolf, “The Generalization of Mutual Information as the Information between a Set of Variables: The Information Correlation Function Hierarchy and the Information Structure of Multi-Agent Systems,” (2004).

[203] R. Yeung, “A new outlook on Shannon’s information measures,” IEEE Transactions on Information Theory **37**, 466–474 (1991).

[204] A. Kitaev and J. Preskill, “Topological entanglement entropy,” Physical Review Letters **96**, 110404 (2006).

[205] P. Hayden, M. Headrick, and A. Maloney, “Holographic mutual information is monogamous,” Physical Review D **87**, 046003 (2013).

[206] P. Hosur, X. L. Qi, D. A. Roberts, and B. Yoshida, “Chaos in quantum channels,” Journal of High Energy Physics **2016**, 1–49 (2016).

[207] M. Rangamani and M. Rota, “Entanglement structures in qubit systems,” Journal of Physics A: Mathematical and Theoretical **48**, 385301 (2015).

[208] M. Rota, “Tripartite information of highly entangled states,” Journal of High Energy Physics **2016**, 1–16 (2016).

[209] A. Seshadri, V. Madhok, and A. Lakshminarayan, “Tripartite mutual information, entanglement, and scrambling in permutation symmetric systems with an application to quantum chaos,” Physical Review E **98**, 052205 (2018).

[210] D. H. Wolpert, “Stochastic thermodynamics of computation,” Journal of Physics A: Mathematical and Theoretical **52**, 193001 (2019).

[211] Z. Zhang, “Generalized Mutual Information,” Stats **3**, 158–165 (2020).

[212] J. Von Neumann, *Mathematische Grundlagen Der Quantenmechanik* (Springer, Berlin, Germany, 1932).

[213] R. P. Feynman, “Simulating physics with computers,” International Journal of Theoretical Physics **21**, 467–488 (1982).

[214] S. Lloyd, “Universal Quantum Simulators,” Science **273**, 1073–1078 (1996).

[215] J. I. Cirac and P. Zoller, “Goals and opportunities in quantum simulation,” Nature Physics **8**, 264–266 (2012).

[216] A. Trabesinger, “Quantum simulation,” Nature Physics **8**, 263–263 (2012).

[217] T. H. Johnson, S. R. Clark, and D. Jaksch, “What is a quantum simulator?” EPJ Quantum Technology **1**, 10 (2014).

[218] I. M. Georgescu, S. Ashhab, and F. Nori, “Quantum simulation,” Reviews of Modern Physics **86**, 153–185 (2014).

[219] C. H. Bennett, G. Brassard, C. Crépeau, R. Jozsa, A. Peres, and W. K. Wootters, “Teleporting an unknown quantum state via dual classical and Einstein-Podolsky-Rosen channels,” Physical Review Letters **70**, 1895–1899 (1993).

[220] B. Schumacher, “Quantum coding,” Physical Review A **51**, 2738–2747 (1995).

[221] M. M. Wilde, *Quantum Information Theory*, 2nd ed. (Cambridge University Press, 2016).

[222] P. Benioff, “The computer as a physical system: A microscopic quantum mechanical Hamiltonian model of computers as represented by Turing machines,” Journal of Statistical Physics **22**, 563–591 (1980).

[223] D. Deutsch, “Quantum theory, the Church–Turing principle and the universal quantum computer,” Proceedings of the Royal Society of London. A. Mathematical and Physical Sciences **400**, 97–117 (1985).

[224] D. Deutsch, “Quantum computational networks,” Proceedings of the Royal Society of London. A. Mathematical and Physical Sciences **425**, 73–90 (1989).

[225] A. Y. Kitaev, “Fault-tolerant quantum computation by anyons,” Annals of Physics **303**, 2–30 (2003).

[226] V. Coffman, J. Kundu, and W. K. Wootters, “Distributed entanglement,” Physical Review A **61**, 052306 (2000).

[227] T. J. Osborne and F. Verstraete, “General Monogamy Inequality for Bipartite Qubit Entanglement,” Physical Review Letters **96**, 220503 (2006).

[228] S. Camalet, “Monogamy Inequality for Any Local Quantum Resource and Entanglement,” Physical Review Letters **119**, 110503 (2017).

[229] N. Linden and A. Winter, “A new inequality for the von Neumann entropy,” Communications in Mathematical Physics **259**, 129–138 (2005).

[230] J. Cadney, N. Linden, and A. Winter, “Infinitely many constrained inequalities for the von Neumann entropy,” IEEE Transactions on Information Theory **58**, 3657–3663 (2012).

[231] S. Sachdev, *Quantum Phase Transitions* (Wiley Online Library, Hoboken, NJ, 2007).

[232] J. Eisert, M. Cramer, and M. B. Plenio, "*Colloquium* : Area laws for the entanglement entropy," Reviews of Modern Physics **82**, 277–306 (2010).

[233] M. Vojta, "Quantum phase transitions," Reports on Progress in Physics **66**, 2069–2110 (2003).

[234] M. B. Hastings, "An Area Law for One Dimensional Quantum Systems," Journal of Statistical Mechanics: Theory and Experiment **2007**, P08024–P08024 (2007).

[235] F. Verstraete and J. I. Cirac, "Matrix product states represent ground states faithfully," Physical Review B **73**, 094423 (2006).

[236] D. N. Page, "Average entropy of a subsystem," Physical Review Letters **71**, 1291–1294 (1993).

[237] S. K. Foong and S. Kanno, "Proof of Page's conjecture on the average entropy of a subsystem," Physical Review Letters **72**, 1148–1151 (1994).

[238] E. Bianchi, L. Hackl, M. Kieburg, M. Rigol, and L. Vidmar, "Volume-Law Entanglement Entropy of Typical Pure Quantum States," PRX Quantum **3**, 030201 (2022).

[239] D. Hilbert, *The Foundations of Geometry* (Prabhat Prakashan, 1950).

[240] D. Bohm, "Quantum theory as an indication of a new order in physics. Part A. The development of new orders as shown through the history of physics," Foundations of Physics **1**, 359–381 (1971).

[241] D. Bohm, "Quantum theory as an indication of a new order in physics. B. Implicate and explicate order in physical law," Foundations of Physics **3**, 139–168 (1973).

[242] G. Wikman, "The Notion of Order in Mathematics and Physics. Similarity, Difference and Indistinguishability," Foundations of Physics **43**, 568–596 (2013).

[243] H. Lipkin, N. Meshkov, and A. Glick, "Validity of many-body approximation methods for a solvable model: (I). Exact solutions and perturbation theory," Nuclear Physics **62**, 188–198 (1965).

[244] N. Meshkov, A. Glick, and H. Lipkin, "Validity of many-body approximation methods for a solvable model: (II). Linearization procedures," Nuclear Physics **62**, 199–210 (1965).

[245] A. Glick, H. Lipkin, and N. Meshkov, "Validity of many-body approximation methods for a solvable model: (III). Diagram summations," Nuclear Physics **62**, 211–224 (1965).

[246] G. J. Milburn, J. Corney, E. M. Wright, and D. F. Walls, "Quantum dynamics of an atomic Bose-Einstein condensate in a double-well potential," Physical Review A **55**, 4318–4324 (1997).

[247] Alexander Ostrowski, "über einige Lösungen der Funktionalgleichung ψ(x)·ψ(x)=ψ(xy)," Acta Mathematica **41**, 271–284 (1916).

[248] A. Monna, "Sur une transformation simple des nombres P-adiques en nombres reels," Indagationes Mathematicae (Proceedings) **55**, 1–9 (1952).

[249] I. V. Volovich, "p-adic space-time and string theory," Theoretical and Mathematical Physics **71**, 574–576 (1987).

[250] E. Melzer, "NONARCHIMEDEAN CONFORMAL FIELD THEORIES," International Journal of Modern Physics A **04**, 4877–4908 (1989).

[251] V. S. Vladimirov and I. V. Volovich, "p-adic quantum mechanics," Communications in Mathematical Physics **123**, 659–676 (1989).

[252] M. Altaisky and B. Sidharth, "P-adic physics below and above planck scales," Chaos, Solitons & Fractals **10**, 167–176 (1999).

[253] B. Dragovich, "P-Adic and adelic quantum mechanics," Proceedings of the First Int. Conf. on p-Adic Mathematical Physics , 1–18 (2003).

[254] B. Dragovich and A. Khrennikov, "P-Adic and adelic superanalysis," Bulg. J. Phys. **33**, 98–113 (2006).

[255] I. V. Volovich, "Number theory as the ultimate physical theory," p-Adic Numbers, Ultrametric Analysis, and Applications **2**, 77–87 (2010).

[256] B. Dragovich, A. Y. Khrennikov, S. V. Kozyrev, I. V. Volovich, and E. I. Zelenov, "p-Adic mathematical physics: the first 30 years," p-Adic Numbers, Ultrametric Analysis and Applications **9**, 87–121 (2017).

[257] D. Harlow, S. Shenker, D. Stanford, and L. Susskind, "Eternal Symmetree," Physical Review D **85**, 063516 (2012).

[258] S. S. Gubser, "A p-adic version of AdS/CFT," Advances in Theoretical and Mathematical Physics **21**, 1655–1678 (2017).

[259] S. S. Gubser, J. Knaute, S. Parikh, A. Samberg, and P. Witaszczyk, "p-adic AdS/CFT," Communications in Mathematical Physics **352**, 1019–1059 (2017).

[260] S. S. Gubser, C. Jepsen, and B. Trundy, "Spin in p-adic AdS/CFT," Journal of Physics A: Mathematical and Theoretical **52**, 144004 (2019).

[261] P. Abramenko, K. S. Brown, and K. S. Brown, *Buildings: Theory and Applications*, Graduate Texts in Mathematics No. 251 (Springer, Charlottesville, VA, 2008).

[262] E. Lorenz, "Predictability: Does the flap of a butterfly's wing in Brazil set off a tornado in Texas?" (1972).

[263] H. Poincaré, *The Three-Body Problem and the Equations of Dynamics*, Astrophysics and Space Science Library, Vol. 443 (Springer International Publishing, Cham, 2017).

[264] A. A. N. Kolmogorov, "On conservation of conditionally periodic motions for a small change in Hamilton's function," Proceedings of the USSR Academy of Sciences **98**, 527–530 (1954).

[265] V. I. Arnol'd, "PROOF OF A THEOREM OF A. N. KOLMOGOROV ON THE INVARIANCE OF QUASI-PERIODIC MOTIONS UNDER SMALL PERTURBATIONS OF THE HAMILTONIAN," Russian Mathematical Surveys **18**, 9–36 (1963).

[266] J. K. Moser, "On invariant curves of area-preserving mappings of an anulus," Matematika **6**, 51–68 (1962).

[267] V. Khemani, D. A. Huse, and A. Nahum, "Velocity-dependent Lyapunov exponents in many-body quantum, semiclassical, and classical chaos," Physical Review B **98**, 144304 (2018).

[268] M. Srednicki, "The approach to thermal equilibrium in quantized chaotic systems," Journal of Physics A: Mathematical and General **32**, 1–15 (1999).

[269] S. Wimberger, *Nonlinear Dynamics and Quantum Chaos : An Introduction*, 1st ed., Graduate Texts in Physics (Springer, Cham, Switzerland, 2014).

[270] J. C. Halimeh, V. Zauner-Stauber, I. P. McCulloch, I. de Vega, U. Schollwöck, and M. Kastner, "Prethermalization and persistent order in the absence of a thermal phase transition," Physical Review B **95**, 024302 (2017).

[271] B. Neyenhuis, J. Zhang, P. W. Hess, J. Smith, A. C. Lee, P. Richerme, Z.-X. Gong, A. V. Gorshkov, and C. Monroe, "Observation of prethermalization in long-range interacting spin chains," Science Advances **3**, e1700672 (2017).

[272] P. Reimann, "Typical fast thermalization processes in closed many-body systems," Nature Communications **7**, 10821 (2016).

[273] K. Hashimoto, K. Murata, and R. Yoshii, "Out-of-time-order correlators in quantum mechanics," Journal of High Energy Physics **2017**, 138 (2017).

[274] X. Chen, T. Zhou, D. A. Huse, and E. Fradkin, "Out-of-time-order correlations in many-body localized and thermal phases," Annalen der Physik **529**, 1600332 (2017).

[275] P. Bordia, F. Alet, and P. Hosur, "Out-of-time-ordered measurements as a probe of quantum dynamics," Physical Review A **97**, 30103 (2018).

[276] H. Bonekamp, "Opleiding wiskunde voor de industrie Eindhoven : Student report," Opleiding wiskunde voor de industrie Eindhoven : student report **9369**, 51 (1993).

[277] J. S. Cotler, D. Ding, and G. R. Penington, "Out-of-time-order operators and the butterfly effect," Annals of Physics **396**, 318–333 (2018).

[278] T. Takahiro, *Hatsu Bi San Pou Endan Genkai* (Japan, 1685).

[279] E. Noether, "Invariante Variationsprobleme," Nachrichten von der Gesellschaft der Wissenschaften zu Göttingen, Mathematisch-Physikalische Klasse **1918**, 235–257 (1918).

[280] M. Stone, *The Physics of Quantum Fields* (Springer Science & Business Media, Berlin, Germany, 2012).

[281] P. Coleman, *Introduction to Many-Body Physics* (Cambridge University Press, Cambridge, England, 2015).

[282] R. A. Horn and C. R. Johnson, *Matrix Analysis* (Cambridge University Press, Cambridge, England, 2012).

[283] C. Moler and C. Van Loan, "Nineteen dubious ways to compute the exponential of a matrix, twenty-five years later," SIAM Review **45**, 3–49 (2003).

[284] C. Lanczos, "An iteration method for the solution of the eigenvalue problem of linear differential and integral operators," Journal of research of the National Bureau of Standards **45**, 255–282 (1950).

[285] L. Orecchia, S. Sachdeva, and N. K. Vishnoi, "Approximating the exponential, the lanczos method and an $\tilde{O}(m)$-time spectral algorithm for balanced separator," in *Proceedings of the 44th symposium on Theory of Computing - STOC '12* (ACM Press, New York, New York, USA, 2012) p. 1141.

[286] William H. Press, S. A. Teukolsky, W. T. Vetterling, and B. P. Flannery, *Numerical Recipes 3rd Edition*, 3rd ed. (Cambridge University Press, Cambridge, England, 2007).

[287] M. Fannes, B. Nachtergaele, and R. F. Werner, "Finitely correlated states on quantum spin chains," Communications in Mathematical Physics **144**, 443–490 (1992).

[288] A. Klümper, A. Schadschneider, and J. Zittartz, "Groundstate properties of a generalized VBS-model," Zeitschrift f ur Physik B Condensed Matter **87**, 281–287 (1992).

[289] F. Verstraete, D. Porras, and J. I. Cirac, "Density Matrix Renormalization Group and Periodic Boundary Conditions: A Quantum Information Perspective," Physical Review Letters **93**, 227205 (2004).

[290] U. Schollwöck, "The density-matrix renormalization group," Reviews of Modern Physics **77**, 259–315 (2005).

[291] D. Perez-Garcia, F. Verstraete, M. M. Wolf, and J. I. Cirac, "Matrix product state representations," Journal of the Physical Society of Japan **81**, 074003 (2006).

[292] J. Jordan, R. Orus, G. Vidal, F. Verstraete, and J. I. Cirac, "Classical simulation of infinite-size quantum lattice systems in two spatial dimensions," Physical Review Letters **101**, 250602 (2008).

[293] F. Verstraete, V. Murg, and J. Cirac, "Matrix product states, projected entangled pair states, and variational renormalization group methods for quantum spin systems," Advances in Physics **57**, 143–224 (2008).

[294] G. Evenbly and G. Vidal, "Tensor network states and geometry," Journal of Statistical Physics **145**, 891–918 (2011).

[295] S. Kung and D. Lin, "Optimal Hankel-norm model reductions: Multivariable systems," IEEE Transactions on Automatic Control **26**, 832–852 (1981).

[296] M. L. Wall, "Matrix product operator representation of polynomial interactions," Journal of Physics A: Mathematical and Theoretical **53**, 215301 (2020).

[297] R. Penrose, "Applications of negative dimensional tensors," Combinatorial mathematics and its applications **1**, 221–244 (1971).

[298] R. Penrose, "Angular momentum: An approach to combinatorial spacetime," in *Living Reviews in Relativity http://www.livingreviews.org/lrr-2008-5 Carlo Rovelli* (University Press, 1971) pp. 151–180.

[299] A. Klumper, A. Schadschneider, and J. Zittartz, "Equivalence and solution of anisotropic spin-1 models and generalized t-J fermion models in one dimension," Journal of Physics A: Mathematical and General **24**, L955–L959 (1991).

[300] F. Verstraete and J. I. Cirac, "Renormalization algorithms for Quantum-Many Body Systems in two and higher dimensions," (2004), arXiv:cond-mat/0407066 .

[301] Y.-Y. Shi, L.-M. Duan, and G. Vidal, "Classical simulation of quantum many-body systems with a tree tensor network," Physical Review A **74**, 022320 (2006).

[302] N. Schuch, M. M. Wolf, F. Verstraete, and J. I. Cirac, "Computational Complexity of Projected Entangled Pair States," Physical Review Letters **98**, 140506 (2007).

[303] S. Singh, R. N. C. Pfeifer, and G. Vidal, "Tensor network decompositions in the presence of a global symmetry," Physical Review A **82**, 050301 (2010).

[304] M. L. Wall and L. D. Carr, "Out-of-equilibrium dynamics with matrix product states," New Journal of Physics **14**, 125015 (2012).

[305] F. Verstraete, M. Wolf, D. Pérez-García, and J. I. Cirac, "PROJECTED ENTANGLED STATES: PROPERTIES AND APPLICATIONS," International Journal of Modern Physics B **20**, 5142–5153 (2006).

[306] A. Rényi, "On measures of entropy and information," in *Proceedings of the Fourth Berkeley Symposium on Mathematical Statistics and Probability*, Vol. 1 (Berkeley, California, USA, 1961).

[307] M. Müller-Lennert, F. Dupuis, O. Szehr, S. Fehr, and M. Tomamichel, "On quantum Rényi entropies: A new generalization and some properties," Journal of Mathematical Physics **54**, 122203 (2013).

[308] B. Swingle, "Entanglement renormalization and holography," Physical Review D **86**, 065007 (2012).

[309] F. Bloch, "Nuclear Induction," Physical Review **70**, 460–474 (1946).

[310] P. Selinger, "Generators and relations for n-qubit Clifford operators," Logical Methods in Computer Science **11**, 80–94 (2015).

[311] I. Danshita, M. Hanada, and M. Tezuka, "Creating and probing the Sachdev–Ye–Kitaev model with ultracold gases: Towards experimental studies of quantum gravity," Progress of Theoretical and Experimental Physics **2017** (2017), 10.1093/ptep/ptx108.

[312] A. Chew, A. Essin, and J. Alicea, "Approximating the Sachdev-Ye-Kitaev model with Majorana wires," Physical Review B **96**, 121119 (2017).

[313] D. A. Roberts and B. Swingle, "Lieb-Robinson Bound and the Butterfly Effect in Quantum Field Theories," Physical Review Letters **117**, 091602 (2016).

[314] M. B. Hastings, "Locality in Quantum Systems," (2010), arXiv:1008.5137 .

[315] M. Foss-Feig, Z.-X. Gong, C. W. Clark, and A. V. Gorshkov, "Nearly Linear Light Cones in Long-Range Interacting Quantum Systems," Physical Review Letters **114**, 157201 (2015).

[316] D. V. Else, F. Machado, C. Nayak, and N. Y. Yao, "Improved Lieb-Robinson bound for many-body Hamiltonians with power-law interactions," Physical Review A **101**, 022333 (2020).

[317] N. W. Ashcroft and N. D. Mermin, *Solid State Physics* (Holt, Rinehart and Winston, New York, 1976).

[318] C. Kittel, *Introduction to Solid State Physics*, 8th ed. (Wiley, Hoboken, NJ, 2005).

[319] A. S. Buyskikh, M. Fagotti, J. Schachenmayer, F. Essler, and A. J. Daley, "Entanglement growth and correlation spreading with variable-range interactions in spin and fermionic tunneling models," Physical Review A **93**, 053620 (2016).

[320] K. Weierstrass, "Uber continuirliche Functionen eines reellen Arguments, die fur keinen Werth des letzteren einen bestimmten Differentialquotienten bezitsen," Mathematische Werke **2**, 71–74 (1872).

[321] B. R. Hunt, "The hausdorff dimension of graphs of weierstrass functions," Proceedings of the American mathematical society **126**, 791–800 (1998).

[322] V. E. Tarasov, "Chains with the fractal dispersion law," Journal of Physics A: Mathematical and Theoretical **41**, 035101 (2008).

[323] M. L. Mehta, *Random Matrices*, 3rd ed., Pure and Applied Mathematics (Academic Press) ; 142 (Academic Press, Amsterdam ; San Diego, CA, 2004).

[324] E. McCulloch and C. W. von Keyserlingk, "Operator spreading in the memory matrix formalism," Journal of Physics A: Mathematical and Theoretical **55**, 274007 (2022).

[325] K. Osterloh, M. Baig, L. Santos, P. Zoller, and M. Lewenstein, "Cold Atoms in Non-Abelian Gauge Potentials: From the Hofstadter "Moth" to Lattice Gauge Theory," Physical Review Letters **95**, 010403 (2005).

[326] J. Steinhauer, "Observation of quantum Hawking radiation and its entanglement in an analogue black hole," Nature Physics **12**, 959–965 (2016).

[327] S. Eckel, A. Kumar, T. Jacobson, I. B. Spielman, and G. K. Campbell, "A Rapidly Expanding Bose-Einstein Condensate: An Expanding Universe in the Lab," Physical Review X **8**, 021021 (2018).

[328] A. Bhattacharyya, L. K. Joshi, and B. Sundar, "Quantum information scrambling: From holography to quantum simulators," The European Physical Journal C **82**, 458 (2022).

[329] G. H. Hardy and C. P. Snow, *A Mathematician's Apology*, 26th ed. (Cambridge Univ. Press, Cambridge, 2019).

[330] M. Kim, Y. Song, J. Kim, and J. Ahn, "Quantum Ising Hamiltonian Programming in Trio, Quartet, and Sextet Qubit Systems," PRX Quantum **1**, 020323 (2020).

[331] A. Browaeys and T. Lahaye, "Many-body physics with individually controlled Rydberg atoms," Nature Physics **16**, 132–142 (2020).

[332] C. S. Adams, J. D. Pritchard, and J. P. Shaffer, "Rydberg atom quantum technologies," Journal of Physics B: Atomic, Molecular and Optical Physics **53** (2020), 10.1088/1361-6455/ab52ef.

[333] S. Weber, C. Tresp, H. Menke, A. Urvoy, O. Firstenberg, H. P. Büchler, and S. Hofferberth, "Calculation of Rydberg interaction potentials," Journal of Physics B: Atomic, Molecular and Optical Physics **50**, 133001 (2017).

[334] Y. Bao, M. Block, and E. Altman, "Finite time teleportation phase transition in random quantum circuits," (2022), arXiv:2110.06963 [cond-mat, physics:quant-ph] .

[335] S. S. Gubser, C. Jepsen, Z. Ji, and B. Trundy, "Mixed field theory," Journal of High Energy Physics **2019**, 136 (2019).

[336] R. Cleve, D. Leung, L. Liu, and C. Wang, "Near-linear constructions of exact unitary 2-designs," Quantum Information and Computation **16**, 0721–0756 (2016).

[337] T. Koshy, *Fibonacci and Lucas Numbers with Applications* (Wiley, New York, 2011).

[338] L. Henriet, L. Beguin, A. Signoles, T. Lahaye, A. Browaeys, G.-O. Reymond, and C. Jurczak, "Quantum computing with neutral atoms," Quantum **4**, 327 (2020).

[339] M. Morgado and S. Whitlock, "Quantum simulation and computing with Rydberg-interacting qubits," AVS Quantum Science **3**, 023501 (2021).

[340] D. Aldous and P. Diaconis, "Shuffling Cards and Stopping Times," The American Mathematical Monthly **93**, 333–348 (1986).

[341] S. Sahu, S.-K. Jian, G. Bentsen, and B. Swingle, "Entanglement Phases in large-N hybrid Brownian circuits with long-range couplings," (2021), arXiv:2109.00013 .

[342] G. S. Bentsen, S. Sahu, and B. Swingle, "Measurement-induced purification in large-N hybrid Brownian circuits," Physical Review B **104**, 094304 (2021).

[343] M. K. Joshi, A. Elben, B. Vermersch, T. Brydges, C. Maier, P. Zoller, R. Blatt, and C. F. Roos, "Quantum Information Scrambling in a Trapped-Ion Quantum Simulator with Tunable Range Interactions," Physical Review Letters **124**, 240505 (2020).

[344] D. N. Page, "Information in black hole radiation," Physical Review Letters **71**, 3743–3746 (1993).

[345] L. Susskind, "Entanglement is not enough," Fortschritte der Physik **64**, 49–71 (2016).

[346] D. I. Pikulin and M. Franz, "Black Hole on a Chip: Proposal for a Physical Realization of the Sachdev-Ye-Kitaev model in a Solid-State System," Physical Review X **7**, 031006 (2017).

[347] M. Leifer and D. Poulin, "Quantum Graphical Models and Belief Propagation," Annals of Physics **323**, 1899–1946 (2008).

[348] F. Pastawski, B. Yoshida, D. Harlow, and J. Preskill, "Holographic quantum error-correcting codes: Toy models for the bulk/boundary correspondence," Journal of High Energy Physics **2015** (2015), 10.1007/JHEP06(2015)149.

[349] M. Heydeman, M. Marcolli, I. A. Saberi, and B. Stoica, "Tensor networks, p-adic fields, and algebraic curves: arithmetic and the $\mathrm{AdS}_3/\mathrm{CFT}_2$ correspondence," Advances in Theoretical and Mathematical Physics **22**, 93–176 (2018).

[350] A. Dymarsky and A. Shapere, "Quantum stabilizer codes, lattices, and CFTs," Journal of High Energy Physics **2021**, 160 (2021).

[351] A. Einstein, A. Beck, and P. Havas, *The Collected Papers of Albert Einstein* (Princeton University Press, Princeton, N.J, 1987).

[352] Y. Li and M. P. A. Fisher, "Statistical mechanics of quantum error correcting codes," Physical Review B **103**, 104306 (2021).

[353] S. Vijay, "Measurement-Driven Phase Transition within a Volume-Law Entangled Phase," (2020), arXiv:2005.03052 .

[354] C. Noel, P. Niroula, D. Zhu, A. Risinger, L. Egan, D. Biswas, M. Cetina, A. V. Gorshkov, M. J. Gullans, D. A. Huse, and C. Monroe, "Measurement-induced quantum phases realized in a trapped-ion quantum computer," Nature Physics **18**, 760–764 (2022).

[355] M. A. Nielsen, "Cluster-state quantum computation," Reports on Mathematical Physics **57**, 147–161 (2006).

[356] A. Mantri, T. F. Demarie, and J. F. Fitzsimons, "Universality of quantum computation with cluster states and (X, Y)-plane measurements," Scientific Reports **7**, 42861 (2017).

[357] D. Stauffer, *Introduction to Percolation Theory*, rev. 2nd ed. (Taylor & Francis, London, 1994).

[358] M. E. J. Newman and R. M. Ziff, "A fast Monte Carlo algorithm for site or bond percolation," Physical Review E **64**, 016706 (2001).

[359] Y. Shang, "Uniqueness of the Infinite Component for Percolation on a Hierarchical Lattice," ISRN Discrete Mathematics **2012**, 1–6 (2012).

[360] F. Radicchi and C. Castellano, "Beyond the locally treelike approximation for percolation on real networks," Physical Review E **93**, 030302 (2016).

[361] H. Kesten, "The critical probability of bond percolation on the square lattice equals $\frac{1}{2}$," Communications in Mathematical Physics **74**, 41–59 (1980).

[362] J. E. Hopcroft and J. D. Ullman, "Set Merging Algorithms," SIAM Journal on Computing **2**, 294–303 (1973).

[363] R. E. Tarjan, “Efficiency of a Good But Not Linear Set Union Algorithm,” Journal of the ACM **22**, 215–225 (1975).

[364] K. Binder, “Finite size scaling analysis of ising model block distribution functions,” Zeitschrift für Physik B Condensed Matter **43**, 119–140 (1981).

[365] O. Melchert, H. G. Katzgraber, and M. A. Novotny, “Site- and bond-percolation thresholds in $K_{n,n}$-based lattices: Vulnerability of quantum annealers to random qubit and coupler failures on chimera topologies,” Physical Review E **93**, 1–9 (2016).

[366] V. Privman and M. E. Fisher, “Universal critical amplitudes in finite-size scaling,” Physical Review B **30**, 322–327 (1984).

[367] D. Hilbert, “Naturerkennen und Logik,” (1930).

[368] N. D. Mermin and H. Wagner, “Absence of ferromagnetism or antiferromagnetism in one- or two-dimensional isotropic Heisenberg models,” Physical Review Letters **17**, 1133–1136 (1966).

[369] P. Bruno, “Absence of spontaneous magnetic order at nonzero temperature in one- and two-dimensional heisenberg and XY systems with long-range interactions,” Physical Review Letters **87**, 3–6 (2001).

[370] J. I. Cirac and F. Verstraete, “Renormalization and tensor product states in spin chains and lattices,” Journal of Physics A: Mathematical and Theoretical **42**, 504004 (2009).

[371] L. Tagliacozzo, A. Celi, A. Zamora, and M. Lewenstein, “Optical Abelian lattice gauge theories,” Annals of Physics **330**, 160–191 (2013).

[372] T. Felser, P. Silvi, M. Collura, and S. Montangero, “Two-Dimensional Quantum-Link Lattice Quantum Electrodynamics at Finite Density,” Physical Review X **10**, 041040 (2020).

[373] S. Lepoutre, J. Schachenmayer, L. Gabardos, B. Zhu, B. Naylor, E. Maréchal, O. Gorceix, A. M. Rey, L. Vernac, and B. Laburthe-Tolra, “Out-of-equilibrium quantum magnetism and thermalization in a spin-3 many-body dipolar lattice system,” Nature Communications **10**, 1714 (2019).

[374] J. Schachenmayer, A. Pikovski, and A. M. Rey, “Many-Body Quantum Spin Dynamics with Monte Carlo Trajectories on a Discrete Phase Space,” Physical Review X **5**, 011022 (2015).

[375] B. Zhu, A. M. Rey, and J. Schachenmayer, “A generalized phase space approach for solving quantum spin dynamics,” New Journal of Physics **21**, 082001 (2019).

[376] K. M. Gutzmann, “Optimal dimension of hypercubes for sorting,” ACM SIGARCH Computer Architecture News **15**, 68–72 (1987).

[377] K. Hwang and F. A. Briggs, *Computer Architecture and Parallel Processing*, McGraw-Hill Series in Computer Organisation and Architecture (McGraw-Hill, New York, NY, 1984).

[378] M. Hein, J. Eisert, and H. J. Briegel, “Multiparty entanglement in graph states,” Physical Review A **69**, 062311 (2004).

[379] S. R. Clark, C. M. Alves, and D. Jaksch, “Efficient generation of graph states for quantum computation,” New Journal of Physics **7**, 124–124 (2005).

[380] Hein, M., Dür, W., Eisert, J., Raussendorf, R., Van den Nest, M., and Briegel H.-J., “Entanglement in graph states and its applications,” in *Proceedings of the International School of Physics ”Enrico Fermi” on ”Quantum Computers, Algorithms and Chaos”*, Vol. 162 (Varenna, Italy, 2005).

[381] W. Fu and S. Sachdev, “Numerical study of fermion and boson models with infinite-range random interactions,” Physical Review B **94**, 1–9 (2016).

[382] A. J. Park, J. Trautmann, N. Šantić, V. Klüsener, A. Heinz, I. Bloch, and S. Blatt, “Cavity-Enhanced Optical Lattices for Scaling Neutral Atom Quantum Technologies to Higher Qubit Numbers,” PRX Quantum **3**, 030314 (2022).

[383] J.-Q. Chen, J. Ping, and F. Wang, *Group Representation Theory for Physicists* (2002).

[384] H. de Guise, O. Di Matteo, and L. L. Sanchez-Soto, “Simple factorization of unitary transformations,” Physical Review A **97**, 022328 (2018).

[385] F. Mezzadri, “How to generate random matrices from the classical compact groups,” (2007), arXiv:math-ph/0609050 .

[386] V. F. Kolchin, "Systems of random linear equations in GF(2)," in *Random Graphs* (Cambridge University Press, Cambridge, England, 1998) pp. 122–180.

[387] G. H. Hardy *et al.*, *An Introduction to the Theory of Numbers* (Oxford university press, Oxford, 1979).

Part VI

Appendices

A Haar Random $SU(2)$ unitary

SU(2) is a group of 2 by 2 unitary matrices with determinant of 1 [383]. For this group, a Haar measure μ is defined as a measure over subset of $S \subseteq SU(2)$ that is invariant under rotation by the element $g \in \mathrm{SU}(2)$: $\mu(S) = \mu(gS)$, where

$$\mu(S) = \int_{s\in S} d\mu(s). \tag{A.1}$$

Since SU(2) matrix can be parameterized as

$$g(\phi,\theta,\chi) = \begin{pmatrix} e^{i\phi}\cos(\theta) & e^{i\chi}\sin(\theta) \\ -e^{-i\chi}\sin(\theta) & e^{-i\phi}\cos(\theta) \end{pmatrix}, \tag{A.2}$$

or equivalently, with real numbers w, x, , y, z

$$g(w,x,y,z) = \begin{pmatrix} w+ix & y+iz \\ -y+iz & w-ix \end{pmatrix}, \tag{A.3}$$

with $w^2 + x^2 + y^2 + z^2 = 1$. This is nothing but the 3-dimensional surface of a 4-dimensional sphere. Since its area is invariant under a rotation, it is a Haar measure. Taking the volume element by calculating the Jacobian and taking the derivative by its radius yields the measure to be

$$d\mu \propto \frac{1}{2}\sin(2\theta)d\theta d\phi d\chi = \frac{1}{2}d\left(\sin^2(\theta)\right)d\phi d\chi. \tag{A.4}$$

Therefore, a random SU(2) unitary can be generated by taking random numbers between 0 and 2π for ϕ and χ, and random number between 0 and 1 for determining $\sin^2(\theta)$. A Haar random two-qubit gate can then be obtained SU(4) by utilizing the decomposition [384]:

$$\mathrm{SU}(N) = \left(I_0 \otimes \mathrm{SU}(N-1)_{1,\ldots,N-1}\right) \times \left(\mathrm{SU}(2) \otimes I_{2,\ldots,N-1}\right) \times \left(I_0 \otimes \mathrm{SU}(N-1)_{1,\ldots,N-1}\right), \tag{A.5}$$

where the subscripts denote the set of qubits which operators SU(N) and the identity I are acting on.

However, this method of generating the Haar random unitary matrix is not practical, as it requires generation of $SU(2)$ operators of $\mathcal{O}(N)$, and contractions of them. Practically, a generation of Haar random unitary is done using QR decomposition [385]. Let M be a random complex matrix where the real and the imaginary part of the elements $(M)_{ij}$ are drawn from a normal distribution with mean 0 and variance 1. QR decomposition decomposes matrix M into an orthogonal matrix Q and an upper triangular matrix R. Since Q is a complex orthonormal matrix, it is already a unitary. Now let Λ be a diagonal matrix with the normalized diagonal elements of R, where the i^{th} element of Λ is given as $(\Lambda)_{ii} = (R)_{ii}/|(R)_{ii}|$. This step takes away an ambiguity in the QR decomposition because any diagonal matrix Λ and its inverse can be inserted $M = Q\Lambda\Lambda^{-1}R$ and yield equally valid QR decomposition with orthonormal matrix $Q' = Q\Lambda$ and upper triangular matrix $R' = \Lambda^{-1}R$. Now the ambiguity is taken away, and the resulting distribution of matrices $M' = Q\Lambda$ is uniformly distributing accordingly to the Haar measure.

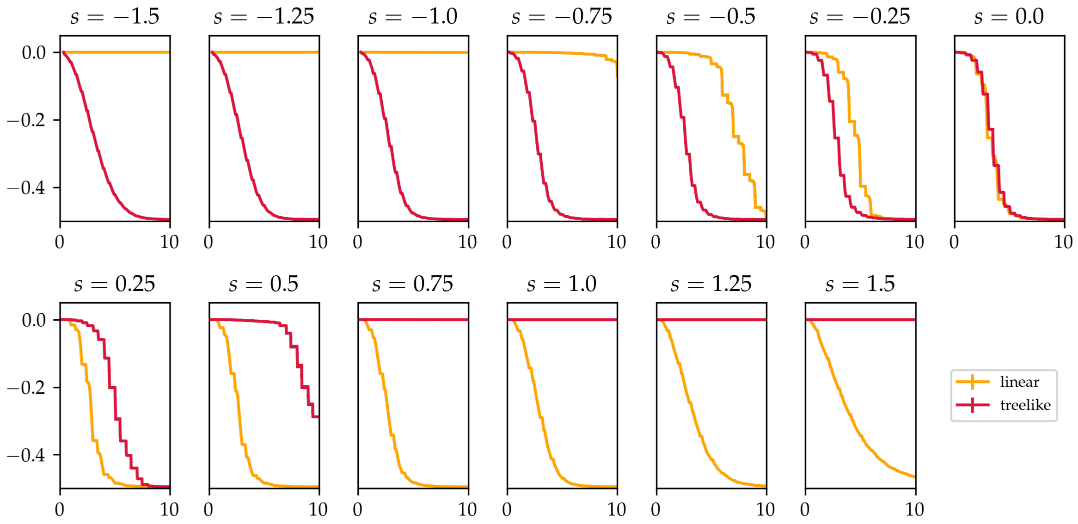

FIGURE B.1: **Time dependence of the tripartite mutual information.** The time dependence of the tripartite mutual information $I(A : B : C)/N \ln 2$ evolved with the sparse Clifford circuit up to $t = 10$ with system size $N = 512$ for $s = -1.5, -1.25, -1.0, -0.5, -0.75, -0.25, 0, 0.25, 0.5, 0.75, 1.0, 1.5$. It is calculated with the four contiguous systems of size $L_{\text{sub}} = N/4$ for linear and treelike geometries (orange and red respectively). The mean values are calculated and the errors are estimated from 1×10^2 trajectories. This figure was reproduced from [187].

B Time Dependence of Tripartite Mutual Information

This section is reproduced from sections that were written by the author of this thesis in the following publication: T. Hashizume, S. Kuriyattil, A. J. Daley, and G. Bentsen, "Tunable Geometries in Sparse Clifford Circuits," *Symmetry*, **14**, 666 (2022). [187].

The color plot in Fig. 6.2 a. is a plot of the tripartite mutual information of a state evolved in the sparse Clifford circuit with system size $N = 512$. It is plotted for the values of s: $s = -1.5, -1.25, -1.0, -0.5, -0.75, -0.25, 0, 0.25, 0.5, 0.75, 1.0,$ and 1.5. In Fig. B.1, we show the time dependence of the quantity in linear and treelike geometries (orange and red respectively) from $t = 0$ to $t = 10$. The mean values are obtained and errors are estimated from 1×10^2 trajectories.

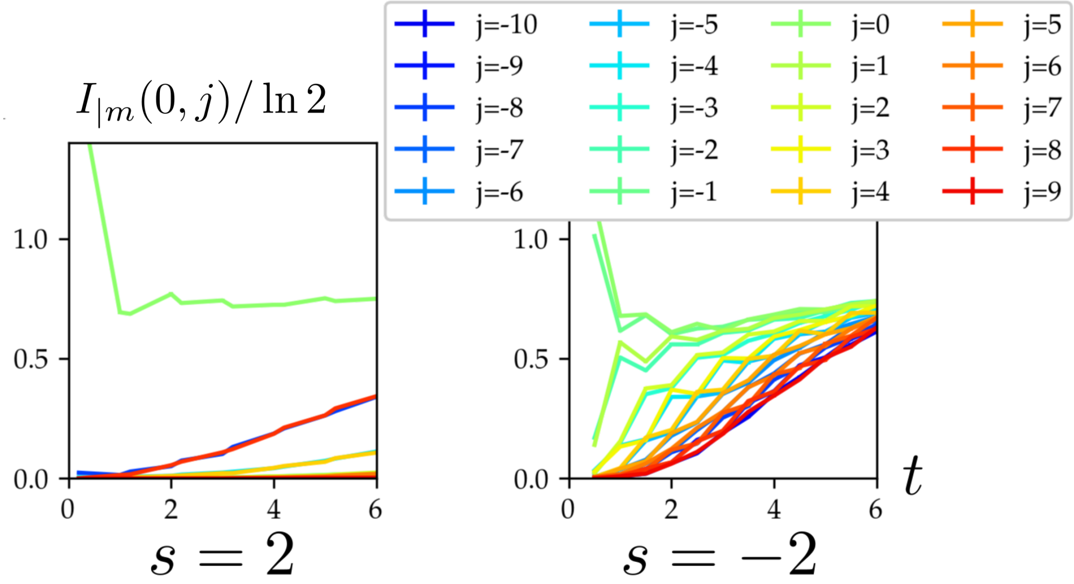

FIGURE C.1: **Time dependence of teleportation fidelity for different sites.** The time dependence of the teleportation fidelity $I_{|m}(0;j)$ evolved up to $t = 6$ with system size $N = 128$ for $s = -2$ and $s = 2$ for $j = -10, -9, \ldots, 8, 9$. The mean values are calculated and the errors are estimated from 1.5×10^4 trajectories. This figure was reproduced from [187].

C Time Dependence of Teleportation Fidelity

This section is reproduced from sections that were written by the author of this thesis in the following publication: T. Hashizume, S. Kuriyattil, A. J. Daley, and G. Bentsen, "Tunable Geometries in Sparse Clifford Circuits," *Symmetry*, **14**, 666 (2022). [187].

C.1 Teleportation Fidelity for Fixed s and Varying sites B

The color plot in Fig. 6.5 a. is a plot of teleportation fidelity $I_{|m}(0,j)$ of a state evolved in the sparse Clifford circuit with system size $N = 128$. It is plotted for $s = -2$ (left) and $s = 2$ (right) for the sites $j = -10, -9, \ldots, 8, 9$. In Fig. C.1, we show the time dependency of the quantity from $t = 0$ to $t = 6$ for $s = 2$ (left) and $s = -2$ (right) at the different sites (the lines of various colors). The mean values are obtained and errors are estimated from 1.5×10^4 trajectories.

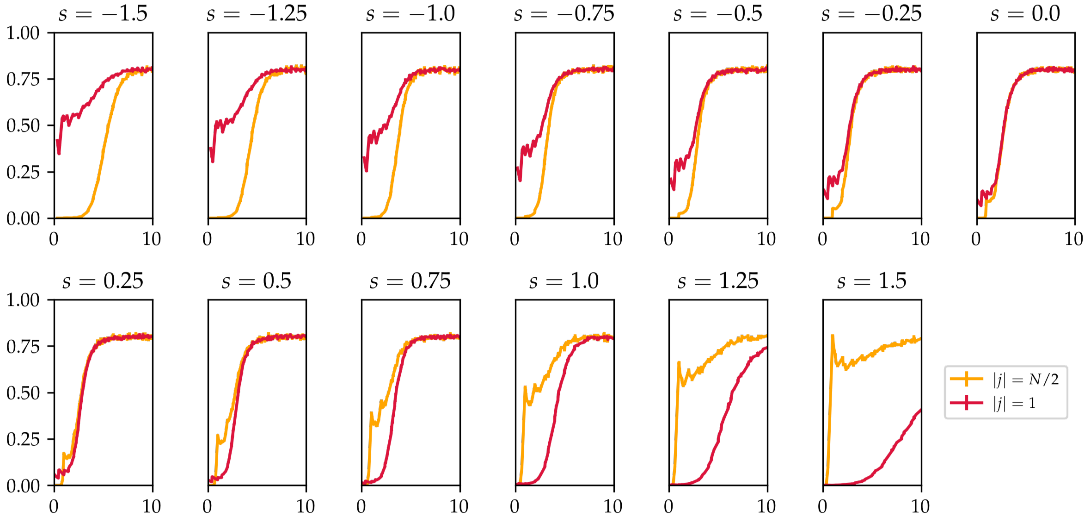

FIGURE C.2: **Time dependence of teleportation fidelity for fixed s.** The time dependence of the teleportation fidelity $I_{|m}(0, j)$ evolved up to $t = 6$ with system size $N = 128$ for $s = -1.5, -1.25, -1, -0.75, -0.5, -0.25, 0, 0.25, 0.5, 0.75, 1, 1.25, 1.5$. The teleportation fidelity is calculated for $|j| = N/2$ for characterizing the linear (Euclidean) geometry and the average of $j = 1$ and $j = -1$ for characterizing the treelike (2-adic) geometry. The mean values are calculated and the errors are estimated from 1.5×10^4 trajectories. This figure was reproduced from [187].

C.2 Teleportation Fidelity for Fixed sites and varying s

The color plot in Fig. 6.5 c. is a plot of teleportation fidelity $I_{|m}(0, j)$ of a state evolved in the sparse Clifford circuit with system size $N = 128$. It is plotted for $j = N/2$ and the average of $j = -1$ and $j = 1$ to characterize the behavior of the teleportation fidelity in linear and treelike respectively for $s = -1.5, -1.25, -1, -0.75, -0.5, -0.25, 0, 0.25, 0.5, 0.75, 1, 1.25, 1.5$. In Fig. C.2, we show the time dependence of the quantity from $t = 0$ to $t = 10$ for the values of s mentioned above, for $j = N/2$ (orange) and average of $j = -1$ and $j = 1$ (red). The mean values are obtained and errors are estimated from 1.5×10^4 trajectories.

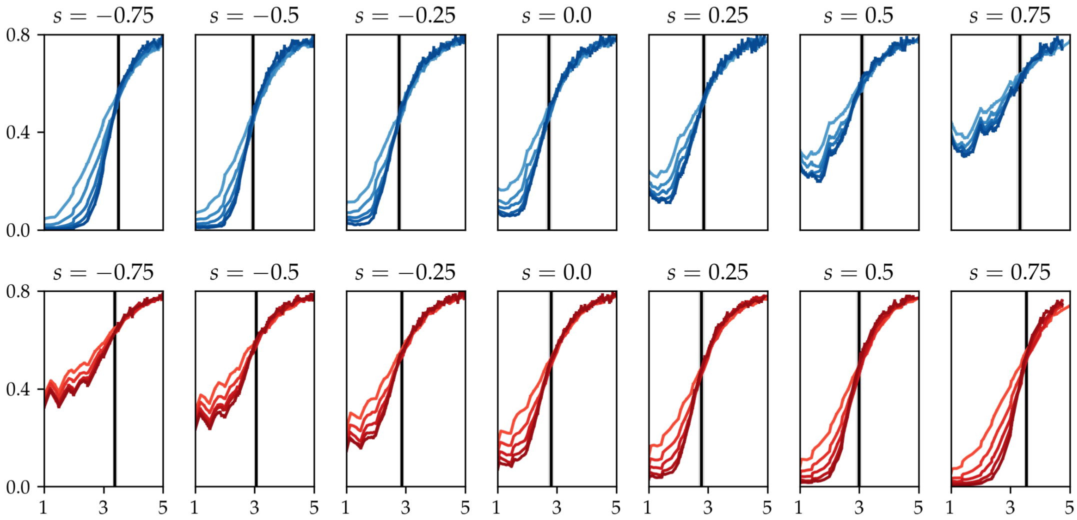

FIGURE C.3: **Time dependence of teleportation fidelity for different system sizes.** The time dependence of the teleportation fidelity $I_{|m}(0, j)$ evolved up to $t = 5$ for $s = -0.75, -0.5, -0.25, 0, 0.25, 0.5, 0.75$ for the system sizes $N = 2^5, 2^6, \ldots, 2^9$ (light to dark). The quantity is calculated for the sites $j = N/2$ for characterizing the linear (Euclidean) geometry (upper panels, blue) and average between $j = -1$ and $j = 1$ for characterizing the treelike geometry (lower panels, red). The mean values are calculated, and the errors are estimated from 1×10^2 (for $N = 2^9$) up to 1.5×10^4 (for $N = 2^5$) trajectories. This figure was reproduced from [187].

C.3 Finite-Size Scaling for Finding t_c of Teleportation Fidelity

The critical time t_c which divides the non-teleporting $t < t_c$ and teleporting $t_c < t$ regimes shown in the black line in Fig. 6.5 c. is calculated from the crossing points of the teleportation fidelity for the different system sizes. Here, in Fig. C.3, the quantity is plotted for the values of $s = -0.75, -0.5, -0.25, 0, 0.25, 0.5, 0.75$ for the system sizes $N = 2^5, 2^6, \ldots, 2^9$ (light to dark). The quantity is calculated for the sites $j = N/2$ for characterizing the linear (Euclidean) geometry (upper panels, blue) and average between $j = -1$ and $j = 1$ for characterizing the treelike geometry (lower panels, red). The mean values are calculated, and the errors are estimated from up to 1.5×10^4 trajectories. Crossings are not observed for $s \leq -1.0$ and $1.0 \leq s$ in the system sizes that we investigated.

D Derivation of the Page-Clifford Limit

This section is reproduced from sections that were written by the author of this thesis in the following publication: T. Hashizume, G. S. Bentsen, S. Weber, and A. J. Daley, "Deterministic Fast Scrambling with Neutral Atom Arrays," *Physical Review Letters*, **126**, 200603 (2021). [185].

As it is shown in Ch. 4.4.5, a stabilizer state of N qubits can be represented by an N by $2N$ binary matrix M. A random stabilizer state can therefore be constructed from a random binary matrix with a constraint $\mathrm{rank}_{\mathrm{GF}(2)}(M) = N$. Also, the entropy of a subsystem of size $|X|$ of a stabilizer state can be obtained by subtracting $|X|$ from the rank of the corresponding region. The average entropy of a random subsystem X of a random stabilizer state, therefore can be estimated by the $\mathrm{rank}_{\mathrm{GF}(2)}(M_X)$ of an N by $2|X|$ random binary matrices M_X.

M_X can be constructed by appending $N-1$ rows of random binary vectors to a $2|X|$ by 1 matrix. Every time a new row is added, the rank does not increase with the probability $2^k/2^{2|X|}$, where k is the current rank, and the rank increases otherwise. Therefore, the probability of M_X having the rank of exactly r is:

$$P(\mathrm{rank}_{\mathrm{GF}(2)}(M_X) = r) = \sum_{t\in\mathcal{T}} \prod_{i=1}^{r} \left(\frac{2^{i-1}}{2^{2|X|}}\right)^{t_i - t_{i-1} - 1} \left(1 - \frac{2^{i-1}}{2^{2|X|}}\right), \tag{D.1}$$

where $\mathcal{T}$ is a set of all the configurations of the row numbers where rank increases by 1 and for all $t \in \mathcal{T}$, $t_0 = 0$. For large $|N|$, the above expression is known to be approximated by the following expression [386]:

$$P\left(\mathrm{rank}_{\mathrm{GF}(2)}(M_{|X|}) = 2|X| - \epsilon\right) \approx 2^{-\epsilon(N-2|X|+\epsilon)} \times \prod_{i=\epsilon+1}^{\infty} \left(1 - \frac{1}{2^i}\right) \prod_{i=1}^{N-2|X|+\epsilon} \left(1 - \frac{1}{2^i}\right)^{-1}. \tag{D.2}$$

The average entropy deficit of a random subsystem of size $|X|$ is

$$\langle \Delta S^{(2)}(X)\rangle = \left(\sum_{\epsilon} \epsilon P\left(\mathrm{rank}_{\mathrm{GF}(2)}(M_X) = 2|A| - \epsilon\right)\right) \ln 2 \approx 2^{2|X|-N} \ln 2, \tag{D.3}$$

where the approximation is made by only considering $\epsilon = 0$ and 1, and taking the limit of $1 \ll N - 2|X|$. This result coincides with but slightly larger than the expected entropy deficit of a Haar random state [236, 237] by a constant factor of $2 \ln 2$, which is of the order 1.

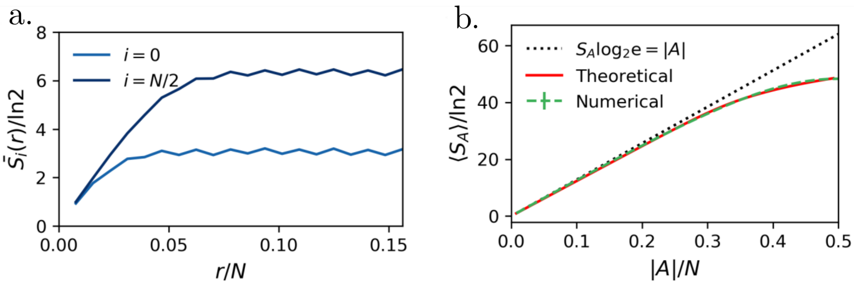

FIGURE E.1: **The average entropy of area-law states.** a. The entanglement entropy of a region consists of r consecutive qubits starting from site i, $S_i(r)$, for $i = 0$ and $i = N/2$ of the nearest-neighbor random Clifford circuit with open boundary condition for $N = 128$ at the number of interactions $t = 2\log_2(N) = 14$ layers. The bar on $\bar{S}_i(r)$ indicates that it is an averaged quantity over the different realizations of the random circuit. For this simulation the average of up to 1000 realizations are taken. b. The average entropy of up to 2e4 random subsystems, A, of an output state of a single trajectory of the random nearest-neighbor circuit ordered by the subsystem size $|A|$ (green dotted line). The theory line (red solid line) is computed using Eq. (E.1) with the entropy as function of r consecutive regions approximated by $S(r) \sim \tilde{S}(r) = \frac{1}{2}\left(\bar{S}_0(r) + \bar{S}_{N/2}(r)\right)$. Here the average of the functions $\bar{S}_0(r)$ and $\bar{S}_{N/2}(r)$ are taken to take account of the effect from the open boundary condition. This figure was reproduced from [185].

E Average Entropy of a Subsystem of Area-Law States in 1-D Quantum Systems

This section is reproduced from sections that were written by the author of this thesis in the following publication: T. Hashizume, G. S. Bentsen, S. Weber, and A. J. Daley, "Deterministic Fast Scrambling with Neutral Atom Arrays," *Physical Review Letters*, **126**, 200603 (2021). [185].

In this section, we derive the expression for average entropy of a subsystems $\mathcal{A}$ consisting of randomly chosen qubits with the subsystem size of $|A|$ drawn from the N-qubit state with area-law entanglement entropy. Let the entanglement entropy of r consecutive region from i^{th} qubit to be expressed as $S_i(r)$. We assume the translational symmetry of this function such that $S_i(r) = S_j(r) = S(r)$ also holds for sites $j \neq i$. Given a particular subsystem and configuration $A \in \mathcal{A}$, one can always find Q_A sets of $q_{A,k}$ ($k = 1, 2, \dots, Q_A$) qubits drawn from a consecutive region in the system. For example a set $A = \{1, 5, 6, 7, 10\}$ has $Q_A = 3$ with $q_{A,1} = 1$ (from $\{1\}$), $q_{A,2} = 3$ (from $\{5, 6, 7\}$), and $q_{A,3} = 1$ (from $\{10\}$). Assuming that the mutual information between the two sets are 0, which is true for the vast majority of cases for the state with the area-law entanglement entropy for $|A| \ll N/2$, one can write the entanglement entropy of a given configuration as $\sum_{k=1}^{Q_A} S(q_{A,k})$. For fixed $|A|$ and Q_A, there are $C(Q_A) = \binom{N-|A|+1}{Q_A}$ possible ways to draw $|A|$ qubits from N qubits such that they have exactly Q_A sets of $\{q_{A,k}\}$ consecutive regions. Finally, there are $p(|A|) = Q_A$ ways to partition a subsystem A into the cells which contains at least 1 consecutive qubits, where $p(|A|)$ is a well known function in number theory called *partition function* (not to be confused with the partition function from the thermodynamics) [387]. From these, the expression for the average entropy of a random subsystem of size $|A|$ of an area-law entangled quantum state is given as

$$\langle S_A \rangle = \frac{\sum_{l=1}^{p(|A|)} C(Q_{A_l}) \sum_{k=1}^{Q_{A_l}} S(q_{A_l,k})}{\sum_{l=1}^{p(|A|)} \sum_{k=1}^{Q_{A_l}} C(Q_{A_l})} \tag{E.1}$$

where A_l (for $l = 1, 2, \ldots, p(|A|)$) goes through all the different ways to partition the subsystems. Shown in Fig. E.1 b. is the average entropy of random subsystems A as a function of its size $|A|$ from the result of a numerical simulation of random nearest-neighbor circuit for $N = 128$ at $t_* = 2m = 14$. The numerical result and the derived formula show excellent agreement with the theoretical values computed explicitly with Eq. (E.1) with $S(r) = \tilde{S}(r) = \frac{1}{2}\left(\bar{S}_0(r) + \bar{S}_{N/2}(r)\right)$, where $\bar{S}_0(r)$ and $\bar{S}_{N/2}(r)$ are estimated by averaging up to 1×10^3 realizations of the circuit (Fig. E.1 a.).

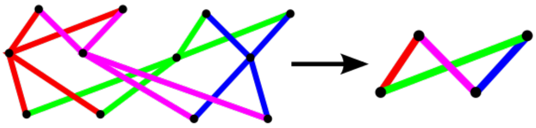

FIGURE E.2: **Block-decimation procedure for the PWR2$_q$ circuit for $q = 2$.** The entire structure on the left is reduced down to a single ribbon-like structure on the right via the renormalization transformation. This figure was reproduced from [186].

E.1 Renormalization Group Solution for full PWR2

This section is reproduced from sections that were written by the author of this thesis in the following publication: T. Hashizume, G. Bentsen, and A. J. Daley, "Measurement-induced phase transitions in sparse nonlocal scramblers," *Physical Review Research*, **4** 013174 (2022). [186].

The PWR2 circuit with size N_0 can be constructed from two sub-systems of size $N_0/2$. This can be done by interleaving the degrees of freedom of the two sub-systems and coupling them together with nearest neighbor interactions.

This self-similar structure allows us to define a renormalization transformation. The transformation consists of two steps: first, a large block as depicted in Fig. E.2 (left), is renormalized to a ribbon-like structure in Fig. E.2 (left). Here the renormalized is done by collapsing the bonds with different colors in Fig. E.2 (left) to the bonds of the corresponding colors in Fig. E.2 (right). This step reduces the size of the vertical dimension by half. In order to reduce the size of the horizontal direction, two of the ribbon-like structure is merged into one. After these steps, the size of the network of $N/2$ by T is reduced to $N/4$ by $T/2$, where N is the number of qubits and T is the number of layers in the original circuit.

Let $\bar{p} = 1 - p$ be the probability of a bond being present in the network. The renormalized probability $R(\bar{p})$ in terms of the probability which a ribbon structure (Fig. E.2, right) is spanned ($\bar{P}_{\text{ribbon}}$) is

$$R(\bar{p}) = \bar{P}_{\text{ribbon}}^2 + 2\bar{P}_{\text{ribbon}}(1 - \bar{P}_{\text{ribbon}}). \tag{E.2}$$

Now we define the condition of the ribbon to be spanned when there exists at least one bond coming out of each the nodes. In terms of the probability of at least a bond being spanned $\bar{p}_{\text{bond}}$, $\bar{P}_{\text{ribbon}}$ is

$$\bar{P}_{\text{ribbon}} = \bar{p}_{\text{bond}}^4 + 4\bar{p}_{\text{bond}}^3(1 - \bar{p}_{\text{bond}}) + 2\bar{p}_{\text{bond}}^2(1 - \bar{p}_{\text{bond}})^2. \tag{E.3}$$

Finally, the probability of the bond being spanned, $\bar{p}_{\text{bond}}$, as a function of $\bar{p}$ is

$$\bar{p}_{\text{bond}} = \bar{p}^4 + 4\bar{p}\bar{p}^3(1-\bar{p}) + 4\bar{p}^2(1-\bar{p})^2. \tag{E.4}$$

The equation $R(\bar{p}^*) = \bar{p}^*$ has a non-trivial fixed point solution in the real domain of $0 < \bar{p}^* < 1$, which is $\bar{p}^* \approx 0.335\ldots$ or equivalently $p^* \approx 0.665\ldots$.

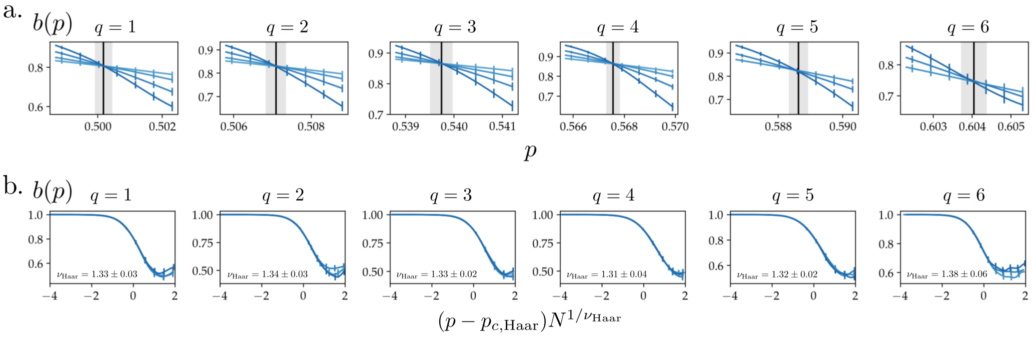

FIGURE F.1: **Full finite-size scaling analysis of the percolation critical points.** a. The binder cumulant $b(p)$ of the percolation network of PWR2_q for $q = 1, 2, \ldots, 6$ for the system sizes $N = 2^8, 2^9, 2^{10}, 2^{11}$ (light to dark blue). The solid vertical lines are the estimated values of the $p_{c,\mathrm{Haar}}$ and the shaded regions are the corresponding 1-sigma errors. b. Collapsed Binder cumulant for $q = 1, 2, \ldots, 6$ for the system sizes $N = 2^8, 2^9, 2^{10}, 2^{11}$ (light to dark blue). This figure was reproduced from [186].

F Finite-Size Scaling of Measurement-Induced Phase Transitions

This section is reproduced from sections that were written by the author of this thesis in the following publication: T. Hashizume, G. Bentsen, and A. J. Daley, "Measurement-induced phase transitions in sparse nonlocal scramblers," *Physical Review Research*, **4** 013174 (2022). [186].

F.1 Finite-Size Scaling for the Percolation Critical Point for $q = 1, \ldots, 6$

Finite-size scaling analysis for the percolation transition of the PWR2_q circuit for $q = 1, 3, 5$ is presented in Fig. 7.2 b. Here we show the finite-size scaling and the crossings of the binder cumulants for all values of $q = 1, 2, \ldots, 6$ for the system sizes $N = 2^8, 2^9, 2^{10}, 2^{11}$.

The error bars are estimated by taking the standard error of the 4000 realizations of the Newman-Ziff algorithm (Ch. 7.3.1). The critical points and their errors are estimated by computing the average intersection points of the curves with 5000 different realizations of the fluctuations added to each of the points. Fluctuations are drawn from the appropriate distribution with the standard error as the standard deviation at each point (Fig. F.1 a.). The critical exponents and their errors

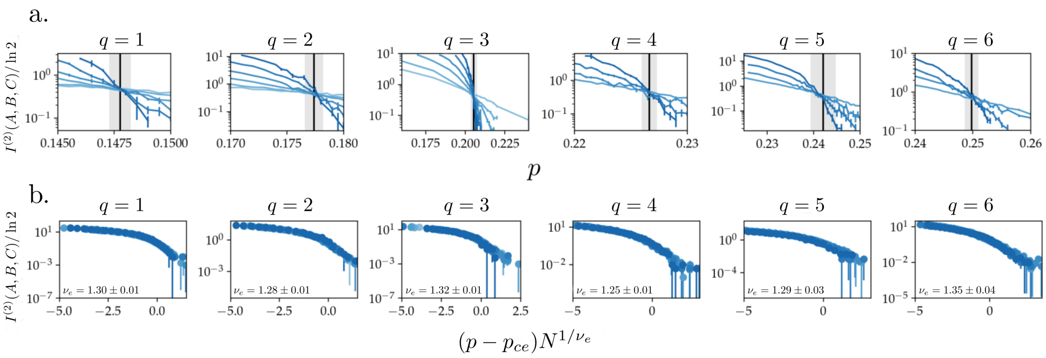

FIGURE F.2: **Full finite-size scaling analysis of the entanglement critical points.** a. The tripartite mutual information $I^{(2)}(A; B; C)$ of initial z-polarized state evolved under a deterministic Clifford PWR2$_q$ circuit until $t = 8N$ for $q = 1, 2, \ldots, 6$ for the system sizes $N = 2^6, \ldots, 2^{11}$ (light to dark blue). The solid vertical lines are the estimated value of the p_{ce} and the shaded region is the corresponding 1-sigma errors. b. Collapsed tripartite mutual information for $q = 1, 2, \ldots 6$ for the system sizes $N = 2^6, \ldots, 2^{11}$ (light to dark blue). This figure was reproduced from [186].

are also estimated by collapsing the 5000 different realizations of the fluctuations added from the same distribution (Fig. F.1 b.).

F.2 Finite-Size Scaling for the Entanglement Critical Point for $q = 1, \ldots, 6$

The finite-size scaling analysis of the entanglement critical points of PWR2$_q$ circuit for $q = 1, 3, 5$ are presented in Fig. 7.3 b. Here we show the finite-size scaling and the crossings of the tripartite mutual information $I^{(2)}(A; B; C)$ for all the values of $q = 1, 2, \ldots, 6$ for system sizes $N = 2^6, \ldots, 2^{11}$ (the system sizes that are smaller than 2^{q+2} are not used in the analysis).

The error bars are estimated by taking the standard error of up to 1000 realizations of the random projective measurement of the evolution to $t = 8N$. The critical points and their errors are calculated by computing the average intersection points of the curves with 5000 different realizations of the fluctuations added to each of the points that are drawn from the appropriate distribution with the standard error as the standard deviation at the point (Fig. F.2 a.). The critical exponents and their errors are also estimated by collapsing the 5000 different realizations of the fluctuations added to the data points from the same distribution (Fig. F.2 b.).

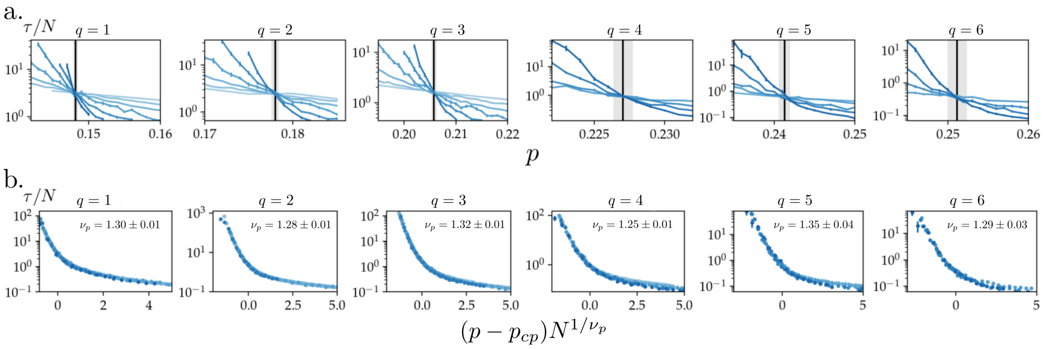

FIGURE F.3: **Full finite-size scaling analysis of the purification critical points.** a. The single-qubit purification time for $q = 1, 2, \ldots, 6$ for the system sizes $N = 2^6, \ldots, 2^{11}$ (light to dark blue). The initial stat is prepared such that there is a qubit entangled to one of the N qubits (system), then the system qubits are scrambled with nearest neighbor random Clifford circuit up to $t = 4N$. The solid vertical lines are the estimated value of the p_{cp} and the shaded region is the corresponding 1-sigma errors. b. Collapsed tripartite mutual information for $q = 1, 2, \ldots, 6$ for the system sizes $N = 2^6, \ldots, 2^{11}$ (light to dark blue). This figure was reproduced from [186].

F.3 Finite-Size Scaling for the Purification Critical Point for $q = 1, \ldots, 6$

The finite-size scaling analysis of the purification critical point of PWR2$_q$ circuit for $q = 1, 3, 5$ are presented in Fig. 7.4 b. Here we show the finite-size scaling and the crossings of the single-qubit purification time for all the values of $q = 1, 2, \ldots, 6$ for system sizes $N = 2^6, \ldots, 2^{11}$, where the system sizes that are smaller than $N < 2^{q+2}$ are not used in the analysis.

The error bars are estimated by taking the standard error of up to 1000 realizations of random projective measurements until the state is purified. The critical points and their errors are estimated by computing the average intersection points of the curves with 5000 different realization of the fluctuations added to each of the points that are drawn from the appropriate distribution with standard error (Fig. F.3 a.). The critical exponents and their errors are also estimated by collapsing the 5000 different realizations of the fluctuations added to the data points from the same distribution (Fig. F.3 b.).

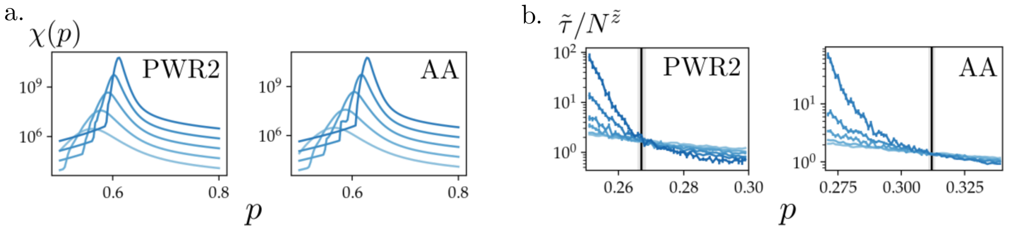

FIGURE F.4: **Detailed finite-size scaling of the MIPT critical points of** $\mathrm{PWR2}_q$ **and AA circuits.** a. Susceptibility, $\chi(p)$, of the complete $\mathrm{PWR2}_q$ (left) and AA (right) percolation networks for the system sizes $N = 2^6, 2^7, \ldots, 2^{10}$. Although there exists sharp peaks, the positions of the peaks depends significantly on the system size. The size of the circuits in these calculations are taken to be $N \times T$. The observables of the bond-percolation of the networks are calculated with Newman-Ziff algorithm by taking the microcanonical ensemble of 4000 trajectories. b. $\tilde{\tau}/N^{\tilde{z}}$ as a function of p without the scaling collapse for complete $\mathrm{PWR2}_q$ (left) and AA (right) circuits for the system sizes $N = 2^6, 2^7, \ldots, 2^{10}$ with $\tilde{z} = 0.21 \pm 0.01$ (PWR2) and $\tilde{z} = 0.170 \pm 0.006$ (AA). The critical point determined from the scaling collapse is marked by the black line and the 1-sigma error is marked by the grey shade. The critical points and their error are $\tilde{p}_c = 0.267 \pm 0.001$ and $\tilde{p}_c = 0.312 \pm 0.001$ respectively. This figure was reproduced from [186].

F.4 Finite-Size Scaling for the Full PWR2 and AA circuits

The finite-size scaling of the MIPTs of the complete $\mathrm{PWR2}_q$ circuit is difficult due to the long-range interactions which give rise to strong boundary effects and the loss of locality. In the percolation transition, this appears as the strong system size dependence of the $p_{\text{peak,Haar}}$ as shown in the figures Fig. 7.6 a. The positions of the peaks are determined from the $\chi(p)$ plotted in Fig. F.4 a.

The loss of locality makes the determination of the entanglement transition impossible. Due to the coupling of distance $N/2$, even in the regime near $p = 1$, the entanglement entropy of the region of size $A < N/2$ is almost guaranteed to be $\sim A(1 - p)$ at the end of the application of $2\log_2 N - 1$ layers of the gates. Therefore we do not argue on the existence of the entanglement transition in the complete $\mathrm{PWR2}_q$ and AA circuits.

The percolation transition suffers from the similar boundary problem. However, the transition does not ask the geometry of the circuit as it only asks the entropy of the reference qubits that are entangled to the system at $t = 0$. The problem in the determination of the critical properties of the purification transition is the number of layers of the even (or odd) blocks which depends on the system size. In this paper, we proposed the potential workaround, which is normalizing the time

t by the number of layers in the even (or odd) blocks by defining $\tilde{t} = t/\log_2 N$. This lead to the empirical scaling law of the form in Eq. (7.10).

As shown in Fig. 7.6 d., the single-qubit purification time $\tau(p)$ collapsed surprisingly well with Eq. (7.10) with the $\tilde{p}_c = 0.27 \pm 0.01$,$\tilde{\nu}_c = 2.08 \pm 0.08$, and $\tilde{z}_c = 0.21 \pm 0.01$ (PWR2) and $\tilde{p}_c = 0.31 \pm 0.01$,$\tilde{\nu}_c = 2.29 \pm 0.05$, and $\tilde{z}_c = 0.170 \pm 0.006$ (AA). For this simulation, $\tilde{\tau}(p)$ is estimated by taking the average over up to 500 realizations of the random projective measurements. The errors in the critical exponents and critical points are estimated by performing the scaling collapse on the 5000 different realizations of the data set with random fluctuations. The random fluctuations are taken from the appropriate distribution with standard deviation of the standard error at each point.

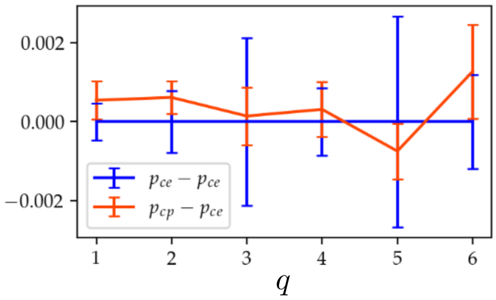

FIGURE G.1: **The differences between entanglement and purification critical points and their errors.** The difference between entanglement and purification critical points of PWR2_q circuit are plotted (red) for $q = 1, 2, \ldots, 6$. The blue line shows the error of entanglement critical points centered at the expected value. There is no statistically significant deviation observed between the entanglement and the purification critical points. This figure was reproduced from [186].

G Gap Between Entanglement (p_{ce}) and Purification (p_{cp}) Critical Points of PWR2_q

This section is reproduced from sections that were written by the author of this thesis in the following publication: T. Hashizume, G. Bentsen, and A. J. Daley, "Measurement-induced phase transitions in sparse nonlocal scramblers," *Physical Review Research*, **4** 013174 (2022). [186].

Whether there exists a gap between the entanglement and purification critical points is a topic of an ongoing debate. Gullans and Huse [123] show that in 1+1D, they occur at the same point in general. Here we show that such a gap is not observed in the PWR2_q circuits for the values of $q = 1, 2, \ldots, 6$. No statistically significant deviations between the entanglement and the purification critical points were observed (Fig. G.1).

Index